博士論文

First Results of Neutrinoless Double Beta Decay Search with KamLAND-Zen

(カムランド禅でのニュートリノを伴わない二重β崩壊探索の最初の結果)

丸藤 (寺島)　亜寿紗

平成 24 年

Abstract

This dissertation presents the first results of KamLAND-Zen, which searches for neutrinoless double-beta decay of ^{136}Xe with xenon loaded liquid scintillator. An observation of the decay would establish the Majorana nature of neutrino and prove the lepton number violation. The decay rate can be translated into the effective neutrino mass if the mechanism of the decay is light Majorana neutrino exchange, which is the most commonly discussed. Some models predict decays with the emission of new bosons so-called Majorons and the effective Majoron-neutrino coupling constant would be evaluated.

Results reported here are based on the data taken from October 12, 2011 to February 9, 2012, corresponding to the exposure of 112.3 days livetime times 125 kg of ^{136}Xe. The measured two-neutrino double-beta decay half-life of ^{136}Xe, $T^{2\nu}_{1/2} = 2.30 \pm 0.02(\mathrm{stat}) \pm 0.12(\mathrm{syst}) \times 10^{21}$ yr, is the most precise value in the world, and is consistent with the recent direct measurement. It supports the conclusion that the directly measured half-life is significantly below the lower limit reported by earlier experiments. From this result, the nuclear matrix element of ^{136}Xe for two-neutrino double-beta decay is evaluated with high accuracy. It will provide useful information for the calculation of that for neutrinoless double-beta decay.

No signal of neutrinoless double-beta decay have been observed. We set a lower limit for the half-life of the decay as $T^{0\nu}_{1/2} > 6.2 \times 10^{24}$ yr at 90% confidence level (C.L.), corresponding to the upper limit on effective neutrino masses of 0.26−0.54 eV (90% C.L.) using recent QRPA and shell model nuclear matrix elements. Such top level sensitivity has been achieved just by initial attempt.

Half-lives of Majoron-emitting neutrinoless double-beta decay with spectral index $n = 1$, 2, 3 and 7 are also estimated. As for "ordinary" decay ($n = 1$), we have obtained lower limit of half-life as $T^{0\nu\chi^0}_{1/2} > 2.6 \times 10^{24}$ yr at 90% C.L. and the corresponding upper limit on the effective Majoron-neutrino coupling constant is less than $(0.8-1.6)\times10^{-5}$ (90% C.L.). This result is the most stringent limit on the effective Majoron-neutrino coupling constant for all double-beta decay nuclei and excludes a previously unconstrained region. The extended limit strongly constrains the possible contribution of ordinary Majoron emitting decay to the light Majorana neutrino exchange in the inverted hierarchy scheme.

Acknowledgements

First of all, I would like to express my great appreciation to my advisor and spokesperson in the KamLAND/KamLAND-Zen experiment, Professor Kunio Inoue. He guided me to experimental particle physics. His continuous advice and suggestions always encouraged me and improved my study.

This work could not have been done without the help of all KamLAND and KamLAND-Zen collaborators over the years. The success of the experiment is supported by the efforts of them. I would like to express my genuine appreciation to every KamLAND and KamLAND-Zen collaborators.

I would like to thank the collaborators especially in Research Center for Neutrino Science (RCNS), Associate Professor Junpei Shirai, Associate Professor Masayuki Koga, Associate Professor Tadao Mitsui, Dr. Kengo Nakamura, Dr. Itaru Shimizu, Dr. Yoshihito Gando, Dr. Haruo Ikeda, Dr. Satoru Yamada and Dr. Kota Ueshima. Their attitude to the study, told me a lot of things to learn. I spent enjoyable research life with them in both Sendai and Kamioka. I also thank to ex-RCNS members, Dr. Yasuhiro Kisihimoto, Dr. Sei Yoshida and Dr. Sanshiro Enomoto. I wish to thank to my fellows, Dr. Hiroko Watanabe and Yasuhiro Takemoto. Thanks to all the graduates and seniors of RCNS, too.

My appreciation goes to all members of the secretarial, technical and other staffs for their support in Sendai and Kamioka life. Special thanks to Dr. Takeshi Koike, Dr. Patrick Decowski and Kana Sasaki for their advice about English.

Finally, I would like to thank my family for their many years of support and a lot of encouragement.

October, 2012
Azusa Gando

Contents

List of Figures

List of Tables

Chapter 1

Introduction

More than 80 years have passed since W. Pauli introduced a new hypothetical particle called the "neutrino" in 1930 [1] to explain the energy deficits and non-conservation of angular momentum in nuclear beta decay processes. The first experimental confirmation of the existence of the neutrino was done by F. Reines and C. L. Cowan in 1950's [2], more than twenty years later. The nature of the neutrino has slowly emerged since then. The most amazing discovery over the past decade is that neutrinos have non-zero masses and mix, demonstrated by neutrino oscillation experiments [3, 4, 5]. These experiments have observed neutrino flavor transition from one to another, and provided the squared-mass differences and mixing angles of neutrinos [6].

One issue arises from non-zero masses of neutrinos, in addition to the absolute mass scale and mass ordering (hierarchy), the question whether neutrinos are Majorana or Dirac particles. Majorana neutrino (*i.e.* if neutrinos are their own antiparticles) was introduced by E. Majorana in 1937 [7]. When the neutrino was treated as being massless, there was no physical distinction between Majorana and Dirac particle. Only electrically neutral massive neutrinos have the possibility to be Majorana particles, making them fundamentally different from other elementary particles. If the neutrino is a Majorana type lepton, it might explain why our universe is dominated by matter, or why only neutrino masses are so light. Currently, the only viable experimental probe of this property is to search for "neutrinoless" double-beta decay.

More than 75 years have passed by since "double-beta decay" was considered by M. Goeppert-Mayer in 1935 [8]. Double-beta decay is a very slow nuclear transition and there are two main modes of the decay. Two neutrino double-beta ($2\nu\beta\beta$) decay which emits two electrons and two anti-neutrinos is described by known physics and those half-lives have been measured in various nuclei. In contrast, neutrinoless double-beta ($0\nu\beta\beta$) decay was predicted theoretically by W. Furry in 1939 [9], but has not yet been observed (excluding one controversial claim). The decay requires two characteristic neutrino properties; the neutrinos must have mass and must be a Majorana type lepton [10]. The decaying nucleus emits only two electrons and no neutrinos, the process thus violates lepton number conservation. This phenomenon is forbidden in the standard model.

Observation of the $0\nu\beta\beta$ decay leads to the conclusion that the neutrino is a

Majorana particle. Furthermore, if $0\nu\beta\beta$ transition is mediated by a light Majorana neutrino (the minimal mechanism of the decay), the $0\nu\beta\beta$ decay rate can translate into an effective neutrino mass, $\langle m_{\beta\beta}\rangle \equiv \left|\Sigma_i U_{ei}^2 m_{\nu_i}\right|$, and it provides the neutrino mass hierarchy and information on the absolute neutrino mass scale. The allowed region of $\langle m_{\beta\beta}\rangle$ as a function of the lightest neutrino is currently provided by oscillation experiments, dividing it into three categories; degenerate hierarchy ($m_1 \sim m_2 \sim m_3$, $\langle m_{\beta\beta}\rangle$ is more than $\sim$60 meV), inverted hierarchy ($m_2 > m_1 \gg m_3$, $\langle m_{\beta\beta}\rangle$ $\sim$20$-$60 meV), and normal hierarchy ($m_3 \gg m_2 > m_1$, $\langle m_{\beta\beta}\rangle$ is less than 20 meV), where m_i is the mass of ν_i. In addition, there is a claim of observation of $0\nu\beta\beta$ decay at a few hundred meV, in the degenerate hierarchy region, with a subset of the collaboration of the ^{76}Ge Heiderberg-Moscow experiment [11, 12, 13]. No experiment has confirmed this claim, and the result is still controversial.

From an experimental point of view, owing to squared-mass constraints from oscillation experiments, specific target of $0\nu\beta\beta$ decay (effective neutrino mass) and required isotopic mass can be determined. Double-beta decay experiments with more than one hundred kilograms of isotopes (called "next generation" experiments) will mostly cover the degenerate hierarchy (100 meV or less) within several years. Searching for the inverted hierarchy (few tens meV of effective neutrino mass) will become possible in the next decade if extension of isotopic mass to an order of one ton is realized. In fact, in 2011, two "next generation" experiments started measurement. Within a few years, several other experiments will also start their measurements. Some experiments already have plans to search for inverted hierarchy in their next phase.

KamLAND-Zen (KamLAND ZEro Neutrino double-beta decay) is one of the "next generation" experiments, which studies ^{136}Xe double-beta decay with xenon loaded liquid scintillator. The detector is part of KamLAND which was primary designed to observe a few MeV neutrinos. It has a large and clean environment such as highly purified 1,000 ton of liquid scintillator. The first phase of KamLAND-Zen was started in September, 2011, with $\sim$300 kg of ^{136}Xe (the largest isotope mass in current double-beta decay experiments), to explore the degenerate hierarchy and to test the claim of observation.

This dissertation presents the first results from KamLAND-Zen, a measurement of half-lives of ^{136}Xe double-beta decay. The paper is organized as follows; physics of neutrinos and double beta decay is summarized in Chapter 2, including the description of various double-beta decay experiments with different techniques. Chapter 3 presents the design and detector description of KamLAND-Zen. Event reconstruction is explained in Chapter 4, and event selection in Chapter 5. Background such as radioactive impurities are assessed in Chapter 6 and the analysis is described in Chapter 7. The conclusions are provided in Chapter 8.

Chapter 2

Neutrino and double beta decay

2.1 Neutrino

The neutrino is one of elementary particles (those are summarized in Tab. 2.1) in the standard model. The three neutrinos are observable via weak interaction, and the existence of only left-handed neutrinos ν_L (or right-handed anti-neutrinos $\overline{\nu}_R$) are experimentally confirmed. The number of active light neutrino was also estimated from the decay width of the Z boson by the accelerator experiment to be 2.984±0.008 [14] in 2006. They are electrically neutral unlike other leptons and quarks.

Table 2.1: Lepton and quark

Particle	Flavor			Charge	Spin
Lepton	e	μ	τ	-1	$1/2$
	ν_e	ν_μ	ν_τ	0	$1/2$
Quark	u	c	t	$+2/3$	$1/2$
	d	s	b	$-1/3$	$1/2$

The neutrino had been traditionally treated as massless lepton in the standard model. However, recent neutrino oscillation experiments have demonstrated that the neutrino has minute but finite mass. Neutrino mass terms can be written as two ways; one is the Dirac mass term

$$\mathcal{L}_D = -m_D\overline{\psi}\psi = -m_D(m\overline{\psi_L}\psi_R + m\overline{\psi_R}\psi_L), \tag{2.1}$$

and another on is the Majorana mass term

$$\mathcal{L}_M = -\frac{m_L}{2}[\overline{(\psi_L)^c}\psi_L + h.c.] - \frac{m_R}{2}[\overline{(\psi_R)^c}\psi_R + \text{h.c.}], \tag{2.2}$$

where ψ is a four component spinor field and satisfies the Dirac equation, $\psi = \psi_R + \psi_L$, $\psi_R = (\frac{1+\gamma^5}{2})\psi$, $\psi_L = (\frac{1-\gamma^5}{2})\psi$, and $\psi^c \equiv \gamma^2\psi$. The Majorana condition, $\psi = \psi^c$ implies $\psi_R = (\psi_L)^c$. The Dirac mass term conserves lepton number. It also

indicates left-handed and right-handed neutrino have the same mass. In contrast, the Majorana mass term violates the lepton number conservation by two units, and it makes a particle and antiparticle indistinguishable. It consists of only left-handed (or right-handed) field. Then left-handed and right-handed neutrino can take different mass scale. When the neutrino has Majorana mass term, it is called the "Majorana neutrino". It is still a question that whether the neutrino is Majorana or Dirac particle. The Majorana neutrino might be a key to answer the following questions.

Very small mass of neutrinos

It is yet to be known that why only the neutrino mass is so small compared with other quarks and leptons as shown in Fig. 2.1. The so-called "see-saw mechanism",

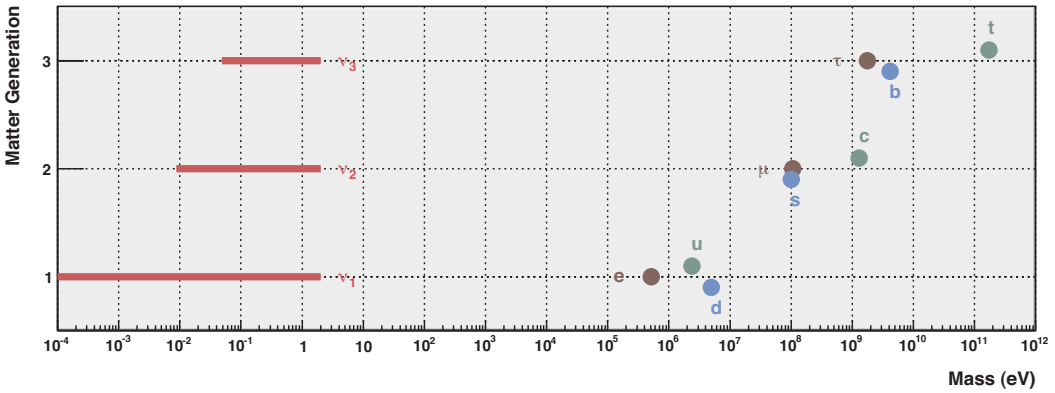

Figure 2.1: Fermion mass hierarchy. Upper limits are provided for the neutrinos assuming the normal hierarchy. Figure from Ref. [15].

introduced by Yanagida and Gell-mann, provides a natural explanation for the question introducing the existence of Majorana neutrinos. In the so called type-I see-saw mechanism, we take $m_L = 0, m_D \neq 0, m_R \neq 0$. Then, from Eq. 2.1 and 2.2, the mass part of the Lagrangian can be rewritten in the matrix form;

$$\mathcal{L}_{D+M} = -\frac{1}{2}\overline{(n_L)^c}\mathcal{M}n_L + \text{h.c.},\ \mathcal{M} = \begin{pmatrix} 0 & m_D \\ m_D & m_R \end{pmatrix}, \tag{2.3}$$

where

$$n_L \equiv \begin{pmatrix} \nu_L \\ (\nu_R)^c \end{pmatrix}. \tag{2.4}$$

The matrices $\mathcal{M}$ and n_L can be written with a unitary matrix $\mathcal{U}$ to see the fields ν_{1L} and N_{1L} with the masses m_1 and M_1, respectively;

$$\mathcal{M}' = \mathcal{U}^T\mathcal{M}\mathcal{U} = \begin{pmatrix} m_1 & 0 \\ 0 & M_1 \end{pmatrix},\ n_L = \mathcal{U}n'_L = \mathcal{U}\begin{pmatrix} \nu_{1L} \\ N_{1L} \end{pmatrix}. \tag{2.5}$$

Then the mass term takes the following form;

$$\mathcal{L}_{D+M} = -\frac{1}{2}\left(m_1\overline{(\nu_{1L})^c}\nu_{1L} + M_1\overline{N^c_{1L}}N_{1L} + \text{h.c.}\right). \tag{2.6}$$

An assumption of $m_R \gg m_D$ derives the mass of neutrinos as $m_1 \cong m_D^2/m_R \ll m_D$ and $M_1 \cong m_R$. Just like the name implies, tiny neutrino mass is derived from large mass scale m_R, which appears in higher unification theories.

The matter-antimatter asymmetry of the universe

The observable universe today is mostly consisted of matter. It indicates the existence of primordial matter-antimatter asymmetry, and it is measured precisely with the ratio of the difference of the number density of matter (n_B) and anti-matter ($n_{\overline{B}}$) relative to the photon number density (n_γ);

$$\eta \equiv \frac{n_B - n_{\overline{B}}}{n_\gamma} = (6.1 \pm 0.3) \times 10^{-10}. \tag{2.7}$$

In order to generate the baryon asymmetry, it requires Sakharov's three conditions [16] as follow,

- Presence of baryon number violating processes,
- C and CP violation,
- Violation of thermodynamic equilibrium.

A system that creates baryon-antibaryon asymmetry (baryogenesis) can be incorporated in the Standard Model (electroweak baryogenesis). However, it constrains Higgs mass [17, 18] lower than the lower bound from LEP experiment or requires supersymmetric extensions to the standard model. Another attempt to explain the asymmetry is leptogenesis, which produced an asymmetry between leptons and anti-leptons in the very early universe. It is then transformed into baryon number asymmetry. Lepton number excess is introduced from assuming the presence of right-handed Majorana neutrinos [19].

2.1.1 Limit on the mass of neutrinos

The neutrino has evidently non-zero mass, but the absolute mass scales and mass ordering remain as unknown. There are wide varieties of the way to measure the neutrino mass. Sensitive measurements and their detectable mass parameters are summarized as follow;

- Neutrino oscillation experiment.
  It provides the difference of squared-mass, $\Delta m_{ij}^2 = |m_i^2 - m_j^2|$, where m_i is the mass of ν_i and i, j are mass eigenstates. It is obtained as a measured value. It is independent on Majorana/Dirac neutrinos.
- Cosmology.
  It provides sum of active three neutrino mass, $m_{\nu_{tot}} \equiv \sum_{i=1}^{3} m_i$. Value depends on the cosmological models and data sets. Upper limits are available at the moment.

- Direct neutrino mass measurement.
  There are three flavors of neutrinos and the most sensitive value comes from the measurement involving electron neutrinos. It provides $m_{\nu_e} \equiv \left[\Sigma |U_{ei}|^2 {m_i}^2\right]^{1/2}$, where U_{ei} is the mixing parameter of the neutrino. Only upper limits are obtained currently. It is independent on Majorana/Dirac neutrinos.

- Neutrinoless double-beta decay.
  It provides the effective neutrino mass $\langle m_{\beta\beta} \rangle \equiv \left| \Sigma_i U_{ei}^2 m_i \right|$. At present, upper limits are provided. It requires Majorana neutrinos.

Each result has a relation with other results. Combining these will provide the understanding of the absolute mass scales of the neutrino. As neutrinoless double-beta decay is described in Section 2.2, the rest of three measurements are summarized here.

Mass constraint from oscillation neutrino experiment

Neutrino oscillation experiments provide neutrino mass information in the form of the difference of squared-mass, which appeared in a survival probability of the neutrino oscillation. Different from other mass measurements, it does not provide an upper limit but a measured value. The value constrains the allowed region of the neutrino mass obtained from other experiments.

Neutrinos change the flavor one to another during propagation. This phenomenon of flavor change is observed with variety of neutrinos (*e.g.* produced in Sun, atmosphere, reactors and accelerators) and known as neutrino oscillation. The oscillation leads to two neutrino properties; non-zero mass and mixing.

The neutrino flavor eigenstates $|\nu_\alpha\rangle$, where $\alpha = e, \mu, \tau$, can be expressed as a linear combination of the mass eigenstates $|\nu_i\rangle$, where i = 1, 2, 3;

$$|\nu_\alpha\rangle = \sum_{i=1}^{3} U_{\alpha i}^* |\nu_i\rangle, \tag{2.8}$$

where U^* is a complex conjugate of Maki-Nakagawa-Sakata (MNS) matrix described with mixing angle θ, and CP phase δ as follows;

$$U_{\alpha i} = \begin{pmatrix} c_{12}c_{13} & s_{12}c_{13} & s_{13}e^{-i\delta} \\ -s_{12}c_{23} - c_{12}s_{23}s_{13}e^{i\delta} & -c_{12}c_{23} - s_{12}s_{23}s_{13}e^{i\delta} & s_{23}c_{13} \\ s_{12}s_{23} - c_{12}c_{23}s_{13}e^{i\delta} & -c_{12}s_{23} - s_{12}c_{23}s_{13}e^{i\delta} & s_{23}c_{13} \end{pmatrix}, \tag{2.9}$$

where $s_{i,j} = \sin\theta_{i,j}$ and $c_{i,j} = \cos\theta_{i,j}$ $(i, j$ = 1,2,3). Considering propagation, a survival probability of neutrinos, $P(\nu_\alpha \to \nu_\beta)$ that one flavor α is changed into another flavor β, can be calculated with the mixing angle and the mass squared difference $\Delta m_{ij}^2 = |m_i^2 - m_j^2|$ as

$$\begin{aligned} P(\nu_\alpha \to \nu_\beta) =& \delta_{\alpha\beta} - 4 \sum_{i>j} \mathrm{Re}(U_{\alpha i}^* U_{\beta i} U_{\alpha j}^* U_{\beta j}^*) \sin^2 \Phi_{ij} \\ &+ 2 \sum_{i>j} \mathrm{Im}(U_{\alpha i}^* U_{\beta i} U_{\alpha j}^* U_{\beta j}^*) \sin^2 2\Phi_{ij}, \end{aligned} \tag{2.10}$$

where

$$\begin{aligned}\delta_{\alpha\beta} =& \begin{cases} 1\ (\alpha = \beta) \\ 0\ (\alpha \neq \beta), \end{cases} \\ \Phi_{ij} \equiv& \frac{\Delta m^2_{ij} L}{2E_\nu} = \frac{1.27 \Delta m^2_{ij}[\mathrm{eV}^2] L[\mathrm{m}]}{E_\nu[\mathrm{MeV}]}, \end{aligned} \tag{2.11}$$

E_ν and L are given values from each oscillation experiment for neutrino energy and the distance between neutrino sources and detection point, respectively. Combining data from different neutrino source, neutrino mixing parameters are obtained. Current values of the best fit taken from Ref. [20] are summarized in Table 2.2. The

Table 2.2: Neutrino mixing parameters for the best fit values and 3σ range from the global 3ν oscillation analysis including recent measurements of θ_{13}. Values taken from Ref. [20]. δm^2 and Δm^2 are defined as $m_2^2 - m_1^2$ and $m_3^2 - (m_1^2 + m_2^2)/2$, respectively with $\Delta m^2 > 0$ for normal hierarchy (NH) and $\Delta m^2 < 0$ for inverted hierarchy (IH).

Parameter	Best fit	3σ range
δm^2 (NH or IH)	$7.54 \times 10^{-5}\mathrm{eV}^2$	(6.99 - 8.18) $\times 10^{-5}\mathrm{eV}^2$
Δm^2 (NH)	$2.43 \times 10^{-3}\mathrm{eV}^2$	(2.15 - 2.66) $\times 10^{-3}\mathrm{eV}^2$
Δm^2 (IH)	$2.42 \times 10^{-3}\mathrm{eV}^2$	(2.14 - 2.65) $\times 10^{-3}\mathrm{eV}^2$
$\sin^2\theta_{12}$ (NH or IH)	0.307	0.259 - 0.359
$\sin^2\theta_{23}$ (NH)	0.398	0.330 - 0.638
$\sin^2\theta_{23}$ (IH)	0.408	0.335 - 0.658
$\sin^2\theta_{13}$ (NH)	0.0245	0.0149 - 0.0344
$\sin^2\theta_{13}$ (NH)	0.0246	0.0150 - 0.0347

results raise new question for the neutrino mass as to which neutrino is the lightest or heaviest (mass hierarchy, see Fig. 2.2). If m_1^2 is the lightest, it is called the normal hierarchy, while in the inverted hierarchy, m_3^2 is the lightest. If the difference is quite smaller than each squared mass, it is called the degenerate hierarchy. This problem remains unknown.

Mass constraint from cosmology

Cosmological observation provides the upper limit of sum of active three neutrino mass, $m_{\nu_{tot}} \equiv \sum m_i$. Calculated value depends on the cosmological model and on how to combine various measurements such as CMB, distribution of galaxies, weak lensing, Hubble constant and so on. The value obtained from seven-year WMAP-only data is $m_{\nu_{tot}} < 1.3$ eV (95% C.L.) [21]. Figure 2.3 (left) shows the allowed region of the neutrino mass obtained from cosmology with each hierarchy. The lightest mass (m_{light}) is evaluated from $m_{\mathrm{light}} \simeq m_{\nu_{tot}}/3 \leq 0.43$ eV and shown as the vertical line in this figure.

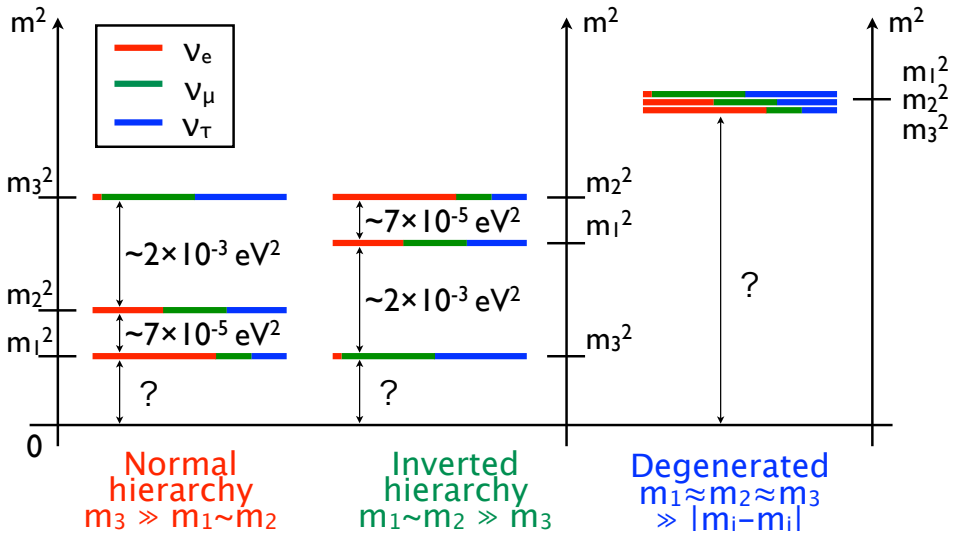

Figure 2.2: Neutrino mass hierarchy information obtained from neutrino oscillation experiments. In the normal hierarchy (left), m_3 is the heaviest similar to other leptons and quarks, while in the inverted hierarchy (center), m_3 is the lightest. In the degenerate hierarchy (right), all of the neutrino mass has quite smaller difference than the each squared mass.

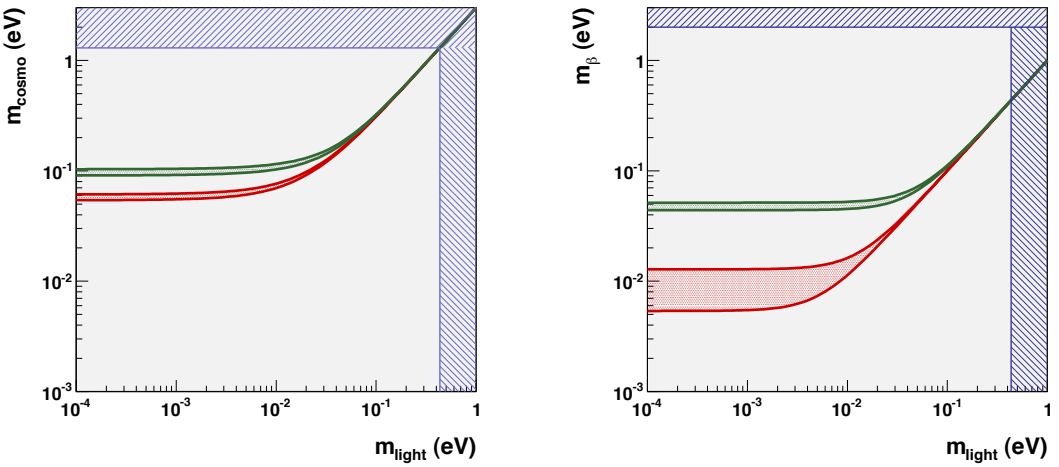

Figure 2.3: Allowed region of the neutrino mass obtained from cosmology (left) and tritium beta decay experiment (right). The m_{light} indicates the lightest mass, $m_{\text{cosmo}} \equiv m_{\nu_{tot}}$, and m_β is the same as m_{ν_e}. The red and green indicate the normal and inverted hierarchy, respectively. Blue region shows current excluded region. Picture is taken from Ref. [15].

Mass constraint from direct neutrino mass measurements

Direct measurements of the neutrino mass are based on the kinematics of a decay. Current best limit of the mass of electron (anti-)neutrino comes from the measurement of differential energy spectrum (especially endpoint) of tritium beta decay via $H^3 \rightarrow He^3 + e^- + \overline{\nu}_e + 18.6$ keV. It implies an upper limit of the lightest neutrino mass. Figure 2.3 (right) shows the constraint on the lightest neutrino mass by beta decay experiments. The limit is obtained from the combined results of the Mainz [22] and Troitsk [23] experiments. It is $m_{\nu_e} < 2$ eV (95% C.L.) [6], and shown as the horizontal line in Figure 2.3 (right). In these measurements, the effective neutrino mass is expressed as $m_\beta \equiv \left[\Sigma |U_{ei}|^2 {m_i}^2\right]^{1/2}$, and it is independent whether the neutrino is a Dirac or Majorana particle. Improvement of the sensitivity will be accomplished by KATRIN experiment in Germany [24]. The measurement will start in 2015, and its targeted sensitivity is 200 meV.

For the reference, the upper limit for the mass of muon neutrino is estimated to be $m_{\nu_\mu} < 0.17$ MeV (90% C.L.) from momentum analysis of the decay $\pi^+ \rightarrow \mu^+ + \nu_\mu$ in 1990's [25]. The upper limit for the mass of tau neutrino is evaluated to be $m_{\nu_\tau} < 18.2$ MeV (95% C.L.) from fitting the distribution of the decay modes, $\tau^- \rightarrow 2\pi^- + \pi^+ + \nu_\tau$ and $\tau^- \rightarrow 3\pi^- + 2\pi^+ + (\pi^0) + \nu_\tau$ in 1990's [26].

2.2 Double beta decay

Double-beta decay is a rare nuclear transition in which a nucleus (A, Z) decays into its isobar $(A, Z+2)$. It has two basic decay modes, two-neutrino double-beta ($2\nu\beta\beta$) decay and neutrinoless double-beta ($0\nu\beta\beta$) decay, detail described in Sections 2.2.1 and 2.2.2, respectively. In addition, there are several decay modes involving the emission of a new boson, called Majoron (Appendix A.1). The $2\nu\beta\beta$ decay is in the standard model, and decay rate of various nuclei has been measured, while $0\nu\beta\beta$ decay requires new physics, and no observation is established. A decay occurs only if the first order decay $(A, Z) \rightarrow (A, Z+1)$ is energetically forbidden or strongly suppressed. A typical double-beta decay candidate is an even-even nucleus due to its paring force. An example of level diagram for A = 136 is shown in Fig. 2.4. In this case, ^{136}Xe, an even-even nucleus, is lighter than ^{136}Cs (odd-odd nucleus). Therefore it is stable against a single beta decay, and it decays into ^{136}Ba via double-beta decay. In nature, more than 60 of isotopes are known as double-beta decay nuclei including β^+ decay and electron capture. From an experimental point of view, isotopes whose transition to single beta decay is completely forbidden are better to use, since single beta decay may become a potential background for the measurement. Exceptions are ^{48}Ca and ^{96}Zr. The decay to (Z, A+1) is allowed energetically, but a large difference of nuclear spin greatly suppresses its transition. Other experimental advantage and disadvantage related to isotopes are summarized in Section 2.3.

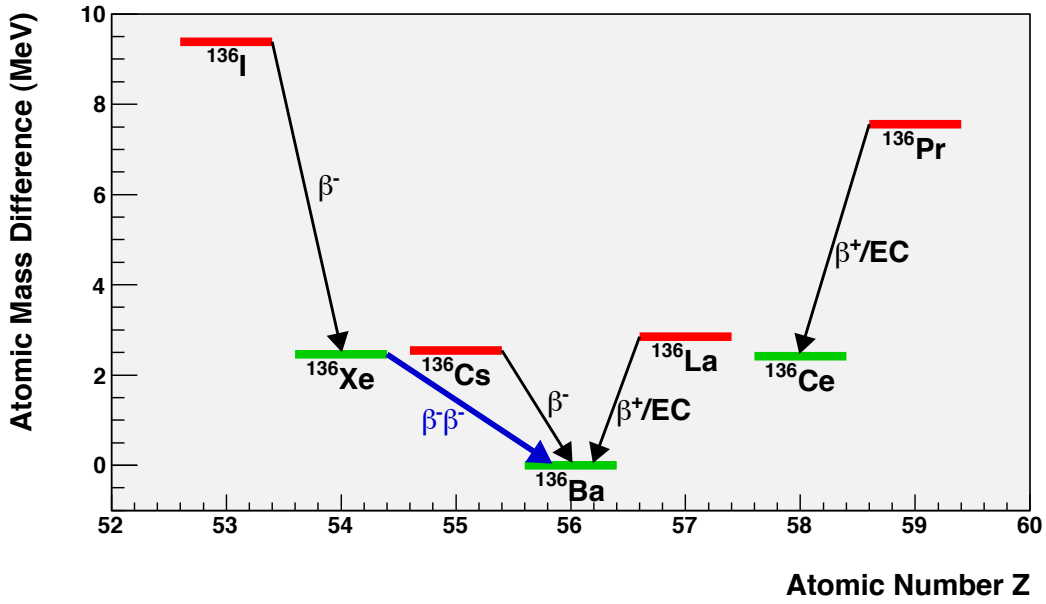

Figure 2.4: Level diagram of A=136 from Ref. [15]

2.2.1 $2\nu\beta\beta$ decay

The standard decay mode, two-neutrino double-beta ($2\nu\beta\beta$) decay was introduced for the first time by M. Mayer in 1935. It consists of two simultaneous beta decays as

$$(A, Z) \rightarrow (A, Z + 2) + 2e^{-} + 2\overline{\nu}_e. \tag{2.12}$$

Feynman diagram of the decay is shown in Fig. 2.5. An observable value is an inverse

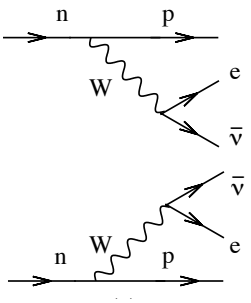

Figure 2.5: Feynman diagram of $2\nu\beta\beta$ decay. Picture taken from Ref. [27].

number of its half-life $T^{2\nu}_{1/2}$, and it is described as follows;

$$(T^{2\nu}_{1/2})^{-1} = G_{2\nu}|M^{2\nu}|^2, \tag{2.13}$$

where $G_{2\nu}$ is a phase space factor and $M^{2\nu}$ is a nuclear matrix element of $2\nu\beta\beta$ decay. A phase space factor is proportional to the 5th power of $(Q_{\beta\beta} - K)$, where $Q_{\beta\beta}$ is Q

value of the double-beta decay, and K is the summed energy of electrons. It can be obtained analytically. Then a nuclear matrix element is derived from $2\nu\beta\beta$ decay experiment. It provides useful information to evaluate the nuclear matrix elements of $0\nu\beta\beta$ decay. Table 2.3 summarizes half-lives measured in several isotopes with various experimental techniques. Measured values are in order of $\sim 10^{19-24}$ yr, the longest time range for radioactive decay process.

Table 2.3: The values of $2\nu\beta\beta$ decay half-lives ($T^{2\nu}_{1/2}$) for various isotopes. Error is not described here. Category of the experiment is summarized in Section 2.3. ECEC stands for the double electron capture process.

Direct measurement		
Isotope	$T^{2\nu}_{1/2}$, yr	Ref.
^{48}Ca	4.4×10^{19}	[28]
^{150}Nd	9.11×10^{18}	[29]
^{150}Nd - ^{150}Sm (0^+_1)	1.33×10^{20}	[30]
^{96}Zr	2.35×10^{19}	[31]
^{100}Mo	7.11×10^{18}	[32]
^{100}Mo - ^{100}Ru (0^+_1)	5.9×10^{20}	[33]
^{82}Se	9.6×10^{19}	[32]
^{116}Cd	2.8×10^{19}	[28]
^{130}Te	7.0×10^{20}	[34]
^{136}Xe	2.30×10^{21}	[35]
^{76}Ge	1.55×10^{21}	[36]

Geochemical measurement		
Isotope	$T^{2\nu}_{1/2}$, yr	Ref.
^{128}Te	$(2.2 - 7.7)\times 10^{24}$	[37]
^{130}Te	$(8 - 27) \times 10^{20}$	[37]
^{130}Ba (ECEC)	2.2×10^{21}	[38]

Radiochemical measurement		
Isotope	$T^{2\nu}_{1/2}$, yr	Ref.
^{238}U	2.0×10^{21}	[39]

2.2.2 $0\nu\beta\beta$ decay

In contrast to $2\nu\beta\beta$ decay, neutrinoless double-beta ($0\nu\beta\beta$) decay,

$$(A, Z) \quad \rightarrow \quad (A, Z+2) + 2e^-, \tag{2.14}$$

violates lepton number conservation, and it points to beyond the standard model. Feynman diagram of the decay is shown in Fig. 2.6. The decay was considered by

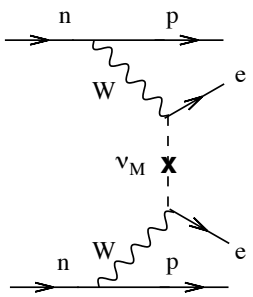

Figure 2.6: Feynman diagram of $0\nu\beta\beta$ decay. Picture taken from Ref. [27].

Furry in 1939. It requires Majorana nature of the neutrino, regardless of the decay mechanism [10]. The $0\nu\beta\beta$ decay has a quite different energy distribution compared to the $2\nu\beta\beta$ decay. As shown in Fig. 2.7, the $2\nu\beta\beta$ decay has a continuous spectrum spread from zero to Q value of a double-beta decay nucleus, while $0\nu\beta\beta$ decay produces a mono-energetic peak at the Q value since all of the decay energy is carried by the electrons except for the negligible kinetic energy of the nuclear recoil. Double-beta decay experiments search for this peak[1]. It has never been observed except for one controversial claim.

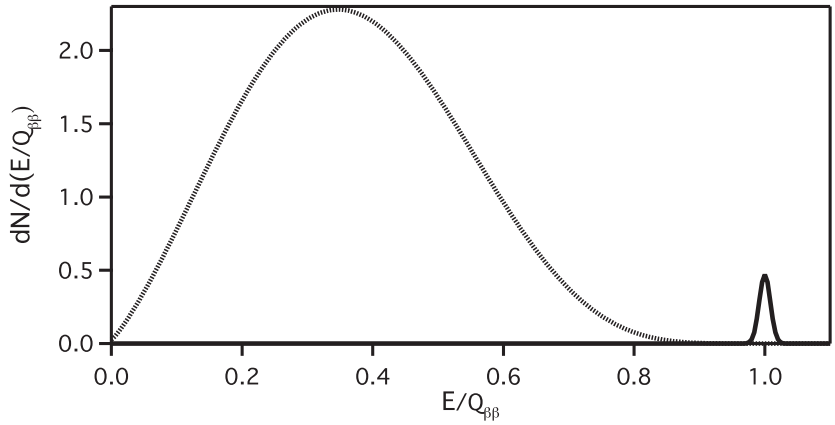

Figure 2.7: Schematic view of energy spectrum of $2\nu\beta\beta$ (left dotted continuum) and $0\nu\beta\beta$ (right solid peak) decay. Assumed a 1-σ energy resolution of 2%. $Q_{\beta\beta}$ is Q value of a nuclei. Picture from Ref. [27].

The minimal mechanism of $0\nu\beta\beta$ decay is a simple exchange of a light Majorana neutrino. It requires no new physics except for the neutrino being a Majorana particle. The decay rate of $0\nu\beta\beta$, $(T^{0\nu}_{1/2})^{-1}$, is expressed as follows;

$$(T^{0\nu}_{1/2})^{-1} = G_{0\nu} \left|M^{0\nu}\right|^2 \langle m_{\beta\beta}\rangle^2, \tag{2.15}$$

where $T^{0\nu}_{1/2}$ is a half-life, $G_{0\nu}$ is a phase space factor, and $M^{0\nu}$ is a nuclear matrix element of $0\nu\beta\beta$ decay. From this relation, we can evaluate the effective neutrino mass, $\langle m_{\beta\beta}\rangle$ and it provides information of the absolute mass scale and mass hierarchy of neutrinos. The phase space factor is proportional to the 5th power of Q value and is calculable. Evaluation of the nuclear matrix element mainly depends on the theoretical calculation, and it is very difficult (Section 2.2.3). This uncertainty becomes the largest uncertainty to estimate the effective neutrino mass. The effective Majorana neutrino mass, $\langle m_{\beta\beta}\rangle$, is defined as

$$\begin{aligned}\langle m_{\beta\beta}\rangle &\equiv \left|\Sigma_i U^2_{ei} m_{\nu_i}\right| \\ &= c^2_{12}c^2_{13}e^{i\alpha_1}m_1 + c^2_{13}s^2_{12}e^{i\alpha_2}m_2 + s^2_{13}e^{-2i\delta}m_3,\end{aligned} \tag{2.16}$$

where α_1 and α_2 are Majorana phases, which consist of diagonal matrix P, $P = diag(e^{i\alpha_1/2}, e^{i\alpha_2/2}, 1)$. If the neutrino is a Majorana particle, PMNS matrix (Eq. 2.9)

[1]Actually, the peak will be widen only by the energy resolution of the detector.

is multiplied by this matrix. The allowed region of the effective neutrino mass can be evaluated from Eq. 2.16, difference of squared-mass, mixing angles and assumption of the mass hierarchy. The relationship of the effective neutrino mass and the lightest neutrino mass is shown in Fig. 2.8. For the normal and inverted hierarchy, the

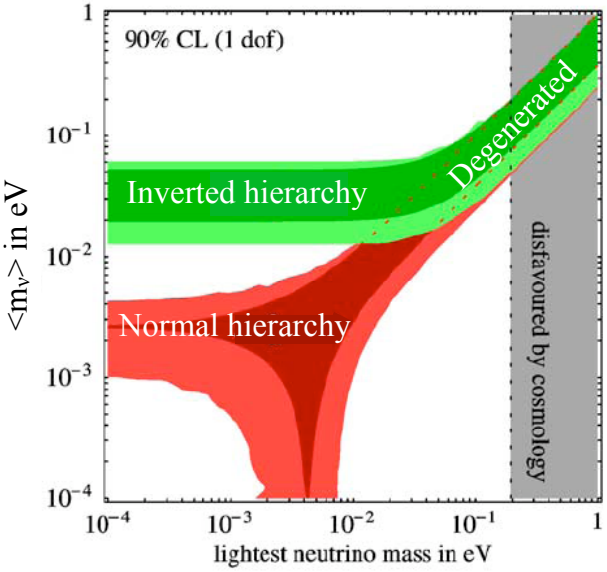

Figure 2.8: Allowed region of the effective neutrino mass as a function of the lightest neutrino mass. The red and green indicate the normal and inverted hierarchy, respectively.

lightest neutrino is m_1 and m_3, respectively. A constraint on the lightest neutrino mass comes from cosmology and it will also come from the beta decay experiment. Observation of $0\nu\beta\beta$ decay establishes the Majorana nature of the neutrino. On the other hand, non-observation of $0\nu\beta\beta$ decay combined with a determination of the neutrino mass by beta decay experiments and/or cosmology will provide the Dirac nature of the neutrino. Similarly, if accelerator experiments succeeds in the determination of the mass hierarchy with non-observation of $0\nu\beta\beta$ decay, it will provide the Dirac nature of the neutrino.

2.2.3 Nuclear matrix element

Considering a translation from $0\nu\beta\beta$ decay half-life to the neutrino effective mass (or effective coupling constant of a Majoron and the neutrino), and then comparing the sensitivity with different isotopes (experiments), knowledge of the nuclear matrix element, denoted as M, becomes essential. Although several attempts are made to evaluate those values experimentally, in general, it is obtained theoretically. The reliability of calculation has improved. However, it is still a significant uncertainty source of the translation, since it includes all nuclear structure effects and it makes the calculation quite difficult.

The nuclear matrix element of $0\nu\beta\beta$ decay ($M^{0\nu}$) is described with sum of the Gamow-Teller (GT), Fermi (F) and tensor (T) contributions,

$$\begin{aligned} M^{0\nu} &= -\frac{M^{0\nu}_{\mathrm{F}}}{(g^{\mathrm{eff}}_{\mathrm{A}})^2} + M^{0\nu}_{\mathrm{GT}} - M_{\mathrm{T}} \\ &=< 0^+_i | \sum_{kl} \tau_k \tau_l [-\frac{H_F(r_{kl})}{(g^{\mathrm{eff}}_{\mathrm{A}})^2} + H_{GT}(r_{kl}) \vec{\sigma}_k \cdot \vec{\sigma}_l - H_T(r_{kl}) S_{kl}] | 0^+_f >, \end{aligned} \tag{2.17}$$

where $g^{\mathrm{eff}}_{\mathrm{A}}$ is the effective axial coupling in nuclear matter, $H(r_{kl})$ is neutrino potential, $\vec{\sigma}_{k(l)}$ is spin Pauli matrix, and S_{kl} is

$$S_{kl} = 3(\vec{\sigma}_k \cdot \hat{\mathbf{r}}_{kl})(\vec{\sigma}_l \cdot \hat{\mathbf{r}}_{kl}) - \vec{\sigma}_k \cdot \vec{\sigma}_l. \tag{2.18}$$

Nuclear matrix element involves many virtual intermediate states.

Evaluation of $M^{0\nu}$ has various approaches. We cannot calculate it exactly as it is due to the complicated nuclear structure and its interactions. Then an approximation is required. For example, Interacting Shell Model (ISM) considers only a limited number of orbits, but all possible correlations are included. In contrast to ISM, Quasi-particle Random-Phase Approximation (QRPA) calculation includes a number of single particle states, but configurations are limited. It includes a parameter g_{pp}, which renormalizes the particle-particle interactions. This value is determined to reproduce the known half-lives of $2\nu\beta\beta$ decay. The QRPA calculation covers almost all nuclei, while ISM faces computational complexity at the large atomic number. Figure 2.9 shows calculation results of nuclear matrix elements with different models.

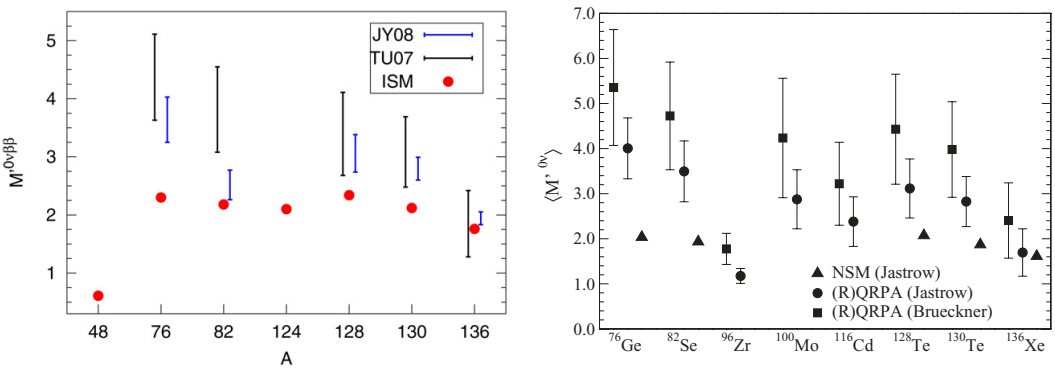

Figure 2.9: Nuclear matrix element calculated by different models. Left figure shows the results of ISM (red point) and QRPA models for the comparison [40]. Right picture presents the result of QRPA and renormalized QRPA models [41]. For the comparison, the results of large-scale shell model (noted as NSM) are also presented.

2.3 Double-beta decay experiment

Double-beta decay experiments also have a long history. The experiments are catego-

rized into two: (1) indirect measurement (Section 2.3.1) and (2) direct measurement (Section 2.3.2). Early indirect (geochemical) measurements had much higher sensitivities than direct measurements. Current mainstream in experiments is direct measurements. Ideal experimental design of the decay has been discussed (see *e.g.* Ref. [27] and references therein). However, realization of all experimental desirable features incorporated in one experiment is impossible. Therefore, there are various experiments with diverse isotopes and techniques.

2.3.1 Indirect measurement

Geochemical measurement

Geochemical double-beta decay experiment was started with ^{130}Te in 1949. This method is suitable for double-beta decay isotopes whose daughters are noble gases such as ^{82}Se (^{82}Kr), ^{128}Te (^{128}Xe) and ^{130}Te (^{130}Xe). Confined noble gas in an ancient rock sample is firstly extracted and then the isotopic composition is measured. After taking into account the contribution from the effect of nuclear reactions such as neutrons and muon induced ones, an excess of amount compared with natural abundance is estimated. Finally it is translated into half-life of the decay. An advantage is that the measurement can provide a quite long half-life as not a lower limit but a measured value (^{128}Te, $\sim 10^{24}$ yr), while a disadvantage is inseparable of $0\nu\beta\beta$ and $2\nu\beta\beta$ decay. First observation of double-beta decay with this method was achieved with ^{130}Te in 1950 [42] (as was understood in many years later). The measurements declined in 1990's but it was revived at the beginning of 2000's. First observation of the double electron capture process of ^{130}Ba was achieved at that time. Measured half-lives are summarized in Table 2.3 in Section 2.2.1.

Radiochemical Measurement

First radiochemical experiment with ^{238}U was also carried out in 1950. An approach is similar to the geochemical measurement. Half-life is provided from the number of accumulated daughter isotopes. On the other hand, this laboratory experiment can decrease uncertainties associated with an amount of original isotopes and a storage time. To detect effectively, suitable isotopes have such daughter isotopes that half-life is short and rarely exist in nature. First observation was reported in 1991 with 33-year stored ^{238}U to be $T_{1/2} = (2.0 \pm 0.6) \times 10^{21}$ yr [39].

2.3.2 Direct measurement

A direct measurement of double-beta decay started in the late 1940's with Geiger counter and 25 g of enriched ^{124}Sn, but we had to wait for the first observation of $2\nu\beta\beta$ decay (^{82}Se, time projection chamber [43]) for about 40 years. Various experiments with a variety of isotopes and techniques have been launched and improved their sensitivities (sometimes, "positive" results appeared and disproved by later experiments). Currently, the half-lives of $2\nu\beta\beta$ decay for about ten nuclei are measured ($\sim 10^{19-21}$ yr). Furthermore, those of the transition to the excited stats are also detected (see Table 2.3 in Section 2.2.1). A lower limit of half-life of $0\nu\beta\beta$ decay is in the order of 10^{24-25} yr, and corresponding neutrino effective mass reaches

to a few hundred meV. In 2011, to search the sensitivity of 10^{25-26} yr half-life or less than 100 meV of the effective neutrino mass region, two next generation experiments, which have more than 100 kg of isotopes, started running. In addition, many prototypes of the next generation experiments are running, and many other experiments are also proposed.

In the following paragraphs, experimental techniques and isotopes including strengths and limitations, and some major experiments are summarized. Quoted values of the effective neutrino mass in the summary are not recalculated for a certain nuclear matrix element model. Therefore its allowed range is different depending on the papers.

Technique and isotopes

Two features of double-beta decay, long half-life ($>10^{19}$ yr at least) and low Q value (a few-MeV at a maximum), require at least two experimental conditions that,

- large isotope mass (high scalability of experiments will be preferable),
- low background environment.

For example, to reach the neutrino effective mass ∼50 meV (in the inverted hierarchy), its half-life becomes an order of 10^{26-27} yr, and a hundred kg to a ton scale of isotopes will be needed for reasonable running time (high detection efficiency is also ideal). In addition, following requirements will improve the sensitivity that

- High energy resolution.
  It will help sensitivity improvement since there is an intrinsic background of $0\nu\beta\beta$ from a tail of $2\nu\beta\beta$ decay.
- Particle identification and angular distribution.
  It will provide good signal/background separation.
- Operation in underground and (active-)shielding.
  It will help to reduce muon-induced backgrounds.

Currently, no experiment exists which satisfies all the described properties above.

Natural abundance and Q value of double-beta decay isotopes are summarized in Fig 2.10. Considering experimentally suitable isotopes, there are eleven nuclei whose Q value is more than 2 MeV (^{48}Ca, ^{150}Nd, ^{96}Zr, ^{100}Mo, ^{82}Se, ^{116}Cd, ^{130}Te, ^{136}Xe, ^{124}Sn, ^{76}Ge and ^{110}Pd, ordering high energy to low energy) summarized in Table 2.4. Desirable features of isotopes are as follow;

- High Q value. (*e.g.* ^{48}Ca (4.27 MeV), ^{150}Nd (3.37 MeV) and ^{96}Zr (3.35 MeV)).
  In the phase space factor, a term, the 5th power of Q value, appears. It is also useful for the background reduction.
- High natural abundance or establishment of the enrichment. (*e.g.*^{130}Te (N.A.[2] = 34%). ^{76}Ge and ^{136}Xe enrichment factor is >80% and ∼90%, respectively).
  It introduces small contamination in double-beta decay isotopes.

[2]N.A. = natural abundance.

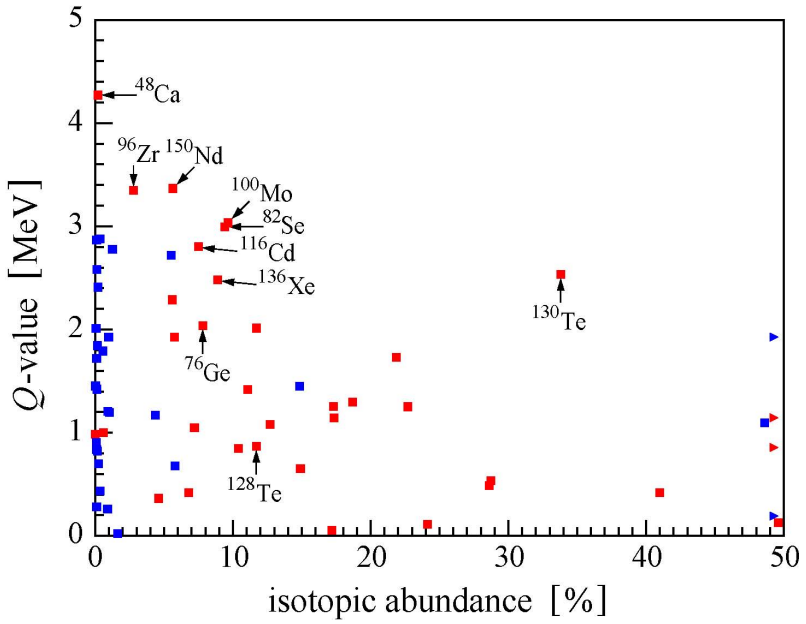

Figure 2.10: Natural abundance and Q value of double-beta decay isotopes. Red points show $\beta^-\beta^-$ decay and blue points show others.

- Slow $2\nu\beta\beta$ decay. (*e.g.* ^{76}Ge and ^{136}Xe ($\sim 10^{21}$ yr)).
  It reduces its tail in $0\nu\beta\beta$ region, and it requires modest energy resolution.

Unfortunately, there is no ideal isotope, too. For example, high Q value isotopes such as ^{48}Ca (N.A. = 0.19%) and ^{150}Nd (N.A. = 5.7%) have difficulty with enrichment (and it results in high cost). These requirements result in various double-beta decay experiments.

Major past experiments

Five experiments are introduced here. Best limits of $0\nu\beta\beta$ decay are provided by the HEIDELBERG-MOSCOW and IGEX experiments with ^{76}Ge and the CUORICINO experiment with ^{130}Te. Their high energy resolution (less than 10 keV at each Q value) made possible to improve their sensitivities. One claim of observation was also reported with ^{76}Ge. The DAMA experiment provides the limit of ^{136}Xe double-beta decay. The NEMO-3 experiment is also notable. It provides the limits of seven(!) double-beta decay isotopes. Only this experiment measured tracking information.

• HEIDELBERG-MOSCOW (Ge detector, ^{76}Ge)
The HEIDELBERG-MOSCOW experiment measured double beta decay of ^{76}Ge with five germanium detectors. It has quite high energy resolution (~4 keV FWHM at Q value). The experiment ran from 1990 to 2003 at Laboratori Nazionali del Gran Sasso (LNGS). The enrichment of ^{76}Ge was 86% and the total active mass of the detector was 10.96 kg. The half-life of ^{76}Ge $2\nu\beta\beta$ decay was evaluated for the first

Table 2.4: Double-beta decay isotopes whose Q values is more than 2 MeV.

Transition	Q value (keV)	N.A.(%)
^{48}Ca $\rightarrow$ ^{48}Ti	4273.6 $\pm$ 4	0.19
^{76}Ge $\rightarrow$ ^{76}Se	2039.006 $\pm$ 0.050	7.6
^{82}Se $\rightarrow$ ^{82}Kr	2995.50 $\pm$ 1.87	8.7
^{96}Zr $\rightarrow$ ^{96}Mo	3347.7 $\pm$ 2.2	2.8
^{100}Mo $\rightarrow$ ^{100}Ru	3034.40 $\pm$ 0.17	9.4
^{110}Pd $\rightarrow$ ^{116}Cd	2017.85 $\pm$ 0.64	7.5
^{116}Cd $\rightarrow$ ^{116}Sn	2813.50 $\pm$ 0.13	7.5
^{124}Sn $\rightarrow$ ^{124}Te	2287.80 $\pm$ 1.52	5.8
^{130}Te $\rightarrow$ ^{130}Xe	2527.01 $\pm$ 0.32	34.1
^{136}Xe $\rightarrow$ ^{136}Ba	2457.83 $\pm$ 0.37	8.9
^{150}Nd $\rightarrow$ ^{150}Sm	3371.38 $\pm$ 0.20	5.7

time as to be $T^{2\nu}_{1/2} = [1.55 \pm 0.01(\text{stat})^{+0.19}_{-0.15}(\text{sys})] \times 10^{21}$ yr with an exposure of 47.7 kg·yr. A lower limit on the half-life of ^{76}Ge $0\nu\beta\beta$ decay was set to $T^{0\nu}_{1/2} > 1.9\times10^{25}$ yr (90% C.L.) with 35.5 kg·yr as shown in Fig. 2.11. The corresponding upper limit of the effective neutrino mass was 0.35 eV. They also evaluated the half-life limits for Majoron-emitting decay with spectral index $n = 1$ and 3 to be 6.4×10^{22} yr and 1.4×10^{22} yr, respectively [36].

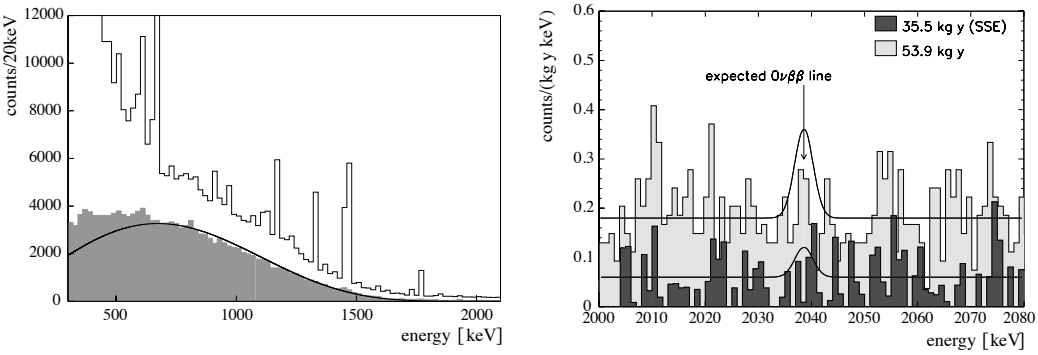

Figure 2.11: Energy spectrum of $2\nu\beta\beta$ decay (left) and $0\nu\beta\beta$ region (right) [36].

• Claim of Observation (Ge detector, ^{76}Ge)
A subset of the Heidelberg-moscow collaboration claimed the observation of $0\nu\beta\beta$ decay with a half-life of 1.5×10^{25} yr (3.1σ C.L.) in 2001 [11]. This statement was disagreed with other part of collaborators [44] and obtained critical replies [45, 46]. They developed their analysis and improved statistical significance. In 2006, they reported half-life of ^{76}Ge $0\nu\beta\beta$ decay, $T^{0\nu}_{1/2} = 2.23^{+0.44}_{-0.31} \times 10^{25}$ yr with more than 6σ significance [13]. Energy spectrum is shown in Fig. 2.12. It corresponds to 0.32 $\pm$ 0.03 eV of the effective neutrino mass. This result has not been accepted by the whole community, but no confirmation or refutation of this claim has been obtained.

The next generation experiment will solve the controversial issue.

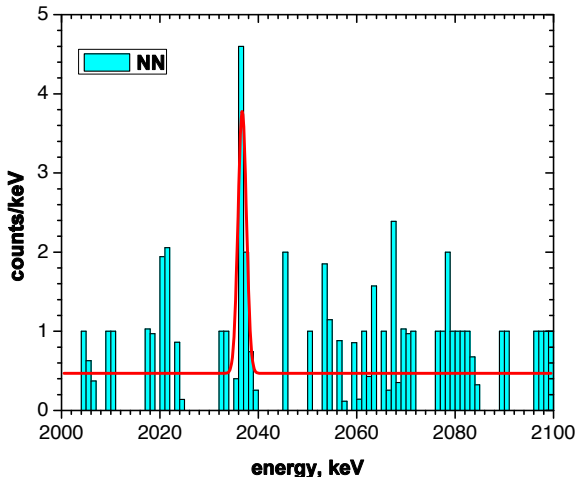

Figure 2.12: Energy spectrum of ^{76}Ge $0\nu\beta\beta$ decay [13]

• IGEX (Ge detector, ^{76}Ge)
The International Germanium Experiment (IGEX) also searched for the ^{76}Ge neutrinoless double-beta decay with 86% isotopically enriched germanium crystals. The experiment started in 1990's and detectors operated in three different laboratories: the Homestake gold mine in USA, the Canfranc in Spain, and the Baskan Neutrino Observatory (BNO) in Russia [47]. In an exposure of 117 mol yr (∼8.8 kg·yr), the ^{76}Ge $0\nu\beta\beta$ half-life of $T^{0\nu}_{1/2} > 1.57 \times 10^{25}$yr (90% C.L.) was obtained. The corresponding effective neutrino mass was in the range of 0.33−1.35 eV [48].

• DAMA (Scintillator, ^{136}Xe)
DAMA searched for the $2\nu\beta\beta$ and $0\nu\beta\beta$ decay of ^{134}Xe and ^{136}Xe with low background liquid xenon scintillator at LNGS. Total amount of liquid xenon was 2 liters (∼6.5 kg) containing 17.1% of ^{134}Xe and 68.8% of ^{136}Xe, and the data collected over 8823.54 h. Corresponding exposure for the ^{134}Xe and ^{136}Xe was 1.1 kg·yr and 4.5 kg·yr, respectively. Obtained lower limits of ^{136}Xe $2\nu\beta\beta$ and $0\nu\beta\beta$ half-life were $T^{2\nu}_{1/2} > 1.0 \times 10^{22}$yr (90% C.L.) and $T^{0\nu}_{1/2} > 1.2 \times 10^{24}$yr (90% C.L.), respectively. For ^{134}Xe, $0\nu\beta\beta$ half-life was set to $T^{0\nu}_{1/2} > 5.8 \times 10^{22}$yr (90% C.L.). They also evaluated the half-life limits for $2\nu\beta\beta(0^+ \rightarrow 2^+)$ and Majoron-emitting decay with spectral index n = 1 for ^{136}Xe to be 9.4 $\times 10^{21}$ yr and 5.0 $\times 10^{23}$ yr, respectively [49].

• CUORICINO (Bolometer, ^{130}Te)
The CUORICINO searched for the ^{130}Te neutrinoless double-beta decay with 40.7 kg of TeO_2 (11.3 kg of ^{130}Te) crystals. ^{130}Te has high natural abundance. This experiment operated between 2003 and 2008 at LNGS, with a total exposure of 19.75 kg·yr of ^{130}Te. The primary detector was a tower array of 62 TeO_2 crystals as bolometric detectors. In the detector, an energy deposit (E) was converted to

the heat, raising temperature of the crystals (ΔT), and it was measured as an electric signal by thermistors. To obtain the detectable ΔT with a small energy deposition, heat capacity C should be sufficiently small since they have the relation that $\Delta T = E/C$. C is proportional to the 3rd power of temperature, then low temperature is required. This detector is operated at $\sim$10 mK, and ΔT at the Q value is 1.77×10^{-4}K. It had also high energy resolution ($\sim$8 keV FWHM at the Q value). The obtained lower limit of the ^{130}Te $0\nu\beta\beta$ half-life was $T^{0\nu}_{1/2} > 2.8 \times 10^{24}$yr (90% C.L.), and the corresponding upper bound on the effective neutrino mass was 300$-$710 meV [50]. They also evaluated the lower limits on the half-lives of the exited 0^+ state in ^{130}Xe for $2\nu\beta\beta$ and $0\nu\beta\beta$ decays to be 1.3 $\times10^{23}$ yr and 9.4 $\times10^{23}$ yr at 90% C.L., respectively [51].

• NEMO-3 (Track-calo detector, ^{100}Mo, ^{82}Se, ^{96}Zr, ^{150}Nd, ^{116}Cd, ^{48}Ca, and ^{130}Te) The NEMO-3 was cylindrical tracking detector holding totally $\sim$9 kg of seven different double-beta decay isotopes. Different from above experiments, isotopes do not play a role of detection part. It can detect the path and energy of the individual electrons, in addition to the total energy deposit. The tracks are reconstructed from information of drift wire chamber in Geiger mode and energy is measured by surrounding plastic scintillators coupled with PMTs. Magnetic field created around the detector is used to identify electron-positron pairs. It ran from 2003 to January, 2011 in Fréjus Underground Laboratory in France. They measured $2\nu\beta\beta$decay clearly with seven isotopes (^{100}Mo (6914 g) [32], ^{82}Se (932 g) [32], ^{96}Zr (9.4 g) [31], ^{150}Nd (37 g) [29], ^{116}Cd (405 g) [28], ^{48}Ca (7 g) [28], and ^{130}Te (454 g) [34]). The energy spectra of ^{100}Mo double-beta decay are shown in Fig. 2.13. The best lower limit of half-life for $0\nu\beta\beta$ decay is obtained from ^{100}Mo to be $T^{0\nu}_{1/2} > 1.1 \times 10^{24}$yr (90% C.L.), and the corresponding upper bound on the effective neutrino mass was set to be 0.45$-$0.93 eV with various kinds of nuclear matrix elements [28]. They also provide lower limits of half-life for other double beta decay process such as Majoron emission (spectral index n = 1, 2, 3 and 7), right-handed currents, and transition to the excited states for each isotope.

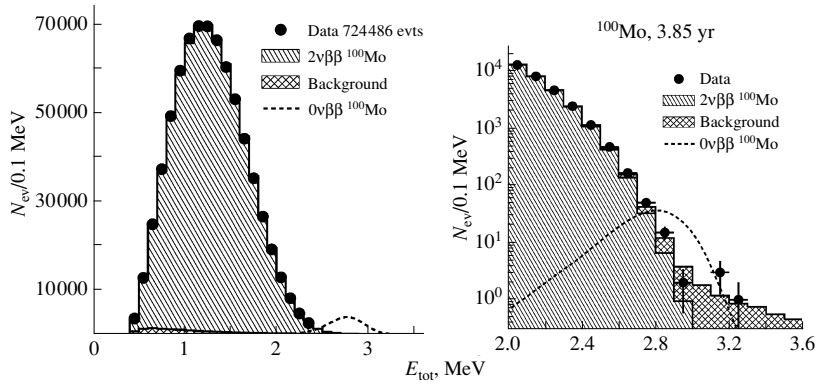

Figure 2.13: Energy spectrum of ^{100}Mo $2\nu\beta\beta$ decay (left) and $0\nu\beta\beta$ (right) region [28]

Major current and future experiments

Although there are many proposal for experiments, only 4 experiments are introduced here. KamLAND-Zen is not included. Common feature of experiments is a large amount of isotopes. Except for EXO, rests are a successor of the past experiment: Ge experiments, CUORICINO and NEMO-3. Their experimental techniques are already established. Therefore they construct the prototypes of the detector with improvements, and then extend them.

• EXO-200 (TPC, ^{136}Xe, running)
The Enriched Xenon Observatory (EXO) is one of the "next generation" experiments. It uses 200 kg of 80% enriched ^{136}Xe with a time projection chamber (TPC), which detects both scintillation and ionization. It started running in early 2011 at Waste Isolation Pilot Plant (WIPP) in America and observed ^{136}Xe $2\nu\beta\beta$ decay for the first time to be $T^{2\nu}_{1/2} = [2.23 \pm 0.017(stat) \pm 0.22(sys)] \times 10^{21}$ yr. Half-life of $0\nu\beta\beta$ decay is also obtained (one of the current best value) that $T^{0\nu}_{1/2} > 1.6 \times 10^{25}$yr and the corresponding effective neutrino mass range of 140−380 meV [52].

Final design of EXO uses 1 ton of ^{136}Xe to search for inverted hierarchy with newly constructed detector. For the technical issue, they aim to identify daughter barium ion to make ^{136}Xe double-beta decay free from backgrounds.

• GERDA and MAJORANA (Ge detector, ^{76}Ge, running and planning)
GERDA searches for ^{76}Ge double-beta decay with arrays of high-purity germanium detectors, which are refurbished from those used in HEIDELBERG-MOSCOW and IGEX. Data taking for the phase I started in early 2011 with ∼18 kg of isotope. Currently no published result is available, but they reported observation of clear $2\nu\beta\beta$ decay and achievement of a low background environment compared to the previous Ge experiment. They will start the phase II in 2013 adding 20 kg of isotopes to reach half-life in the order of 10^{26} yr.

MAJORANA is also a proposed experiment which uses high-purity germanium detectors. With 20 kg of isotopes, it will start running in 2013.

• CUORE (Bolometer, ^{130}Te, running and planning)
The Cryogenic Underground Observatory for Rare Events (CUORE) is a successor of CUORICINO (TeO_2 bolometer tower). An array of 19 vertical towers will include ∼200 kg of ^{130}Te. A prototype of CUORE, a single tower, CUORE-0 started operation in 2012 to test newly constructed assembly line and level of backgrounds. Target of CUORE-0 is to reach half-life in the order of 10^{24-25} yr and CUORE's in 10^{26} yr. The corresponding neutrino effective mass is less than 100 meV.

• Super-NEMO (Track-calo detector, ^{82}Se, demonstrator construction)
Super-NEMO is a new installment of the NEMO detector series. 100 kg of ^{82}Se with combination of improved tracking and calorimeter detectors aim to search for half-life in order of 10^{26} yr. The corresponding neutrino effective mass is less than 100 meV. Its demonstrator which has 7 kg of ^{82}Se started construction in the laboratory and will start operation in 2014.

Except for above, many experiments are running or proposed such as CANDLES (CaF_2 crystals in liquid scintillator, ^{48}Ca), DCBA (drift chamber, ^{150}Nd), AMORE ($CaMoO_4$ crystals, ^{48}Ca), COBRA (CdZnTe semiconductors,^{116}Cd), NEXT (TPC, ^{136}Xe), SNO+ (liquid scintillator, ^{150}Nd) and so on. In Table 2.5, current best results for $0\nu\beta\beta$ decay obtained from the direct measurement are summarized.

Table 2.5: Lower limits of $0\nu\beta\beta$ half-lives and corresponding upper limits of the effective neutrino mass (Q value > 2 MeV). All values are at 90% C.L.

Isotope	$T^{0\nu}_{1/2}$ (yr)	$\langle m_{\beta\beta}\rangle$ (eV)	Experiment	NME Ref.
^{48}Ca	5.8×10^{22}	3.5−22	ELEGANT VI (2008) [53]	[54, 55]
^{150}Nd	1.8×10^{22}	4.0−6.3	NEMO-3 (2009) [29]	[56, 57]
^{96}Zr	9.2×10^{21}	7.2−19.5	NEMO-3 (2010) [31]	[55, 57, 58, 59, 60, 61]
^{100}Mo	1.1×10^{24}	0.45−0.93	NEMO-3 (2011) [28]	[57, 58, 59, 60, 61]
^{82}Se	3.6×10^{23}	0.89−2.43	NEMO-3 (2011) [28]	[55, 58, 59, 60, 61]
^{116}Cd	1.7×10^{23}	1.7	Solotvina (2003) [62]	[63]
^{130}Te	2.8×10^{24}	0.300−0.710	CUORICINO (2011) [50]	[40, 60, 61, 64]
^{136}Xe	6.2×10^{24}	0.26−0.54	this work (2012) [35]	[40, 41]
	1.6×10^{25}	0.140−0.380	EXO-200 (2012) [52]	[40, 41, 61, 63, 65]
^{124}Sn	2.0×10^{19}	150−408	Korea (2009) [66]	[46, 63, 67, 68]
^{76}Ge	1.9×10^{25}	0.35	H-M (2001) [36]	[63]
	1.57×10^{25}	0.33−1.35	IGEX (2002) [48]	[63, 69, 70, 71, 72]

† H-M denotes HEIDELBERG-MOSCOW.

Chapter 3

Double beta decay with KamLAND-Zen

KamLAND-Zen is a modification of the existing KamLAND. In this chapter, its experimental design, structure of KamLAND and details of KamLAND-Zen items are described.

3.1 Experimental design

As written in Chapter 2, there are many experiments, which search for neutrinoless double-beta decay with various techniques and isotopes. Non-existence of ideal experiments makes many choices of experimental design.

Our experiment, KamLAND-Zen studies ^{136}Xe double-beta decay with 13 tons of Xe loaded liquid scintillator (Xe-LS). We measure the scintillation light proportional to the summed energy of two electrons with photo-multiplier tubes. The detector is a part of KamLAND which was primary designed to observe a few MeV neutrinos with 1,000 tons of highly purified liquid scintillator. The neutrino experiment has a similar feature with double-beta decay's to the extent of searching for a rare event and requirement of large amount of target and low background environment. KamLAND-Zen is placed in the center of KamLAND (detail described in following sections). Utilization of KamLAND brought us the following advantages;

- KamLAND is located and operated at the underground. Rock overburden corresponding to 2,700 m water equivalent reduces the cosmic-ray muon flux by five orders of magnitude compared with ground level. It reduces muon-induced backgrounds.

- No big modification to the detector is necessary to accommodate double-beta decay nuclei. Relatively low cost and fast construction is possible. In addition, well known detector (running for $\sim$10 years) provides established analysis tools. It enables to monitor the detector condition during the modification.

- The detector has a high scalability. It is possible in one detector to reach inverted hierarchy region with ton-scale isotope mass. Considering 3% by

weight of ^{136}Xe dissolved into the liquid scintillator, ∼30 tons of the nucleus is soluble at the maximum.

- Original purpose of KamLAND, reactor- and geo-antineutrino observations can be continued since detection method is different from double-beta decay.
- Ultra low radioactivity environment based on ultra pure liquid scintillator works as ∼4-m-thick active shield of external backgrounds. It also works as a detector for internal double-beta decay target and radioactive impurities.

Our choice of double-beta decay isotope is ^{136}Xe. It has 2.458 MeV Q value [73] and $\sim 10^{21}$ years half-life of $2\nu\beta\beta$ decay. Its slow half-life of $2\nu\beta\beta$ decay reduces intrinsic background (tail of $2\nu\beta\beta$ decay) in $0\nu\beta\beta$ region and it requires a modest energy resolution. The fact that xenon is one of the noble gas also provides advantages. It is known that the noble gas dissolves into organic solvent in general and xenon is no exception. Xenon is soluble to the liquid scintillator for ∼3% by weight, furthermore, easily extracted. Xenon is chemically stable, so it does not degrade the liquid scintillator or other materials. It is not liquid xenon, then, low temperature or pressure control is not required. ^{136}Xe has relatively high natural abundance (8.7%) and method of isotopic enrichment (centrifugation) is established. Actually, KamLAND-Zen uses ∼91% enriched ^{136}Xe. Colorless and transparency are also important features.

It will be contemplated that a possible serious background for $0\nu\beta\beta$ decay search is well-known 2.614-MeV γ coming from ^{208}Tl (β^-, $Q = 5.0$ MeV) in ^{232}Th decay chain, but it would not. KamLAND (or KamLAND-Zen) cannot distinguish its β and γ rays. Then ^{208}Tl is detected with coincident β/γ in the liquid scintillator, and its 2.614 MeV γ distribute in 3−5 MeV. Level diagram of ^{208}Tl is found in Appendix C.1.1.

3.2 Detector (KamLAND)

KamLAND (**Kam**ioka **L**iquid scintillator **A**nti-**N**eurino **D**etector) is a low energy (anti-)neutrino detector with a highly purified 1,000-ton liquid scintillator. Construction started in 1997 and data taking started in January, 2002. Over 10 years, KamLAND has observed various kinds of neutrinos between sub-MeV to several tens of MeV, and produced results such as precise measurement of Δm^2_{21} by reactor neutrinos [5, 74, 75, 76], constraint for θ_{13} [76], the first detection and measurement of geo neutrinos [77, 78], observation of ^{8}B neutrino flux from Sun [79], and search for $\overline{\nu}_e$ source from the sun and other sources [80].

KamLAND is located in the former Kamiokande site of the Kamioka mine, 1,000 m under the top of Mt. Ikenoyama, in Gifu prefecture, Japan. Owing to the rock overburden equivalent to 2,700 m water, the cosmic-ray muon flux in the inner detector is about 10^5 less than the ground level. Figure 3.1 shows a muon flux at each experimental site as a function of depth in km water equivalent. Thanks to its surrounding environment, Kamioka mine contains other experimental halls for CANDLES (double beta decay experiment), Super-Kamiokande (neutrino experiment) and XMASS (dark matter experiment).

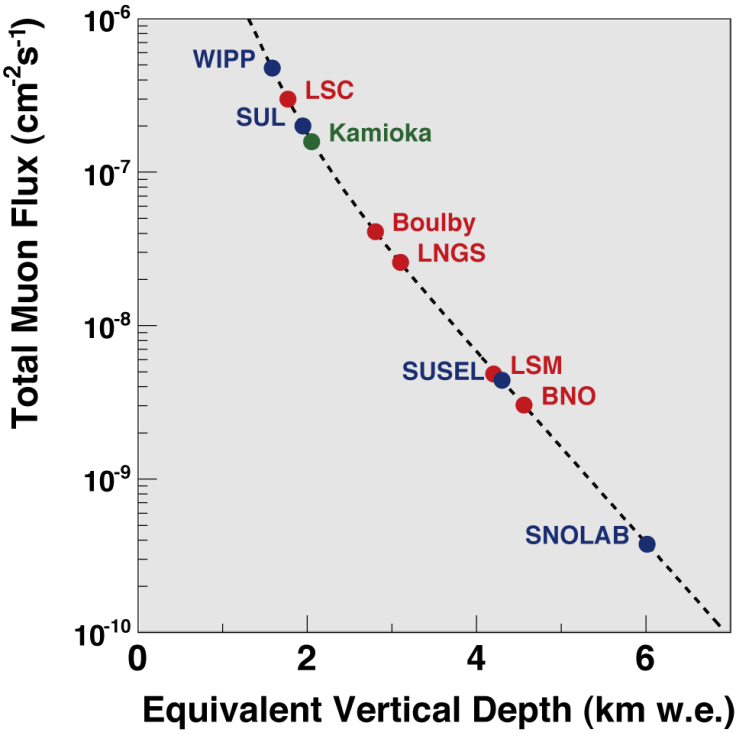

Figure 3.1: Total muon flux as a function of vertical depth in water equivalent [15]. In descending order, name of facility, country, major double beta decay experiment(s) are
· WIPP (Waste Isolation Pilot Plant), America, EXO,
· LSC (Laboratorio Subterráneo de Canfranc), Spain, NEXT,
· SUL (Soudan Underground Laboratory), America,
· Kamioka (Kamioka Observatory), Japan, KamLAND-Zen and CANDLES,
· Boulby (Boulby Undergound Laboratory), UK,
· LNGS (Laboratori Nazionali del Gran Sasso), Italy, Heidelberg-Moscow, CUORICINO, CUORE, GERDA, DAMA/Libra and COBRA,
· LSM (Laboratoire Souterrain de Modane), France, NEMO and Super NEMO,
· SUSEL (Sanford Underground Laboratory at Homestake), America, MAJORANA DEMONSTRATOR,
· BNO (Baksan Neutrino Observatory), Russia, Copper proportional counters,
· SNOLAB, Canada, SNO+.
Red, blue and green dots show facilities located in Europe, America and Asia, respectively.

The KamLAND experimental site is shown in Fig. 3.2. The detector is straight 2 km far from the entrance of the Kamioka mine. Two purification systems for liquid scintillator (one is not shown in this picture), water purification system for outer detector and high purity nitrogen system were installed. In the control room, computer system is installed to control and monitor the data acquisition. Electronics hut and calibration device are built on the detector, called dome area. Clean room called HV room is connected to the dome area. High voltage (HV) power supply systems for PMTs are placed in this room. There are also many gauges to check detector conditions such as load of balloon, oil and water temperature, oxygen concentration and so on. Details of each components are described in each sub-sections.

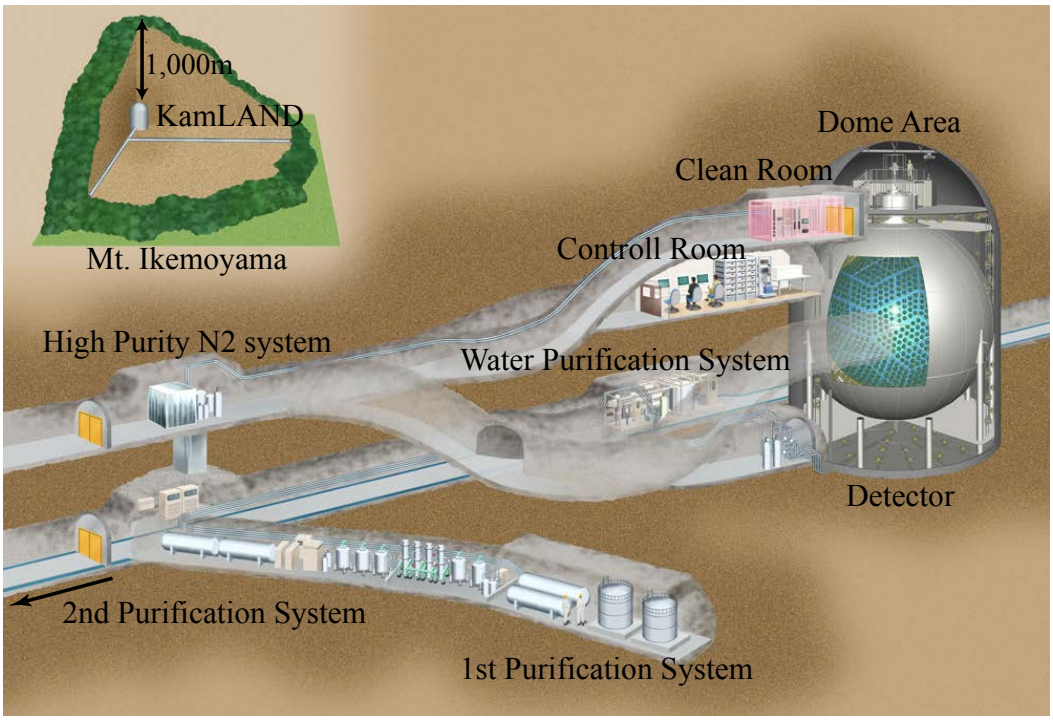

Figure 3.2: A diagram of the KamLAND experimental site.

3.2.1 Detector structure

The KamLAND's main 2 components are liquid scintillator detector (inner detector, ID), and water Cherenkov detector (outer detector, OD). These are divided by 18-m-diameter spherical stainless steel contaminant tank. Figure 3.3 shows a schematic of the detector structure. The ID is designed for detection of neutrino signals, while the OD tags and/or absorbs backgrounds coming from outside such as cosmic ray muons, γ-rays and neutrons from surrounding rocks. Details are described below.

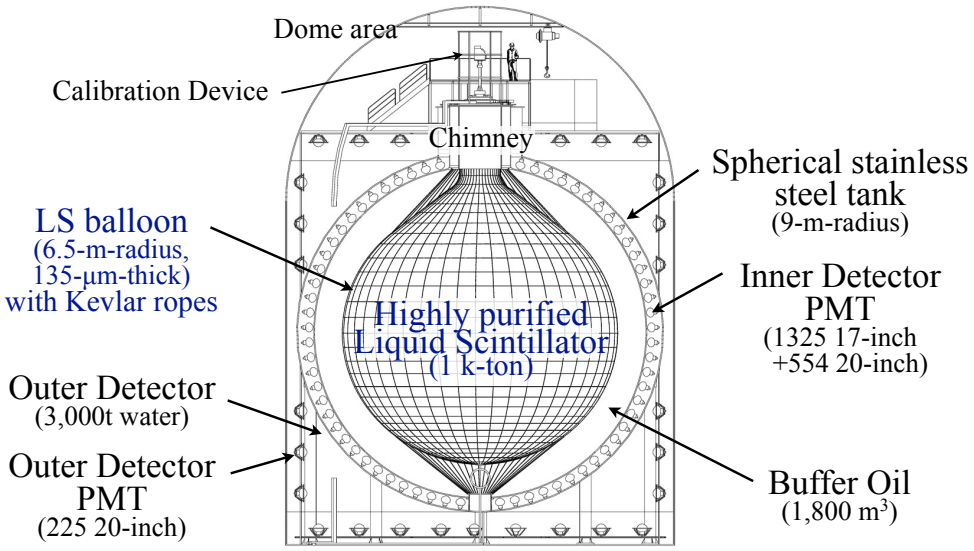

Figure 3.3: A schematic diagram of the detector.

Inner detector (ID)

The heart of KamLAND is 1,000 tons of highly purified liquid scintillator (see section 3.2.2) contained in a 13-m-diameter spherical balloon. It is suspended by high strength Kevlar ropes and placed at the center of the 18-m-diameter spherical stainless steel contaminant tank. Outer side of the balloon is 1,800 m^3 of buffer oil. It reduces the load for balloon by careful control of density difference within 0.04% with liquid scintillator, since only 135-μm-thick, transparent, nylon-based balloon holds 1,000 tons of liquid scintillator. The balloon is made of 5 layers of 15-μm-thick EVOH[1] and 25-μm-thick nylon (EVOH/nylon×3/EVOH). Nylon has a high strength and transparency, while EVOH provides very low gas permeability. The light transparency of balloon is more than 90 % for wavelength between 370 and 500 nm, and 96 % at 400 nm[2]. The balloon is kept its spherical shape by 44 of longitudinal and 30 of lateral Kevlar ropes[3]. There are 44 load cells for each longitudinal ropes to balance and to monitor their tension. The radioactivity contained in the balloon and Kevlar ropes are summarized in Table 3.1.

Scintillation light produced by signal/background is detected by 1,325 of 17-inch and 554 of 20-inch photo-multiplier tubes (PMTs)[4] mounted on the inner surface of the stainless steel tank. The photo-cathode coverage for 17-inch and 20-inch PMTs are 22 % and 12 %, respectively, and 34 % in total.

In front of the PMTs, a 16.6-m-diameter triacontahedron acrylic barrier composed from 120 of 3-mm-thick and 2.8-m-side transparent rhombus is placed to

[1] ethylene vinyl alcohol copolymer

[2] Our light sensor, photo-multiplier tubes has good quantum efficiency in this wavelength range. Detail is in Section 3.2.5

[3] Kevlar is one of super fiber. It has quite high strength.

[4] 1,879 of PMTs are placed in total.

Table 3.1: Radioactivities in the balloon film and Kevlar ropes.

Balloon film	U	Th	^{40}K
Concentration [ppb]	0.08	0.8	1.2
Decays [Bq]	0.1	0.33	31

Kevlar ropes	U	Th	^{40}K
Concentration [ppb]	0.018	0.014	0.27
Decays [Bq]	0.02	0.006	7.2

prevent the radon emanating from the PMT glass and the stainless steel tank. It is shown in Figure 3.4. Upper part of ID is called chimney. In this part, as liquid scintillator faced to gas phase, nitrogen gas is continuously supplied as a seal gas to prevent oxygen, radon, and krypton from diffusing into the liquid scintillator[5].

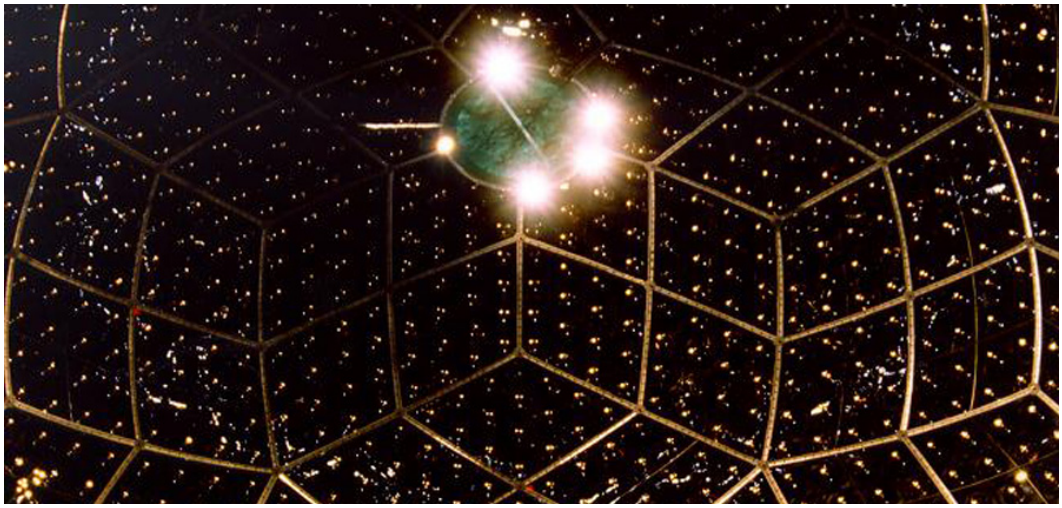

Figure 3.4: Inside view of KamLAND from the bottom. This picture was taken during the detector construction. Each dim points are PMTs and rhombus is acrylic barrier.

Outer detector (OD)

The OD (19-m-diameter and 20-m-height cylindrical rock cavity) is fulfilled with 3,000 tons of pure water and it surrounds the inner detector. It vetoes/shields muons, their induced fast neutrons, and external gamma rays from surrounding

[5]Radon, and krypton are radioactivity (background), while oxygen decrease light emission of liquid scintillator. Nitrogen gas is also supplied for a safety since liquid scintillator and its vapor are flammable.

rock with 225 of 20-inch PMTs. The wall is covered with Tyveck sheet to increase a light collection efficiency. A water purification system (written in Sec. 3.2.4) supplies pure water. It is always circulating from the detector bottom to top in order to avoid a rise in temperature of liquid scintillator and the detector itself, and to compensate a leak of water.

3.2.2 Liquid scintillator and buffer oil

The target of KamLAND is 1,000 tons of ultra pure liquid scintillator (LS). It also acts as an active shield for double-beta decay measurement in KamLAND-Zen. Components of LS are two kinds of organic solvent, 80 % of dodecane and 20 % of pseudocumene (1,2,4-Trimethylbenzene, called PC), and one fluorescent solutes, 1.36 g/l of PPO (2,5-Diphenyloxazole). Dodecane is a mineral oil and PC is a popular solvent for liquid scintillator. Each chemical characteristics are summarized in Table 3.2. This hand-made scintillator was developed to satisfy the following requirements, (1) high light outputs and optical transparency for the good energy resolution and low energy event detection, (2) very low radioactive impurities for the low background experiment, (3) long term stability, (4) high flash point and less toxicity for a safety. Due to the detector size, the light yield depends on the light transparency of the scintillator as well as the light output. In general, PC increases the light emission but worsens transparency than mineral oil. Concerning these pros and cons, the composition ratio of the scintillator was adjusted to get the maximum light yield for central events. The obtained values are 300 p.e./MeV and 500 p.e./MeV with 17-inch PMTs and 17+20-inch PMTs, respectively. The measured attenuation length by a dye-laser is about 10 m at 400 nm wavelength and light output is 8,300 photons/MeV[6] [81]. Radioactivity in the LS is extremely low thanks to two kinds of purification, water extraction and distillation (Sec. 3.2.3).

Table 3.2: Chemical characterization of KamLAND LS components.

	dodecane	PC	PPO
molecular structure	$C_{12}H_{26}$	C_9H_{12}	$C_5H_{11}NO$
molecular weight	170.3	120.2	221.3
density (g/cm^3,15°C)	0.752	0.8797	-
melting point (°C)	-12	-43.9	$69 \sim 74$
boiling point (°C)	216.2	169.4	-
flashing point (°C)	74	44	-

The buffer oil which surrounds the LS is composed of 53 % of normalparaffin ($C_{12}H_{26}$) and 47 % of isoparaffin (C_nH_{2n+2}, n$\sim$14). Mixture ratio was optimized by adjusting density difference of LS and buffer oil within 0.04% to keep the spherical shape and reduce the load for the balloon.

[6]Cited values are those of before 2nd purification

3.2.3 Liquid scintillator purification system

The KamLAND LS or each component, dodecane, pseudocumen and PPO is purified by two purification systems, water extraction and distillation. Water extraction called the 1st purification was done at the construction of the detector and achieved sufficient reduction of impurities for $\overline{\nu}_e$ measurement. A few years later, however, KamLAND needed to reduce backgrounds in the low energy region for the measurement of the next target, ^{7}Be solar neutrinos. From various laboratory studies, distillation and nitrogen purging with high quality nitrogen were adopted, and in 2007, distillation, nitrogen-purge system and high purity nitrogen supply system were newly constructed at the experimental site. KamLAND LS was purified with the system from March 2007 to August 2007, and from June 2008 to February 2009. This purification is called the 2nd purification.

Water extraction (1st purification)

A liquid-liquid extraction clears dissolved impurities in a liquid by mixing with another liquid which is immiscible with the first liquid but has higher solubility of the impurities. To purify the KamLAND LS and buffer oil (LS/BO)[7], pure water was used (water extraction). A schematic view of the 1st purification system is shown in Figure 3.5. As a first step, LS/BO is sent to the water extraction tower

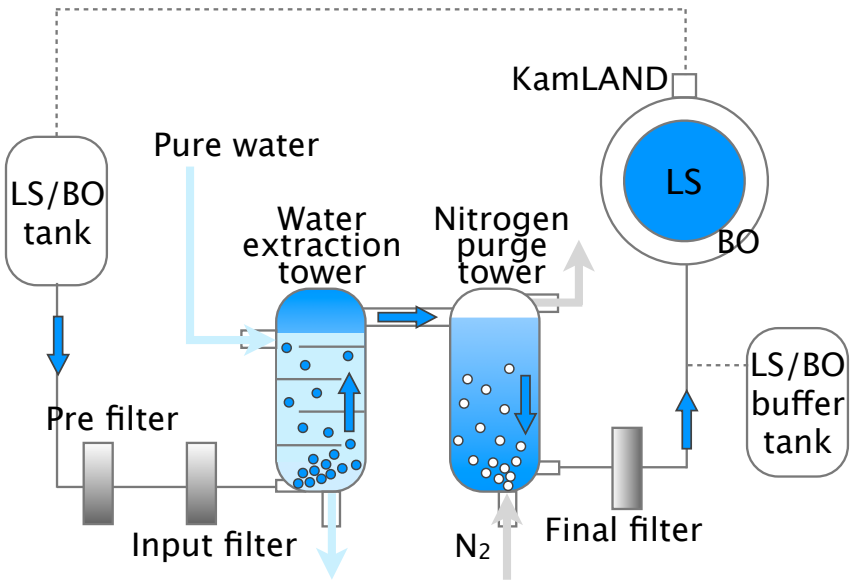

Figure 3.5: A schematic view of water extraction and nitrogen purge.

to mix with a pure water. Thanks to the polar character of H_2O, ions such as U, Th and K in LS/BO move to water. LS/BO is filled from the bottom of the tower in contrast to water from the top. The tower has some boards inside to obstruct the flow for well stirred of water and oil, and it improves the efficiency of impurity

[7]Purification was done independently.

removal. After this extraction, only oil is sent to the nitrogen purge tower. As a next step, the nitrogen purging is done for drying and removing moisture and oxygen[8]. Finally, purified LS/BO goes to the detector after passing thorough the final filter to remove remained minute dust. Table 3.3 summarize the targeted value and actual radioactivity level in the LS before and after this purification. The value before the purification was measured by ICP-MS, while that of after the purification was estimated from KamLAND data since it was too small to measure by ex-situ detector. The measured value after purification is well below the targeted one. Required reduction ratio is about $1-4$ orders of magnitude and actual one is about 5 orders of that.

Table 3.3: Radioactivity of KamLAND LS before/after 1st purification [82].

	^{238}U [g/g]	^{232}Th [g/g]	^{40}K [g/g]
Before purification	10^{-13}	$< 10^{-12}$	7×10^{-11}
Targeted value	$< 10^{-14}$	$< 10^{-14}$	$< 10^{-15}$
After purification	3.5×10^{-18} †	5.2×10^{-17} †	$< 2.7\times10^{-16}$

† Estimated from Bi-Po coincidence event assuming secular equilibrium.

Distillation (2nd purification)

As written in the previous paragraph, the 1st purification achieved sufficient reduction of radioactivities for $\overline{\nu}_e$ measurement, however, backgrounds at low energy remained and ^{7}Be solar neutrino observation was impossible. Then distillation and nitrogen purging for each LS component was done. Distillation reduces high-boiling metal elements such as ^{210}Pb and ^{40}K, while nitrogen purging is intended to remove the radioactive noble gases such as ^{222}Rn, ^{85}Kr and ^{39}Ar. A schematic view of the 2nd purification system is shown in Figure 3.6. The KamLAND LS is directly sent from the balloon to the buffer tank and each component of LS is distilled with its own distillation tower in ascending order of boiling point. To distill each components with manageable temperature for safety and to prevent change of those properties, reduced-pressure distillation is adopted. After distillation, each component is sent to the mixing tank to adjust its composition balance and density, and then, sent to the nitrogen purging tower. Fresh, high purity nitrogen is always supplied to the tower. The flow rate is 30 m^3/h, 20 times higher than that of liquid scintillator. To improve the reduction efficiency, liquid passes through the staggered path and the whole system is depressurized down to 40 kPa. Thanks to its size, the number of tower, nitrogen flow rate and its pressure, the Rn concentration in LS is down to about 1%. High purity nitrogen gas system also supplies fresh nitrogen gas to the buffer tank, distillation system, mixing tank and KamLAND detector in order to prevent radioactive gases being mixed into the liquid scintillator. Quality of the

[8]Different from the purging of the 2nd purification, same nitrogen was used for many times since main purpose was to dry the liquid scintillator.

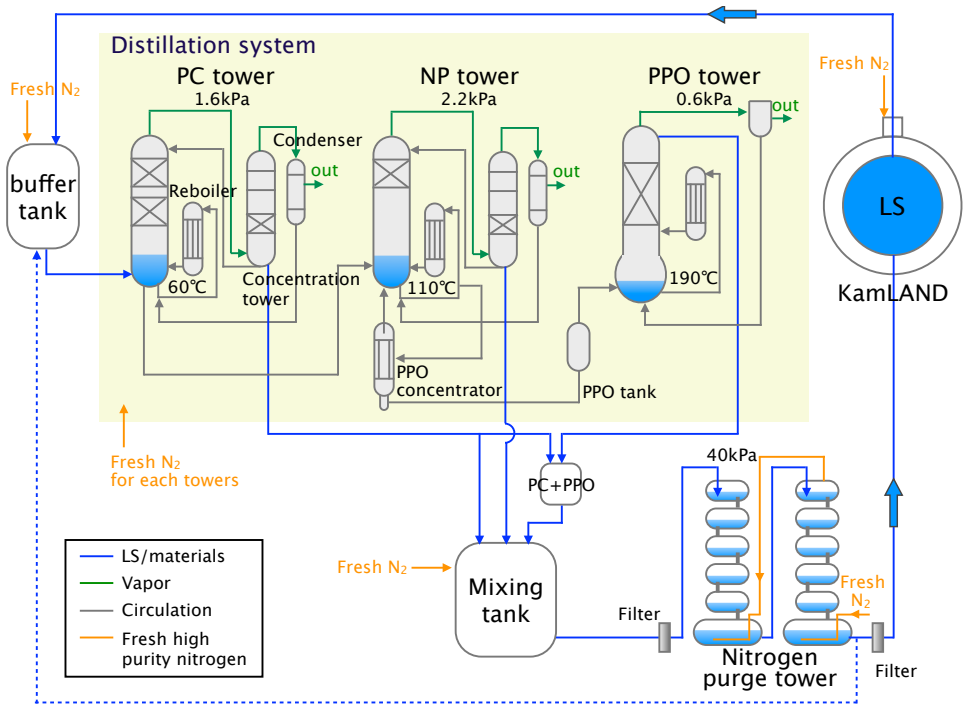

Figure 3.6: A schematic view of distillation. NP stands for normal paraffin or dodecane. Noted temperatures and pressures are at the operation.

LS such as density, light emission, light transparency, Kr and Rn concentration are measured regularly to monitor its condition[9]. The total amount of processed LS was over 5,000 m^3, corresponding to four full volume exchanges of the LS.

3.2.4 Water purification system

Large amount of OD pure water is obtained from groundwater in the Kamioka mine through the water purification system. This system consists of pre-filters (1μm and 5μm), UV sterilizer, ion exchanger, vacuum degasser and reverse osmosis (RO) filters in order to remove dust, metal ions, natural radioisotopes such as ^{222}Rn and to eliminate bacterias. Thanks to this system, $\sim$10 m^3/h of pure water is supplied to outer detector and concentration of ^{238}U and ^{232}Th is order of 10^{-13}g/g.

3.2.5 Photo-multiplier tubes

In KamLAND inner detector, two kinds of PMTs, called 17-inch and 20-inch PMTs, are used for the detection of scintillation light. The 20-inch PMTs are originally made for Kamiokande experiment. The 17-inch PMTs are based on 20-inch but newly developed for KamLAND to improve time and charge responses. The number, "17-inch" and "20-inch" indicate diameter of effective photocathode, but size of

[9]Kr was measured by residual gas analyzer and Rn was estimated by time-space correlated Bi-Po events.

those are almost the same. A diagram of PMTs are shown in Figure 3.7. The

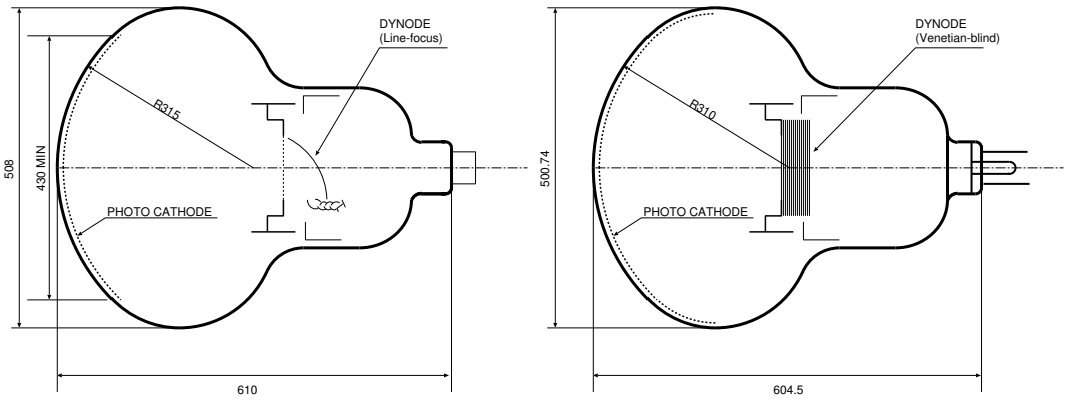

Figure 3.7: A diagram of 17-inch (left) and 20-inch (right) PMTs.

17-inch PMTs, which mainly used in KamLAND, are masked their photocathode edge with black plastic plates and different type of dynode (line-focus) from the 20-inch PMTs (venetian-blind) are adopted. It results in the better time and energy responses. They improve transit-time-spread[10] from 5.4 to 3.1 nsec and the peak-to-valley ratio[11] from 1.7 to 3.4 compared to the 20-inch PMTs as shown in Fig. 3.8. Typical gain and voltage are about 5.0×10^6 and 2,000 volts, respectively. Figure 3.9 shows a quantum efficiency as a function of wavelength. Typical value is 20 to 22% for 350 to 400 nm wavelength which is corresponding to emission wavelength of PPO.

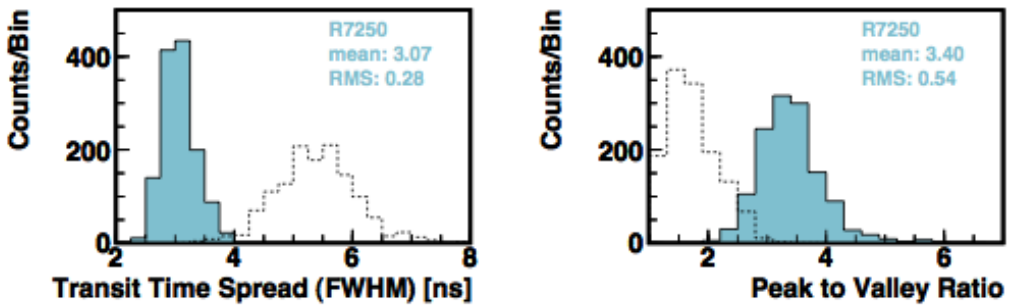

Figure 3.8: Transit spread time (left) and peak to valley ratio (right) for 17-inch (blue histogram) and 20-inch (dotted-histogram) PMTs (taken from Ref. [82]).

A magnetic field affects the 1 p.e. pulse height. If magnetic fields are below 50 mGauss, its variation is less than 20%. To obtain the uniform response, a set of compensating coils were installed in the cavern against the terrestrial magnetism (originally ∼500 mGauss) which is controlled sufficiently below 50 mGauss.

[10]FWHM of transit time which is time from photon hit to electrical pulse output.
[11]The height of 1 photo-electron peak in ratio to the height of valley.

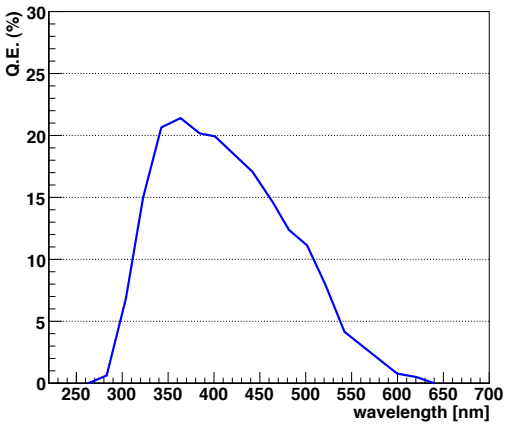

Figure 3.9: Quantum efficiency (Q.E.) of the 17-inch PMTs as a function of wavelength.

3.2.6 Electronics, triggers and data acquisition system

Analog signals from PMTs are converted into a digital data and stored onto data storage devices when certain conditions are satisfied. This interactional sequence is formed by a front-end electronics (FEE) designed for KamLAND, a trigger system, and a data acquisition (DAQ) system (detail described in the following paragraphs). These three components communicate each other. For example, if a threshold of the trigger system is set to 70 and the number of PMT hit within a 125 nsec window is more than that, a trigger is issued and the FEE records waveform of every PMT hit signal and digitizes it. The trigger system has an internal 40 MHz clock, and it is also distributed to the all 200 FEE boards to keep synchronized. The data from electronics and trigger system are sent to the DAQ system and stored onto storage devices. On the other hand, the DAQ system sends various commands to the FEE and the trigger system separately and controls the run conditions.

Currently KamLAND/KamLAND-Zen has two electronics systems that one is FEE which is installed at the beginning of KamLAND operation, and another one is called MoGURA which is a dead time free electronics newly installed for ^{7}Be solar neutrino observation. In this double beta decay analysis, MoGURA data has not been used yet, but have scheduled to be used for reduction of ^{10}C which will become the biggest background in the future. Detail of MoGURA is not written in this thesis, but its most distinctive feature, "dead time free'" enables to reduce $\sim$90% of ^{10}C by a triple coincidence tag of muon, neutron and ^{10}C decay.

Electronics

A PMT signal (voltage) is sampled by KamLAND FEE boards shown in Fig. 3.10. Each board has 12 channels and one PMT connected to one corresponding channel. A type of PMTs in one board coordinates with the same one such as 17-inch in ID, 20-inch in ID or 20-inch in OD. The PMT hit signal is divided into two. One firstly passes through the discriminator whose threshold is 1/3 p.e. pulse height,

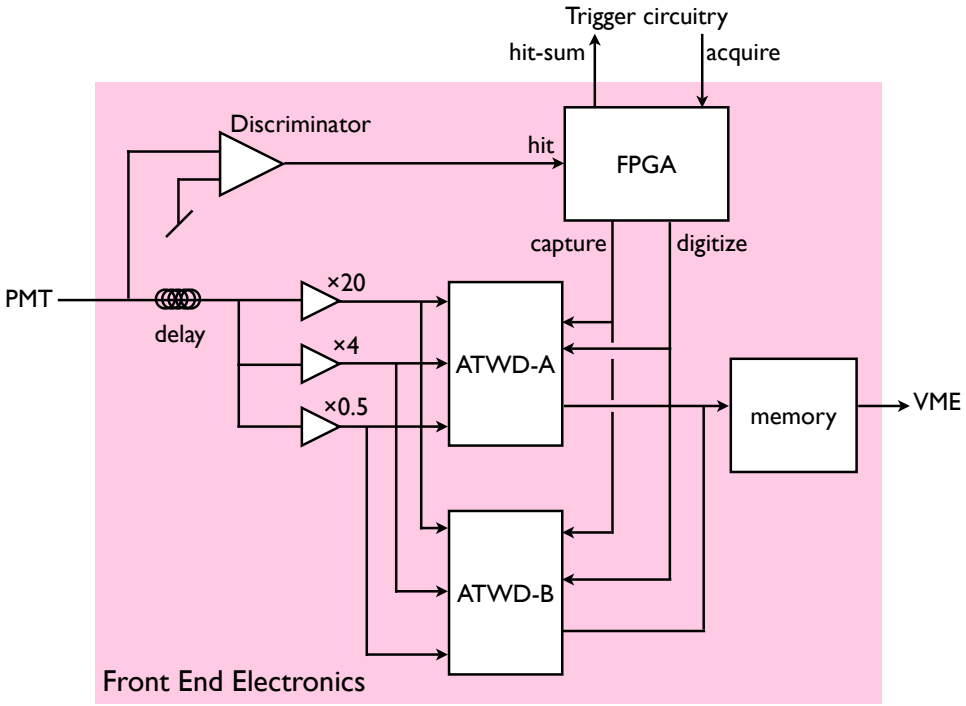

Figure 3.10: Diagram of KamLAND Front-End Electronics.

corresponding to 0.5 mV. The hit information in one board is compiled on a Field Programmable Gate Array (FPGA) chip and sent to the trigger module as the "hit-sum". While the discriminator logic is working, another signal travels through the 40 nsec delay line to Analog Transit Waveform Digitizer (ATWDs) and waveforms are captured up to 175 nsec. The ATWD is the key part of the FEE, which holds analog signal waveform on arrays of capacitors, and digitizes the waveform on request. If a trigger is issued to collect the event, 'acquire' signal is sent to the FEE boards and FPGA issues the 'digitize' signal to the ATWD, and the waveform converted to data consists of 128 of 10-bit samples with ∼1.5 nsec sampling interval. The 40 MHz clock signal is connected to every ATWD in order to calibrate the waveform sampling interval. To reduce the dead time during analog/digital conversion, two ATWD chips (ATWD-A and ATWD-B) are connected to one PMT channel and utilized alternately. For each PMT channels, three amplifiers with different gains are connected since KamLAND should be able to detect from a sub-MeV signals to very high-energy cosmic muons. A low energy event makes a single photo-electron hit, while a high energy event makes more than 1,000 photo-electron hits to every PMTs. This means the FEE needs to manage over 10,000 magnitude of dynamic range. High-gain ($\times$ 20) is used for single photo-electron signals, middle-gain ($\times$ 4) for a case of saturation of high-gain channels and low-gain ($\times$ 0.5) for large signals caused by high energy muons. Digitized data are transferred to a memory and read by DAQ system via VME.

Trigger system

Trigger issue is determined by "Nsum", the number of hit PMTs within a 125 nsec window. Nsum is calculated by summing "hit-sum" on every FEE boards. If Nsum excesses a preset threshold, the 'acquire' command is sent to the FEE boards. Time information used in the system is synchronized to the GPS time. The 40 MHz clock which is provided to the FEE boards to generate event timestamps is also synchronized to the GPS time. Timestamp given to each waveforms is used later to re-arrange the waveform data in time.

Main trigger type and its threshold of the current data acquisition for KamLAND-Zen are set as follow;

1. 1 pps trigger. It is issued every one second in synchronization with the GPS time. The hit ID PMT's waveforms are digitized.

2. ID history trigger (threshold = 40) based on the ID Nsum. This trigger does not send any acquisition command to the FEE boards. It means it does not acquire waveforms. It is issued every 25 nsec during ID PMT hits above its threshold (up to 200 nsec). The maximum of Nsum is called "NsumMax".

3. ID prompt and ID delay trigger (threshold = 70 and 50, respectively). The ID prompt trigger is issued when the ID Nsum excesses its threshold. The ID delay trigger is issued if it is above the threshold within 1 msec window following the prompt one. The hit ID PMT's waveforms are digitized.

4. ID prescale trigger (threshold = 40, percentage = 1.024). It is issued every second with prescaling of a preset fraction when the ID Nsum excesses its threshold. This trigger is used for a high rate data acquisition. The hit ID PMT's waveforms are digitized.

5. ID 5-inch trigger (threshold = 7). It is for chimney 5-inch PMT's. When this trigger is issued, the hit ID PMT's waveforms are digitized.

6. ID to OD trigger. It is issued when any of ID Nsum triggers are issued. When this trigger is issued, hit OD PMT's waveforms are digitized.

7. OD top history, OD upper history, OD lower history and OD bottom history trigger (threshold = 6, 5, 6, and 7, respectively). These triggers are issued during the Nsum of the OD excesses each threshold. The behavior of these are the same as (2).

8. OD top singles, OD upper singles, OD lower singles and OD bottom singles trigger (threshold = 6, 5, 6, and 7, respectively). These are issued when they are above each threshold. The hit OD PMT's waveforms are digitized.

9. OD to ID trigger. It is issued when any of OD Nsum triggers are issued. When this trigger is issued, hit ID PMT's waveforms are digitized.

10. Forced acquistion on GPS trigger.

For the ID triggers, only 17-inch PMTs are used since 20-inch PMTs are not quite sensitive to the single photoelectron pulse.

Data acquisition system

The DAQ system works for reading data from the FEE and the trigger system, transporting and storing it onto storage devices. The DAQ software is called KiNOKO [83]. Data monitoring including quick online data analysis is also important task of the DAQ system since it is directly connected to the electronics devises. It uses the realtime data and enable to monitor data flow rate, trigger rate and so on. In addition, control of DAQ running condition is also one of the task of the system. The system intermediate the data and an operator. For example, a run[12] is started/stopped by an operator. Run type such as "normal" and "calibration" is also selected depending on the conditions.

3.3 Overview of KamLAND-Zen

As written in Section 3.2, KamLAND has a huge amount of highly purified liquid scintillator to detect low energy neutrinos, and its environment is suitable for double-beta decay experiment.

Figure 3.11 shows a schematic view of KamLAND-Zen. The $\beta\beta$ source/detector

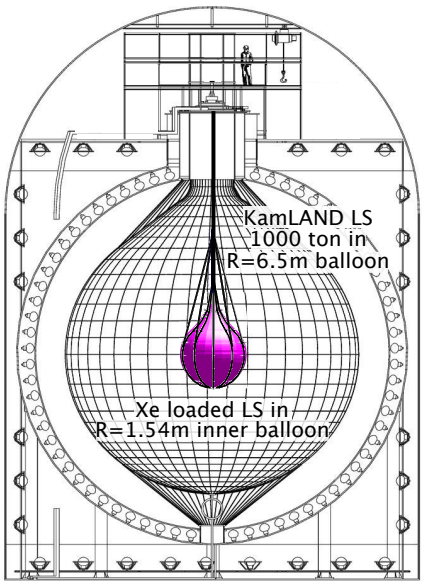

Figure 3.11: A schematic view of KamLAND-Zen.

for the 1st phase of KamLAND-Zen is 13 tons of Xe-loaded liquid scintillator (Xe-LS, Section 3.4) contained in a 3.08-m-diameter spherical inner balloon (IB). The IB is constructed from 25-μm-thick transparent nylon film and is suspended at the center of the KamLAND detector by 12 film straps made of the same material as the IB. The design, material and fabrication of the IB, and its supporting structure are summarized in Section 3.5. Outside of the IB is 1 kton of KamLAND liquid scintillator, which acts as an active shield for external γ's and as a detector for

[12]It is a period of continuous data taking and typically lasting 24 hours.

internal radiation from the Xe-LS and/or IB. The density difference between Xe-LS and KamLAND LS is carefully controlled within 0.04% to reduce the load for the IB, especially for the neck part. This is the same method used for KamLAND balloon. To handle Xe gas, Xe handling system was newly constructed (Section 3.7). Two new 25 m^3 tanks for a liquid storage were also built. We repeated various tests and established the method of installation of the IB to KamLAND. It is summarized in Section 3.6. Detector modification of KamLAND was carried out successfully in the summer of 2011 and data acquisition started on September, 2011.

3.4 Xe-loaded liquid scintillator

The requirements for Xe-LS compared to KamLAN-LS are (1) Xe dissolved into LS, (2) quite small density difference after Xe solution and (3) light yield difference within ±10%. Research and developments determines the recipe of the Xe-LS. It consists of 82% of decane, 18% of pseudocumene (1,2,4-trimethylbenzene) by volume, 2.7 g/liter of the fluor PPO (2,5-diphenyloxazole). Dissolved enriched xenon is about 2.5% by weight. The isotopic abundances in the enriched xenon were measured by residual gas analyzer to be $(90.93 \pm 0.05)\%$ ^{136}Xe and $(8.89 \pm 0.01)\%$ ^{134}Xe, and other xenon isotopes are negligible. To control density difference with KamLAND LS within 0.1 %, dodecane used for KamLAND LS is replaced to decane which has ∼2 % light density, and ratio of PC is slightly decreased. Twice the amount of PPO compared to KamLAND LS recovers shortfall of light emission caused by low ratio of PC and loading Xe. Actual value of the light yield of the Xe-LS is 3% lower but within the required value. This Xe-LS has enough light transparency, too. Radioactivity of Xe-LS are summarized in Table. 3.4. As shown in Figure 3.12, PC was purified with water extraction and distillation, while decane and PPO were purified with distillation. Just before the filling into the IB, mixed components

Table 3.4: Radioactivities of Xe-LS.

	^{238}U [g/g]	^{232}Th [g/g]
Estimated value from data	$(3.5\pm0.6)\times10^{-16}$	$(2.2\pm0.3)\times10^{-15}$

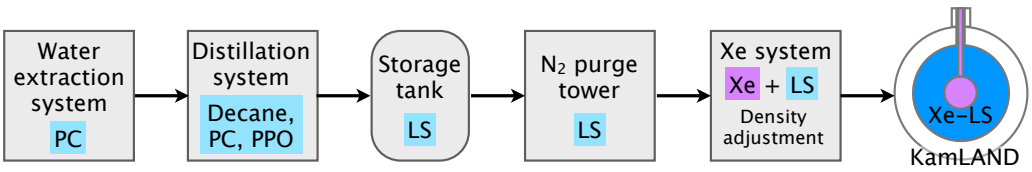

Figure 3.12: A flow chart of Xe-LS.

without Xe are purged with nitrogen to remove noble gases, and then sent to Xe system in order to dissolve Xe and adjust the density .

3.5 Inner balloon and supporting structure

3.5.1 Design

Figure 3.13 shows a diagram of IB, supporting structure, and a picture of real scale test balloon. The IB consists of main sphere with 24 gores, polar caps, 1.5-m straight tube and cone. All of them are made of a heat-welded 25-μm-thick clean nylon film. Twelve suspending belts are also made of the same material with the same method. The IB is connected to the top flange of the detector with $\sim$7 m of corrugated nylon tube and suspended by 12 belts connected to 12 Vectran strings[13].

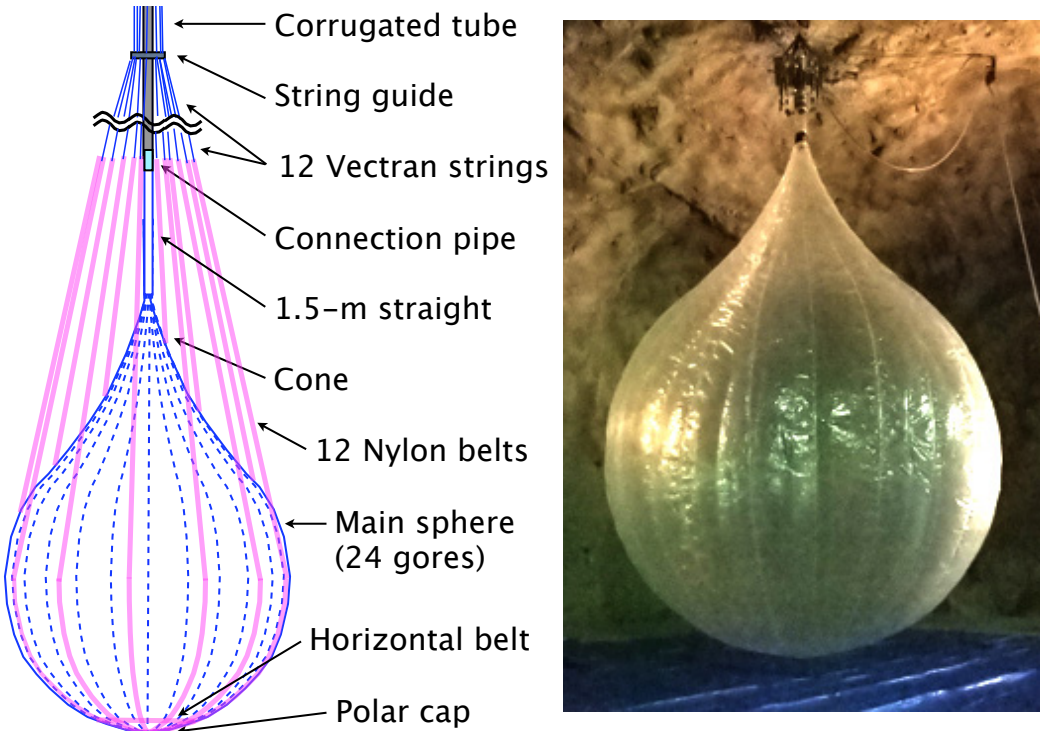

Figure 3.13: A diagram of IB and supporting structure (left) and a picture of real scale test balloon (right). Real scale test balloon is made of 85-μm-thick polyethylene, so transparency is worse than the real inner balloon.

3.5.2 Supporting structure

Figure 3.14 shows parts of the IB supporting structure written below.

Corrugated nylon tube and connection pipe

To place the IB at the center of the detector, the length of the connection with the IB and the top flange becomes almost 7 m. It may be desirable to make a whole connection part with a clean nylon film to reduce backgrounds, but it is unrealistic

[13]Vectran is one of the super fiber. We use commercial product of kuraray company.

Figure 3.14: Pictures of supporting structures. Corrugated nylon tube cut in a ∼2-m-pieces and made it straight by a heat blower (top-left). String guide (top-center). Connection pipe made of PEEK material (top-right). Film belt with Vectran strings (bottom left). Film belt structure at the polar (bottom-right).

when we consider a strength and handling during the installation. For that reason, we chose a corrugated nylon tube as a connection. It is flexible and easy handling, and it has enough strength against the pressure at liquid level. A string guide which fixes the direction of suspension strings is placed at the bottom of the tube. From impurity standpoint, however, this tube and IB should keep a certain distance since it is massive and has many radioactivities compared to films. Then, main sphere/cone and corrugated nylon tube are connected by 1.5-m-straight nylon film tube with connection pipe made of PEEK[14] material.

Strings and belts

The IB is suspended by 12 belts/strings. The belts directly support the IB and it is made of the same film as IB. These belts are connected to Vectran strings around the connection pipe, and tied to the load cell at the top of the detector[15]. Vectran has enough strength and chemical compatibility with LS. We cannot make whole of suspension with Vecran strings since its radioactivity is too high for our

[14]PolyEther-Ether-Keton. A kind of thermoplastic resin.

[15]To consider the method of fixation to the load cell and to adjust the length, at least one side of suspension part should be strings.

requirement. On the other hand, string made by film with low radioactivity is also difficult. Then, we use the combination of strings and belts for the IB supporting structure like corrugated tube and 1.5-m straight film tube.

3.5.3 Film selection and condition

From the experience of KamLAND balloon fabrication, EVOH and/or nylon can be a candidate of the IB material. A film used for KamLAND-Zen experiment needs to satisfy the following conditions;

- Enough strength (> 10 N/cm).
- Light transparency is more than 95%.
- Good Xe gas tightness ($< 1\%$ of total xenon amount, $\sim$3 kg).
- Radioactivity of ^{238}U and ^{232}Th is less than 10^{-12} g/g and that of ^{40}K is less than 10^{-11} g/g.
- Less than 25-μm-thick is desirable. It enables to tag film-contained ^{214}Bi (in ^{238}U chain and one of the background in $0\nu\beta\beta$ region) by sequential decay of β and α decay. Detection efficiency of α decay depends on the film thickness.
- Possible to weld, not to use adhesive.

From thickness and low radioactivity requirements, single layer film is desirable. As a result of radioactivity measurements of various sample of films, EVOH includes much K, while nylon includes U and Th. Since U and Th become direct backgrounds, especially for ^{136}Xe $0\nu\beta\beta$ region, EVOH (low-U and Th than nylon) single layer balloon was made as a first trial. However, it had crisply texture and tore easily, we were forced to give up using it. Then we searched for a good nylon film, but there were no commercial product to satisfy our requirement of impurities. So we decided to make an original film. Problem is when contamination is included to a film. We measured impurities of film ingredients, called pellets. Some of pellets include the "mineral filler", which looks like pebbles. It is used to smooth the surface of films for easy roll up, and has much radioactivities. Table 3.5 shows the measured value of radioactivities of nylon ingredients with various companies, and conditions. Radioactivities of films made from these pellets are also measured and summarized in Table 3.6. From these results, a film made by Toyobo with pellets from company A is selected for a film candidate.

The rupture strength, light transparency, Xe gas tightness of the selected film (25-μm-thick) were tested and it revealed that all of parameters satisfied our requirements. The value of rupture strength is 4.9 kgf/cm. This value is possible to keep the IB up to 6% density difference between KamLAND LS and Xe-LS, while our target value is 0.1% at a maximum and control within 0.01%. Light transparency of the film is 99.4$\pm$0.3% at 400 nm wavelength. Xe gas tightness falls below the detector sensitivity and the amount of Xe loss is estimated to < 1.3 kg/5 yr. It has also enough compatibility against liquid scintillator. Welding procedure, its condition (temperature, welding and cooling time) and how to repair a leak point are also tested with selected film and well established.

Table 3.5: Radioactivities of nylon ingredients ($\times 10^{-12}$g/g). ^{40}K is estimated by its natural abundance, 0.0117%.

Company of pellettes	^{238}U [g/g]	^{232}Th [g/g]	K (^{40}K) [g/g]
Company A (Taiwan)	0.6	1.1	1.3×10^{4} (1.5)
Company B (Japan)	< 0.1	< 0.1	2.5×10^{3} (2.5)
Company C (Germany)	0.8	< 0.1	6.0×10^{3} (0.29)
Company D (Netherlands)	1.0	15.0	1.5×10^{3} (0.18)
Company E (Japan, with mineral filler)	6.8×10^{3}	3.2×10^{4}	2.6×10^{6} (304)
Company E (Japan, no mineral filler)	86	5.0×10^{2}	$< 1.0\times10^{5}$ (< 12)
Company F (Japan, with mineral filler)	1.2×10^{2}	2.7×10^{2}	$< 1.0\times10^{5}$ (< 12)
Company F (Japan, no mineral filler)	< 5	< 5	$< 1.0\times10^{5}$ (< 12)

Table 3.6: Radioactivities of films ($\times 10^{-12}$g/g). ^{40}K is estimated by its natural abundance, 0.0117%. "After washing" means sample washed with ultra pure water by an analysis company.

Company of film/Company of pelletts	^{238}U [g/g]	^{232}Th [g/g]	K (^{40}K) [g/g]
Toyobo/Company A (Before washing)	9	11	$< 1.0\times10^{5}$ (< 12)
Toyobo/Company A (After washing)	2	3	2.0×10^{4} (2.3)
Toyobo/Company B (Before washing)	20	28	$< 1.0\times10^{5}$ (< 12)
Commercial product of Toyobo	24	420	$< 1.0\times10^{5}$ (< 12)
Commercial product of company G	150	590	1.2×10^{6} (140)

3.5.4 Fabrication of inner balloon

To avoid the interfusion of no matter how tiny amount of radioactivity from dust, the IB was fabricated at the super clean room, classified as "class 1" cleanliness. Ordinary "1" means the number of a dust in 1 feet^3 and the size is more than 0.5 μm, however, in this clean room, counted dust size is more than 0.1 μm. Everything brought to this room is thoroughly washed/wiped by alcohol and/or pure water, sometimes with cleanser, and dried with nitrogen to keep its cleanness.

Procedure of the IB fabrication (it is also summarized in Fig. 3.15) is the following;

1. film cutting, washing, and checking scratch,
2. clipping and welding,
3. leak check and patching,
4. assembly with supporting structure,
5. wrapping and sending to the experimental site.

Figure 3.15: Pictures of the IB fabrication. [(1)-1] The film washing by the ultrasonic cleaning with pure water. [(1)-2] Checking scratches/pin holes by eyes. [(2)-1] Clipping the gores. [(2)-2] Welding. [(3)-1] Leak check with helium detector. [(3)-2] Patching the film with glue. (4) Assembling the IB, connection pipe, supporting belts and Vectran strings. The IB covered with inner envelopes. (5) The wrapped IB in the plastic box. The box covered with an air tight bag and filled N_2. It sent to the experimental site.

The radioactivity measurements of the film shows that washing is effective to decrease impurities. Then cut film with 5.5/7.5-m-length is washed by supersonic cleaning with pure water. Washed film is dried with nitrogen and examined patiently for scratch/pin holes by eyes. Trouble-free films are stored in a clean box with nitrogen gas purging. After washing all of the films, they are clipped to each parts like 24 gores for main sphere, polar caps and so on. Pattern is marked by a blue pen and after clipping, residual ink is wiped with iso propyl-alcohol. Of course, radioactivity of the ink was measured and confirmed to be negligible. The IB is made by heat welding of the films, so less welding lines are better. The 60-cm-width of the film, however, nearly determines the number of gores. To make the sphere shape from 24 gores, each 2 gores are welded at first (12 of doubled gores left). Then 2 of doubled gore are welded to one gore, 2 of four-in-one gore are welded... and finally one sphere is accomplished. Due to the sphere shape and its size, mounting big size welding machine cannot be used for this work. To make one welding line for one gore, we need welding many times with a handy 30-cm-long machine. After welding all parts of the balloon, leak check was done with a He leak detector. There was no leak on the film but some leaks were found at the multi-welding or complicated lines like the bottom part called polar. All the leaks were repaired with a glue (aron alpha[16]) and patching nylon film pieces. An accomplished balloon was folded, put nylon belts through the valleys of folded films, and covered with inner envelopes which keep the balloon folded during the installation. Connection pipe and Vectran strings are also attached and covered with a protection film. Assembled things are put in a plastic box and fixed to that. The box is put in an air-tight bag, filled nitrogen and wrapped several times. It is sent to the experimental site with a truck. This fabrication was started in the end of May and finished in Aug. 2011.

3.6 Inner balloon installation

One can say, "just putting the Xe loaded LS (with an inner balloon) into the KamLAND, KamLAND-Zen can start", however it is easier said than done. We should establish the procedure how to keep its cleanness, install, and confirm its condition since failure won't be tolerated. We decide the procedure by repeating tests and improvements, and finally succeeded in the installation.

3.6.1 Procedure and requirements

The procedure of the IB installation is mainly divided to 3 steps.

1. Installation of folded IB with heavy dummy-LS as a weight,
2. inflation with dummy-LS (Xe-free LS),
3. replacement of dummy-LS with Xe-LS.

It is also shown in Fig. 3.16 with pictures of the real scale test balloon. Each step satisfies the following requirements.

[16]This glue (popular in Japan) has good LS compatibility and good Xe-LS tightness confirmed with repaired samples.

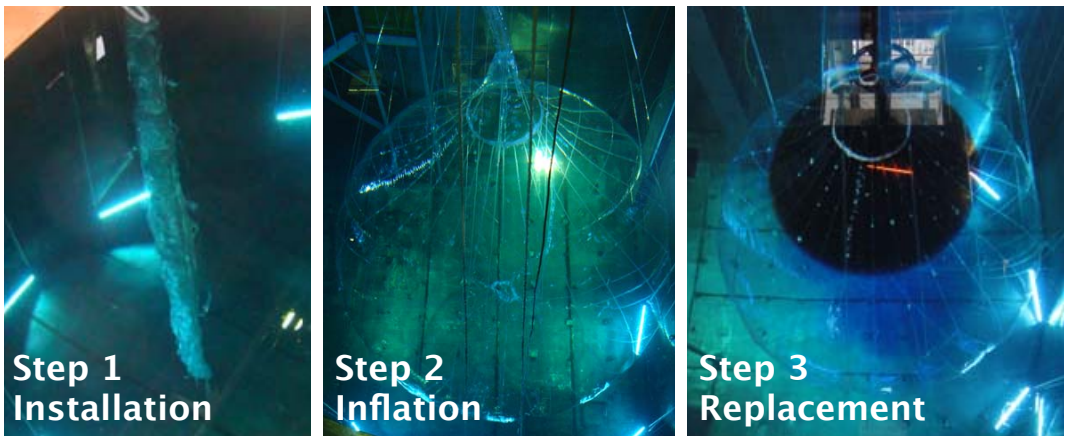

Figure 3.16: Pictures of the real scale test balloon used for the installation rehearsal. Instead of liquid scintillator, water used. Folded balloon just after the installation (left), inflated with +0.2% by weight water (center), and layer production test (right). In the right picture, red at the top is ±0.0% by weight, transparent at the center part is +0.2% by weight and blue at the bottom is +0.4% by weight density. Density difference is made by sugar and water is colored with food additive.

Step 1 comes from two requirements that (i) a limitation of an opening section and (ii) submerging the IB in LS wholly. Due to the spherical shape of KamLAND balloon and a stainless tank, its connection between the inside and the outside of the detector is placed at the top of the detector and its flange size is only 50-cm-diameter. So 1.54-m-radius nylon IB should be folded up like a tube and keep its shape during the installation. To keep folded shape, the IB is covered with the films (inner envelope) and tied with a mesh sheet as shown in Fig. 3.17. Of course, these shape keepers should be removed completely from the detector after the installation. Then ropes are connected to one vertex of every films. Mesh sheets are held by nylon pins. Pins are also connected to another ropes. When pull the ropes, pins come out and mesh sheets come untied, and all items are drawn up. For the requirement (ii), we use +0.4% by weight of heavy LS (∼90 litter in total) as a weight to sink the IB straight with keeping its folded shape. Although nylon density is heavier than KamLAND LS, the IB contains air/nitrogen inside and it gives buoyancy force to the IB. By the repetition of sending small amount of liquid and sinking, the IB sinks straight slowly. A teflon tube supplies LS in the IB. Its end is at the bottom of the corrugated tube.

After the installation, the IB is inflated by dummy-LS firstly to investigate whether it has a leak point or not. This is step 2. Dummy-LS composition is decane, PC and PPO. It does not contain xenon. During this step, we collect the data with KamLAND and if some leaks are found, the IB will be pulled out from the inner detector immediately. Density is also controlled during the filling.

When dummy-LS filling finishes successfully, it is replaced to the Xe-LS (step 3). To replace the LS, density difference between dummy-LS and Xe-LS is needed to keep layers. This method looks difficult but from the experience of distillation

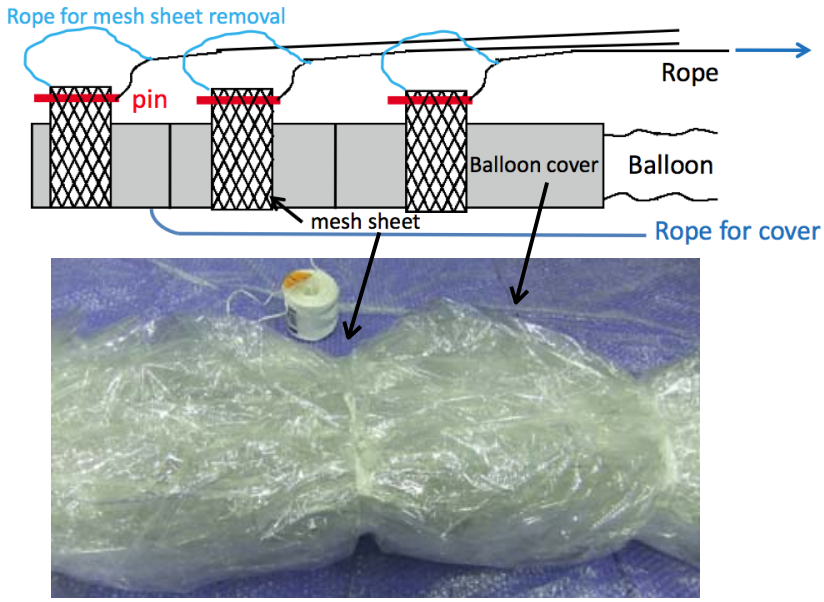

Figure 3.17: A schematic and picture of the IB holding structure.

for solar neutrinos, we succeeded to keep layers by controlling density difference. To produce the layer, we need to fill the Xe-LS from the bottom and drain the dummy-LS form the top of the IB. Then, another long teflon tube is inserted in the IB[17].

In addition, there are other requirements which is not related directly to each of the steps. For example, we cannot see the inside of the detector or status of the IB by eyes due to a light shielding flapper covered with black sheets. It causes lack of lighting. We should also pay attention to a narrow-entry that may break the IB. So we need a monitoring system such as cameras and lights to confirm the status of the IB. During the preparation and real part for the installation, we would like to avoid the interfusion of radioactivity from dust, so we need a clean room around the entrance of the detector and keep it clean. Then we install the monitoring system and the clean room at the top of the detector as described in the next section.

3.6.2 Installation of inner balloon

Fabricated inner balloon was sent to Kamioka mine in Aug. 2012. The dome area where has a entrance to the inside of the detector was clean as "class 2000", but considering the environment and the working space, we needed to construct a "class ∼100" clean room there. Its floor plan and pictures are shown in Fig. 3.18. In order to install the IB, calibration device and its glove box were already removed in June, and construction of the clean room pushed. The finished clean room was cleaned from the top to the bottom, and kept its cleanness as 10∼100 even when people were working. To keep this environment, tools and parts ranging from some flanges,

[17]This long teflon tube was removed after all works were finished.

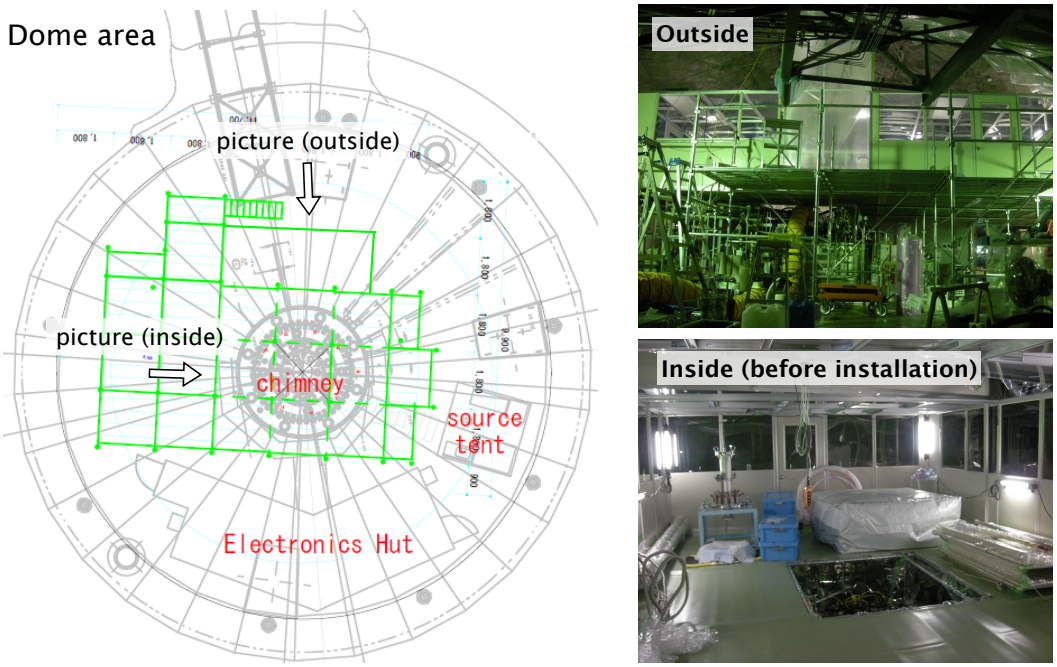

Figure 3.18: Floor plan of the dome area (left) and pictures of the clean room (right). In the left picture, green line shows an outline of the clean room. The entrance to the detector (or top big flange) is placed about one meter higher than the floor. Then a floor of the clean room is adjusted to that height.

teflon tubes, spanners to every bolts, nuts, and washers were completely washed at the "class 1" clean room and carefully sent to Kamioka. Air in mine contains much Rn than the outside. Rn free air is send to the clean room and kept its level to 1.5∼2.0 pCi/l, corresponding to 56∼74 Bq/m^3.

At first, the monitoring system consists of two camera housings and two LED lights, which have LS compatibility, were installed to the inside of the detector. The system is presented in Fig. 3.19. In addition to monitor the IB condition, two camera housings watched each other to confirm each position. It helped to avoid touching the IB by accident. Due to the limitation of the location to access the inside of the detector, cameras and lights were installed from small flanges where is very close to the main big flange used for the IB installation. For the installation of the system, we made holes to the light shielding. Due to this light shielding, no one saw the inside of the detector after KamLAND data taking started. Owing to the monitor system, we were able see the inside of the KamLAND for the first time in about 10 years.

After the installation of the monitor system, folded IB connected with the corrugated tube started putting into the detector (step 1). Since it has ∼14m long in total, ten and a few people held that and slowly moved it forward. The IB was slowly submerged in the LS on the straight with keeping its shape. The installation successfully finished within 2 hours. Inner envelope removal, flange mounting and

Figure 3.19: Pictures of a monitoring system. (Left) Two LED lights compensate for the lack of light in the detector. (Center) Web camera housing. The housing is made from acrylic and stainless. One housing has two web cameras at the side and the bottom indicated with white arrows. A light is also built in the housing. We use two camera housings. (Right) Monitor connected with web cameras. The screen shows a side camera picture of another camera housing located in the detector. A laptop controls camera's tilt, zoom in/out and so on.

load cell setting were also succeeded. Some works are shown in Fig 3.20. Inflation of the IB with dummy-LS (step 2) took 6 days and finished at the end of August in 2011. During the inflation, the IB was monitored with cameras. At the end of the inflation, we took data to check its shape and to find a possibility of leakage by Rn distribution. Thanks to the KamLAND, the existing detector, established DAQ system and the analysis tool, it was possible. Fortunately, no leak was found. After the inflation with 17 m^3 of dummy-LS, to equalize a density with first dense and later light one, we agitated the LS by the filling from the bottom and the draining from the top. To break the layer of dense LS, 5°C lower LS filling and 3 days circulation were done. After checking a uniformity of the LS by Rn distribution, we started Xe-LS filling to replace it from dummy-LS. The Xe-LS was made by Xe system with purified LS. Density difference with dummy-LS is 0.02% by weight and with KamLAND LS is 0.035% by weight. Filling speed from the bottom was 150 l/hour and drained from the top as the same speed. Rn distribution told us the boundary of Xe-LS and dummy LS. Returned LS was also monitored by gas-chromatography to check whether Xe returns or not. Finally 316 kg of Xe corresponding to 287 kg of ^{136}Xe dissolved into LS was installed successfully in KamLAND. After finishing the Xe-LS filling, the Xe-LS was circulated and confirmed its uniformity. Diagrams of the Rn distribution during Xe-LS filling and agitation mode are shown in Fig. 3.21. All of the works related to the installation were done at the middle of September in 2011.

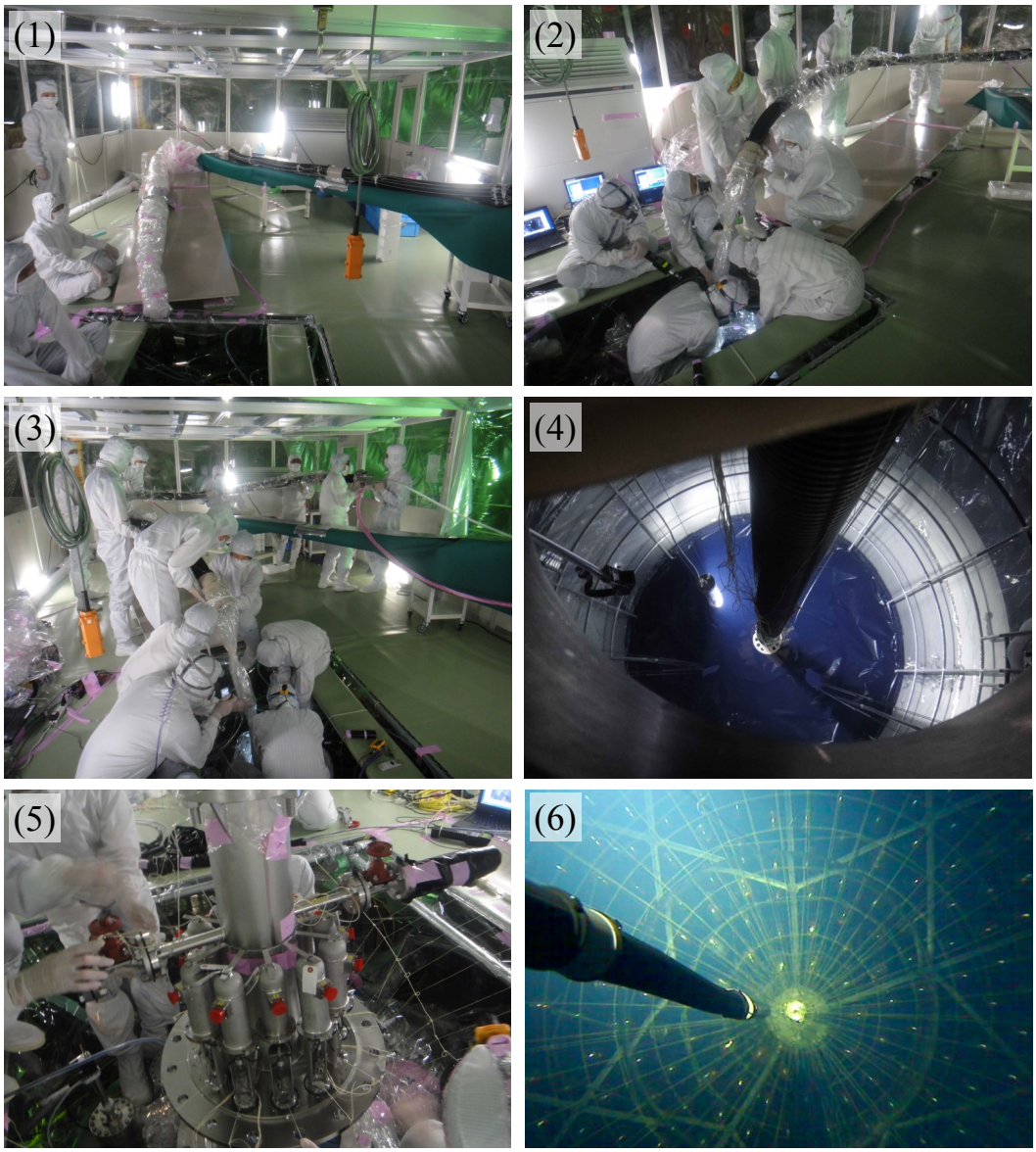

Figure 3.20: Pictures of IB installation. (1) Just before the installation. (2) During the installation. (3) During the installation, too. (4) Top view. Black straight line is corrugated tube and dark blue sheet is light shielding flapper covered with black sheets. (5) Flange connection. Below part is load cell for 12 strings. (6) A picture of the inside KamLAND after the installation. Black tube is corrugated tube connected to the IB. You may see the boundary of IB by difference of refractive index. Dim points show PMTs.

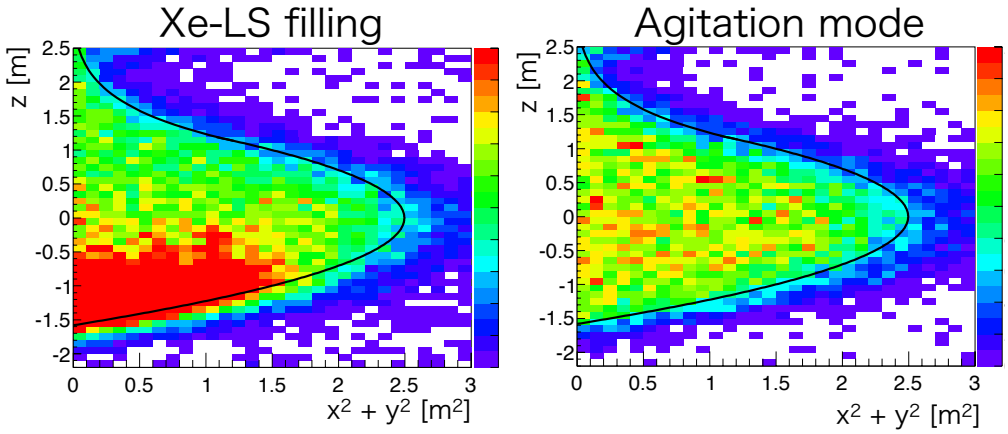

Figure 3.21: Rn distribution during Xe-LS filling (left) and agitation mode (right). Black line shows the IB. A clear boundary is seen in the left but not in the right figure.

3.7 Xe handling system

Figure 3.22 shows a diagram and pictures of Xe handling system. The system has the following features;

- dissolve Xe into LS by bubbling,
- control the density of (Xe-)LS with 0.005∼0.01% accuracy,
- control the amount of sending and returning (Xe-)LS and its flow speed,
- collect Xe from Xe-LS by degassing and gas bubbling.

The system is composed of four tanks (main tank, sub tank, control tank and reservoir tank), two traps (Xe trap and LS trap) and two compressors. When making Xe-LS, Xe gas held in the reservoir tank is sent to the main tank and bubbling to the liquid scintillator. Xe loaded LS in the main tank is sent to the sub tank, adjusted the density with PC in the control tank and finally sent to the IB. On the contrary, when collecting Xe gas from Xe-LS, Xe gas is extracted by degassing and bubbling. Since the extracted Xe gas contains vaporized LS, there are two traps that one is LS trap cooled down to $-70 \sim 50$°C and another ons is Xe trap cooled down to less than -105°C by liquid nitrogen. Collection efficiency is 99.99∼99.999% depending on the control condition. Concentration of Xe in LS is calculated by amount of Xe used in. There are three ways to check the amount; pressure of Xe tank, mass difference of Xe gas, and measurement of Xe-LS density.

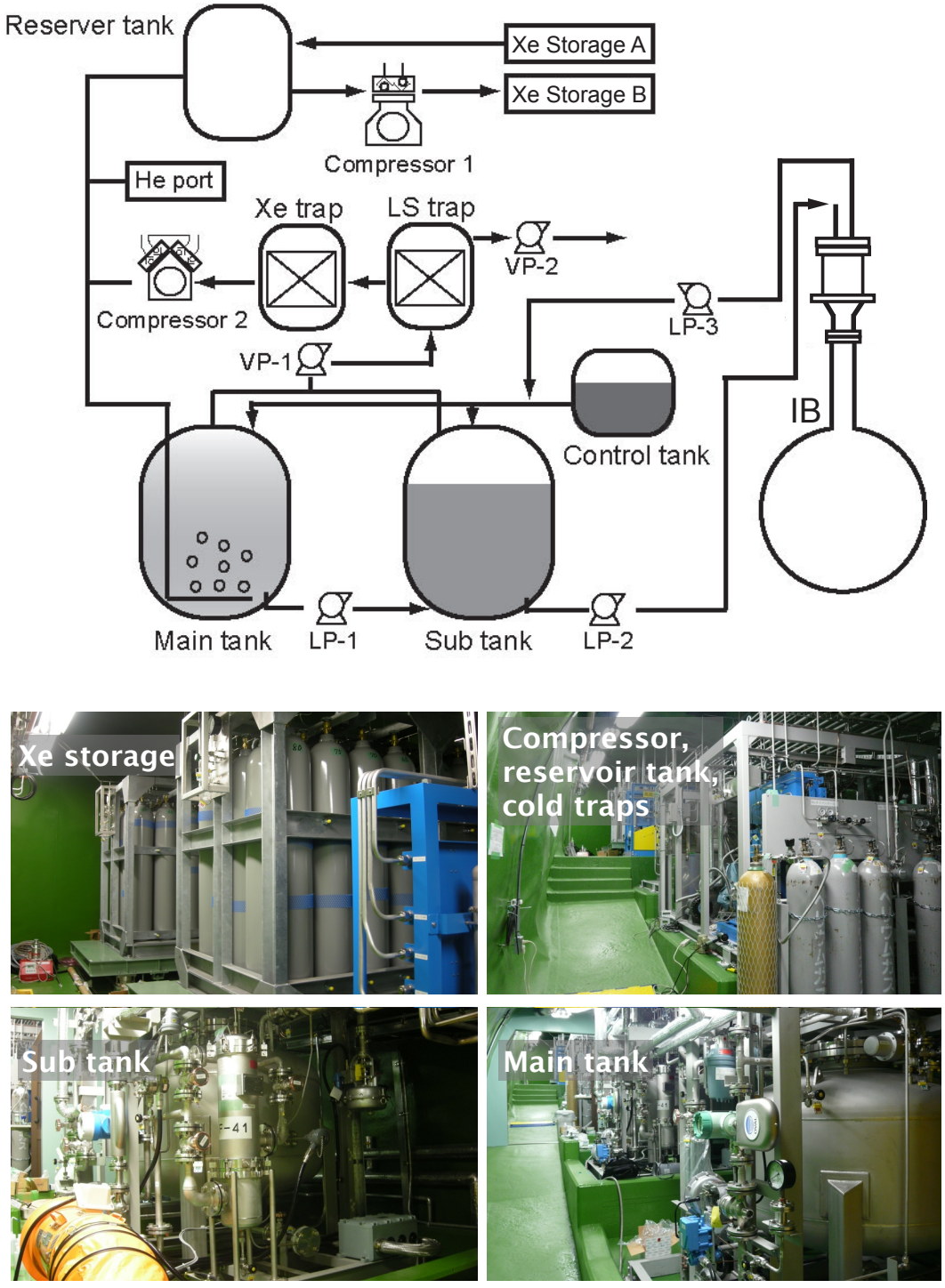

Figure 3.22: A schematic view of Xe handling system and each picture.

3.8 Calibration system

3.8.1 Calibration system for KamLAND

Various radioactive sources with known energies were deployed into the inner detector to estimate and monitor the vertices and energy reconstruction performance. Table 3.7 lists the radioactive sources used for KamLAND. Calibration system installed in the glove box was located at the top of the center of the detector. To prevent the interfusion of oxygen and radon into the detector, the chimney was tightly shielded by a gate valve and nitrogen gas was always supplied. Nitrogen gas was also supplied to the glove box and oxygen level was monitored. If oxygen level was low enough, we were able to start the calibration.

Table 3.7: Calibration sources used for KamLAND.

Source	Decay	Visible Particle
^{60}Co	β	1.173 MeV γ + 1.332 MeV γ
^{68}Ge	β^+	0.511 MeV $\gamma \times 2$
^{137}Cs	β	0.661 MeV γ
^{203}Hg	β	0.279 MeV γ
^{85}Sr	Electron capture	0.511 MeV γ
^{65}Zn	Electron capture	1.115 MeV γ
^{241}Am^{9}Be	^{9}Be(α, n)^{12}C	4.4 MeV γ, n (<10 MeV)

There were three generations of calibration systems. Before December 2005, all of calibration with various radioactive isotopes, LASER light diffuser and LED were done along the vertical center axis of the detector (z-axis) by "Z-axis deployment system". In December 2005, full volume "4π" calibration system consisted of a segmented calibration pole was installed, and it enabled to deploy the source both on/off axis, although detector is spherical shape and it has one small (15.24-cm-diameter) entrance to the inside [84]. Third system is called "MiniCal", z-axis calibration system, which was installed and commissioned onsite from February to March, 2009. The concept of this system is compact and clean in order to use for the solar neutrino observation phase (Feb. 2009 $\sim$ Jul. 2011).

As for z-axis calibration, the calibration sources are connected to a stainless steel cable and bring to the inside of the detector. They are placed at mechanically determinable positions from z = $-$6m to z = 6m[18]. This calibration (especially for composite ^{60}Co^{68}Ge source calibration at the center) was done regularly and provided the essential data for the vertex reconstruction, energy estimation and time variation of those. At the beginning of the KamLAND, a LASER light calibration was also done to calibrate PMT hit timing.

Off-axis (4π) calibration was performed at any coordinates in the detector controlled with 2 cables attached at the top and the bottom of the assembled pole. A pole is made by 90-cm-long hollow titanium and radioactivity sources are attached

[18]The center of the detector is z = 0m.

to the end of the pole. This calibration was done in 2007 and 2011. It improved the systematic error coming from fiducial volume (the dominant uncertainty for the detection of anti-neutrinos) by factor of two at a radius of 5.5 m. Radial distribution of composite source and the reconstruction deviations of energy and position are shown in Fig. 3.23.

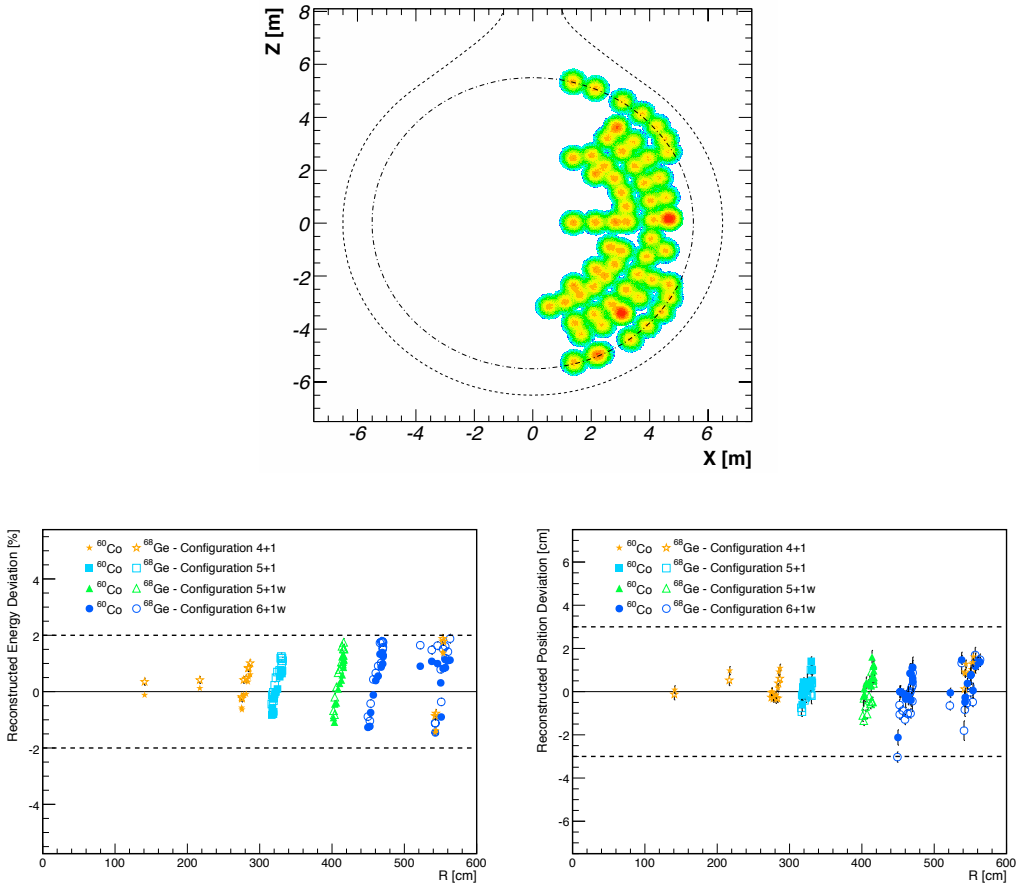

Figure 3.23: Radial distribution of composite ^{60}Co^{68}Ge source (top), and the reconstruction deviations of energy (bottom-left) and position (bottom-right) as function of detector radius. Pictures from Ref. [84].

3.8.2 Calibration system for KamLAND-Zen

Currently, a source calibration along z-axis with previous system is very difficult since we cannot use anything which has possibility of scratching/breaking the IB. Its straight part has 10-cm-diameter and film thickness is only 25 μm. In addition, the glove box at the top of the chimney, which stored z-axis/off-axis calibration system was removed due to the installation of the IB.

The ThO_2-W (^{208}Tl) source, contained in a ∼5-mm-thick lead capsule, was deployed close to the outer surface of the IB with another glove box. Its decay scheme

and main visible particles are presented in Table 3.8. A schematic and picture of the source, and calibration position are shown in Figure 3.24. The 2.615 MeV γ's, close to the Q value of ^{136}Xe (2.458 MeV), are used for the energy calibration, determination of the energy resolution and so on. Detail is found in Section 4.7.4.

Table 3.8: Calibration source used for KamLAND-Zen.

Source	Decay	Main Visible Particle
^{208}Tl	β	2.615 MeV γ (+ 0.583 MeV γ)

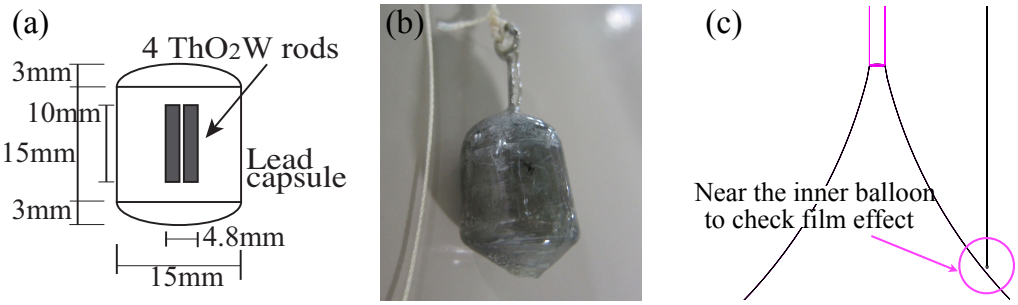

Figure 3.24: ThO_2-W source and calibration position. (a) A schematic view of ThO_2-W source and (b) its picture. (c) shows source position during the calibration.

In the future, modified "MiniCAL" system will be re-installed to perform z-axis calibration in the IB with various sources.

Chapter 4

Event reconstruction

This chapter summarizes how hit-times and charges are extracted from PMT signals and then translated into event properties such as energy and position.

4.1 Procedure of event reconstruction

The procedure of event reconstruction is as follow:

0. Data acquisition (Section 3.2.6).
   When an event deposits the energy in the liquid scintillator, it generates a scintillation photon(s). PMTs detect it as an analog signal, and electronics convert it to digitized one which is recorded into the storage device. This digitized PMT hit data is called waveform data.

1. Waveform analysis (Section 4.2).
   Time and charge information are extracted from obtained digital waveforms.

2. Gain and timing calibration and bad channel selection (Section 4.3 - 4.4).
   PMTs have individual charge and time distributions. The transit time of PMT is calibrated by laser pulse. The position of 1 p.e.[1] peak (gain) is calibrated run by run. Correlation of time and charge is also corrected run by run (TQ correction). At that time, dead or unstable PMTs (bad channels) are selected and masked in order not to be used in the reconstruction.

3. Muon track reconstruction (Section 4.5).
   Different from normal events (point-like events), most of muons have high energy and go through the liquid scintillator (track-like events). Muons make after-pulses and many spallation events. In order to identify and reject/estimate those events, muon events are selected from charge and the number of hits, and then tracks are reconstructed with time and charge information of PMTs.

4. Event vertex reconstruction (Section 4.6).
   For the point-like events, event vertices are reconstructed from mainly hit time distribution of PMTs.

[1] photo-electron

5. Event energy reconstruction (Section 4.7).
   Event energy (visible energy) is estimated from hit, charge and time information of PMTs for point-like events after applying additional charge correction and consideration of photon yield efficiency. Non linear response of energy between deposited and visible energy is also estimated.

Each reconstruction qualities are also evaluated in each section.

4.2 Waveform analysis

In the waveform analysis, time and charge information is extracted from smoothed digital waveform after pedestal subtraction. These "time" and "charge" information is used for the event reconstruction after some correction applied. A waveform of typical single photo electron (1 p.e.) signal is shown in Fig. 4.1 (left). The total

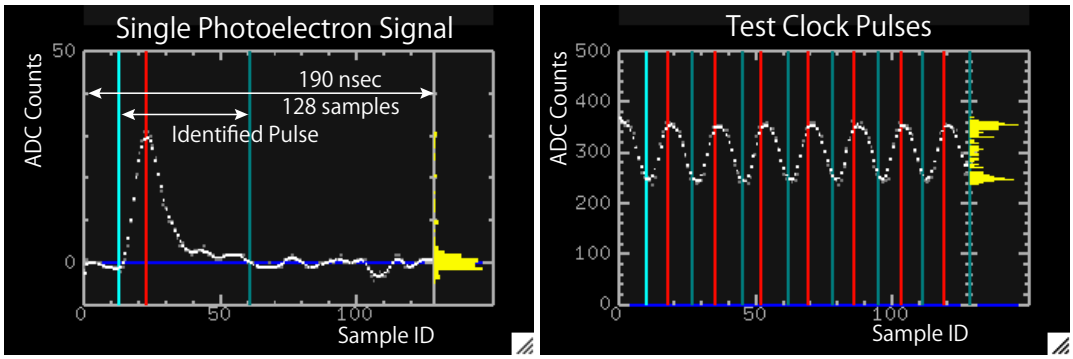

Figure 4.1: Waveform of a typical single photoelectron signal (left) and test clock pulses (right). In the left figure, red line shows the analyzed peak position, cyan line shows the start and end of the peak, and blue line shows the estimated baseline. The vertical scale of the waveform corresponds to voltage (calibrated with test-pulser waveforms), and the horizontal scale corresponds to time (calibrated with 40 MHz clock). In the right figure, test clock pulse with 25 nsec timing interval (between red/cyan lines) is shown. Both events are taken from run011133.

sampling time for one channel is about 190 nsec and the number of sampling is 128. The sampling width is ∼1.48 nsec, which is almost comparable to the transit time spread of the 17-inch PMTs. The charge is recorded in 10 bit of the ADC channels for each sample, and it is enough to see a single photo-electron peak.

4.2.1 Algorithm of waveform analysis

At the beginning, a pedestal is subtracted from waveforms since each ADC has particular offsets for each channel and each sampling bin. These offsets are estimated by averaged pedestal waveforms without noise or dark hit pulse. Usually, fifty pedestal waveforms are recorded at the beginning of each run. The waveform is then smoothed to avoid a high frequency noise. After the subtraction, waveforms have still non-zero offset due to the baseline. The offset is different from event by event and channel by channel due to after-effects of previous pulses. It is subtracted

to adjust the baseline. Peaks in the waveform are searched with derivatives, and leading edge of the first peak defines the first photon arrival time. The charge is defined as the total area of each pulse from start time to end time, and it is normalized later with the mean charge of the single photo electron pulse, as described in Section 4.3.1.

4.2.2 Calibration of time bin width

The time bin width for each channel is calibrated by test clock pulse. Fifty of 40 MHz clock pulses are generated and taken for each channel at the beginning of each run. A typical number of sampling is about 17 per one clock pulse, as shown in Fig 4.1 (right). The time information for each channel is corrected by this calibration.

4.3 Gain and timing calibration

4.3.1 Gain calibration

For the gain calibration, we use a single photo-electron (p.e.) charge since it is not influenced by quantum efficiency of PMTs or collection efficiency. Furthermore, typical event energy of our target is a few MeV and it makes 1 p.e. signals. A 1 p.e. charge is defined by area of a 1 p.e. pulse in a waveform. In order to obtain the pure 1 p.e. signals, the following hit signals of 17-inch PMTs are collected, and 1 p.e. charge is normalized channel by channel and run by run. The selection criteria of 1 p.e. pulses are;

- muon and noise events veto[2],
- 2 msec veto after muon,
- 100 μsec veto after missing waveform events,
- $120 \leq \mathrm{NsumMax}^3 \leq 230$ (low occupancy event cut),
- distance between PMT and reconstructed vertex > 6 m,
- 1 peak in waveform.

The typical 1 p.e. peak distribution of 17-inch and 20-inch PMTs are shown in Fig. 4.2. Difference of dynode structure makes the distribution different. The distribution of 17-inch PMTs have clear peak thanks to the better time resolution, while that of 20-inch do not. A peak position of 17-inch PMT is simply obtained from Gaussian distribution and used for the gain calibration. On the other hand, for 20-inch PMT gain calibration, charge ratio (relative charge) of 20-inch PMT to neighboring 8 of 17-inch PMTs is used. Relative charge is defined as follows;

$$\text{Relative charge} = \frac{\text{Charge of target 20-inch PMT}}{\text{Average charge of 8 neighboring 17-inch PMTs}} \tag{4.1}$$

[2]Muon event selection is later found in Section 4.5. How to select noise events and missing waveform events are described in Section 5.3 in later chapter.

[3]The maximum number of hit PMTs within 125 nsec after trigger issued.

The time variation of the average 1 p.e. charges is shown in Fig. 4.3.

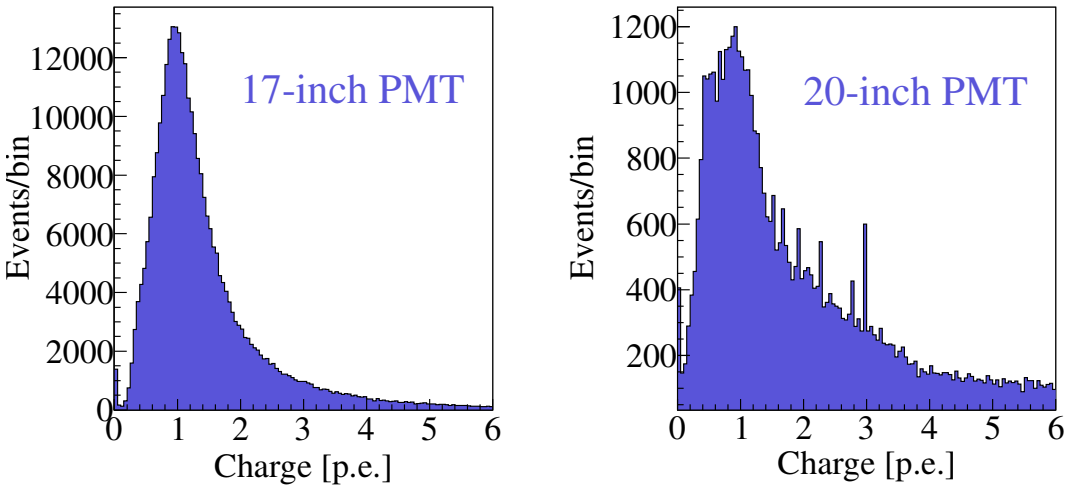

Figure 4.2: Single photo electron distribution of typical 17-inch (left) and 20-inch (right) PMTs.

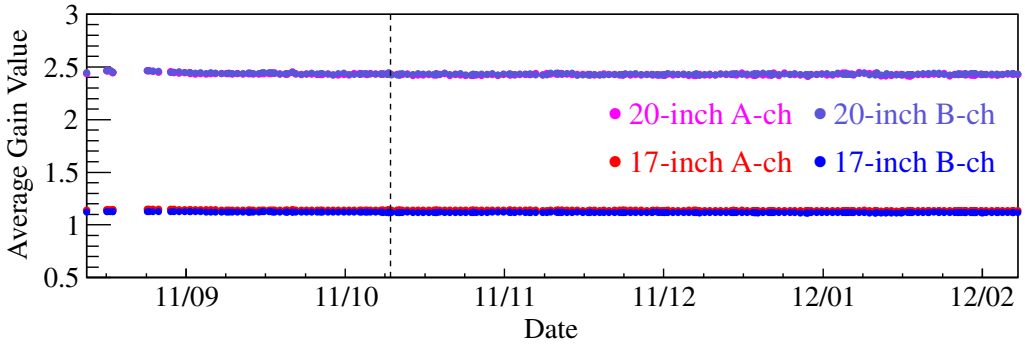

Figure 4.3: The time variation of the average 1 p.e. charge of 17-inch and 20-inch PMTs for A and B channel. Start time is August 20, 2011, the day of the first run taken after the IB installation (KamLAND-Zen period only). Vertical line indicates the start day of analysis period. Data are shown as in year/month.

4.3.2 Timing calibration and TQ correction

The leading edge of the first peak in the waveform defines the first photon arrival time. Then charge dependence of time is quite restrained. However, it may still exist. The transit time of each PMT is calibrated by the dye laser pulse which has about 1.2 nsec width. The pulse is led to the diffuser ball located at the center of the detector through a quartz optical fiber, and illuminates the PMTs in all directions. The wavelength of the laser is 500 nm. This wavelength is not absorbed (nor reemission) in the liquid scintillator. So the same timing should be indicated independent on the light intensity. The intensity is controlled from a single photo

electron to a few thousand photo electrons by filter. The diffuser ball has two same length optical fiber that one is from dye-laser to diffuser ball and another one is from dye laser to the 2-inch monitor PMT. A diagram of the calibration is show in Fig 4.4. The information of pulse time and trigger issued time are compared, and offsets caused by the time delay of the trigger are removed.

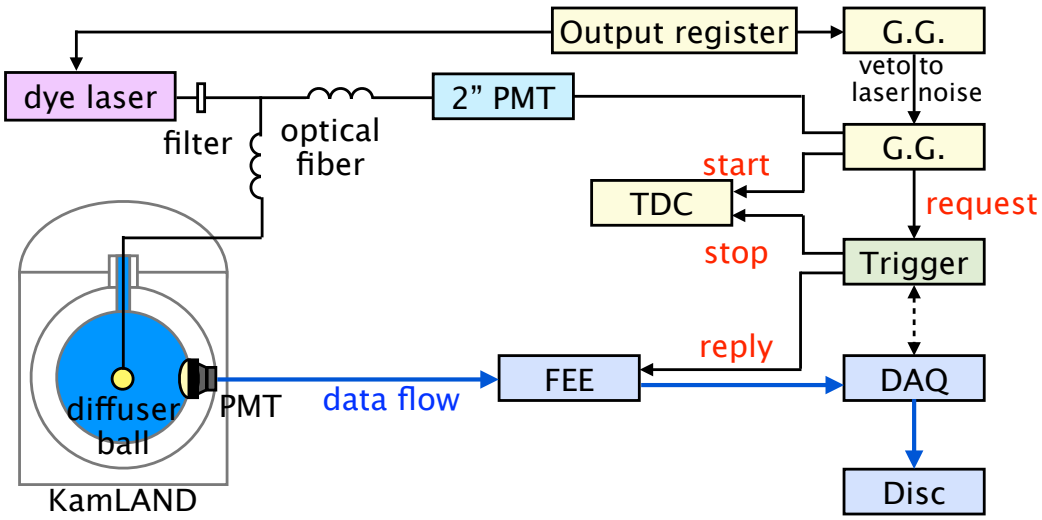

Figure 4.4: A schematic of the dye-laser calibration. G.G. and TDC stand for a gate generator and time to digital converter, respectively.

In addition, data of ^{60}Co calibration run taken at the center of the detector are used for additional timing correction since liquid scintillator condition has changed after distillation campaign. The ^{60}Co source runs were taken almost every 2 weeks after the 2nd purification. It is useful to monitor the timing distribution of PMT hits.

The rise time of a pulse is also different due to PMT gain and FEE amplifier gain. So correlation between time and charge is evaluated channel by channel with various intensity of dye laser and corrected (TQ correction). Figure 4.5 shows an example of the measured timing offset as a function of hit charge. The fitting function $T(Q)$ is expressed as follows;

$$\Delta T(Q) = P_0 + P_1 \cdot \log_{10} Q + P_2 \cdot (\log_{10} Q)^2 \tag{4.2}$$

where P_0, P_1 and P_2 are free parameters. P_0 indicates the absolute timing offset. The fit is made for each PMTs and ATWD channel individually. Figure 4.6 shows the hit time distribution before and after TQ correction. It indicates the improvement of timing resolution from 6.7 to 2.0 nsec.

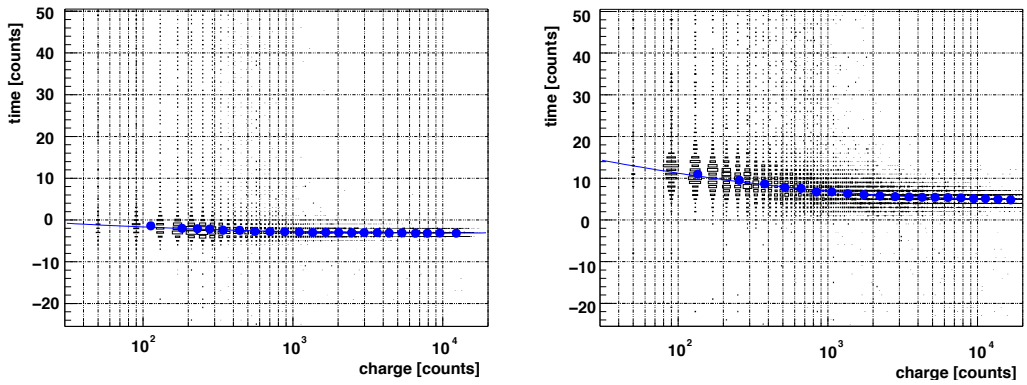

Figure 4.5: Correlation between time and charge for a typical channel of 17-inch (left) and 20-inch (right) PMT, taken from laser calibration data [85].

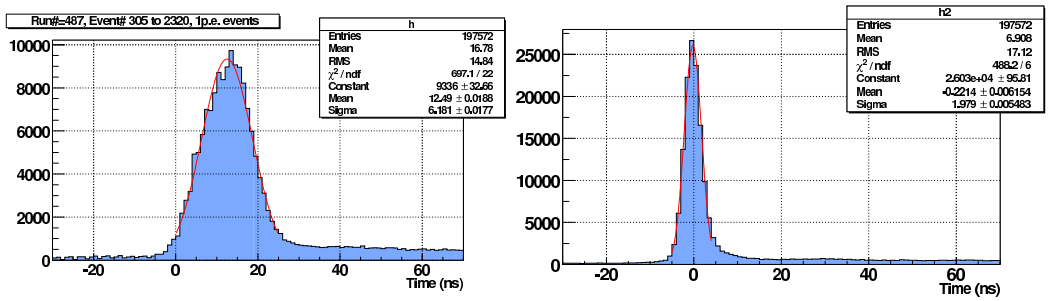

Figure 4.6: Hit time distribution before (left) and after (right) TQ correction [86].

4.4 Bad channel selection

KamLAND uses 1,325 of 17-inch and 554 of 20-inch PMTs (in total 1,879 PMTs) in the inner detector (ID) and 225 of 20-inch PMTs in the outer detector (OD). In these PMTs, some unstable channels, called "bad channels", are included. They have too many hits, no hits or strange charge due to broken PMTs, unstable HV supply or the mis-connection of signal cables. These bad channels are masked in the event reconstruction processes to prevent systematic biases, while they are used to monitor the detector condition and to estimate the bad period. Current criteria of the bad channel selection for the ID is as follow;

1. (1) Hit rate (< 600 hits / 10,000 events).
   (2) Hit rate (< 480 hits / 10,000 events except for muon events).
   To find low response channels due to electronics failure.

2. No-hit rate (> 1,000 no-hits / 10,000 events).
   To find no response channels due to a high voltage problem.

3. Hit rate in high charge muon event (< 80 hits / 100 muon events).
   To find excessively low gain channel.

4. Difference of hit rate between A and B channel ($> 22\%$ in 10,000 events).
   To find bad channels due to FEE failure.

5. Charge difference (badness) in 100 of high charge muon event which satisfied the following relation;

$$\frac{1}{N_i}\sum_{j=1}^{N_i}\frac{(Q_j - Q_i)^2}{Q_j} > 1,000 \text{ p.e. } (Q_j > 0,\ j : \text{neighbor PMTs}).$$

   To find channels with a large gain difference by a comparison of the gain between neighbor channels.

6. ADC counts for 1 p.e. is low ($< \overline{Q}_{\mathrm{ADC}} \times 1/4$) or high ($> \overline{Q}_{\mathrm{ADC}} \times 4$).
   To find very low gain or very high gain channels. $\overline{Q}_{\mathrm{ADC}}$ is the mean of ADC counts which correspond to 1 p.e. of all 17-inch channels.

For the OD, selection criteria 1 is applied as follows;

1. Hit rate (< 5 hits / 10,000 events).

Figure 4.7 shows the time variation of the number of bad channels after KamLAND-Zen data taking started. The number of bad channel has increased gradually. However, in this period, it is almost stable. There are many bad PMTs in the OD due to water leakage, and currently, 70% of them are masked.

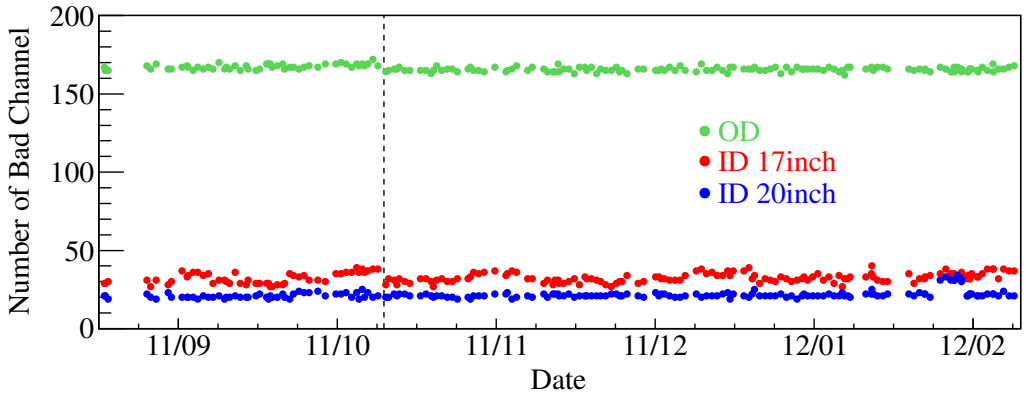

Figure 4.7: Time variation of the number of bad channels. Horizontal axis is shown as in year/month. Start time is August 20, 2011, the day of the first run taken after the IB installation (KamLAND-Zen period only). The green, red and blue points show OD, ID 17-inch and ID 20-inch PMTs, respectively, and vertical line indicates the start day of analysis period.

4.5 Muon track reconstruction

Cosmic ray muons passing through the detector interact with scintillator materials and make various spallation products such as ^{10}C which is a serious background for ^{136}Xe double-beta decay. Then muon event reconstruction to identify the muon events and remove the correlated backgrounds is essential.

4.5.1 Selection criteria

Cosmic muon events are easily identified by their enormous light output in the ID/OD by scintillation/Cherenkov light. In KamLAND, selection criteria for muon events are as follow;

- $Q_{17} \geq 10{,}000$ p.e.
  Q_{17} is a total charge of the 17-inch PMTs in the ID. The event rate of this selection is ∼0.34 Hz.

- $Q_{17} \geq 500$ p.e. and $N_{200OD} \geq 5$ hits.
  N_{200OD} is the number of hits in the OD within a 200 nsec time window. This selection searches for the muons that go through only buffer oil. They emit only Cherenkov photons resulting lower charge sum. The event rate of this selection is ∼0.01 Hz.

The charge distribution of muons is shown in Figure 4.8. Two clear peaks indi-

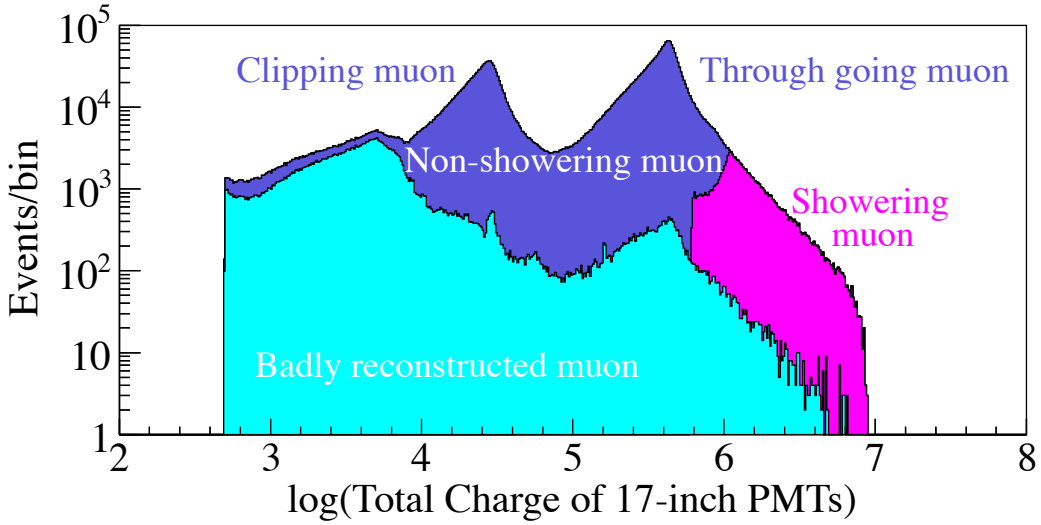

Figure 4.8: Charge distribution of muon events. The highest peak filled with blue histogram is produced by "through going muon" which emits mainly scintillation light, while the second peak is by "clipping muon", which emits only Cherenkov photons. The cyan histogram indicates the badly reconstructed muons, and magenta histogram shows showering muons whose residual charge is more than 10^6 p.e.

cate "through going muons" (scintillation light (dominant) + Cherenkov light) and "clipping muons" (Cherenkov light only). These muon types are dependent on muon tracks that through going muons pass through the buffer oil and the liquid scintillator, while clipping muons do only the buffer oil. Thorough going muons are further categorized into the following two types that (1) showering muon ($\Delta Q > 10^6$ p.e.) and (2) non-showering muon ($\Delta Q < 10^6$ p.e.), where ΔQ is "residual charge" described in Section 4.5.3. About 10^6 p.e. of the residual charge corresponds to 3 GeV. Then showering muons are very energetic muons. They often produce the spallation

events and after-pulses. The ratio of them to all the muons is about 2.5%. The ratio of badly reconstructed muons (badness > 100) is about 8.7% in all muons, and it increases in the lower charge. The muon rate is estimated to be about 0.35 Hz from the time difference between muon events as shown in Fig. 4.9, and it is stable during this analysis period. Time variation of the mean charge of through going muon and clipping muon is shown in Fig. 4.10.

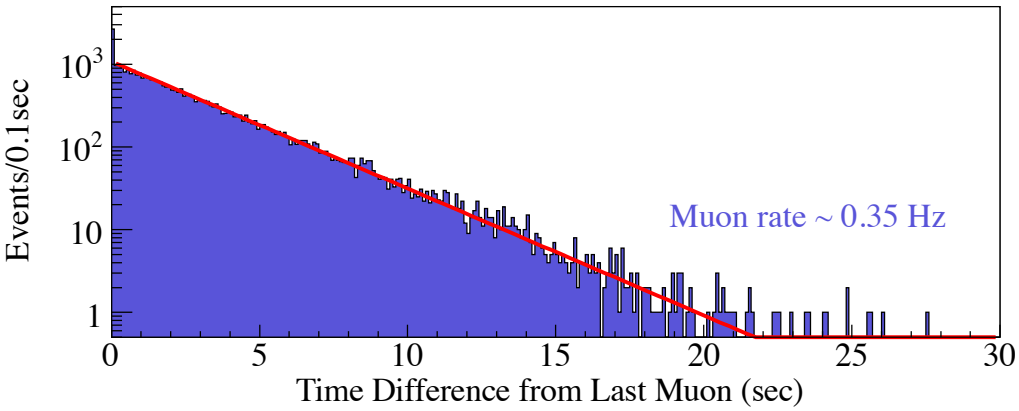

Figure 4.9: Time difference from muon to muon taken from typical 24 h physics run. Estimated muon rate is ∼0.35 Hz.

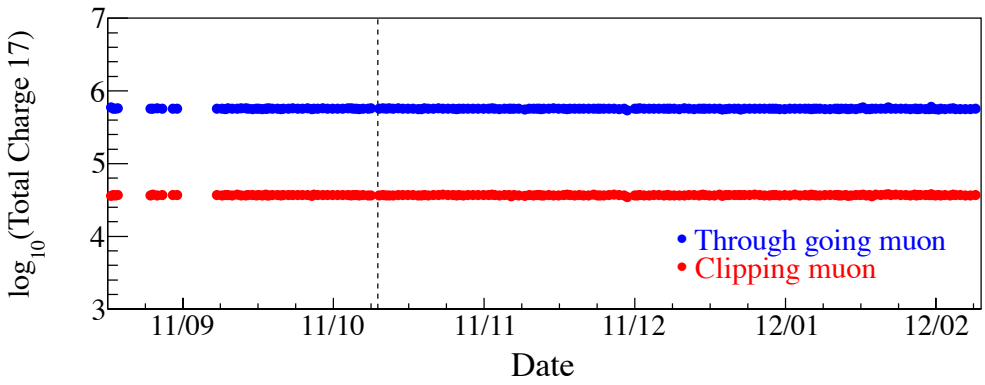

Figure 4.10: Time variation of the mean charge of through going muons (blue) and clipping muons (red). Vertical line indicates the start day of analysis period and horizontal axis is shown as in year/month.

4.5.2 Algorithm of muon track reconstruction

The muon track reconstruction is based on the timing information of PMT hits. In the liquid scintillator, muons emit both Cherenkov and scintillation photons along their tracks. As shown in Fig. 4.11 (a), the direction of Cherenkov photon emission is determined just by Cherenkov angle, $\cos\theta_c = 1/n$, where n is refractive index of the liquid scintillator. On the other hand, the scintillation photons are emitted

isotropically from each point of the muon track. With the notation of Fig. 4.11 (b), the observed time t, which is the arriving time of the earliest light to the PMT, is expressed as a function of l using simple geometrical relation;

$$\begin{aligned} t &= t_0 + \frac{l}{c} + \frac{z-l}{cos\theta} \cdot \frac{n}{c} \\ &= t_0 + \frac{l}{c} + \sqrt{(z-l)^2 + \rho^2} \cdot \frac{n}{c} \end{aligned} \tag{4.3}$$

where t_0 is the time when a muon entered to the detector and c is a speed of light. In this relation, the velocity of the muon is approximated to be the speed of light. To obtain the minimized t, we just calculate $dt/dl = 0$ of Eq. 4.3 and find $\cos\theta = 1/\mathrm{n}$ which corresponds to the angle of Cherenkov light emission. The refractive index of

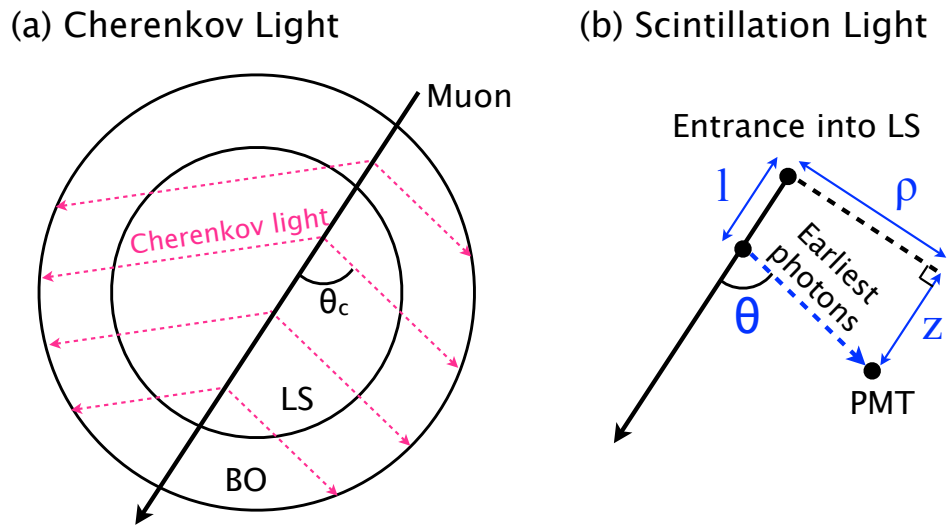

Figure 4.11: The schematic view of muon track for (a) Cherenkov light and (b) scintillation llight.

the liquid scintillator and the buffer oil are measured to be 1.44 to 1.47 in the various wavelength of the light, and parameterization of the speed of light depending on the position is introduced to handle the difference of reflective index between the liquid scintillator and the buffer oil.

In the case such that a muon stops in the detector (too small charge deposit) and/or multiple muons go through the detector at the same time, muon tracks are not appropriately reconstructed. Such muons are classified into "mis-reconstructed muons", defined by badness and total charge of 17-inch PMTs. The ratio of mis-reconstructed through going muons to all muons is about 0.7%.

4.5.3 Tracking performance

Relation between the total charge of 17-inch PMTs and the distance to muon tracks from the detector center (impact parameter) with well-reconstructed muon is shown

in Fig 4.12. A boundary of the liquid scintillator and the buffer oil is located at 650 cm, and this plot clearly indicates it. Figure 4.13 shows the relation between the reconstructed track length and a total charge of 17-inch PMTs. These two parameters have a linear correlation.

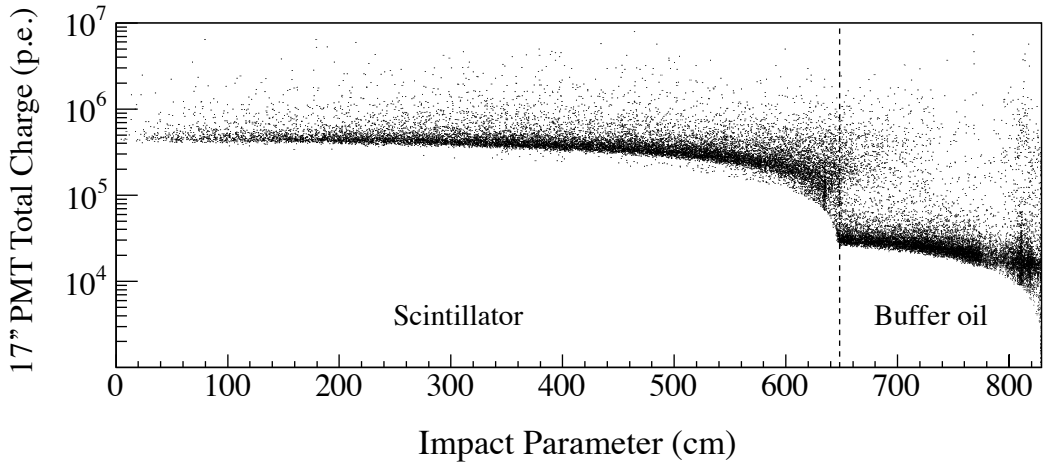

Figure 4.12: Relation between muon total charge (Q_{17}) and track impact parameter. The clear boundary around 650 cm corresponds to the actual balloon edge.

The distribution of normalized charge divided by reconstructed muon track length (dQ/dL) in the buffer oil and the liquid scintillator is shown in Figure 4.14, where dQ/dL is defined as follow;

$$\left(\frac{dQ}{dL}\right)_{Cherenkov} = \frac{Q_{17}}{L_{ID}} \ (r > 650\ cm) \tag{4.4}$$

$$\left(\frac{dQ}{dL}\right)_{Scintillation} = \frac{Q_{17} - L_{ID}(dQ/dL)_{Cherenkov}}{L_{LS}} \tag{4.5}$$

where r, L_{ID} and L_{LS} is an impact parameter, track length in the inner detector and track length in the liquid scintillator, respectively. That of Cherenkov is estimated by clipping muons, and scintillation are evaluated by through going muons. The ideal value of normalized charge, $(dQ/dL)^{ideal}$ is estimated to 31.45 p.e./cm and 629.4 p.e./cm for Cherenkov and scintillation, respectively, which was obtained by the mean of Gaussian distribution. From these dQ/dL values, residual charge, ΔQ is estimated to discriminate showering muons ($\Delta Q > 10^6$ p.e.). Value of $(dQ/dL)_{scintillation}$ changes due to the liquid scintillator condition such as before/after purification, while $(dQ/dL)_{Cherenkov}$ remains almost unchanged from the beginning of KamLAND. One example of normalized charge taken from recent data is shown in Fig. 4.14, and time variation of those is shown in Fig. 4.15.

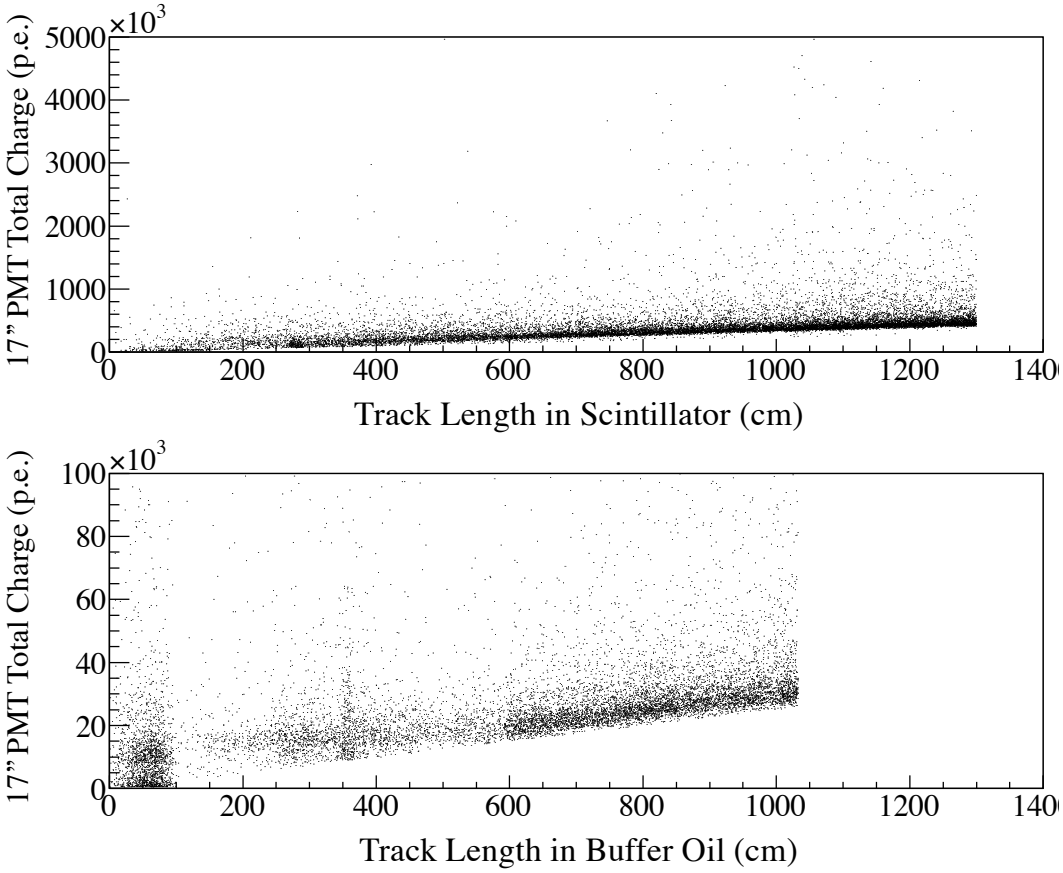

Figure 4.13: Relation between muon total charge (Q_{17}) and track length. (Top) in the liquid scintillator and (bottom) in the buffer oil.

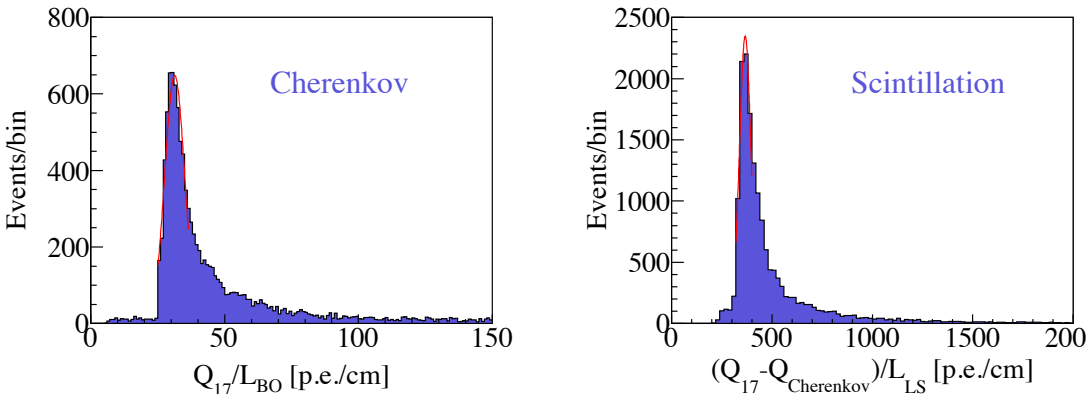

Figure 4.14: An example of normalized charge of (left) Cherenkov and (right) scintillation light emission estimated from clipping muons and through going muons, respectively.

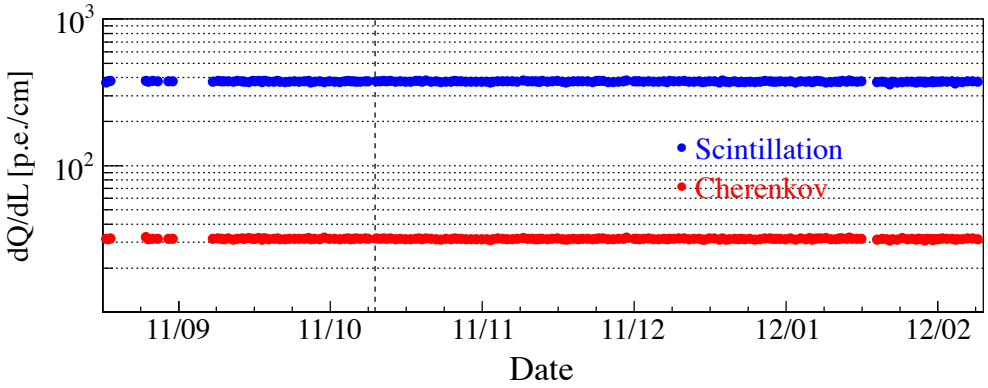

Figure 4.15: Time variation of normalized charge for Cherenkov and scintillation light emission. Both are stable during this period. Vertex line indicates the start day of the analysis, and horizontal axis is shown as in year/month.

4.6 Vertex reconstruction

4.6.1 Algorithm of vertex reconstruction

The vertex reconstruction is based on a "pulse shape". It is a PMT hit time distribution, and the maximum likelihood approach is applied to determine the vertex position after correcting for photon time-of-flight. Pulse shapes generally depend on the PMT type (17-inch or 20-inch), the distance from the source to the PMT, the intensity of the signal, the origin of the signal (gamma, beta, neutron, positron), and the distance traveled through the scintillator. Typical pulse shapes at various points are collected as a pattern from source calibration data, and used for producing likelihood functions.

For an event occurring at a position (x, y, z) and time t, the delay of the signal timing for i-th PMT τ_i is calculated by the following expression;

$$\tau_i \;=\; t_i - t - TOF_i \;(i:\ \text{index of PMTs}) \tag{4.6}$$

where t_i is the observed timing of the i-th PMT, and TOF_i (for Time Of Flight) is the distance from the event occurring position to the i-th PMT divided by the speed of light in the scintillator. The likelihood function that takes into account only the signal timing can be written as;

$$L \;=\; \prod_{i}^{Nhits} \varphi(\tau_i(x, y, z, t)) \tag{4.7}$$

or more convenient shape for computation;

$$\log(L) \;=\; \sum_{i}^{Nhits} \log(\varphi(\tau_i(x, y, z, t))) \tag{4.8}$$

where $\varphi(\tau_i)$ is a pulse shape evaluated at τ_i. The multiplication is made only over the hit PMTs which have signals. The maximum of the Eq. 4.8 is achieved at a

point where its 4-dimensional gradient turns into zero, i.e. partial derivatives with respect to x, y, z and t all vanish;

$$\frac{\partial(\log(L))}{\partial x_j} = 0 \ (x_j = (x, y, z, t)) \tag{4.9}$$

or,

$$\sum_i^{Nhits} \frac{d(\log(\varphi(\tau_i)))}{d\tau_i} \frac{\partial \tau_i}{\partial x_j} = \sum_i^{Nhits} \frac{1}{\varphi(\tau_i)} \frac{d\varphi(\tau_i)}{d\tau_i} \frac{\partial \tau_i}{\partial x_j} = 0. \tag{4.10}$$

The vertex fitter searches for the solution and gives the best vertex parameters x, y, z and t.

4.6.2 Vertex quality for KamLAND-Zen data

Determination of the center of inner balloon

The center of reconstructed vertices of the KamLAND balloon $(x, y, z = 0)$ is not exactly equal to that of the IB. Then additional vertex correction to tune the center is applied. The z-bias is estimated from radial distribution of events in the energy region $1.0 < E < 2.0$ MeV with each cosθ. In Fig. 4.16 (left), the coordinate of an

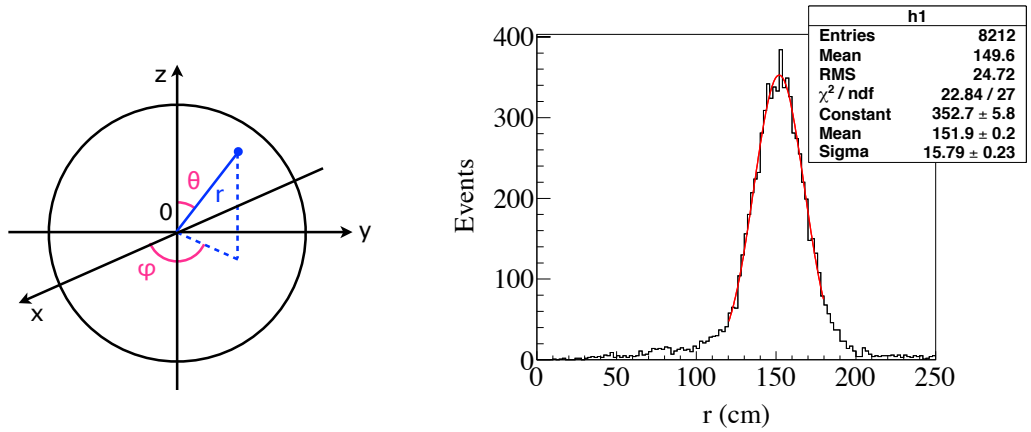

Figure 4.16: Coordinate of KamLAND/KamLAND-Zen (left) and a sample histogram of radial distribution in a certain cosθ (right).

event is described, and in the right figure, a sample histogram of radial distribution in a certain cosθ is shown. Note that the fitted value is not equal to the IB radius since ^{136}Xe $2\nu\beta\beta$ decay is only observed inside the IB. From fitting of cosθ distribution, offset for z-axis is estimated to be -10.28 cm from the center of KamLAND vertices as shown in Fig. 4.17 (left). Due to the drop shape of the IB, in large cosθ, which corresponds to the cone part, the value of radial distribution becomes larger. The cosθ distribution after correction is also shown in Fig. 4.17 (right). Bias of x and y are also estimated from radial distribution of events in -1.0 < z < 1.0 m with each ϕ, shown in Fig 4.18. In contrast to z dependence, almost all of the data is in $\pm$ 3 cm, therefore x-y correction is not applied in this data-set.

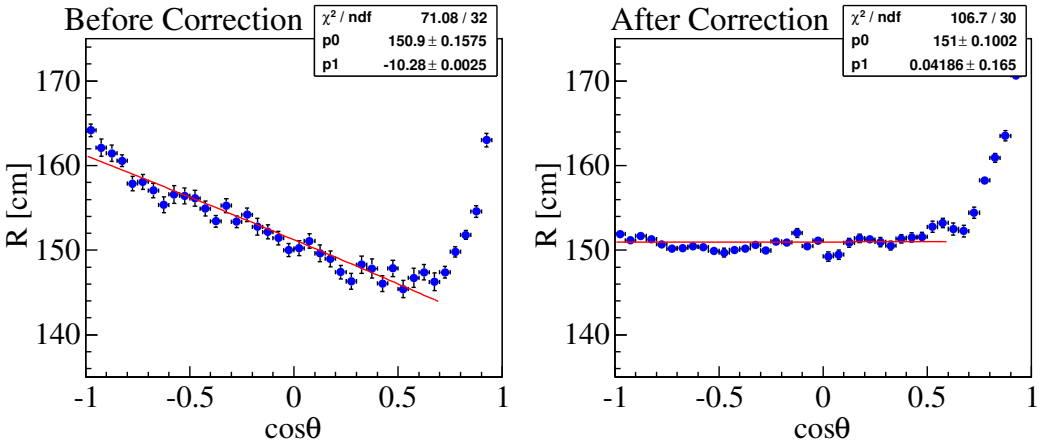

Figure 4.17: The cosθ distribution before (left) and after (right) z-axis correction. Actual shape of the IB is drop, so in large cosθ, fitting value becomes large.

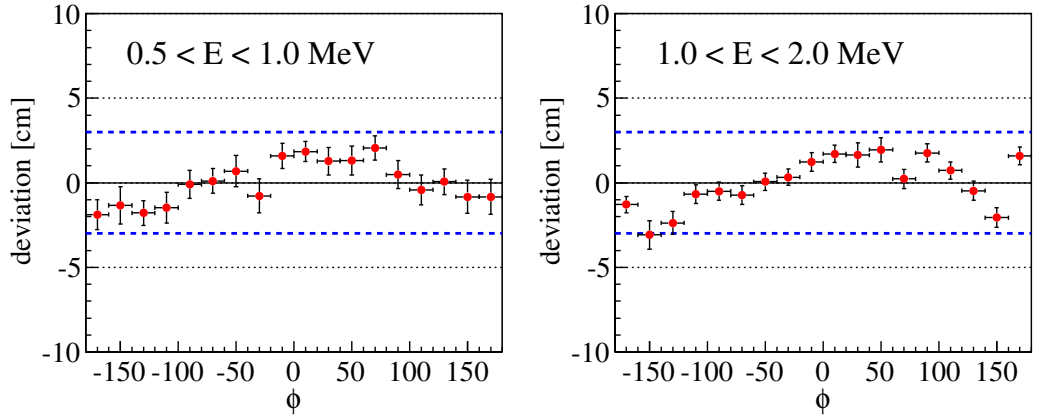

Figure 4.18: The deviation of ϕ distribution in -1.0 < z < 1.0 m for energy range of 0.5 <E < 1.0 (left) and 1.0 <E < 2.0 MeV (right) after z-axis correction. Average value of these plot is defined as zero, and values are within ±3 cm.

Vertex resolution

Vertex resolution is evaluated from radial distribution of events for $1.2 < E < 2.0$ MeV compared with simulation data to be 15 cm/$\sqrt{E(\mathrm{MeV})}$, later shown in Fig. 6.1 in Chapter 6.

Vertex bias

Vertex bias is estimated from photon simulation obtained from GEANT4 and it is negligibly small.

Fiducial volume

Fiducial volume selection and its uncertainty are written in Section 5.7 (Event selection) and Section 7.2 (Analysis).

4.7 Energy reconstruction

The reconstructed energy is called "visible energy". Reconstruction of energy requires hit, charge and time information of PMTs after some corrections applied. Basic correction is summarized in Section 4.7.1, and the algorithm is described in 4.7.2. After the reconstruction, additional energy correction for the data of KamLAND-Zen is applied (Section 4.7.3), and its quality of reconstructed energy is estimated in Section 4.7.4.

The visible energy and the deposited energy in the detector has non-linear relation due to quenching effect of the liquid scintillator and contribution of Cherenkov photons and so on. These non-linear sources generate uncertainties of energy scale, and it is also summarized in Section 4.7.4.

4.7.1 Basic correction

Charge correction

For the correct charge estimation, two corrections in addition to already described gain correction and bad channel selection, are applied to reduce time variation caused by detector status. One is setting of the software discriminator threshold to 0.3 p.e. for each PMT. The detection efficiency is estimated to be 0.964, determined from 1 p.e. distribution.

Another one is dark hit subtraction. Figure 4.19 shows a time spectrum of the light emission (17-inch PMTs) after the correction of time-of-flight. The dark hit

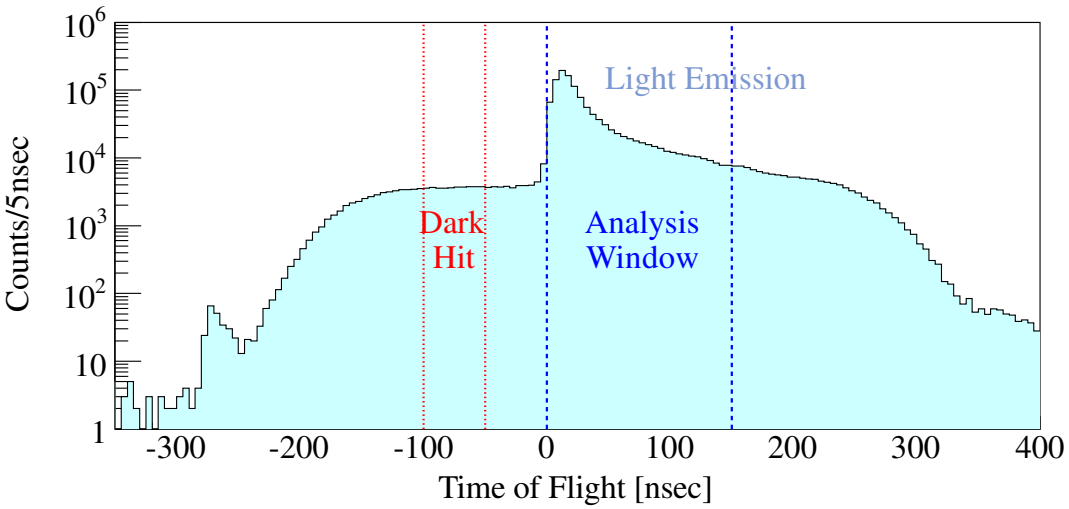

Figure 4.19: Time spectrum of PMT hits after the correction of time of flight. From -100 to -50 nsec is used for the evaluation of dark hit.

charge is estimated from 50 nsec off-time window in the spectrum. It is defined as the mean of the number of photo-electrons of charge distribution. The contribution of dark hit charge in analysis window (150 nsec) is about 10 p.e., and it corresponds to ∼5% for 1 MeV event (∼200 p.e.). In order to reduce the non-linear bias of the visible energy, dark charge is estimated run by run and subtracted from event by event in on-time window. Time variation of dark charge is shown in Fig. 4.20. It is almost stable except for the IB installation and the liquid scintillator filling continued until middle of September, 2011.

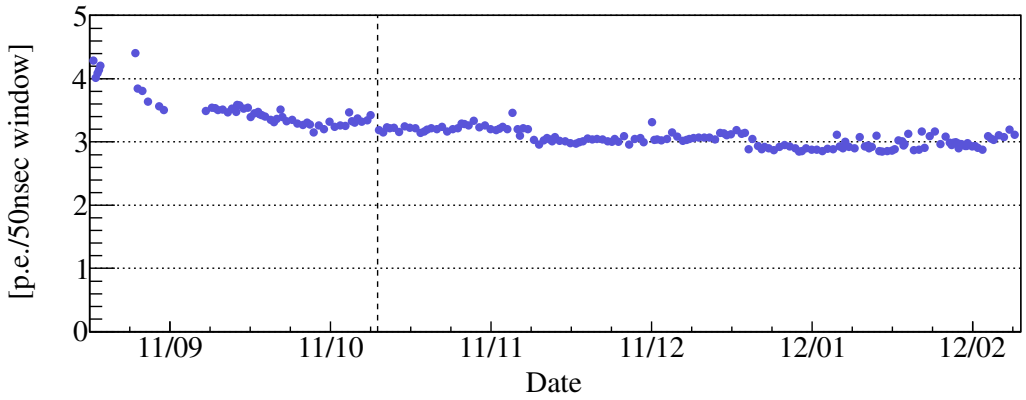

Figure 4.20: Time variation of dark charge in 50 nsec timing window. Vertex line indicate the start day of the analysis and horizontal axis is shown as year/month.

Photon yield efficiency

Photon yield also affects the energy estimation. Three parameters (shadowing effect, light attenuation length and single photo-electron efficiency) are considered here.

First one is shadowing effect. The shadow of the KamLAND balloon and its supporting ropes affect the photon yield for each PMT especially for the top and the bottom ones due to the shape of the detector. The light loss is calculated from its geometrical information and then calibrated with source calibration data of ^{60}Co placed at the center ($z = 0$). It improves the (z-dependence) symmetry of the photon yield of the PMTs.

Second one is light attenuation length. The effective attenuation length includes the effect of photon absorption and re-emission during photon flight and it is evaluated to 18.0 ± 1.6 m by uniformly distributed events, neutron captured gamma's.

Third one is a single photo-electron efficiency. The 0.3 p.e. discriminator threshold makes inefficiency of 1 p.e. detection, and it causes non-linear bias for the visible energy if multi photo-electrons are involved. Considering the mean number of photo-electrons in the j-th PMT, μ, it is calculated with an expected charge for each PMT that

$$\mu \equiv \sum_i Q_i^{\text{observed}} \times \frac{Q_j^{\text{expected-no-threshold}}}{\sum_i Q_i^{\text{expected-no-threshold}}} \tag{4.11}$$

Using 1 p.e. detection efficiency, ϵ, and the mean number of photo-electrons μ, the probabilities of the detection efficiency of 0 p.e., 1 p.e. and N p.e. ($N \geq 2$) are given by Poisson statistics as follow;

$$\begin{aligned} P(0) &= e^{-\mu} + (1-\epsilon)\mu e^{-\mu} \\ &= e^{-\mu}[1 + (1-\epsilon)\mu], \\ P(1) &= \epsilon\mu e^{-\mu}, \\ P(N) &= \frac{\mu^N}{N!} e^{-\mu} \ (N \geq 2). \end{aligned} \tag{4.12}$$

Then, the expected charge is calculated by summing up of charges.

$$Q_i^{\text{expected}} = q(1) \times P(1) + \sum_{N \geq 2} [q(N) \times P(N)]. \tag{4.13}$$

Here, normalization factor is omitted because it does not affect the energy non-linearity. If there is no threshold effect,

$$\sum_{N \geq 1} [q(N) \times P(N)] = \mu q_i \equiv Q_i^{\text{expected-no-threshold}}. \tag{4.14}$$

where q_1 is the mean charge of 1 p.e. distribution without threshold effect. Then, considering that only 1 p.e. events are affected by the threshold effect, Eq. 4.13 is converted to

$$\begin{aligned} Q_i^{\text{expected}} &= \mu q_1 - \mu e^{-\mu} q_1 + q(1)\epsilon\mu e^{-\mu} \\ &= Q_i^{\text{expected-no-threshold}} \left[1 - e^{-\mu} \left(1 - \frac{q(1)}{q_1} \epsilon \right) \right] \end{aligned} \tag{4.15}$$

Here, the $q(1)$ is determined from the relation that $q_1 = q(1)\epsilon + q_{\text{loss}}(1-\epsilon)$, where q_{loss} is the mean loss charge under threshold. Thus,

$$\begin{aligned} Q_i^{\text{expected}} &= Q_i^{\text{expected-no-threshold}} (1 - e^{-\mu}\delta), \\ \delta &\equiv \frac{q_{\text{loss}}}{q_1}(1-\epsilon). \end{aligned} \tag{4.16}$$

The parameter δ is estimated from calibration data to be 0.03.

4.7.2 Algorithm of energy reconstruction

The visible energy is reconstructed by A2 energy fitter with hit, charge and time information of PMTs. In general, the hit information is used for the reconstruction of low energy event since it is not affected by the charge resolution and one photo-electron threshold, while for the high energy event reconstruction, charge information has better performance due to high occupancy. Although implementation of combined fitter is even harder, the fitter newly developed for KamLAND provides a natural and seamless transition from a purely hit-based estimator at lower energies to a mostly charge-based one at higher energies.

The energy estimator determines the energy through maximum likelihood function method. The likelihood function consists of the probability density functions of hit, charge and hit time for each PMT, given as follows;

$$L = \prod_{i=1}^{\text{no hit}} \kappa_{i,0}(\overrightarrow{R}_{\text{PMT}_i}, \overrightarrow{R}_{\text{source}}, E_{\text{vis}}) \prod_{i=1}^{hit} \left[\sum_{j=1}^{\infty} \kappa_{i,j}(\overrightarrow{R}_{\text{PMT}_i}, \overrightarrow{R}_{\text{source}}, E_{\text{vis}}) f_{i,j}(q_i) \right] \eta_i(t_i|\mu_i)$$
$$(i,\ j:\ \text{the unique number of each PMT, and the number of hit-generated photon}) \tag{4.17}$$

where $\kappa_{i,j}$ and $f_{i,j}(q_i)$ is probability and charge probability density function of j-photons hit at i-th PMT, respectively. A function $\eta_i(t_i|\mu_i)$ is hit time probability density function for i-th PMT, given by the time t_i and the expected number of incident photons $\mu_i = \mu(\overrightarrow{R}_{\text{PMT}_i}, \overrightarrow{R}_{\text{source}}, E_{\text{vis}})$. These functions and parameters are expressed with basic and corrected parameters described in Section 4.7.1. For example, $\kappa_{i,j}$ is provided by Poisson distribution as a function of μ_i and the function includes the detection efficiency of 1 p.e. threshold signal above 0.3 p.e., and μ_i contains effective solid angle including attenuation and shadowing effect. The charge probability density function $f_{i,j}(q_i)$ is modeled by Gaussian distribution including sigma of 1 p.e. distribution, which is evaluated to be 0.39. The hit time probability density function $\eta_i(t_i|\mu_i)$ is a function of actual pulse shape function divided by μ_i.

From a definition of each function with observable and expected parameters, the likelihood function can be written with four terms (no-hit, hit, charge and time), and the best reconstruction energy is derived from the maximization of log-likelihood function,

$$\frac{\partial(\log(L))}{\partial E} = 0. \tag{4.18}$$

For the low energy region, no-hit, hit and time terms work effectively. On the other hand, charge term works effectually for high energy region. For computation, Eq. 4.18 is solved with modified Newton-Raphson method;

$$\Delta E_{\text{vis}} = -\frac{\partial(\log(L))/\partial E}{\partial^2(\log(L))/\partial E^2}. \tag{4.19}$$

The visible energy (E_{vis}) is reconstructed by summing up of Eq. 4.19 after several iterations. More detail description for each function, first and second derivatives are found in Ref. [86].

Reconstructed energy noted above is actually evaluated for 17-inch PMTs and 20-inch PMTs, respectively and then combined, since those PMTs have different characteristics such as sensitive area, time resolution and charge resolution. In particular, clear single photo-electron peak observed in 17-inch PMTs is not found in 20-inch PMTs. Hence, the mean value of visible energy from 20-inch PMTs ($E_{\text{20-inch}}$) is calibrated with those of 17-inch PMTs ($E_{\text{17-inch}}$), and visible energy is provided with combination of both energies to obtain better energy resolution that,

$$E_{\text{visible}} = (1-\alpha) \cdot E_{\text{17-inch}} + \alpha \cdot E_{\text{20-inch}}, \tag{4.20}$$

where α is the weighting and estimated to 0.3 from the past various calibration data.

4.7.3 Additional correction for KamLAND-Zen data

Described energy estimation is established for the liquid scintillator used in KamLAND. The Xe-LS for KamLAND-Zen consists of a slightly different components and has different parameters. So its energy is corrected with photon simulation data. The parameters of Monte Carlo simulation are tuned with actual ^{214}Po distribution tagged by delayed coincidence method (detail described in Section 5.5). With MC data generated in various radius and θ, energy is corrected and evaluated. Figure 4.21 shows cosθ distribution of ^{214}Po (α decay, $Q = 7.83$MeV[4]) after the correction.

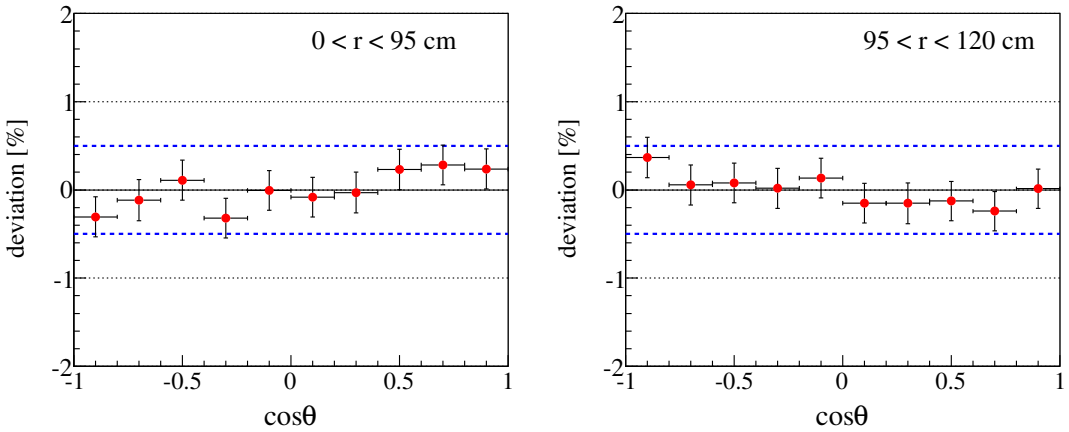

Figure 4.21: An example of cosθ distribution of ^{214}Po energy deviation. Horizontal blue dot lines show the region of deviation within $\pm 0.5\%$.

4.7.4 Energy response

The energy response is calibrated with three kind of sources that (1) ^{208}Tl 2.614 MeV γ's from artificial calibration source of ThO_2-W, (2) 2.225 MeV γ's from spallation neutrons capture on protons, and (3) ^{214}Bi ($\beta + \gamma$) from ^{222}Rn ($\tau = 5.5$ days) introduced during the filling of the liquid scintillator. Those event distributions in the detector are shown in Fig. 4.22. Black line shows the boundary of the IB. Its inside is filled with the Xe-LS, while outside is KamLAND-LS. The ^{208}Tl events are obtained from the artificial source, then high intensity events have a gathering at the calibration point. On the other hand, 2.225 MeV γ's from spallation neutrons capture on protons are uniformly distributed in both KamLAND LS and the Xe LS due to muon-induced events. ^{214}Bi ($\beta + \gamma$) is uniformly distributed only in the IB due to introduction of ^{222}Rn by the initial filling of the liquid scintillator.

[4] Alpha energy quenches in the liquid scintillator.

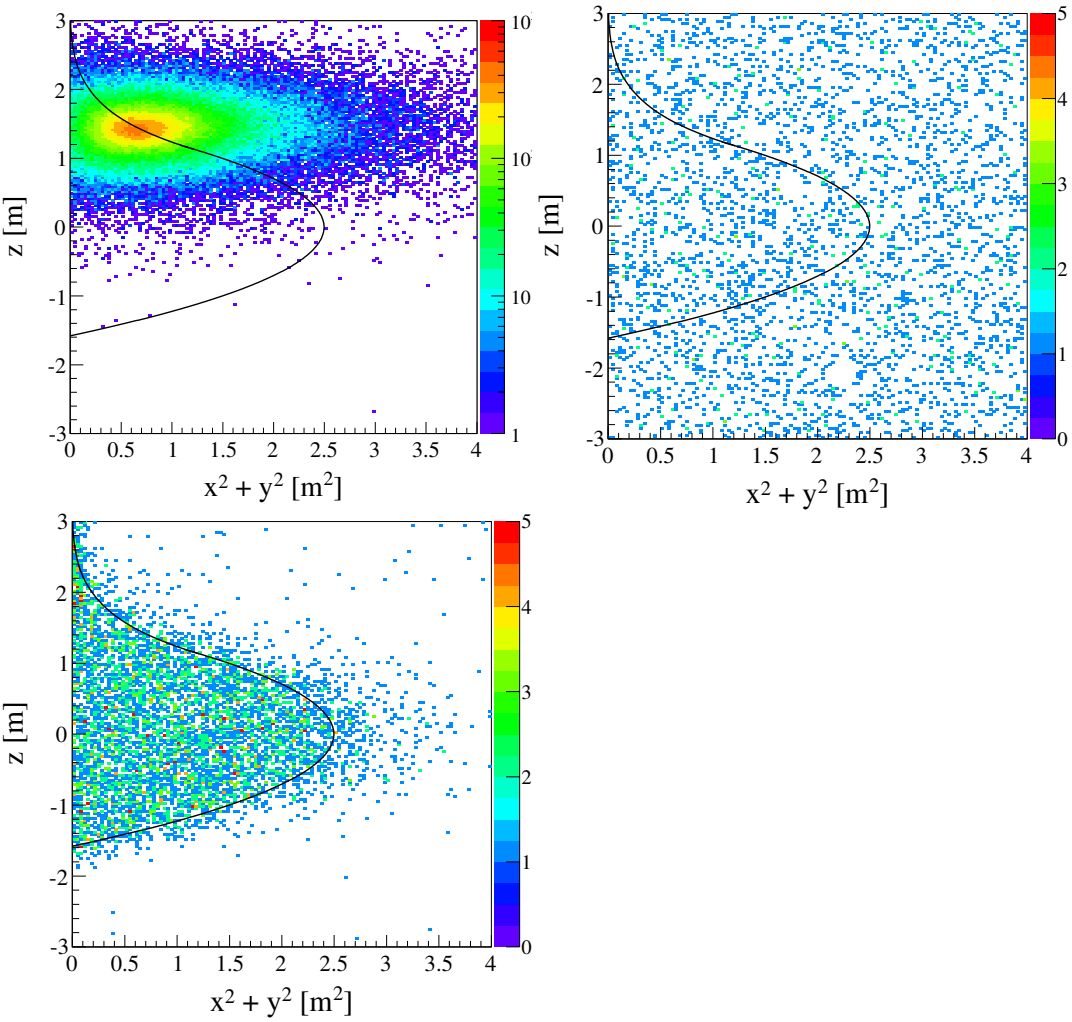

Figure 4.22: Event distribution of ^{208}Tl (top left), neutron capture 2.225 MeVγ's (top right) and ^{214}Bi (bottom left). Black line shows shape of the IB. Right axis shows the number of events. ^{208}Tl events are concentrate on the calibration point and its intensity is much higher than rest two reactions. Neutron capture events are found in both KamLAND-LS and the Xe-LS since muon cause these events, while ^{214}Bi is observed only in the Xe-LS due to ^{222}Rn introduced by the filing.

ThO_2-W calibration

Energy distribution of γ's from ThO_2-W source is shown in Fig. 4.23. The source is contained in a 5-mm-thick lead capsule and deployed close to the outer surface of the IB (Section 3.8.2). The most intense peak is primary γ's of ^{208}Tl (2.614 MeV), and second one near $\sim$3.1 MeV is from multiple-γ cascades of ^{208}Tl. The level diagram of ^{208}Tl is found in Appendix C.1.1. Comparison of the mean and width of primary peak with Monte Carlo simulation provides the energy resolution to be $\sigma = (6.6 \pm 0.3)\%/\sqrt{E(\mathrm{MeV})}$. Figure 4.24 shows the light yield radial dependence of ^{208}Tl peak

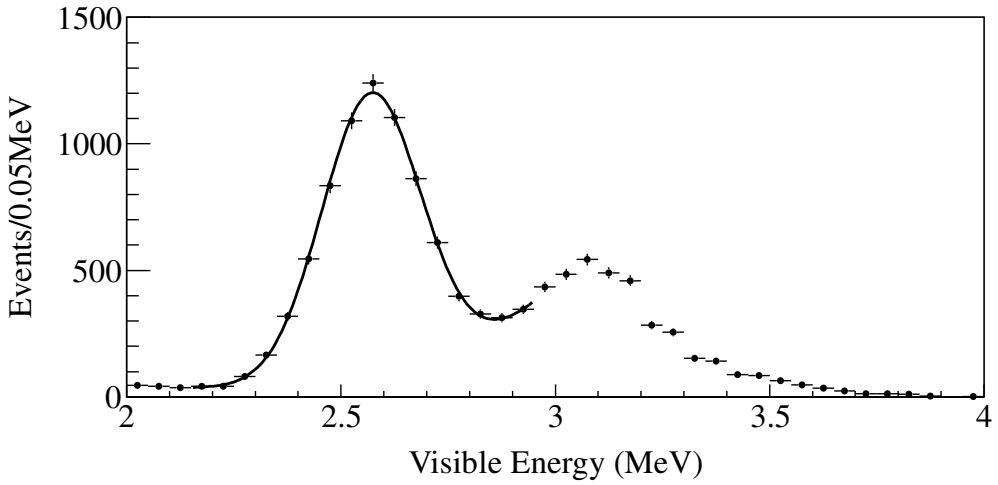

Figure 4.23: Visible energy distribution of γ's from ThO_2-W (^{208}Tl) source. The line indicate the best-fit curve. It has a χ^2/d.o.f. = 5.0/8.

energy. Compared with those of KamLAND (radius is more than 154 cm), Xe-LS has 3% lower light yield and is within the expected value.

Spallation neutron capture on protons

The neutrons produced by muons are captured by mainly protons within several hundred μsec and emit 2.225 MeV gamma rays. These events are simply selected with NsumMax (the number of hits when trigger was issued) and time difference from muons. Figure 4.25 shows the NsumMax distribution of neutron capture events with the time difference cut, $150 < \Delta T_{\mathrm{muon}} < 1,000$ μsec and good event selection cut (the number of waveforms (PMT hits) should be larger than the NsumMax) to reduce the effect of missing waveforms. Clear peak found in 350 < NsumMax < 500 is caused by neutron capture on protons. Fig. 4.26 shows the visible energy distribution with selected NsumMax. Visible energy is estimated to be 2.22 MeV. The position dependence and time variation of the visible energy is within $\pm$1.0% during data-set, shown in Figure 4.27 left and right, respectively.

Table 4.1 summarizes the estimated visible energy for above two γ emitting reactions as well as its real energy.

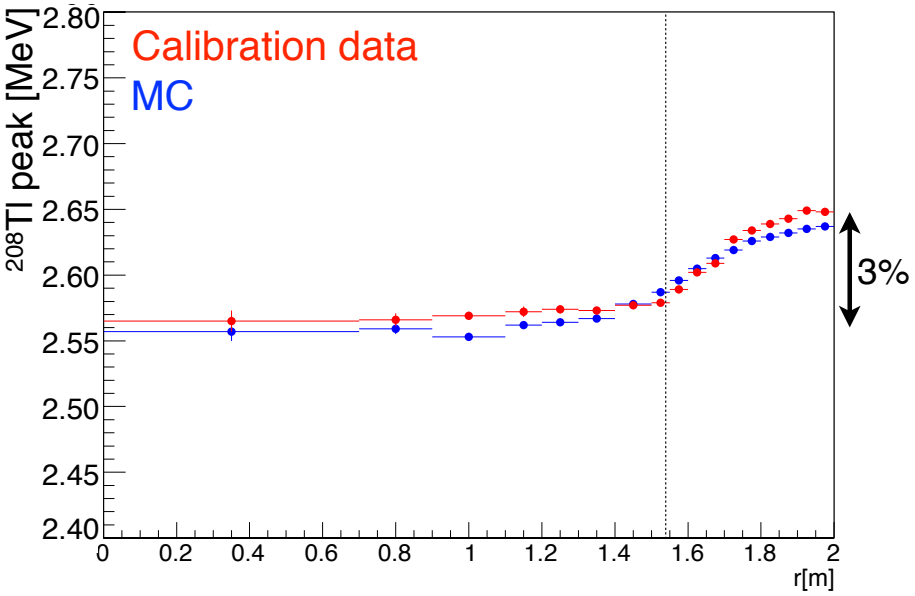

Figure 4.24: Radial distribution of the energy peak of ^{208}Tl. The red points are obtained from data and blue points from Monte Carlo study. Vertical line at 154-cm-radius is edge of the IB.

Table 4.1: Reconstructed visible energies for γ sources.

Source	Gamma energy (MeV)	Visible energy (MeV)
^{208}Tl	2.614	2.571
$np \to d\gamma$	2.225	2.219

Non-linear response of energy

As shown in Table 4.1, estimated visible energy is not exactly equal to the (real) deposited energy in the detector since it has non-linear relation due to quenching effects of the liquid scintillator, contribution of Cherenkov photons and so on. These non-linear sources generate uncertainties of energy scale.

The quenching effect reduce the photon yield due to the different efficiency of light emission depending on the particle's ionization density. For example, the quenching factor of a few MeV alpha particles is 1/10, while that of electron is only a few percent. The contribution of this effect is estimated from Birks formula as a function of energy deposition dE/dx as follows,

$$\Delta E_{\text{vis}} = \frac{A}{1 + k_B(dE/dx)} \Delta E \tag{4.21}$$

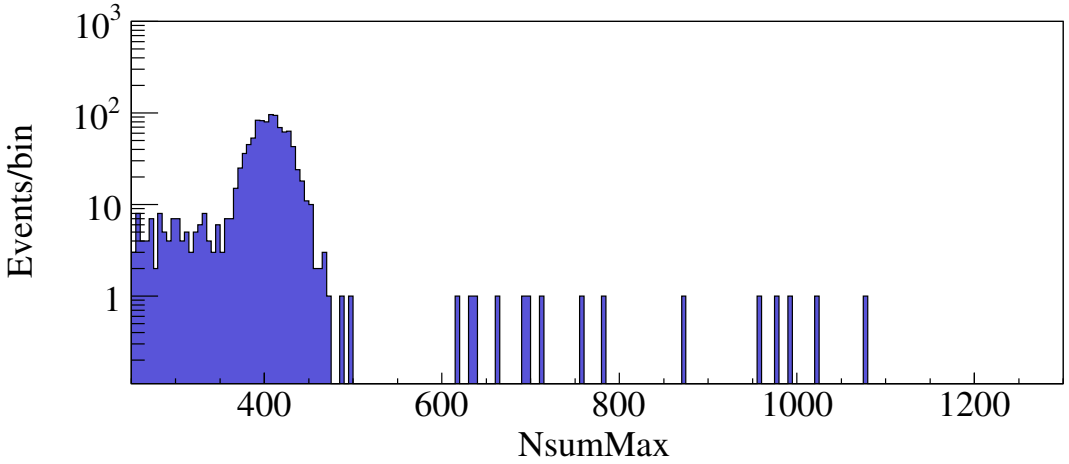

Figure 4.25: NsumMax distribution of spallation neutrons captures.

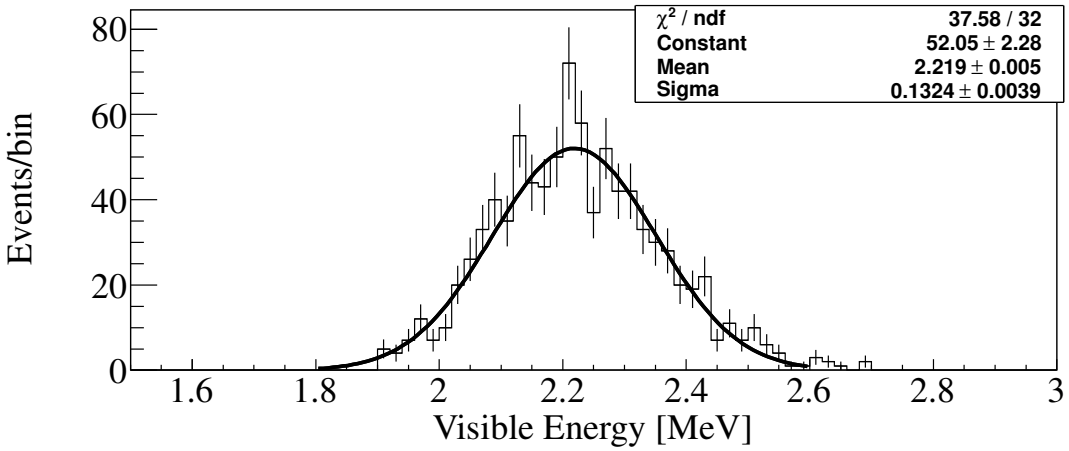

Figure 4.26: Visible energy distribution of 2.225 MeV γ's from spallation neutrons capture on protons selected with NsumMax.

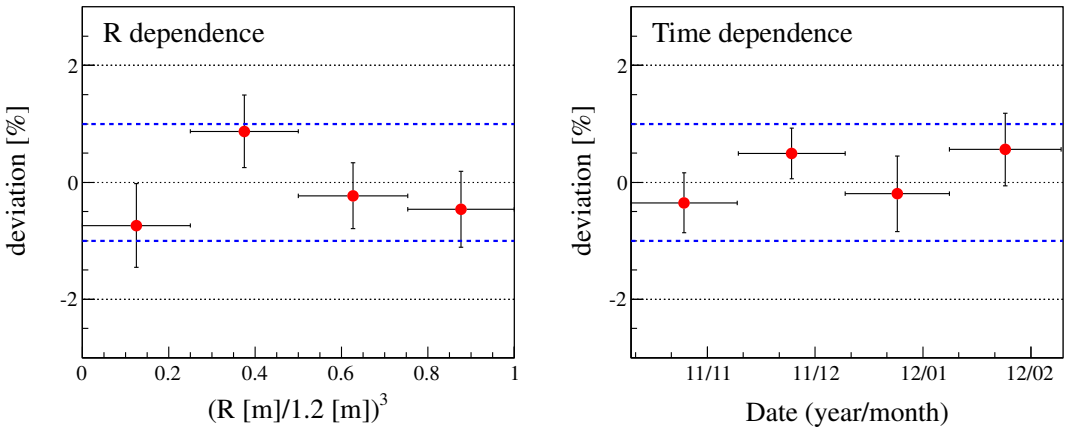

Figure 4.27: The position dependence (left) and time variation (right) of the visible energy of neutron capture γ's. Blue dot line shows $\pm 1.0\%$ deviation.

where k_B is Birks constant determined by characteristics of the liquid scintillator and A is a factor to convert photon yield to estimated energy.

Cherenkov photons are emitted only by electrons and positrons and the number of photons of those depend on their energy. The direct contribution of Cherenkov light is ignorable since most of photons are absorbed in the liquid scintillator. However, re-emission light of those make significant contribution to the total charge.

The total photon yield (i.e. visible energy) is expressed as sum of scintillation and Cherenkov photon contributions as

$$\begin{aligned} \Delta E_{\mathrm{vis}} &= \left(A_{\mathrm{sci}} \cdot \frac{dN_{\mathrm{sci}}}{dE} + A_{\mathrm{Ch}} \cdot \frac{dN_{\mathrm{Ch}}}{dE} \right) \Delta E \\ &= A \left\{ \frac{1}{1+R} \cdot \frac{1}{1+k_B(dE/dx)} + \frac{R}{1+R} \cdot \frac{dN_{\mathrm{Ch}}}{dE} \right\} \Delta E \end{aligned} \tag{4.22}$$

where N_{sci} and N_{Ch} are the number of scintillation and Cherenkov photons, respectively, and A_{sci} and A_{Ch} are normalization parameters to be determined.

For this analysis, the contribution of the quenching effect and Cherenkov light is tuned with combined data that the peak position of ^{208}Tl and spectral shape of ^{214}Bi events. ^{214}Bi events are tagged with time and space correlation of ^{214}Po with delayed coincidence method (Section 5.5). Visible energy distribution of ^{214}Bi is shown in Fig. 4.28 with best fit curves (simulated spectrum). Its level diagrams are found in Appendix C.1.2.

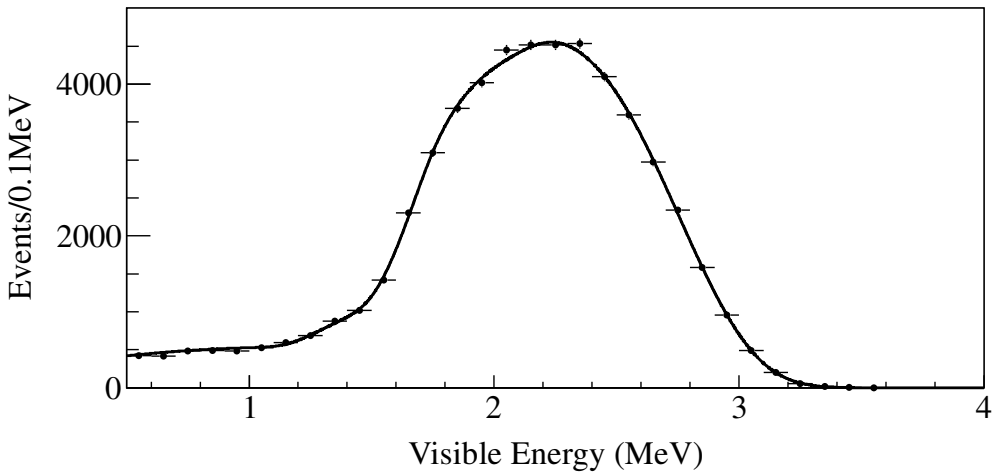

Figure 4.28: Visible energy distribution of ^{214}Bi ($\beta+\gamma$) supplied by ^{222}Rn from the initial filling. The line indicate the best-fit curve. It has a χ^2/d.o.f. = 27.0/29.

The parameters of a detector non-linearity, Birks constant (k_B) and ratio of scintillation photons to Cherenkov photons are constrained from ^{214}Bi and ^{208}Tl. The correlation of parameters is shown in Fig. 4.29. It has strong anti-correlation. Figure 4.30 shows the ratio of visible energy to real energy as a function of real energy for electron and gamma's.

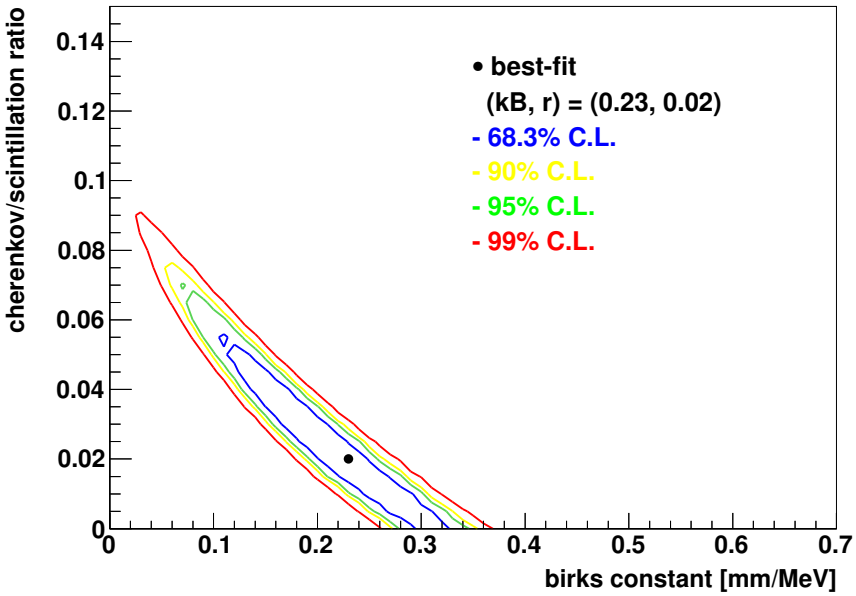

Figure 4.29: Correlation of Birks constant and ratio of Cherenkov and scintillation photons. Best fit value is shown with black point. The blue, yellow, green and red contour shows 68.3% (1σ), 90%, 95%, 99% C.L., respectively. "r" means the ratio of scintillation photons to Cherenkov photons.

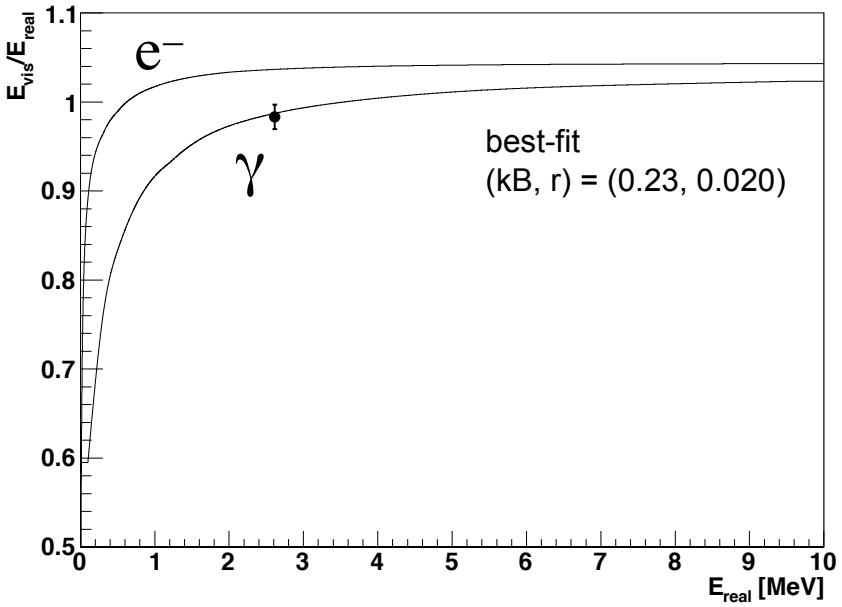

Figure 4.30: Energy non-linearity correction for electron and gamma energy scale. The data point is obtained from source calibration (^{208}Tl 2.614 MeV γ's).

Chapter 5

Event selection

Not all reconstructed events are physical events. Some of them are bad events (or bad periods), muon events, or post-muon events within a time window of 2 msec. Hence these non-physical events should be rejected (Section 5.2 and 5.3). Physical events consist of signals (the summed energy of two electrons in double-beta decay) and various backgrounds (detail described in the next chapter). In KamLAND-Zen, if a signal and a background event have the same energy and vertex, identification of those is difficult. However, some of backgrounds can be identified by searching for time-space correlation with two events. For example, ^{214}Bi, which is one of the backgrounds for $0\nu\beta\beta$ decay search, can be vetoed by sequential decay of ^{214}Po with those time-space correlations. It is called "delayed coincidence method". Its rejection efficiency is more than 99%. In addition, reactor anti-neutrinos, which are not serious background due to quite small contribution, are also vetoed with the same method. These "background rejections" in advance are written in Section 5.4 and 5.5. Rest of events is finally tested with "badness" to search for possibly remaining noise (unphysical) events. It is presented in Section 5.6. Fiducial volume selection is also described in Section 5.7.

5.1 Dataset summary

The data used for this double beta decay analysis were collected between October 12, 2011 and February 9, 2012 or run011000 - 011212. The calculated livetime is 112.3 days (detail described in Chapter 7), which correspond to ∼94% of the elapsed time, 120 days.

5.2 Run selection

In the 120 days of data collected period, totally 213 runs were taken. Almost all of runs are "physics run" aiming to be used for data analysis, while some of them are calibration runs, test runs, and so on. In physics runs, some runs are not appropriate to the analysis due to strange behavior, mis-configuration of data taking, or external troubles such as power supply failure. To keep the data quality, run condition is monitored with the number of bad channels, run time, trigger rate, hit rate, muon

rate and event rate, and "run grade" is defined run by run such as "good run", "bad run" or "half bad run". A run which has many bad channels, short run time (< 6 minutes) and/or strange rate is classified as a bad run and excluded. Some runs have bad data quality for a certain period due to (for example) failure of HV supply or readout of FEE boards. These runs are called half bad runs. Only good runs and good periods in half bad runs are used for an analysis, and the total number of analyzed run is 147.

5.3 Non-physical event rejection

Cut selections to reject non-physical events are described in this section. Non-physical events are characterized from their abnormal PMT hit time distribution as shown in Fig. 5.1. The hit time distribution of normal event is concentrated on

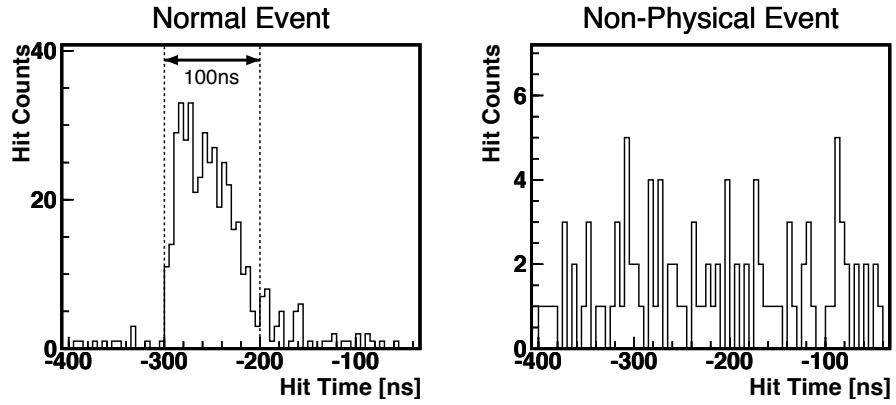

Figure 5.1: PMT hit time distribution of a typical normal event (left) and a non-physical event (right) taken from Ref. [82].

within $\sim 100-150$ nsec. In contrast, a non-physical event distributes widely without any clear peaks. Mainly muon generates such non-physical events since muon causes many continuous events in a short period, and it makes electronics too busy to deal with such signals. Various kinds of non-physical events in addition to physical events are shown in Figure 5.2 as a function of the total charge of 17-inch PMTs. Each events are explained in the following sections.

5.3.1 Flasher event cut

Sometimes, a PMT emits a light due to electric discharge of dynodes or strong spark noises. Neighboring PMTs detect this light and make a hit. Such events are called "flasher events". Figure 5.3 (left) shows the event display of a typical flasher event. Although these signals have a similar distribution of hit timing as normal events and mimic high energy events up to ~20 MeV, charge distribution helps to distinguish those. The selection criteria of flasher events are,

- Not muon events or noise events.

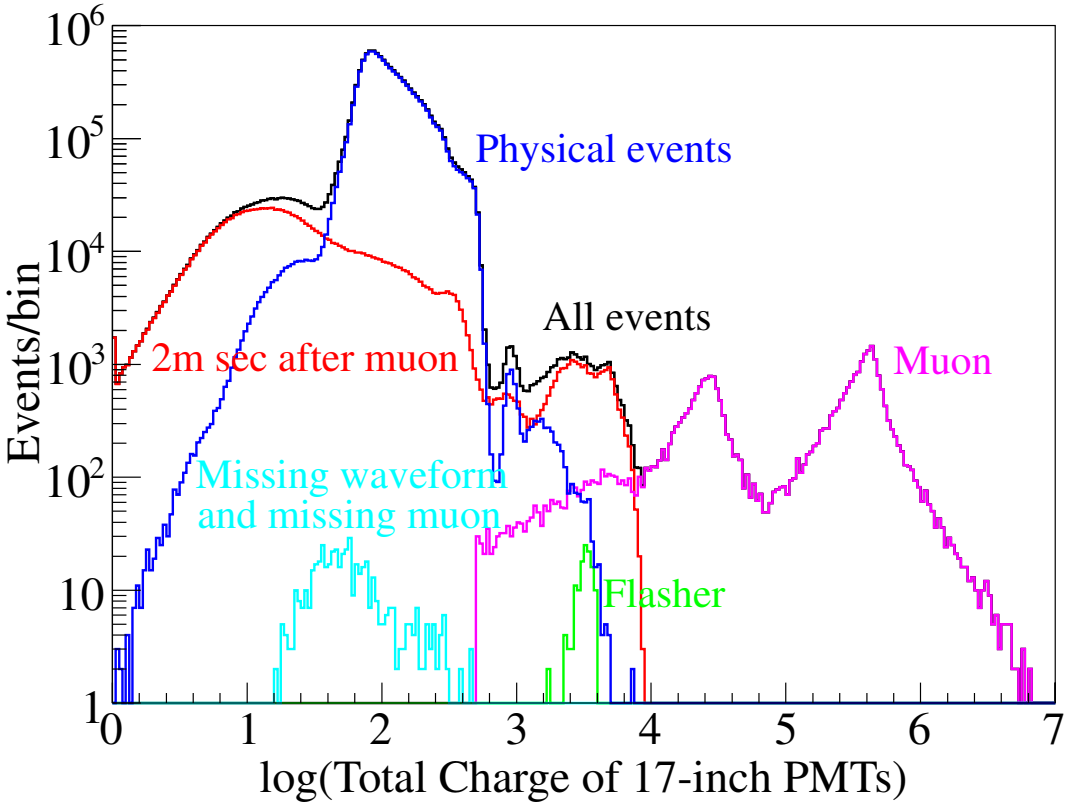

Figure 5.2: Distribution of total charge of 17 inch PMTs for various type of events.

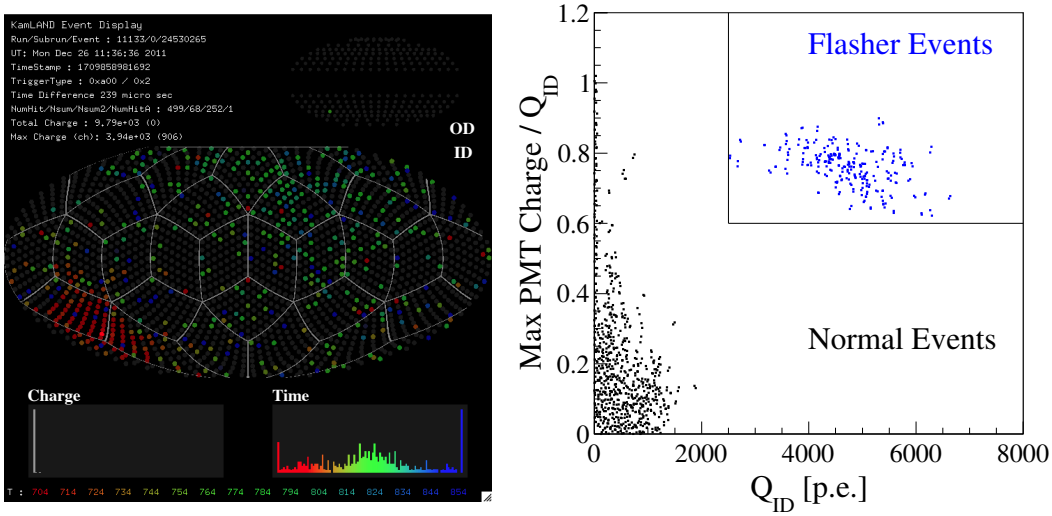

Figure 5.3: Event display of a typical flasher event (left) and selection criteria (right). Data from typical one day run with whole volume of KamLAND. In right figure, lined region is selected area and flasher events show in blue while normal events in black.

- Total charge of the inner detector (Q_{ID}) > 2,500 p.e.
- Ratio of maximum single PMT charge to Q_{ID} $\geq$ 0.6.
- Mean charge of the neighbor PMTs surrounding the flasher PMT $\geq$ 20 p.e.

Here, noise events are defined with the number of maximum PMT hits within 100 nsec (N_{100}) and the number of all PMT hits in an event ($Nhit_{ID}$) as $N_{100} \leq (Nhit_{ID} + 50)/2$. Selected flasher events and normal events are shown in Fig.5.3 (right).

5.3.2 Muon event veto

Interaction of cosmic ray muons with nuclei in the liquid scintillator generates neutrons. Most of them are captured on protons and make 2.2 MeV signals. Those noisy multiple signals occur within a short period (a few hundred μsec) and make non-physical events. Thus muon itself and post-muon events within a time window of 2 msec are eliminated. Muon selection criteria are summarized in Section 4.5.

5.3.3 Noise event cut

The waveform information of PMTs would be sometimes lost for a short time, since muon and post-muon events cause high event rate and make ATWD channels quite busy. These events are called "missing waveform events" and removed if they cannot satisfy the following relation;

$$Nhit_{17} > NsumMax \tag{5.1}$$

where $Nhit_{17}$ is the number of 17-inch PMTs whose waveforms are recorded, and NsumMax is the maximum number of 17-inch PMT hits within a 125 nsec after a trigger issue. Selection criteria are also shown in Fig. 5.4. If NsumMax of those

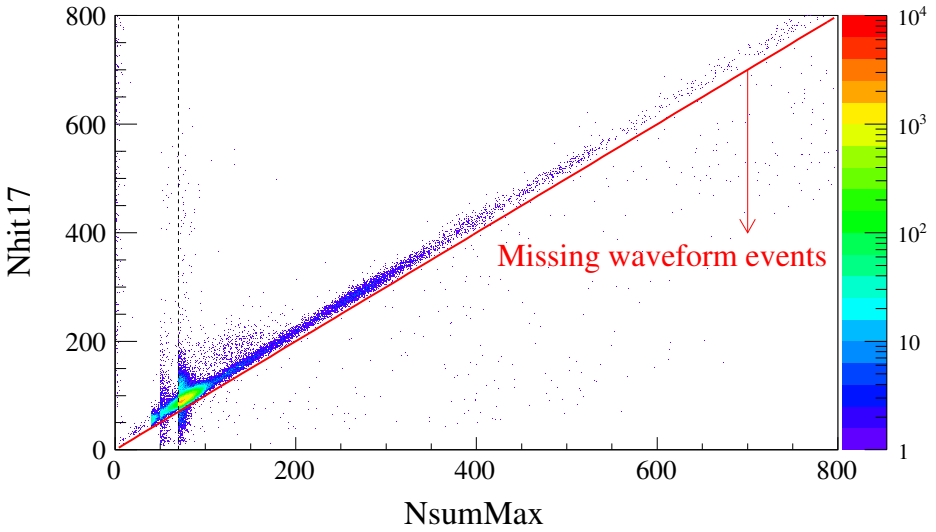

Figure 5.4: Selection criteria of missing waveform events. Vertical line shows threshold of NsumMax.

events is more than 200, 2 msec veto is applied, and if it is more than 1200, 2 sec veto is applied.

There is another noise event. The cluster of noise events sometimes appears in spite of no muon information before the cluster due to unknown dead time. These events are called "missing muon". Noise events are selected by combination of N_{100} (the number of maximum PMT hits within 100 nsec) and $Nhit_{ID}$ (the number of all PMT hits), which satisfied the following relations;

$$\begin{aligned} &Nhit_{ID} > 100, \\ &N_{100} < (Nhit_{ID} - 20)/2. \end{aligned} \tag{5.2}$$

If selected noise events make cluster and are preceded by no muons within 1 msec, those events are rejected.

5.4 Anti-neutrino veto

The electron antineutrinos mainly from nuclear power reactors[1] are tagged with delayed coincidence method. As shown in Fig. 5.5, $\overline{\nu}_e$ reacts with proton in the liquid

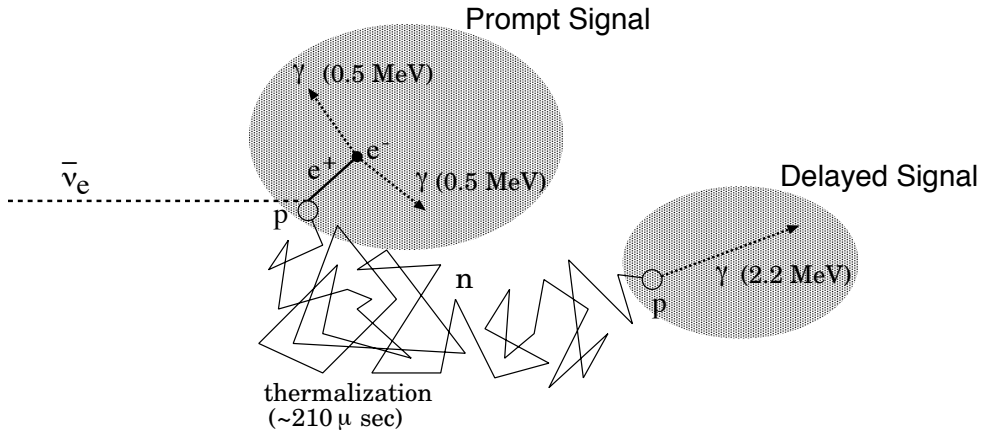

Figure 5.5: Schematic view of $\overline{\nu}_e$ tagging taken from Ref. [82].

scintillator via inverse β-decay $\overline{\nu}_e + p \rightarrow e^+ + n$, and generates time-space correlated events. Positron releases its kinetic energy and annihilates with a nearby electron, producing two 511 keV γ rays as prompt signal, and a thermalized neutron captured by a proton within $\sim$210 μsec emits 2.2 MeV γ ray as a delayed signal.

Veto selection criteria are determined by delayed energy (1.5 MeV $\leq E_d$), distance of prompt and delayed signals ($\Delta R < 200$ cm), and timing correlation of prompt and delayed signals ($\Delta T <$ 1,000 μse). As a result, only one coincidence is tagged in the fiducial volume.

[1]There are 56 Japanese reactor located in flux-averaged distance of $\sim$180 km from KamLAND. Reactor fuels are mainly composed of ^{235}U, ^{238}U, ^{239}Pu and ^{241}Pu. Their energies are released by nuclear fission and $\overline{\nu}_e$ accompanied.

5.5 Sequential Bi-Po decays veto

^{214}Bi and ^{212}Bi are one of the backgrounds in $0\nu\beta\beta$ region. They can be vetoed since a sequential Bi-Po decay also has time-space correlation. The decay of ^{214}Bi - ^{214}Po in the ^{238}U chain and ^{212}Bi - ^{212}Po in the ^{232}Th chain are as follow;

$$^{214}\mathrm{Bi} \xrightarrow[\mathrm{Q}_\beta=3.272\mathrm{MeV},\ 99.989\%]{\mathrm{T}_{1/2}=19.9\ \mathrm{min}} {}^{214}\mathrm{Po} \xrightarrow[\mathrm{Q}_\alpha=7.687\mathrm{MeV}]{\mathrm{T}_{1/2}=164\mu\mathrm{sec}} {}^{210}\mathrm{Pb},$$

$$^{212}\mathrm{Bi} \xrightarrow[\mathrm{Q}_\beta=2.254\mathrm{MeV},\ 64.06\%]{\mathrm{T}_{1/2}=60.55\ \mathrm{min}} {}^{212}\mathrm{Po} \xrightarrow[\mathrm{Q}_\alpha=8.954\mathrm{MeV}]{\mathrm{T}_{1/2}=299\mathrm{nsec}} {}^{208}\mathrm{Pb}.$$

These events are vetoed with 2 ways: (1) a delayed coincidence rejection and (2) pile-up rejection by waveform analysis.

Almost all of the sequential Bi-Po decays are tagged with delayed coincidence method. Prompt signal is a bismuth ($\beta+\gamma$) decay and delayed signal is a polonium (α) decay. Alpha decay energy is quenched in the liquid scintillator. So those peaks of visible energy become less than 1 MeV. Like anti-neutrino, veto selection criteria are determined by delayed energy ($0.35 \leq \mathrm{E_d} < 1.5$ MeV), distance between prompt and delayed signals ($\Delta\mathrm{R} < 300$ cm), and timing correlation of prompt and delayed signals ($\Delta\mathrm{T} < 3{,}000$ μsec). Figure 5.6 shows vetoed ^{214}Bi-^{214}Po coincidence events (only used for $\Delta\mathrm{T} > 5\mu$sec). Time correlation plot is fitted with an exponential curve, and it provides a half-life of the decay. It is consistent with a half-life of ^{214}Po (164.3 μsec) within error.

Pile-up Bi-Po events are rejected by waveforms of hit PMTs in order to veto events efficiently. These events are selected from the shape of histogram (whether double pulses exists), time difference of the pulses ($\Delta\mathrm{T} > 20$ nsec), the delayed energy ($0.35 \leq \mathrm{E_d} < 1.2$ MeV), and its badness (badness > 1.5, detail described in next section). Badness of a pileup event tends to be higher than a usual event. An example of selected event as a function of time is shown in Fig. 5.7. Thanks to this selection, more Bi-Po events are selected effectively.

From two kinds of Bi-Po rejection method, ^{214}Bi rejection efficiency is estimated to be $(99.97 \pm 0.01)\%$. It comes from ^{214}Po tagging inefficiency estimated by ΔT, and ^{214}Bi tagging inefficiency estimated by the ^{222}Rn decay curve. ^{212}Bi rejection efficiency is estimated to be $(89 \pm 2)\%$. These cuts introduce less than 0.1% of detection inefficiency.

5.6 Badness cut

After passing through the all described event selections, remained events still have a possibility of noise events. Then they should finally pass a vertex-time-charge (VTQ) test. The reconstructed "point-like" events have a vertex and energy based on the time and charge information obtained from PMTs. By comparison of observed charge and hit time distribution with the expected ones based on the reconstructed vertex, remained unphysical events such as accidentally reconstructed ones are filtered out. The parameter of event quality evaluation is called "badness", consist of the following 9 parameters;

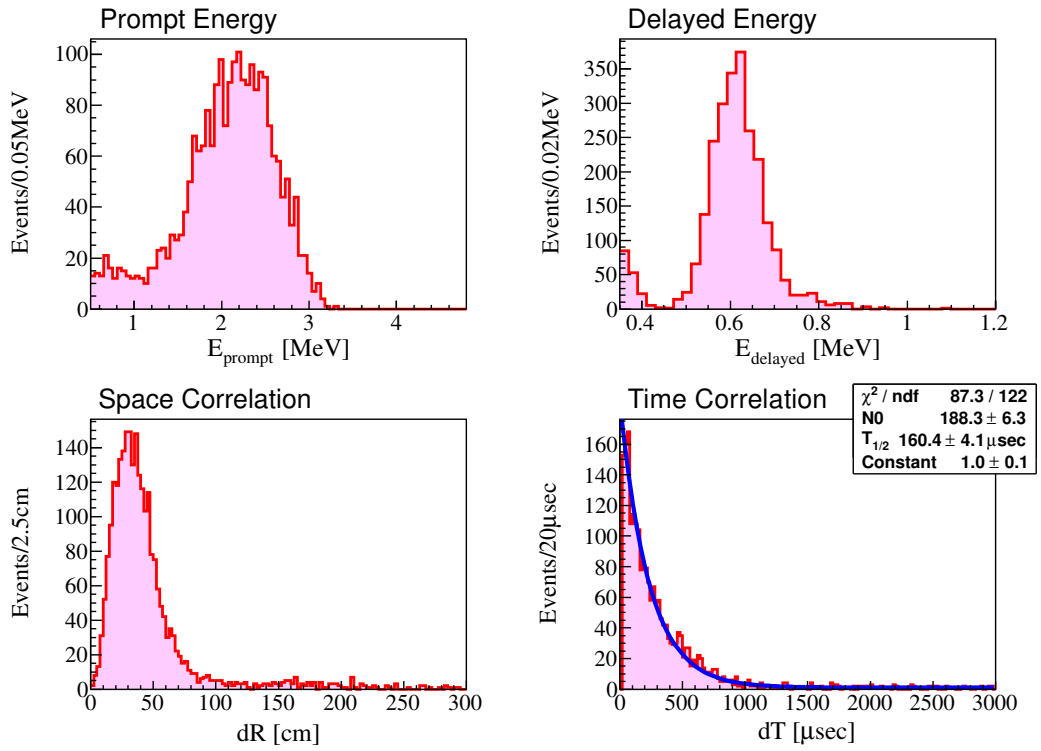

Figure 5.6: ^{214}Bi-^{214}Po delayed coincidence events. (Top-left) Prompt (^{214}Bi) energy distribution. (Top-right) Delayed (^{214}Po) energy distribution. (Bottom-left) The distance of prompt and delayed signals. (Bottom-right) Time difference of prompt and delayed events.

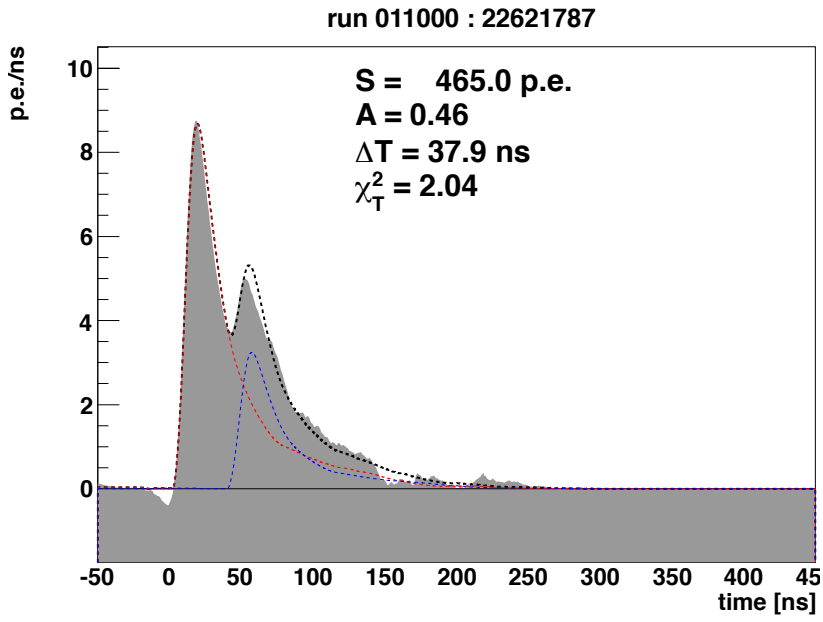

Figure 5.7: An example of Bi-Po double pulse event evaluated from a waveform.

- $\tilde{\chi}^2_{\rm T}$: Reduced χ^2 for time-distance relation.
  PMT hit time and the distance between the reconstructed vertex and the PMT has linear correlation as shown in Fig. 5.8 (a). $\chi^2_{\rm T}$ is evaluated for each event and its typical value is less than 2 for 1∼15 MeV energy region. An event which has worse $\chi^2_{\rm T}$ is not a "point-like" events, or fails the event reconstruction.

- $\sigma_{\rm T}$ and $\rm H_T$: Sigma and height of time-spectrum-subtracted time of flight.
  The time spectrum of scintillation light emission shown in Fig 5.8 (b) is reproduced from the time distribution of PMT after subtraction of time of flight. It includes transit time spread and vertex resolution. The peak width and height of the spectrum are denoted as $\sigma_{\rm T}$ and $\rm H_T$ and those typical values are 8∼11 nsec and less than 2, respectively. Those parameters also evaluate the quality of the vertex reconstruction.

- $\tilde{\chi}^2_{\rm Q}$: Reduced χ^2 for charge-distance relation.
  The correlation of PMT charge and the distance between the reconstructed vertex and the PMT is shown in Fig. 5.8 (c). The expectation is calculated from the expected charge. $\tilde{\chi}^2_{\rm Q}$ is evaluated for each event and its typical value is less than 2. An event which has worse $\tilde{\chi}^2_{\rm Q}$ means the energy estimation is not reliable.

- $\tilde{\chi}^2_{\rm hit}$ and $\rm R_{hit}$: Reduced χ^2 for hit occupancy-distance relation, and ratio of the number of total hits to the integrated expected occupancy.
  The number of hit can substitute for the charge information. In a low energy event, the ratio of the hit number to the total number of PMTs (occupancy) is a good parameter to estimate the expected number of photo-electrons (the expected charge). It is also useful to evaluate the reconstruction quality. The correlation between the occupancy and the distance is shown in Fig. 5.8 (d). The occupancy is calculated for each bin. The expected occupancy is calculated with Poisson probability, $1-e^{-\mu}$ where μ is the expected photo-electrons obtained from the ratio of the total expected charge to the total number of PMTs. $\tilde{\chi}^2_{\rm hit}$ is calculated from the scaled expectation with Poisson probability. Its normalized parameter is evaluated form the ratio of the number of total hits to the integrated expected occupancy ($\rm R_{hit}$, also shown in Fig. 5.8 (d)).

- $\sigma_{\rm Q}$, $\rm R_{N150}$ and $\rm R_{N48}$: sigma of Q / $\rm Q_{\mathit{expected}}$ distribution, the ratio of $\rm N_{150}$ to NsumMax and the ratio of $\rm N_{48}$ to $\rm N_{150}$.
  In Fig. 5.8 (e), the distribution of charge divided by the expected charge is shown. The width of the distribution is parameterized by the rms value. This parameter also evaluate the quality of the energy reconstruction. The ratio of the number of hit within 150 nsec ($\rm N_{150}$) to NsumMax, $\rm R_{N150}$ and ratio of the number of hit within 48 nsec ($\rm N_{48}$) to $\rm N_{150}$, $\rm R_{N48}$ are also evaluated.

The badness is evaluated for each event to checke whether it is physical event. In Fig. 5.9, each parameter for typical normal event (left) and noise event (right) are shown. Figure 5.10 shows the badness distribution as a function of visible energy. The distribution has energy dependence, so cut condition is also a function of visible energy drawn with solid line. The inefficiency caused by this cut is estimated to 0.1%.

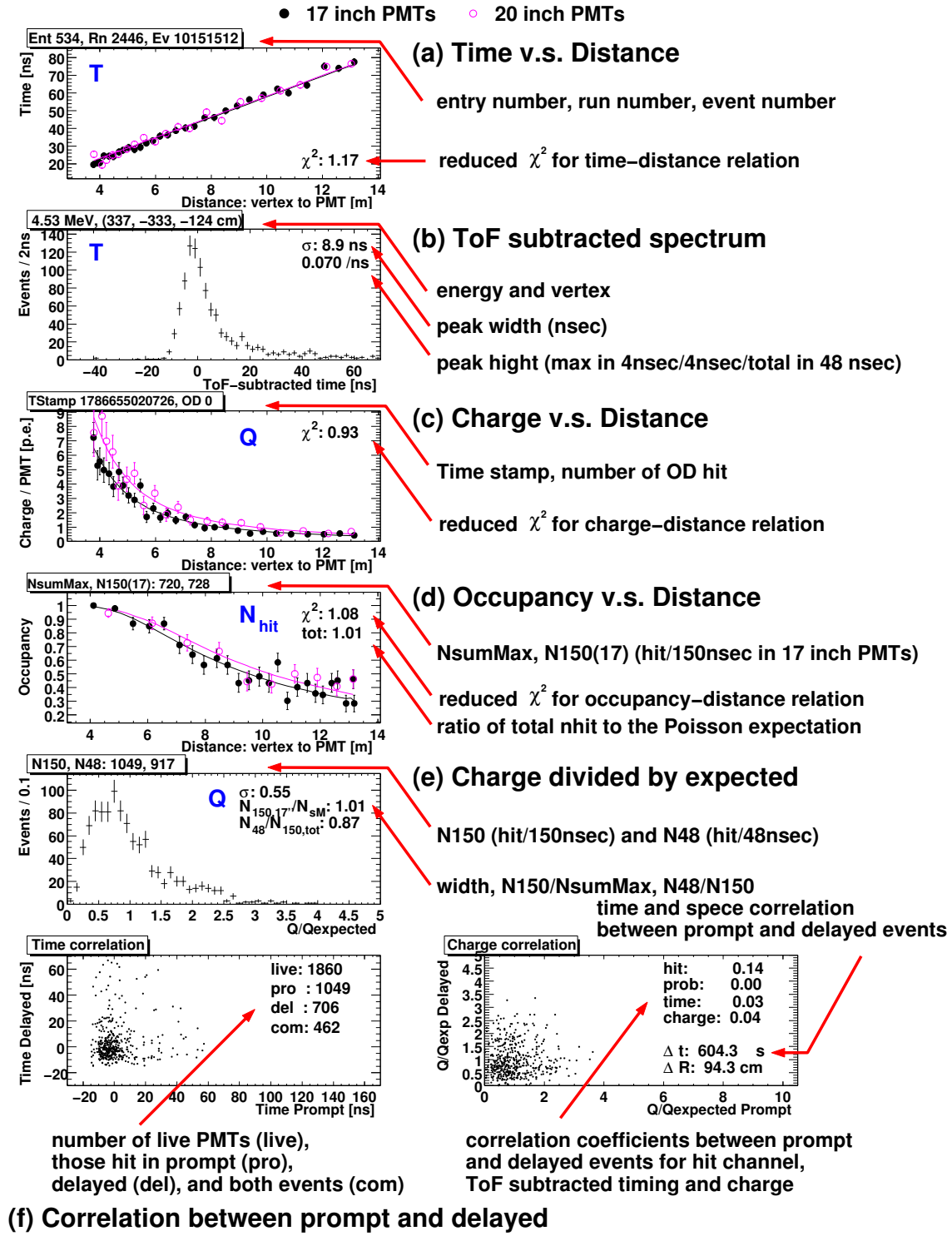

Figure 5.8: Explanation of each badness parameter used for the reconstruction quality check. Pictures from [85]. (a) - (e) is evaluated for each event, while (f) is calculated only for delayed coincidence event set.

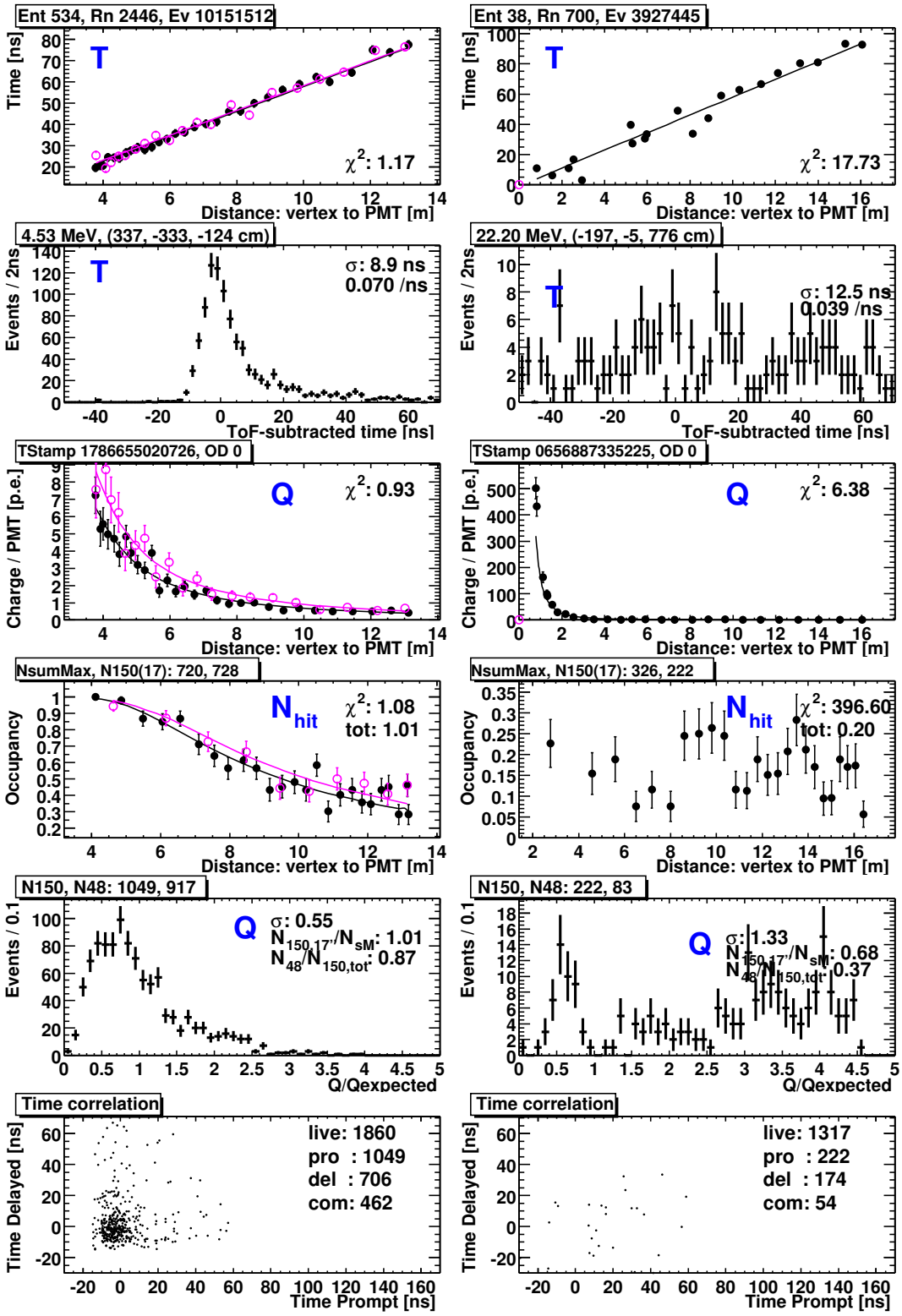

Figure 5.9: Reconstruction quality of each parameter for typical normal event (left) and noise event (right) taken from [85].

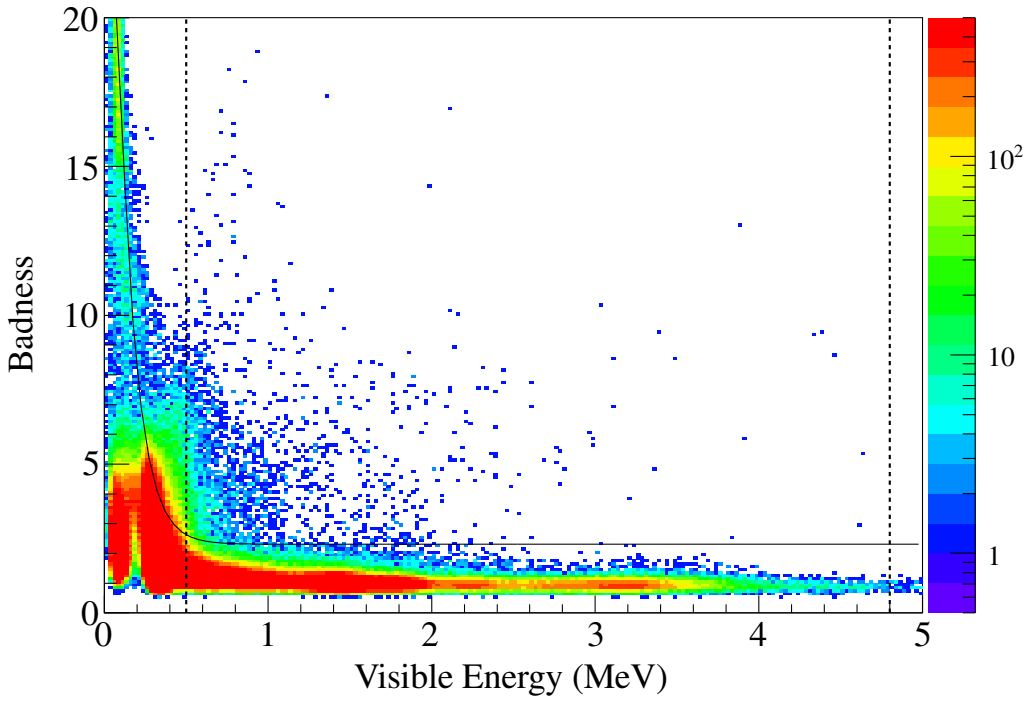

Figure 5.10: Badness distribution as a function of visible energy. Right axis shows the number of event. Dotted vertical lines show the lower and upper energy boundary used for the analysis. Solid line shows cut selection. Events above the line are removed.

5.7 Fiducial volume selection

The 1.2-m-radius fiducial volume is selected to suppress the backgrounds from material of the IB. Figure 5.11 shows single event vertex distribution of selected events. It indicates higher concentration of events around the IB. The IB is drawn as a black solid line there. Many events have a gathering at north and south poles. It would appear that 24 gores gathering into one point and complex welding line increases the event rate. What is the backgrounds and why they are distributed on the IB are described in next chapter. The radial distribution of the selected events in 1.2 $< E <$ 2.0 MeV is shown in Figure 5.12. It also indicates high event rate at the IB. This energy region is appropriate for $2\nu\beta\beta$ decay. Here, the ratio of signal to noise is more than 10 in the fiducial volume.

The θ-ϕ distribution of selected events in 1.6-m-radius and in the fiducial volume are also shown in Fig. 5.13 and Fig. 5.14, respectively. Before the fiducial volume cut, there are some high rate points such as south pole and cosθ $\sim$0.8, and event distribution is irregular. After the fiducial volume cut, its evenness is disappeared.

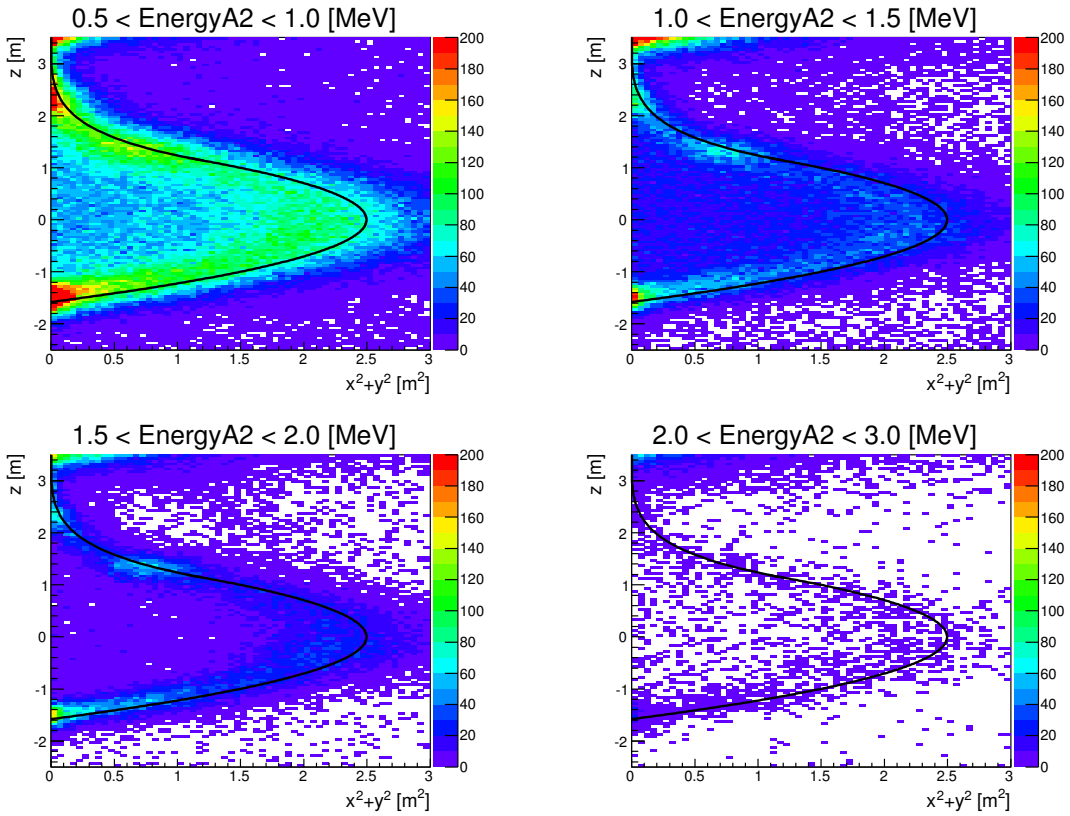

Figure 5.11: Single vertex distribution of selected events in each energy range. The IB is drawn as a black solid line. EnergyA2 stands for visible energy.

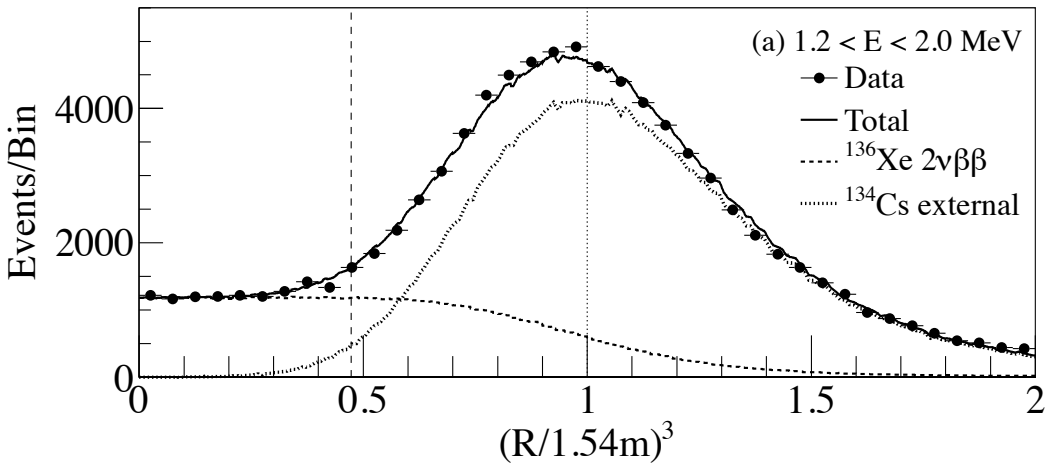

Figure 5.12: Radial distribution of selected events in $1.2 < E < 2.0$ MeV. Dotted line shows the surface of the IB and dashed line indicate the fiducial volume. ^{136}Xe $2\nu\beta\beta$ is signal and ^{134}Cs is major contributed background from the IB.

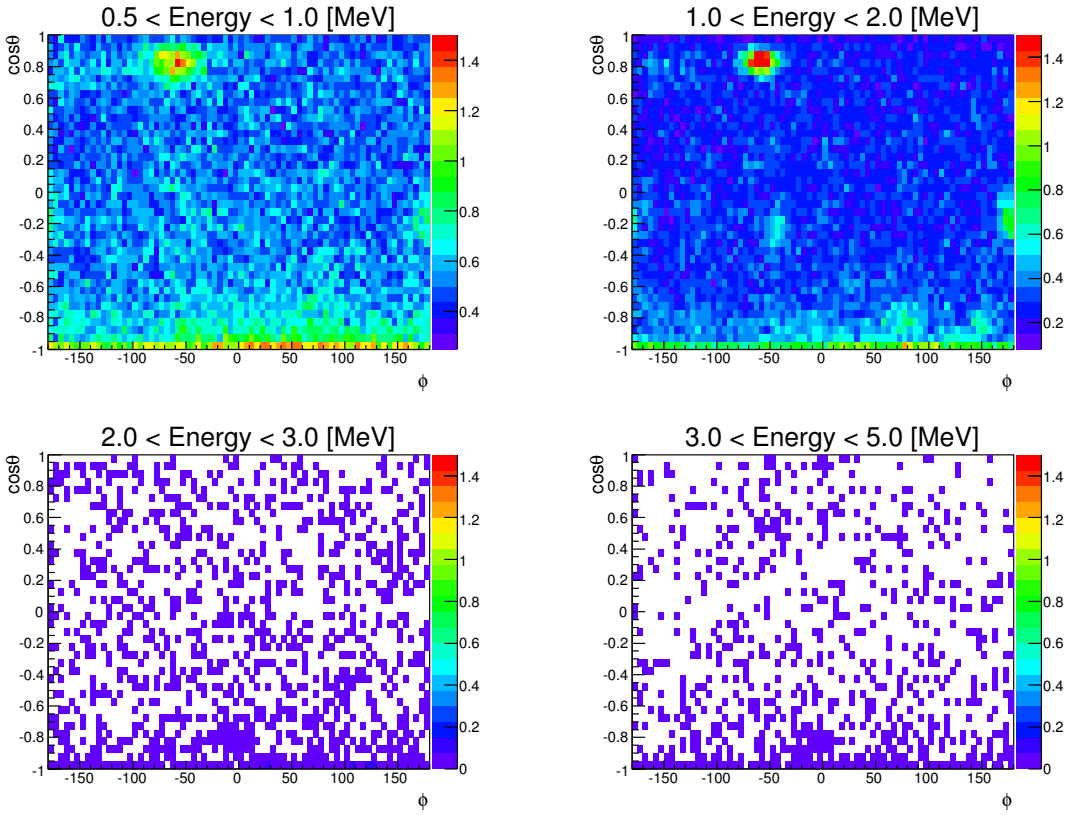

Figure 5.13: The θ-ϕ distribution of selected events in 1.6-m-radius.

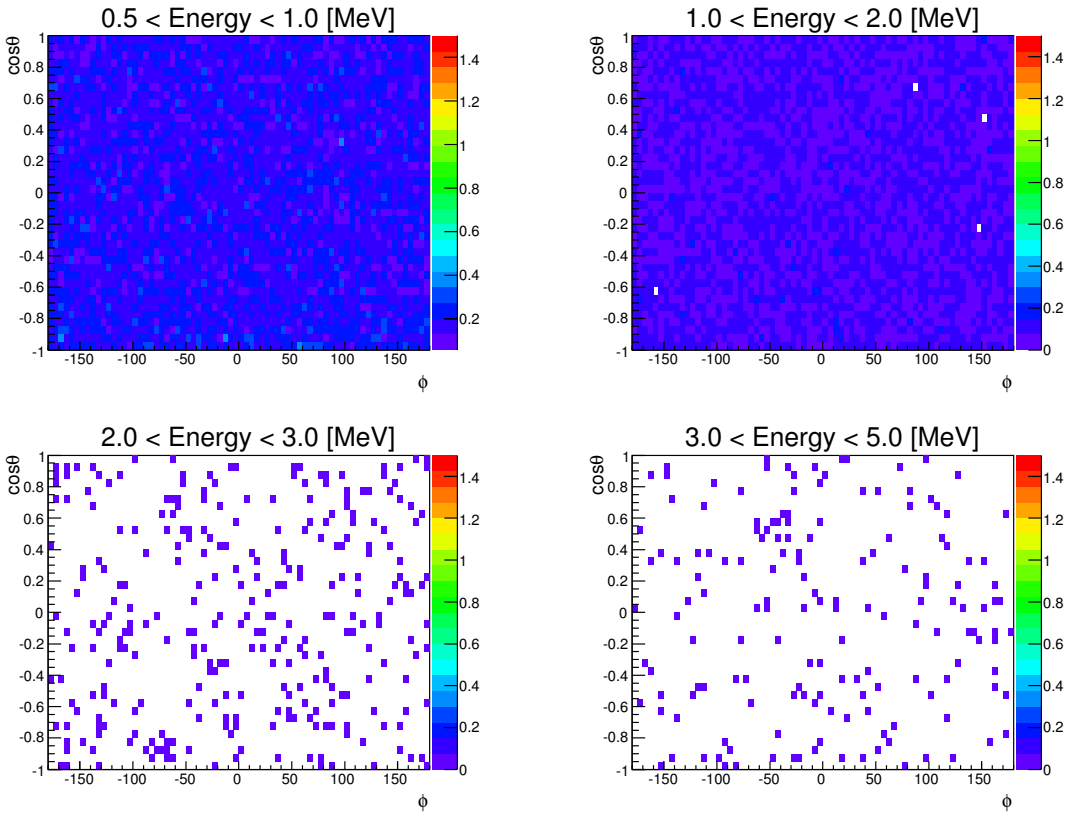

Figure 5.14: The θ-ϕ distribution in 1.2-m-radius fiducial volume.

Chapter 6

Background estimation

The half-lives of ^{136}Xe double-beta decay are calculated from the decay rate obtained by the energy spectral fitting. The spectrum contains signals produced by double-beta decay and various backgrounds such as radioactive impurities and spallation products induced by cosmic ray muons. For appropriate estimation of half-lives, it is important to understand the backgrounds, especially coming from newly installed Xe-LS and the IB.

6.1 Background category

In KamLAND single event selecition, the backgrounds were usually categorized into three kinds that (1) radioactive impurities from the balloon (externals), (2) those from the liquid sicntillator, and (3) muon induced products. However, in KamLAND-Zen, we find unexpected peak in the $0\nu\beta\beta$ window (called 2.6 MeV peak). It is distributed in the Xe-LS uniformly and the event rate is stable. As detailed description will be found in later section, the spectral fitting reveals that it is one of the backgrounds. Thus, we describe the backgrounds as follow;

- External backgrounds from the the IB material (Section 6.2),
- muon induced products at the underground (Section 6.3),
- residual radioactivities in the Xe-LS (Section 6.4),
- search for an origin of 2.6 MeV peak (Section 6.5).

Possible candidate and contamination route of 2.6 MeV peak is finally discussed in Section 6.6, and all of the backgrounds are summarized. The tagged event by the delayed coincidence method such as Bi-Po decay and reactor anti-neutrinos reactions are already described in Chapter 5, so not to be discussed in this Chapter. Some of estimated event rate come from the simultaneous fitting (noted as final fitting) described in Chapter 7.

6.2 External background from inner balloon material

The IB is made of single layer nylon. External backgrounds were originally thought to be dominated by natural radioactivity such as ^{238}U and ^{232}Th decay chains and ^{40}K. Those amounts in film were actually measured by ICP-MS before the fabrication of the IB (Section 3.5). However, from a radial distribution, it reveals that ^{134}Cs ($\beta + \gamma$) activity dominates in the energy region of $1.2 < E < 2.0$ MeV ($2\nu\beta\beta$ window, Fig. 6.1 (a)), while in the region of $2.2 < E < 3.0$ MeV ($0\nu\beta\beta$ window, Fig. 6.1 (b)), the spectrum is consistent with the uniform distribution of ^{214}Bi ($\beta + \gamma$, daughter of ^{238}U). The distribution is fitted with two components, a uniform source in/on the

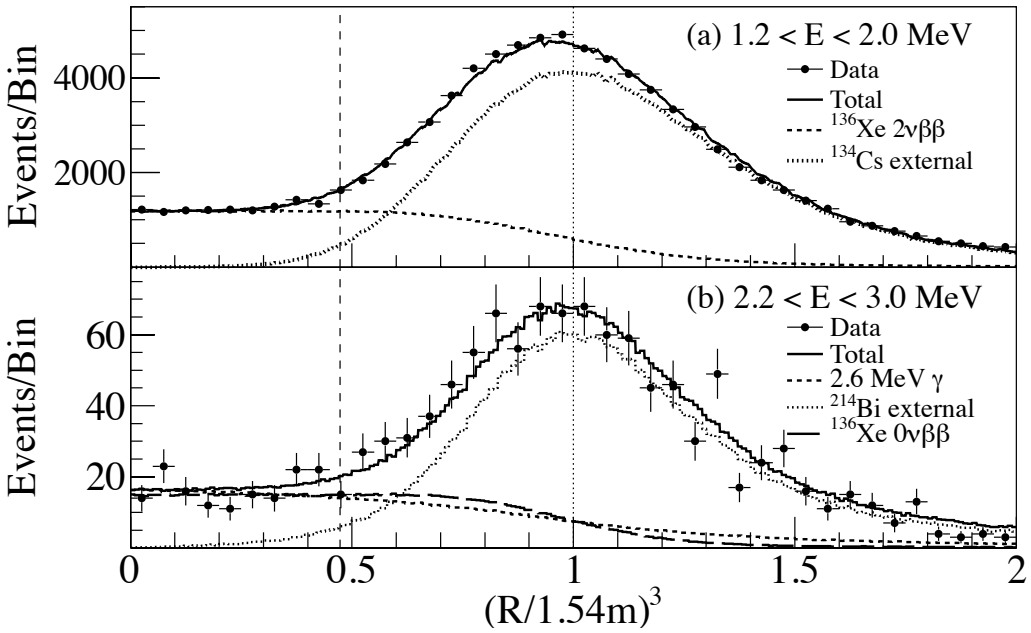

Figure 6.1: Radial distribution for (a) $1.2 < E < 2.0$ MeV and (b) $2.2 < E < 3.0$ MeV. (a) is reprint of Fig. 5.12. The lines show best-fit components for (a) ^{136}Xe $2\nu\beta\beta$ and ^{134}Cs. For (b), those are ^{214}Bi and 2.6 MeV γ (described in Sec. 6.5). $0\nu\beta\beta$ line is also described instead of γ's. The vertical lines show the 1.2-m-radius fiducial volume (dashed, described in next chapter) and IB radius (dotted).

IB material and those in the Xe-LS, generated by Monte-Carlo simulation. A 2.6 MeV γ's appeared in the $0\nu\beta\beta$ window is explained in Sec. 6.5. In addition to the existence of ^{134}Cs, ^{137}Cs (0.662 MeV γ) is also observed on the IB surface. These rare artificial nuclei are brought by the fallout of the Fukushima I reactor accident in March 2011. Basic properties (decay type, Q-value and half-life) of ^{134}Cs and ^{137}Cs are summarized in Table 6.1, and the level diagram of those are found in Appendix C.3. The foundation for the existence of those is that,

- Location of the IB fabrication facility.
  The IB fabrication facility is located in Sendai, which is ∼100 km away from

the Fukushima I reactor. From the soil sample measurement around Sendai, the existence of those nuclei is confirmed.

- Ratio of observed activity of ^{134}Cs/^{137}Cs.
  The observed amount of ^{137}Cs compared to ^{134}Cs cannot be explained by the spallation of ^{136}Xe. ^{137}Cs is heavier than ^{136}Xe, but the ratio of observed activity of ^{134}Cs/^{137}Cs is $\sim$0.8 (Fig. 6.2). In addition, its ratio is consistent with the contamination ratio of soil samples by the fallout.

- Distribution of ^{134}Cs and ^{137}Cs.
  ^{134}Cs and ^{137}Cs are only distributed on the IB. In the Xe-LS, amount of those are estimated but only upper limits are obtained. We measured the water and oil which soil sample dissolved into and filtrated, with Ge detecter, and confirmed that Cs is easily dissolved into water but not to liquid scintillator.

Table 6.1: Basic properties of ^{134}Cs and ^{137}Cs. The level diagram of those are found in Appendix C.3.

Isotope	Decay	Q-value (MeV)	Half-life (yr)
^{134}Cs	$\beta^- + \gamma$ (99.9997%)	2.06	2.06
	EC (0.0003%)	1.23	
^{137}Cs	$\beta^- + \gamma$ (Mainly 0.662 MeV γ)	1.18	30.7

Figure 6.2 shows the energy spectrum within 2.0-m-radius. Only external backgrounds are color-lined in this histogram. The clear peak of ^{137}Cs is observed in $0.5 < E < 0.8$ MeV with purple line, and the two peaks of ^{134}Cs are seen in $1.0 < E < 2.0$ MeV with light blue line. External ^{238}U, ^{232}Th and ^{40}K are also indicated with orange, brown and blue line, respectively. A schematic of ^{238}U, ^{232}Th decay series are shown in Appendix B. In Fig. 6.3, energy distribution as a function of the cubed radius is shown. Horizontal line at 1.0 shows the position of the IB surface. It also indicates the two peaks of ^{134}Cs on the IB between 1.2 and 1.9 MeV with two yellow cluster.

One of the backgrounds in $0\nu\beta\beta$ region, ^{214}Bi (a daughter of ^{238}U) is distributed in $2.2 < E < 3.0$ MeV in Fig. 6.3. ^{208}Tl, a daughter of ^{232}Th, is also found in $3.2 < E < 4.6$ MeV. Note that ^{208}Tl (β^-, $Q = 5.0$ MeV) is detected with coincident β/γ in liquid scintillator. Thus well-known 2.6 MeV peak does not appear, but distributes in 3−5 MeV. The amount of ^{238}U coming from the IB is estimated from radial distribution of ^{214}Bi with assuming radiative equilibrium. Only the latter period of dataset is used since ^{222}Rn was induced in the detector during the modification. The estimated value is 1.8×10^{-11} g/g. It is higher than the amount obtained by ex-situ measurement of the film. Then radioactivity of ^{238}U in the IB is estimated by the energy distribution of ^{214}Po. The distribution of ^{214}Po around the IB has two peaks and it reveals that ^{238}U exists on the IB, too. Considering the detection efficiency and assuming radiative equilibrium, estimated amount of ^{238}U in the IB is 3.1×10^{-12} g/g. It is almost consistent with ex-situ measurement.

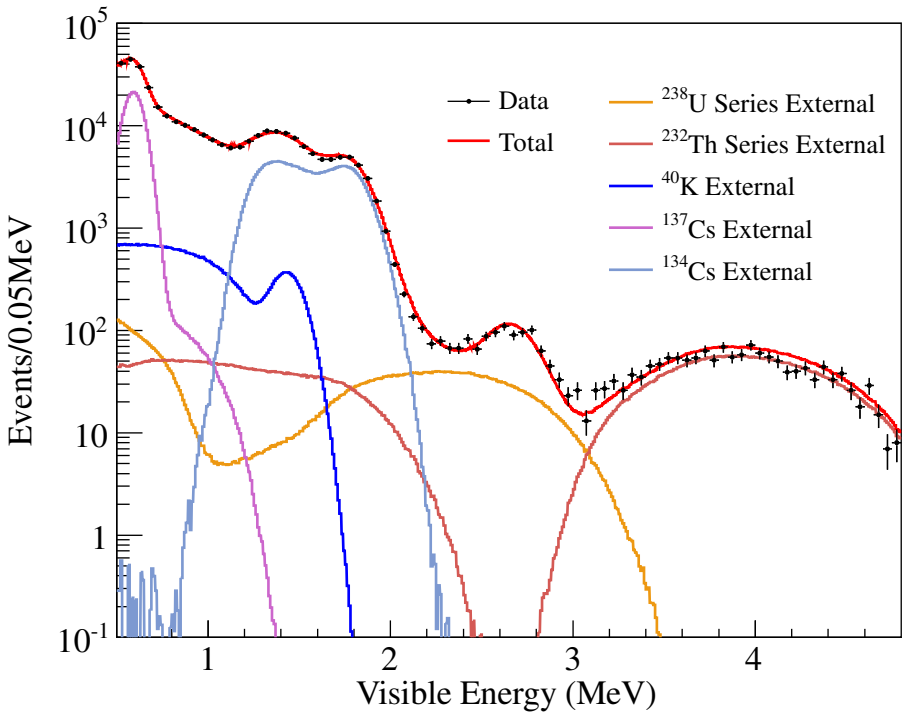

Figure 6.2: Energy spectrum within 2.0-m-radius. Only external backgrounds are color-lined. Clear peak of ^{137}Cs and two peak of ^{134}Cs are appeared.

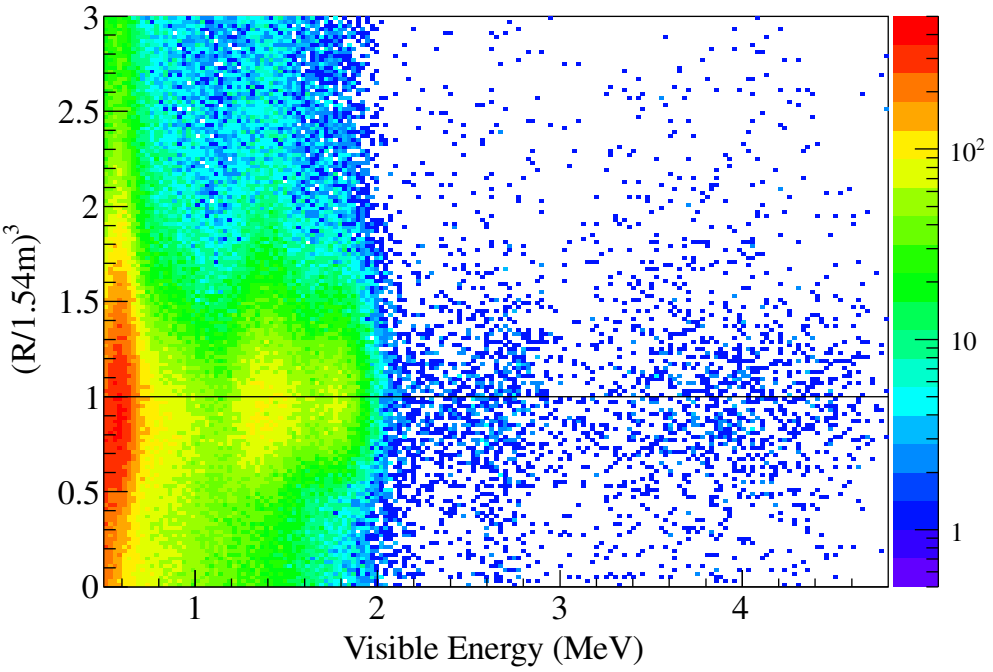

Figure 6.3: Energy distribution as a function of R^3. Horizontal line shows radius correspond to 154 cm (IB edge). On that line, red cluster at 0.6 MeV indicate ^{137}Cs and two yellow clusters between 1.2 and 1.9 MeV shows two peaks of ^{134}Cs. Blue cluster between 2.2 and 3.0 MeV shows ^{214}Bi, and cluster between 3.2 and 4.6 MeV indicate ^{208}Tl.

6.3 Muon induced products

Cosmic ray muons interact with liquid scintillator or other material and produce various kinds of unstable isotopes and/or neutrons. These muon-induced products are evaluated from time correlation of observed muons with known neutron capture time or life-time of generated isotopes. In the Xe-LS, they are categorized into three kinds as follow;

1. Spallation neutrons,
2. Spallation product from ^{12}C,
3. Spallation product from ^{136}Xe.

The first and the second ones are well studied in KamLAND. Third one is newly considered. Whether it makes 2.6 MeV peak is also of interest. Not only long-lived spallation, but also short-lived ones are candidate backgrounds since spallation products are always supplied in the detector.

6.3.1 Spallation neutrons

In KamLAND, neutrons produced by muons are captured on protons (energy of capture γ's = 2.225 MeV) or ^{12}C (4.946 MeV) with neutron capture time 210 μsec. Protons and carbons are the main components of the liquid scintillator. In KamLAND-Zen, in addition to those, neutrons may be captured on ^{136}Xe (4.026 MeV), or ^{134}Xe (6.364 MeV) and may produce ^{137}Xe (β^- decay, $\tau = 5.5$ min, $Q = 4.17$ MeV). This product becomes a possible background of $0\nu\beta\beta$ decay. Then, ^{137}Xe evaluation is needed although the whole detector volume is 2 msec vetoed after every muon events and the probability that a neutron survives longer than the veto time is calculated to be 7.3×10^{-5}. The expected fractions of protons, ^{12}C, ^{136}Xe and ^{134}Xe are 0.994, 0.006, 9.5×10^{-4}, and 9.4×10^{-5}, respectively. They are calculated from their cross sections and number of targets. Energy distribution of neutron capture events is shown in Fig. 6.4 with a cut of time difference from muons $150 < \Delta T_{muon} < 1,000$ μsec in 1.6-m-radius (light blue histogram) and 1.2-m-radius (green histogram). To reduce the effect of missing waveforms, the good event selection that the number of waveforms (i.e. PMT hits) is larger than NsumMax is also applied to the blue histogram. The clear peak from neutron capture on protons (2.225 MeV γ) and a few events in ^{12}C energy region are seen in this picture. These 2.225 MeV events can be used to evaluate the energy response, already described in Section 4.7.4. For ^{136}Xe and ^{134}Xe, no candidates of neutron capture events are found. The expected production rate of ^{137}Xe is $\sim 2.9 \times 10^{-3}$ (ton·day)$^{-1}$, calculated from neutron production rate and its fraction. It is negligible in the current search.

6.3.2 Spallation products from ^{12}C

The production rates of spallation isotopes of ^{12}C were estimated experimentally with accelerator-based muon beam [87]. Based on the measured cross sections, the production rates in KamLAND are calculated [88] and used for this estimation.

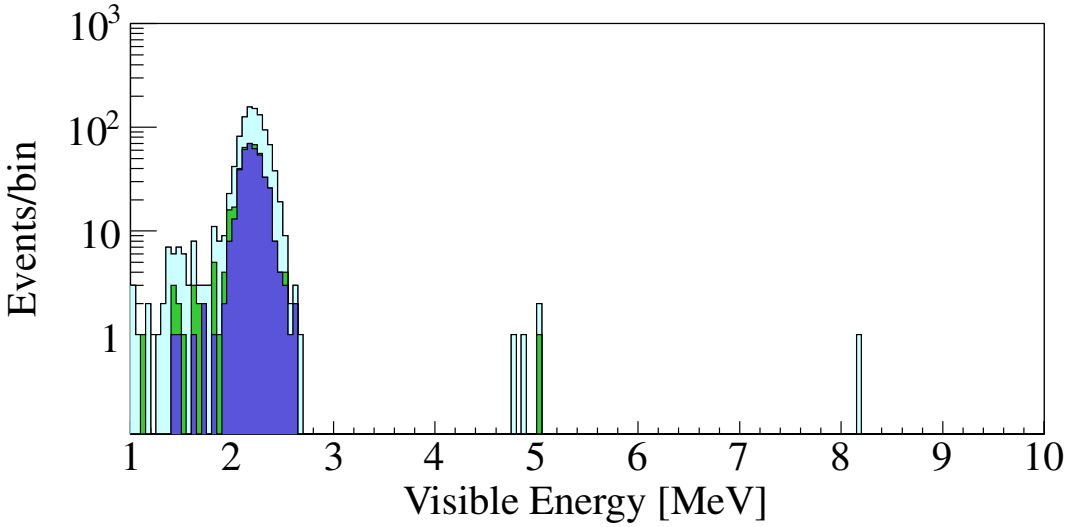

Figure 6.4: Energy distribution of neutron capture events with cut for time difference from muons $150 < \Delta T_{muon} < 1,000$ μsec (light blue in r <1.6 m and green in r <1.2 m) and good event selection (number of waveforms > NsumMax) (blue). The clear peak from neutron capture on protons (2.225 MeV) appeared and a few events in ^{12}C energy region. No event found at 4.026 MeV (^{136}Xe) or 6.364 MeV (^{134}Xe).

There are more than 10 spallation products measured in KamLAND and dominated ones in the double-beta decay energy range are ^{10}C (β^+ decay, $\tau = 27.8$ s, $Q = 3.65$ MeV) and ^{11}C (β^+, $\tau = 29.4$ min, $Q = 1.98$ MeV). Since these events are generated uniformly in the detector, the amount of these backgrounds depends on the fiducial volume. Theoretical visible energy spectra considering the energy resolution ($6.6\%/\sqrt{E[\mathrm{MeV}]}$) are shown in Figure 6.5. In the spectra, area ratio of each spectrum is fixed to one. The basic properties are summarized in Table 6.2. Other spallation products considered in KamLAND are ignored due to its small contribution in $0.5 < E < 4.8$ MeV.

Table 6.2: Basic properties of ^{10}C and ^{11}C.

Isotope	Decay	Q-value (MeV)	Half-life
^{10}C	β^+	3.65	19.3 sec
^{11}C	β^+	1.98	20.4 min

From a measurement of spallation neutron flux in the Xe-LS, we obtained a (13±6)% increase compared to the outer KamLAND-LS. Then we asses a 19% systematic uncertainties on the calculated spallation yields. Event rates of ^{10}C and ^{11}C are estimated from the final fitting to $(2.16 \pm 0.43) \times 10^{-2}$ (ton·day)$^{-1}$ and 0.999 ± 0.014 (ton·day)$^{-1}$ respectively. Although ^{10}C will be the largest background in the future, it will be able to reduce by tagging of triple coincidence with muon, neutron and ^{10}C [88].

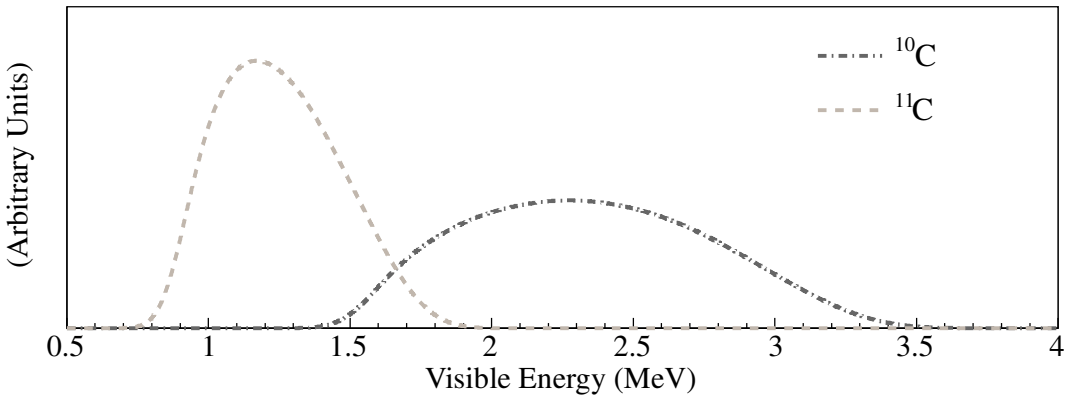

Figure 6.5: Theoretical visible energy spectra of ^{10}C (gray, dot-lined) and ^{11}C (light gray, lined) considering the energy resolution of KamLAND-Zen. The area ratio of each spectrum is fixed to one.

6.3.3 Spallation products from ^{136}Xe

Short-lived nuclei ($T_{1/2}$ < 100 sec)

For the muon induced products from xenon, we have no past experimental data. Spallation products from ^{136}Xe whose half-live are less than 100 sec, are studied with present data whether a event has time correlation with muons which depositing more than ∼3 GeV (called showering muons). As a result, no correlated event is found in the energy range $1.2 < E < 2.0$ MeV ($2\nu\beta\beta$ window). The 90% C.L. upper limit is calculated with Feldman Cousins method [89] to be 171 events or 0.27 (ton·day)$^{-1}$ by counting the number of events in on-time window ($\Delta T_{muon} < 500$ sec) and off-time window ($500 \leq \Delta T_{muon} < 5{,}000$ sec). Event time distribution is shown in Fig. 6.6 (top). In the energy range $2.2 < E < 3.0$ MeV ($0\nu\beta\beta$ window), there is also no correlated event. To calculate the upper limit in this energy range, spallation products from ^{12}C are also considered as backgrounds. They are summarized in Table 6.3. Event time distribution is shown in Fig. 6.6 (bottom). The obtained 90% C.L. upper limit is 4.87 events or 7.67 $\times 10^{-3}$ (ton·day)$^{-1}$. So short-lived spallation nuclei seldom or never contribute to the signals nor be candidate of 2.6 MeV peak.

Long-lived nuclei (100 sec < $T_{1/2}$ < 30 days)

Ref. [90] provides cross section data evaluated from ^{136}Xe + 1 GeV proton. Spallation products from ^{136}Xe whose half-lives are less than 30 days, are studied with energy spectra scaled by the cross sections. This study is focused on the possibility that the unknown 2.6 MeV peak is provided from continuous muon spallation. If the 2.6 MeV peak is produced by muons, other nuclei which have close A and Z, should be also produced with yields proportional to their cross sections. Candidates of 2.6 MeV event are selected from ENSDF database [91] and summarized in Table 6.4. They have a peak in $2.4 < E < 2.8$ MeV. From comparison of KamLAND-Zen data with energy spectra of co-generate with 2.6 MeV peak scaled by their cross sections,

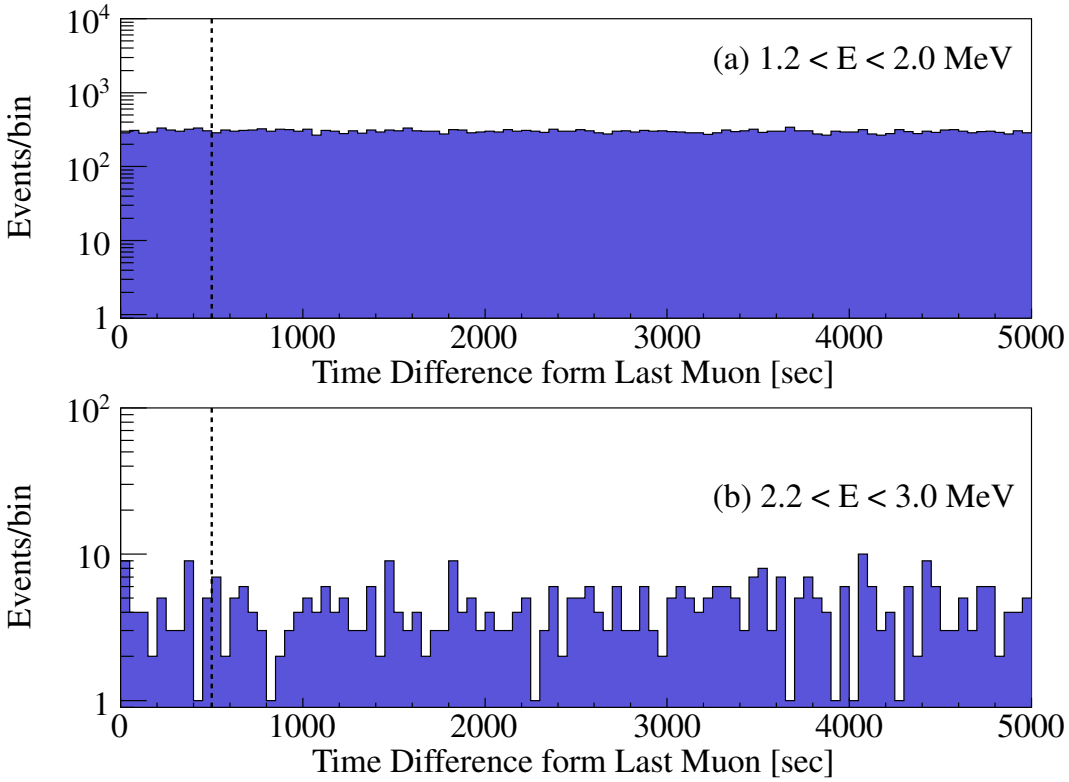

Figure 6.6: Time distribution from last muon events in the energy range $1.2 < E < 2.0$ (top) and $2.2 < E < 3.0$ MeV (bottom).

Table 6.3: Spallation products from ^{12}C considered as backgrounds to calculate the upper limit in $2.2 < E < 3.0$ MeV. The number of event is in 112.3 days livetime.

Isotope	Decay	Q-value (MeV)	Half-life (sec)	N of event in $2.2 < E < 3.0$ MeV
^{10}C	β^+	3.65	19.3	6.86
^{12}B	β^-	13.4	20.2×10^{-3}	1.58
^{8}Li	$\beta^- + \alpha$	16.0	0.84	0.61
^{8}B	β^+	18.0	0.77	0.22
^{9}Li	β^-	13.6	0.18	0.10
^{6}He	β^+	3.51	0.81	2.13†
Total				11.49

† ^{6}He is not observed in KamLAND data, so the value is estimated from [87].

it reveals their contributions are negligible.

Table 6.4: Candidates of 2.6 MeV event (100 sec $< T_{1/2} <$ 30 days).

Candidate isotope	Decay mode	Cross section (mb)†
$^{82}Br^{m}$	β^-	0.0583
$^{83}Se^{m}$	β^-	0.00098
$^{116}Im^{m}$	β^-	4.79
^{52}Mn	β^+/EC	0.0384
^{57}Ni	β^+/EC	Not detected
^{86}Y	β^+/EC	1.298
^{82}Rb	β^+/EC	0.778
^{93}Mo	β^+/EC	3.16
^{92}Tc	β^+/EC	0.301
^{93}Tc	β^+/EC	1.23
^{100}Rh	β^+/EC	5.63
^{106}Ag	β^+/EC	8.56
^{108}In	β^+/EC	5.81
^{110}In	β^+/EC	9.87
^{115}Te	β^+/EC	2.97

† Values from Ref. [90].

6.4 Residual radioactivity in Xe-LS

Liquid scintillator can achieve quite ultra-pure environment with relative ease, but still there remain some radioactivities. In the KamLAND LS, ^{238}U and ^{232}Th decay series and ^{40}K, as commonly seen in natural environment, are observed. It also contains noble gas ^{85}Kr and ^{210}Bi, a daughter isotope of ling-lived ^{210}Pb (down stream of ^{222}Rn) in the low energy. In the Xe-LS, residual radioactivities written above are observed (Section 6.4.1 and 6.4.2). In addition to those, unknown 2.6 MeV peak is observed in the $0\nu\beta\beta$ window. It is summarized in the later section. Potential backgrounds from fallout nuclei are also discussed in Section 6.4.3.

6.4.1 ^{238}U and ^{232}Th chains

From studies of sequential decays of ^{214}Bi-^{214}Po and ^{212}Bi-^{212}Po with radial distribution, the residual ^{238}U and ^{232}Th concentrations in the Xe-LS are estimated to be $(3.5 \pm 0.6) \times 10^{-16}$ g/g and $(2.2 \pm 0.3) \times 10^{-15}$ g/g, respectively, assuming secular equilibrium. In this estimation, we do not use the former period of the data set to avoid a effect from initial ^{222}Rn contamination to the detector during the Xe-LS filling. In the final fitting, since equilibrium may be broken, Bi-Po studies are only used to estimate the backgrounds from ^{222}Rn-^{210}Pb and ^{228}Th-^{208}Pb subchains of ^{238}U and ^{232}Th. Other decays in the chain are treated as unconstrained parameters,

and it revealed that they are very small amount. The obtained 90% C.L. upper limits of each event rate are < 1.17 and < 0.45 (ton·day)$^{-1}$ for ^{238}U-^{222}Rn (^{234}Pa) and ^{232}Th-^{228}Th (^{228}Ac), respectively.

6.4.2 Other radioactive contaminants

As mentioned at the beginning of this section, ^{85}Kr and ^{210}Bi in the low energy and ^{40}K are evaluated as backgrounds in the Xe-LS. Basic properties of them are summarized in Table 6.5. For ^{40}K, the 90% C.L. upper limit of the decay is obtained

Table 6.5: Basic properties of ^{85}Kr, ^{210}Bi and ^{40}K

Isotope	Decay	Q-value (MeV)	Half-life
^{85}Kr	β^-	0.687	10.756 yr
^{210}B	β^-	1.162	5.013 day
^{40}K	β^- (89.28%)	1.311	1.277×10^9 yr
	EC (10.2%)	1.504	

as 8.5 (ton·day)$^{-1}$. ^{85}Kr and ^{210}Bi are much contained in the Xe-LS and their decay rates are 200 ± 7.3 and 101 ± 2.9 (ton·day)$^{-1}$, respectively. The theoretical visible energy spectra of them are shown in Fig. 6.7.

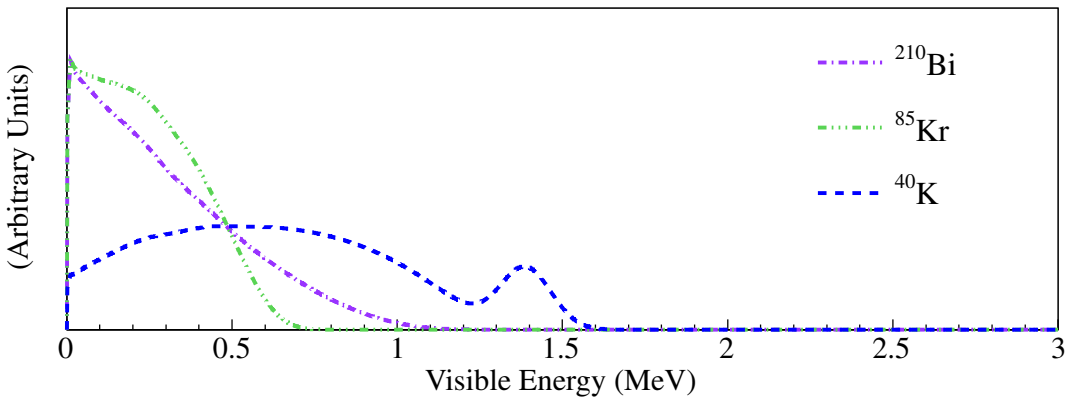

Figure 6.7: Theoretical visible energy spectra of ^{210}Bi, ^{85}Kr and ^{40}K considering the energy resolution of KamLAND-Zen. The area ratio of each spectrum is fixed to one.

6.4.3 Potential background from fallout

We also consider potential backgrounds from fallout nuclei caused by the Fukushima-I reactor accident. There are seven nuclei whose half-lives are longer than 30 days and the existence are confirmed form the ex-situ measurement of soil sample or ocean sample around Fukushima: ^{137}Cs, ^{134}Cs, ^{110}Ag^m, ^{129}Te^m, ^{95}Nb, ^{90}Y (from ^{90}Sr) and ^{89}Sr. All isotopes are included as unconstrained parameters in the fitting. ^{110}Ag^m

is one of 2.6-MeV peak candidates (detail in the next section). For ^{137}Cs and ^{134}Cs, the 90% C.L. upper limits of each event rate are obtained from spectral fitting as < 0.94 and < 0.25 (ton·day)$^{-1}$, respectively. Other fallout isotopes, ^{129}Te^{m}, ^{95}Nb, ^{90}Y and ^{89}Sr, are revealed to be negligible. The theoretical visible energy spectra of the latter four nuclei are shown in Fig. 6.8.

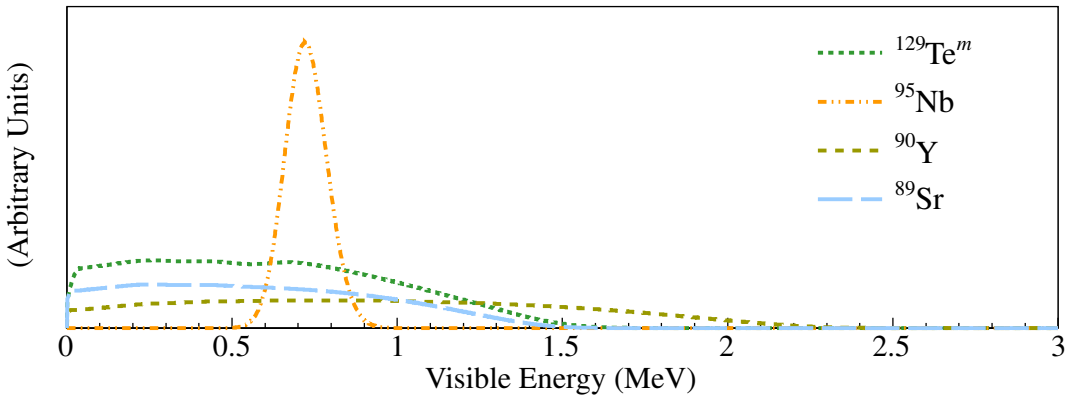

Figure 6.8: Theoretical visible energy spectra of ^{129}Te^{m}, ^{95}Nb, ^{90}Y and ^{89}Sr considering the energy resolution of KamLAND-Zen. They are not 2.6 MeV peak candidates. The area ratio of each spectrum is fixed to one.

6.5 Search for an origin of 2.6 MeV peak

We found the unexpected peak in the $0\nu\beta\beta$ window as shown in Fig. 6.9. The number of event is 157 in 1.2-m-radius fiducial volume and 112.3 days livetime, or 0.248 (ton·day)$^{-1}$. It is almost stable in time and distribute uniformly in the Xe-LS. No such a peak is found in the KamLAND-LS. It was fitted with $0\nu\beta\beta$ spectrum firstly, and it revealed the peak position has ∼3% difference (later shown in Fig. 6.11, (b)). Furthermore, the hypothesis that the peak is solely explained by $0\nu\beta\beta$ events is excluded at more than 5σ C.L. by a χ^2 test. The well known 2.614 MeV gamma from ^{208}Tl (β^- decay, Q=5.0 MeV) cannot be the peak since it distributes to 3−5 MeV due to the simultaneous β/γ detection in the surrounding LS. Thus, we conclude the peak is unknown background, and there are two possibility of the origin of the peak; long-lived radioactive impurities or cosmogenic spallation nuclei. Unfortunately, identification of β or γ from radial distribution is difficult (Fig. 6.1 (b)). In addition, ex-situ measurements cannot determine what kind of isotopes are contaminants due to their small amount.

6.5.1 Unknown peak search with ENSDF database

To consider the possibility of long-lived radioactive impurities (half-life is more than 30 days), we search for a possible 2.6 MeV peak from all isotopes and decay path in ENSDF database according to the following procedures.

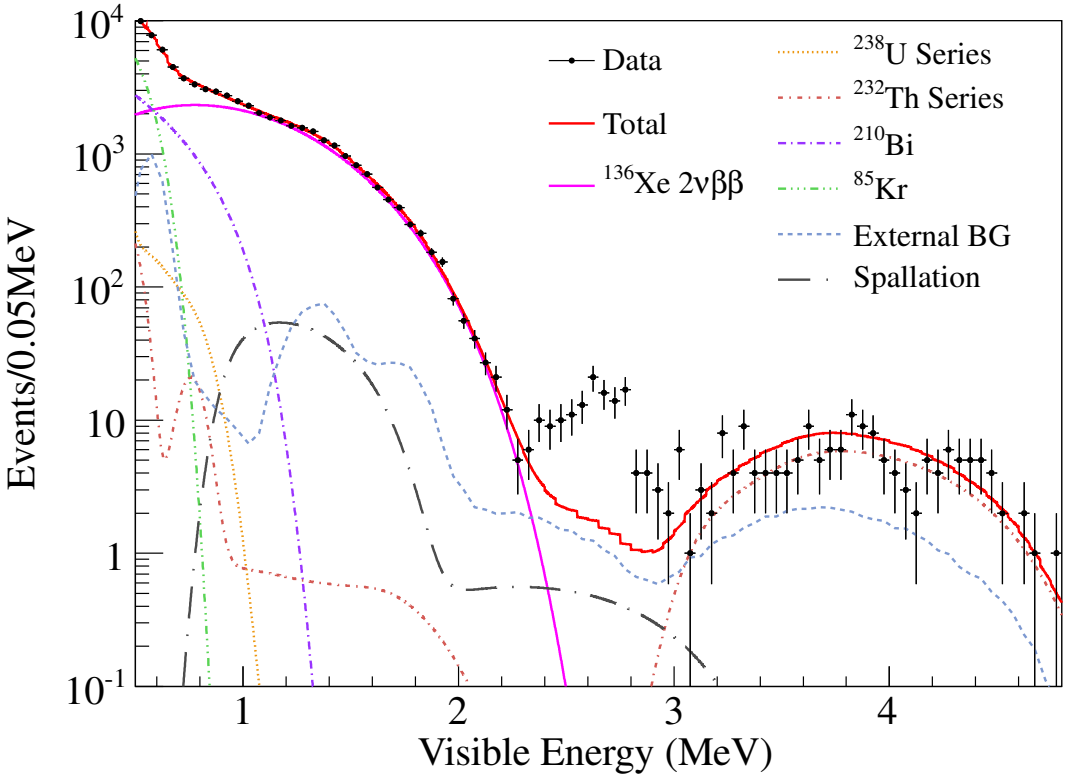

Figure 6.9: Energy spectrum out of consideration of the peak in the $0\nu\beta\beta$ window. 1.2-m-radius fiducial volume and 112.3 days livetime.

1. Making extracted decay database from ENSDF.
   For all tabulated decay chains in the database, basic decay information such as Q value, life time, and the following cascade paths with energies of γ rays and their life time is extracted from ENSDF database. In the cascade decay, the effect of quenching of multiple γ rays and meta stable state are also considered.

2. Making energy spectrum.
   From (1), KamLAND visible energy spectrum is calculated for each β^-, β^+, and electron capture decay, taking into account of alpha quenching, energy resolution ($7\%/\sqrt{E(MeV)}$), energy non-linearity and so on.

3. Search for a 2.6 MeV peak from calculated spectra.
   With spectra shape calculated from (2), we search for the candidate isotopes whose spectra have peak (should be sharp) within 2.4−2.8 MeV, and no tail in high energy. Isotopes whose half-lives are longer than 30 days are selected. In addition, if candidates have a long lived parent ($>$ 30 days), they are also selected.

As a result, there are only 4 nuclei corresponding to these conditions remained as potential background sources;

- $^{110}\mathrm{Ag}^{m}$ (β^{-} decay, $\tau = 360$ day, $Q = 3.01$ MeV),
- $^{88}\mathrm{Y}$ (EC decay, $\tau = 154$ day, $Q = 3.62$ MeV),
- $^{208}\mathrm{Bi}$ (EC decay, $\tau = 5.31 \times 10^{5}$ yr, $Q = 2.88$ MeV),
- $^{60}\mathrm{Co}$ (β^{-} decay, $\tau = 7.61$ yr, $Q = 2.82$ MeV).

The level diagram of those are found in Appendix C.2. Theoretical visible energy spectra of 4 nuclei considering the energy resolution of KamLAND-Zen are shown in Figure 6.10. ^{208}Bi and ^{88}Y have very similar shapes. The peak position of ^{60}Co

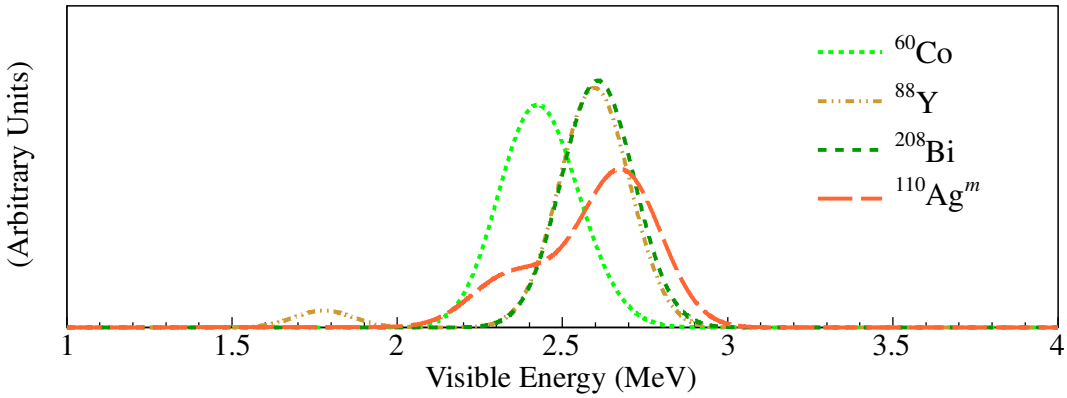

Figure 6.10: Theoretical visible energy spectra of ^{60}Co, ^{88}Y, ^{208}Bi and $^{110}\mathrm{Ag}^{m}$ considering the energy resolution of KamLAND-Zen. The area ratio of each spectrum is fixed to one.

is lower than the other three nuclei. $^{110}\mathrm{Ag}^{m}$ has distinguishing shape. Although ^{88}Y is a little bit constrained by its half-life and ^{60}Co by the shape, remaining 4 background candidates are all included in the final fitting as free parameters. There is no clear evidence that which background exists, or it is difficult to determine each contribution separately by an ex-situ measurement. The energy spectrum fitted with those four backgrounds and closeup in $2.2 < E < 3.0$ MeV is shown in Figure 6.11 (a)[1]. It has a $\chi^2_{energy} = 11.6$ in this energy region. The best-fit numbers provided from this spectrum are 101, 7.7, 18.6 and 0.41 events for $^{110}\mathrm{Ag}^{m}$, ^{88}Y, ^{208}Bi and ^{60}Co, respectively. In Figure 6.11 (b), data is fitted with $0\nu\beta\beta$ spectrum. It provides quite different χ^2_{energy} compared with Figure 6.11 (a) that $\Delta\chi^2 = 73$ (8.6 σ) including systematic uncertainties of the energy scale model. For a reference, the fitting results are shown in Fig. 6.11 (c)$-$(f) with an assumption that only one kind of nucleus among 4 backgrounds is relevant to the background. In (f), ^{60}Co is much constrained (event rate is almost zero) due to its spectrum shape, and $0\nu\beta\beta$ is dominant. Comparison of those χ^2_{energy} provides that a dominant contribution of $^{110}\mathrm{Ag}^{m}$ is preferred. Residuals of Figure 6.11 (a)$-$(f) are shown in Fig. 6.12.

[1]Energy spectra shown in Fig. 6.11 (a)$-$(f), fitting energy range is between 0.5 and 4.8 MeV and just shows $2.2 < E < 3.0$ MeV.

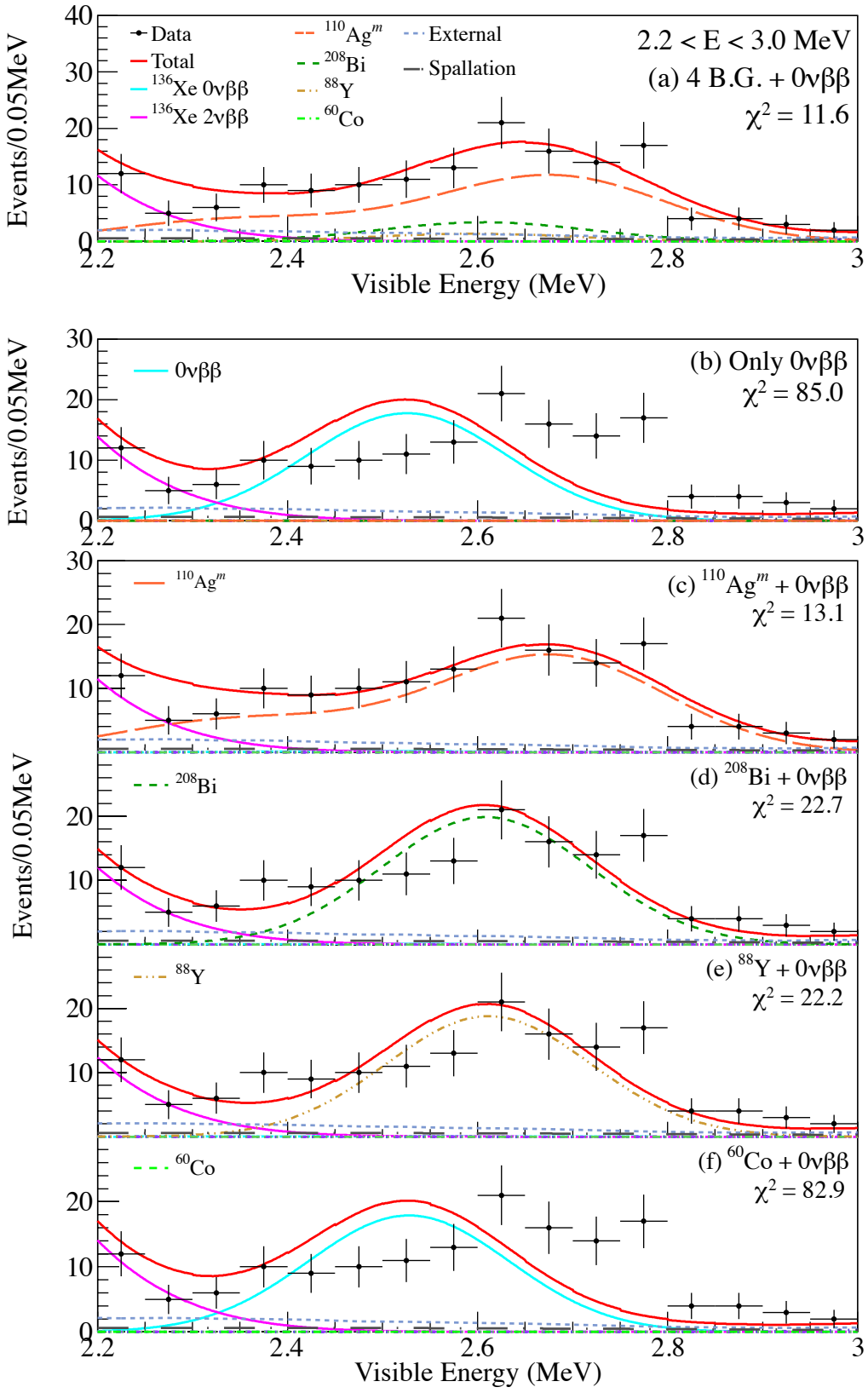

Figure 6.11: Energy spectra of $2.2 < E < 3.0$ MeV. (a) Closeup of Figure 7.4. (b) Assuming no background in this energy region. (c)-(f) Assumption of one background and $0\nu\beta\beta$ existed, for comparison. For (f), $0\nu\beta\beta$ is dominated. Provided χ^2 is taken from the data in the shown energy range.

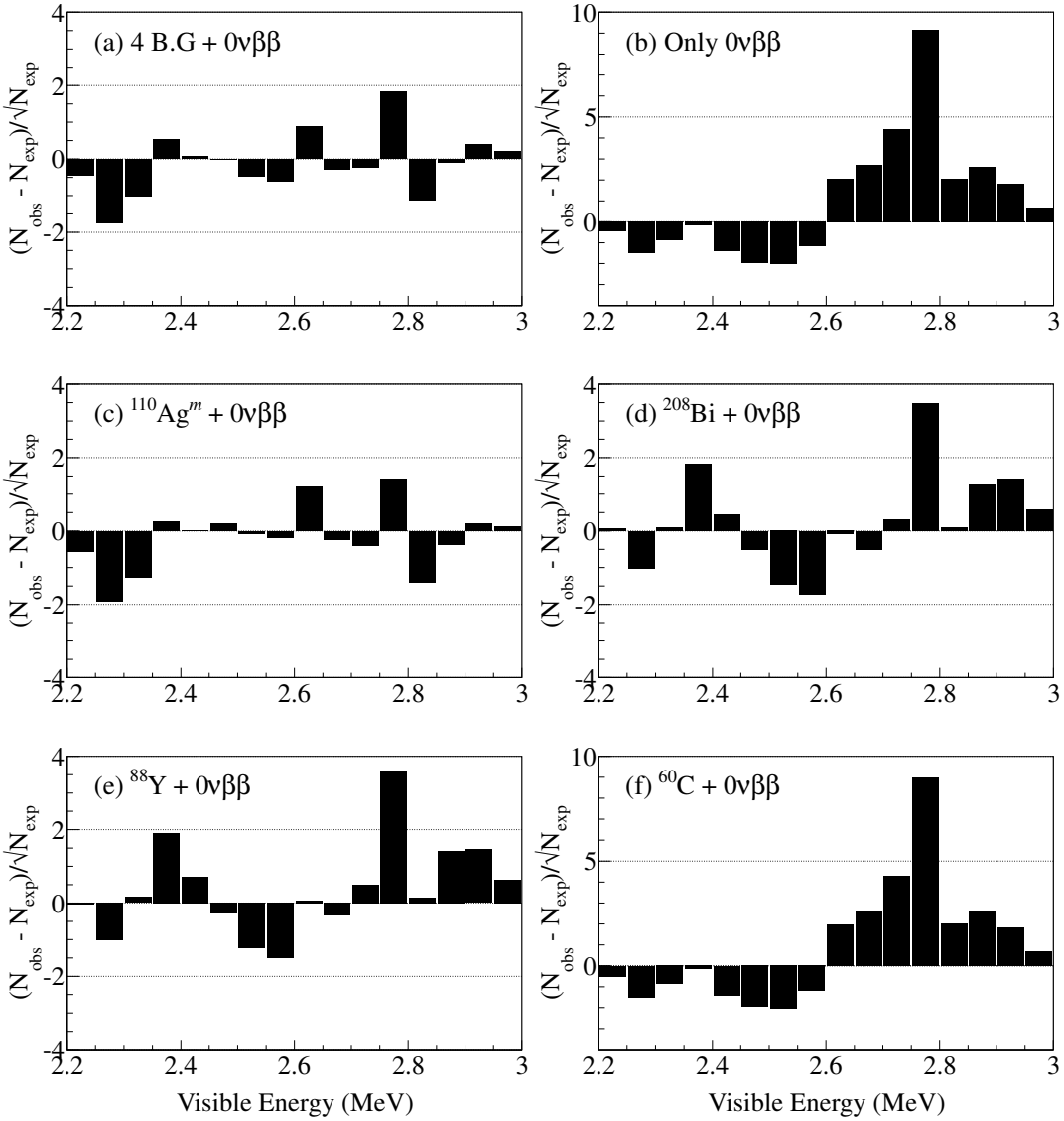

Figure 6.12: Residuals of Figure 6.11 (a)−(f) ($2.2 < E < 3.0$ MeV). (a) $0\nu\beta\beta$ + 4 backgrounds remained from ENSDF search. (b) Assuming only $0\nu\beta\beta$ exists in this region. (c)-(f) Assumption of one background and $0\nu\beta\beta$ existed, for comparison. For (b) and (f), different y-axis scale is adopted due to its big residuals.

Event rate in $2.2 < E < 3.0$ MeV shows little time variation as shown in Fig. 6.13. It limits a ^{88}Y contribution to a small amount if the parent ^{88}Zr ($T_{1/2} = 83$ days) is absent. ^{110}Ag^m has a relatively short half-life (250 days,) compared to ^{208}Bi. However, it does not have enough statistical power to distinguish them due to the small statistics. It has a χ^2/d.o.f. = 32.2/31, 32.6/31 and 36.0/31 for ^{110}Ag^m, ^{208}Bi and ^{88}Y, respectively.

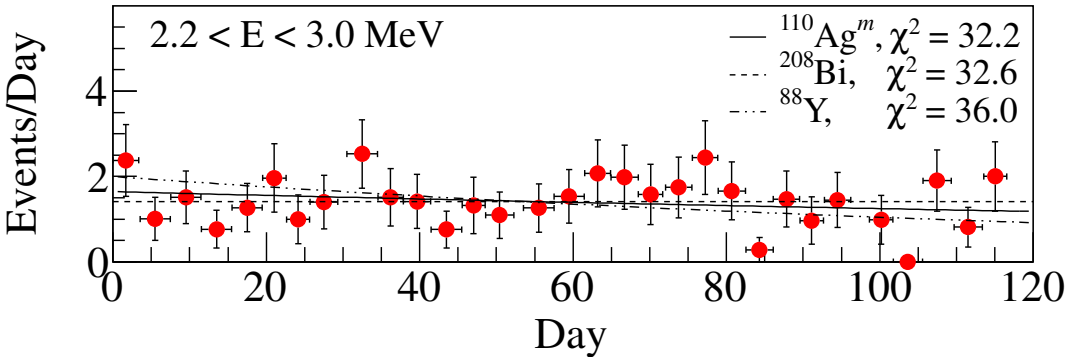

Figure 6.13: Event rate time variation in $2.2 < E < 3.0$ MeV. Fitted lines correspond to the expected time variation assuming all the events in this energy window are explained from one background candidate.

6.5.2 Cosmogenic spallation at aboveground

The spallation products whose half-lives are less than 30 days are already discussed in Section 6.3.3, and it is revealed to be negligible. In this section, then, we discuss the long-lived (half-life is more than 30 days) 2.6 MeV peak generated from the ^{136}Xe cosmogenic spallation at aboveground. Our xenon was enriched in Russia and the gas bottles were sent to Japan by airplane. At the airplane altitude, the cosmic-ray flux is ∼100 times higher than the sea level. It may bring the backgrounds in xenon. Actually, aboveground spallation products are found in other experiments like ^{57}Co, ^{54}Mn, ^{68}Ge, ^{65}Zn and ^{60}Co from the ^{76}Ge experiment [92] and ^{110}Ag^m and ^{106}Ru from the ^{116}Cd experiment [93]. It is difficult to estimate the amount of background quantitatively due to transportation loss in the gas system. Then we evaluate what kind of isotopes can remain in the xenon gas. To estimate the background, we assume xenon gas stored on surface for 100 days (= X) and then stored in the mine for 0, 100, 300 and 500 days (=Y), respectively. 100 days on the surface corresponds to one day airplane trip with ∼100 times higher cosmic-ray flux. On the surface, cross-section of ^{136}Xe + 1 GeV proton [90] is applied, while in the mine, spallation rate is assumed to be 10^{-5} smaller than those on the surface. The energy spectra of remnant radioactivities after X+Y days arechecked. Four energy spectra are shown in Fig. 6.14, and it revealed that ^{88}Y and ^{110}Ag^m remain around 2.6 MeV.

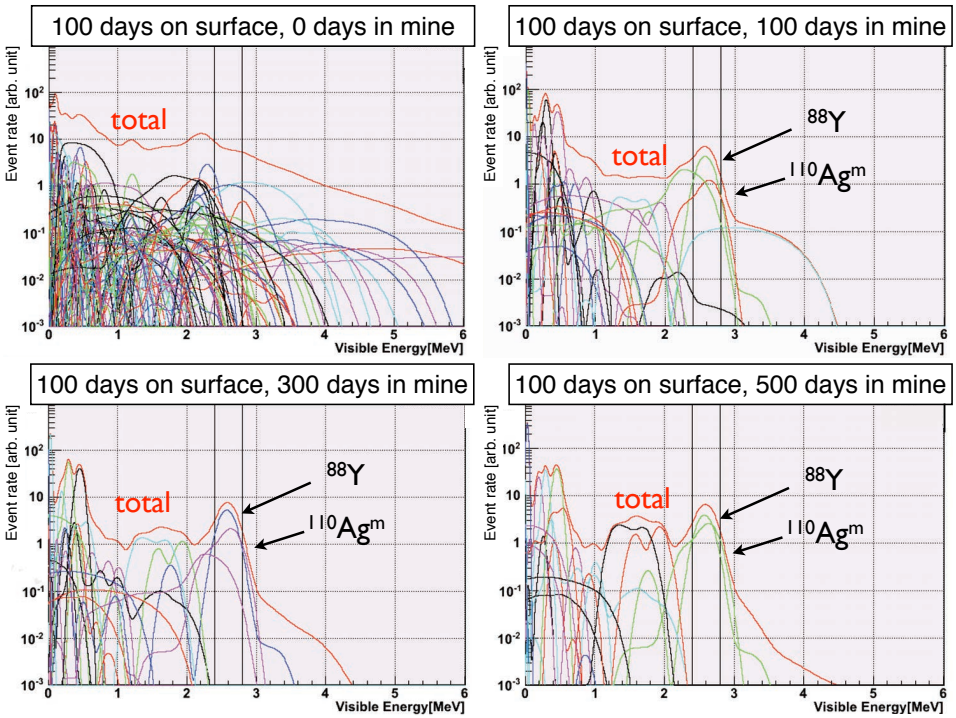

Figure 6.14: Energy spectra of remnant radioactivities. Note that histogram color correspond to each isotope are different in each picture.

6.6 Background summary

6.6.1 Discussion of 2.6 MeV peak

The candidates of 2.6 MeV peak are only 4 nuclei that ^{60}Co, ^{88}Y, ^{208}Bi and ^{110}Ag^{m} obtained from the ENSDF data search. Contamination route will be categorized to three that (1) incorporate/attached in/on the IB, (2) contained in the Xe-LS (Xe system), and (3) generated from spallation. For example, fallout radioactivities are contained in (1), while cosmogenic spallation at aboveground is classified in (3). From a standpoint of the result of the spectrum fitting and the contamination route, we summarize possibilities of the existence of each isotope.

^{110}Ag^{m} and ^{60}Co

Currently, the presence of ^{110}Ag^{m} is the most preferable from the energy spectrum fitting. The contamination route can be supported from (1) and/or (3). In contrast, ^{60}Co is strongly constrained from the spectral fitting.

^{208}Bi

From (2), we can constrain the possibility of the main contribution of ^{208}Bi. To check (2), we did impurity analysis with ICP-MS. Checked items are (i) a 50-nm

filter used in the Xe-system, (ii) a Xe contained bottle, and (iii) the Xe-LS without Xe. Measured values are summarized in Table. 6.6. From the filter and the Xe

Table 6.6: Results of impurity analysis. Unit of the filter and the Xe bottle is [ng].

	^{209}Bi	^{205}Tl	^{100}Mo	^{93}Nb	^{90}Zr	^{107}Ag
Filter (50nm)†	48	<5	2,100	<500	<500	2,300
Xe bottle†	40	<5	<100	<100	<100	<100
Xe-LS (no Xe)	<10 ppt	<10 ppt				

† Detection efficiency is not taken into account.

bottle, ^{209}Bi is detected. ^{209}Bi is the most stable and popular isotope in all kinds of bismuth, and its natural abundance is almost 100%. If these ^{209}Bi is transferred to the Xe-LS, it needs ∼1 ppb concentration of ^{209}Bi in the Xe-LS to explain current background level, since the activity of ^{208}Bi is estimated to be 1.8 mBq/g (^{209}Bi) [94]. The amount of ^{209}Bi in the Xe-LS is measured but only the upper limit, 10 ppt was obtained. Thus, we can conclude that a possibility of ^{208}Bi in the Xe-LS supplied from the Xe-system or Xe is difficult.

If ^{208}Bi is produced in the past atmospheric nuclear tests and included in the Xe-LS, another radioactive bismuth isotope ^{207}Bi (EC decay, $\tau = 45.5$ yr, $Q = 2.40$ MeV) will also be obtained from the Xe-LS. The activity ratio of ^{208}Bi to ^{207}Bi will range from 0.001 to 0.017 [95]. However, we obtain only the upper limit of ^{207}Bi as 0.12 (ton·day)$^{-1}$, and it is inconsistent with the referred value. Therefore, the possibility that ^{208}Bi production solely explained the 2.6 MeV background by nuclear tests is ruled out. As a result, the existence of environmental/artificial ^{208}Bi is strongly constrained.

^{88}Y

Currently, the existence of ^{88}Y is not strongly constrained or supported. The contamination route can be supported from (3). Event rate time variation in $2.2 < E < 3.0$ MeV and the energy spectrum fitting cannot conclude that ^{88}Y is excluded. Event rate time variation with more statistics will make clear the contribution of ^{88}Y since it has the shortest half-life (107 days) in four remained backgrounds.

6.6.2 Background summary

In Table 6.7, all backgrounds discussed above are summarized.

Table 6.7: Summary of the backgrounds in the fiducial volume.

Isotope		Event rate $(\text{ton}\cdot\text{day})^{-1}$
External (Radioactivities in the IB)		
^{238}U series	^{222}Rn-^{210}Pb	$(3.20 \pm 0.31) \times 10^{-2}$
^{232}Th series	^{228}Th-^{208}Pb	$(3.49 \pm 0.25) \times 10^{-2}$
	^{40}K	0.242 ± 0.133
	^{134}Cs	0.492 ± 0.057
	^{137}Cs	0.332 ± 0.050
Residual radioactivities in the Xe-LS		
^{238}U series	^{238}U-^{222}Rn (^{234}Pa)	<1.17
	^{222}Rn-^{210}Pb	3.40 ± 017
^{232}Th series	^{232}Th-^{228}Th (^{228}Ac)	<0.45
	^{228}Th-^{208}Pb	0.548 ± 0.055
	^{85}Kr	200 ± 7.3
	^{210}Bi	101 ± 2.9
	^{40}K	<8.5
	^{134}Cs	<0.25
	^{137}Cs	<0.94
Spallation products from ^{12}C †		
	^{10}C	$(2.16 \pm 0.43) \times 10^{-2}$
	^{11}C	0.999 ± 0.014
Spallation products from xenon with lifetime < 100 s		
1.2 MeV < E < 2.0 MeV		< 0.27
2.2 MeV < E < 3.0 MeV		< 7.7 $\times 10^{-3}$
Around ^{136}Xe $0\nu\beta\beta$ (ENSDF search)		
^{60}Co, ^{88}Y, ^{110}Ag^m and ^{208}Bi		0.20 ± 0.03
Potential backgrounds from fallout		
^{134}Cs, ^{137}Cs, ^{110}Ag^m		listed above
^{129}Te^m, ^{95}Nb, ^{90}Y, ^{89}Sr		negligible

Note. ^{134}Xe $\beta\beta$ contribution is expected to be negligible because of much smaller phase space factor and isotopic abundance relative to ^{136}Xe. The backgrounds from nuclear reactions such as (α, γ) and (α, $\alpha\gamma$) are expected to be negligible due to their small cross sections. The rate of (n, γ) is stringently constrained from the data.

† Other spallation products are negligible [88].

Chapter 7

Analysis

7.1 Live time calculation

The total live time of this double beta decay analysis is 112.3 days, collected between October 12, 2011 and February 9, 2012 (run011000-011212).

The live time is defined as the sensitive time of the detector for neutrino observation. Only normal (physics) run with good condition is used for an analysis, while calibration, hardware/software maintenance and other bad periods are not included (run selection is summarized in Section 5.2). The live time is calculated from every single run with run time, dead time and veto time. These period's lengths are determined by the timestamp of the first and the last event counted by 40 MHz clock synchronized with GPS system. Each period and calculation method are summarized in the following sections.

7.1.1 Explanation of each period

Run Time

Run time is defined as a data taking period between the first and last recorded event. In this analysis, the number of physics runs is 147, and a total run time except for bad run is 113.4 days. The uncertainty is estimated to be ∼7 msec coming from the ∼140 Hz of trigger rate in the inner detector. This corresponds to 8×10^{-6}% for a typical 24 hours run time.

Dead time

Dead time is categorized into the following 4 types;

- Bad run
  The data quality is poor for use for an analysis throughout the run. These runs are discarded for a whole period.

- Bad period (Half bad run)
  If a part of run is classified to be a bad period, but the rest is normal, the run is categorized into a half bad run. Generally, HV supply failure for a certain

crate triggers bad periods. Only a bad period is classified as a dead time, and rest of the run is used in the analysis.

- Trigger disable/dead period
  The disable trigger flag is sometimes recorded in the data due to busy trigger module. It lasts for a few milli seconds. This period is classified as a dead time. Another possible dead time related to triggers is broken data packets due to the network trouble. This trigger dead period is tagged by the large time interval more than 100 msec between events.

- Noisy period (missing muon) and missing waveform
  The multiple noise events are sometimes caused by muons within 150 μsec along with a ringing on the FEE baseline. There can be also cluster of noise events but no related muon observed in the data due to unknown dead time. These events are called "missing muon" and tagged if multiple noise events preceded by no muons within 1 msec. This period is conservatively taken to be a dead time . In addition, missing waveform events (detail described in Chapter 5) are vetoed for 2 msec or 2 sec depending on the value of NsumMax (more than 200 and 1200, respectively).

Uncertainty of dead time

The uncertainty of dead time is estimated from 1 pps trigger since this forced acquisition trigger is issued every second to synchronize with GPS module except for during supernova trigger issued. Thus, the following expression holds ideally.

$$\text{(Number of 1 pps trigger)} = \text{(run time)} - \text{(dead time)} \tag{7.1}$$

Then, the unknown deadtime ratio is estimated by the following expression.

$$\text{ratio} = \left| 1 \; - \; \frac{\text{Number of 1 pps trigger} \; \times \; 1 \text{ sec}}{\text{(run time)} - \text{(dead time)}} \right| \tag{7.2}$$

Fig. 7.1 shows the ratio of unknown dead time for each good runs. The average ratio for all good runs is 0.0017%.

Veto time Veto time is a period to reject the background(s).

- 2 msec veto after muon
  Whole volume of the detector is vetoed for 2 msec after muon events. Muon selection is described in Section 4.5. Veto time corresponds to 0.07% of the total run time owing to the muon rate (0.35 Hz).

- Delayed coincidence veto
  As explained in Section 5.4 and 5.5, if a delayed event has time-space correlated prompt event within the certain energy window, these events are vetoed for a certain time window. For the anti-neutrino veto, veto time is 1 msec and for the Bi-Po selection, veto time is 3 msec. Introduced veto time is very small.

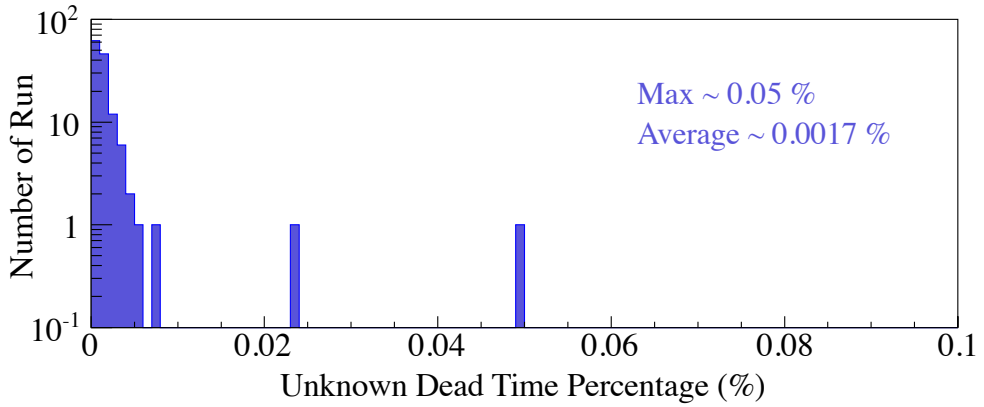

Figure 7.1: Ratio of unknown dead time.

7.1.2 Live time calculation

As written above, the live time is calculated by run time, dead time, and veto time for every run. In addition, actual live time calculation uses simple Monte Carlo simulation (MC) in order to consider the overlap of each veto in time and volume. The generated MC events uniformly distribute uniformly in the fiducial volume and run time. The ratio of live time to run time is given by the following relation.

$$\frac{\text{LiveTime}}{\text{RunTime}} = \frac{\text{The number of events in FV after applying all cuts}}{\text{Tne number of events in FV}} \tag{7.3}$$

The uncertainty of this calculation is dominated by the statistics of the generated events. About 10^7 events are generated for a typical one day run, and the vetoed events are about 1% of those. The error for the ratio of vetoed events to the total generated events is estimated to be 3.0×10^{-5}, therefore the uncertainty of the calculation is 0.003%. Fig. 7.2 shows the ratio of live time to run time as

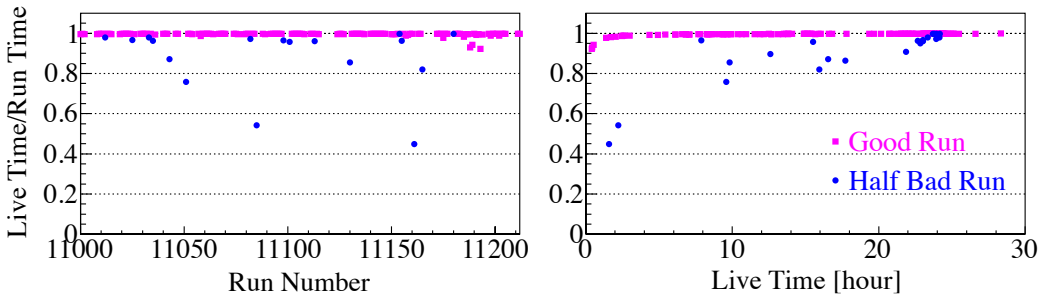

Figure 7.2: Ratio of live time to run time as a function of run number (left) and live time (right). The magenta squares show the good runs and blue circles show half bad runs. The average ratio of live time to run time for this analysis period is estimated to be ∼99%.

a function of run number and live time for every good and half bad runs. As was mentioned at the beginning of this section, the total live time is calculated to be 112.3 days from October 12, 2011 to February 9, 2012 with 147 of good and half bad runs (run011000−011212). Total live time uncertainty is addressed with a quadratic sum of uncertainties of run time (8×10^{-6}%), dead time (0.0017%) and calculation (0.003%) to be 0.003%.

7.2 Fiducial volume

Fiducial volume (1.2-m-radius) is selected to mitigate backgrounds from IB material. Fig. 5.14 in Chapter 5 and Fig. 6.1 (a) and (b) in Chapter 6 show $\theta - \phi$ distribution and radial distribution, respectively. In this fiducial volume, the ratio of signal to noise in $2\nu\beta\beta$ region ($1.2 < E < 2.0$ MeV) is more than 10, and we can see clear $2\nu\beta\beta$ decay spectrum.

The Xe-LS volume in the fiducial region is 7.24 m^3, simply calculated with geometrical sphere. The volume ratio of the fiducial volume to the total volume, $R_{\rm volume}$, is 0.438 ± 0.005, where the total volume was measured by the flow meter to be (16.51 ± 0.17) m^3 during the Xe-LS filling.

To estimate the fiducial volume fraction coming from errors of vertex reconstruction, the event counting ratio of ^{214}Bi is also calculated from its vertex distribution (Fig. 7.3). ^{214}Bi was supplied from introduced ^{222}Rn during the de-

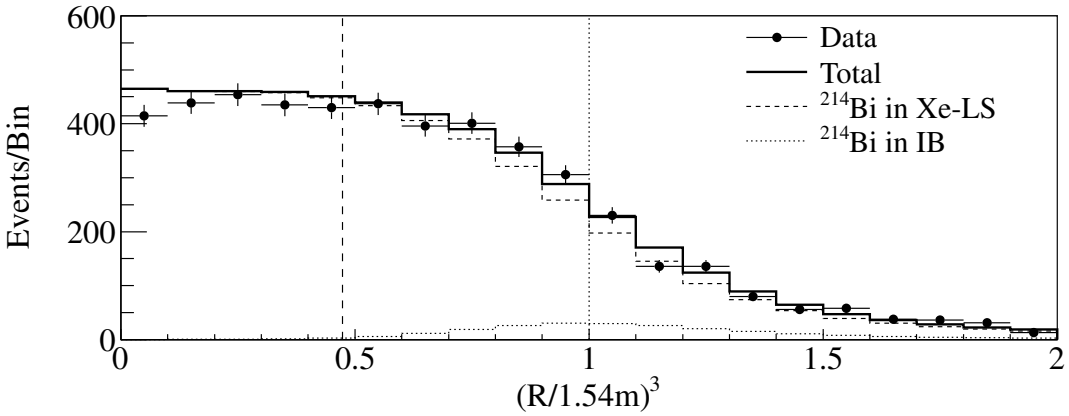

Figure 7.3: Vertex distribution of ^{214}Bi.

tector modification. Its uniform distribution in the Xe-LS is already shown in Fig. 4.22 (bottom) in Chapter 4. The number of ^{214}Bi events in the Xe-LS is evaluated from delayed coincidence method with delayed energy ($0.4 \leq E_d < 1.2$ MeV), space correlation (dR $<$ 100 cm) and time correlation ($5 \leq$ dT $<$ 1,000 μsec). In the calculation, counted ^{214}Bi should be only included in the Xe-LS. Then the IB surface contribution is subtracted first and its uncertainty is included to the volume ratio uncertainty. The number of ^{214}Bi events in the IB is estimated from radial distribution with the latter period of data. The difference of data and simulation around the IB center is also considered as statistical uncertainty. From the distribution, the event counting ratio of ^{214}Bi, $R_{\rm count}$ is estimated

to be $0.423 \pm 0.007(\text{stat}) \pm 0.004(\text{syst})$. The discrepancy between these ratios are R_{volume}-$R_{\text{count}} = 0.015 \pm 0.007(c, \text{stat}) \pm 0.004(c, \text{syst}) \pm 0.005(v, \text{syst})$, where c means count and v means volume. As whole discrepancy is considered to be fiducial volume error, σ, we obtain $\sigma = (0.015 + 0.007) \oplus 0.004 \oplus 0.005 = 0.0223$, where $\oplus$ denotes quadratic sum. This value correspond to the 5.2% systematic error on the fiducial volume.

7.3 Number of target

The number of xenon target for ^{136}Xe double-beta decay is evaluated from the components of the Xe-LS and its density. As described in Section 3.4, the Xe-LS consists of the followings.

- Decane ($C_{10}H_{22}$), 82% by volume.
- Psesudocumene (C_9H_{12}), 18% by volume.
- PPO ($C_5H_{11}NO$), 2.7 g/l.
- Enriched xenon, 2.44 % by weight.
  The isotopic abundances; 90.93% (^{136}Xe) and 8.89% (^{134}Xe).
- Density 0.78013 g/cm^3 at 11.5 °C.

In the 1.2-m-radius fiducial volume (7.24 m^3), corresponding amount of ^{136}Xe is 125 kg. The number of ^{136}Xe target is estimated to be 5.56×10^{26} with mass number (= 135.722) and Avogadoro's number (= 6.02×10^{23}). The mass number is evaluated from the measurement of enriched xenon gas with residual gas analyzer.

Uncertainty of the xenon amount comes from isotopic abundance of enriched xenon and its concentration in the liquid scintillator. The isotopic abundance is measured by residual gas analyzer, and its uncertainty is estimated to be 0.05%. The xenon concentration is estimated by two approaches. One is gas chromatography measurement. It provides the ^{136}Xe concentration as (2.52 ± 0.07)% by weight. Another one is based on the total xenon weight and liquid scintillator volume, which actually introduced into the IB during the filling. Introduced xenon amount is calculated from weight scale, and volume of liquid scintillator is measured by the flow meter. It provides a much more precise estimation to be (2.44 ± 0.01)% by weight. From weighted average of those, the ^{136}Xe concentration is evaluated to be (2.44 ± 0.01)% by weight and its uncertainty is 0.34%.

7.4 Systematic uncertainty

Systematic uncertainties are summarized in Table 7.1. The dominant contribution comes from the fiducial volume uncertainty (5.2%) as shown in Section 7.2. It will be improved by enlargement of the fiducial volume and the source calibration inside the IB with new miniCAL system. Other systematic uncertainty comes from enrichment of ^{136}Xe (0.05%), Xe concentration (0.34%), detector energy scale (0.36%), Xe-LS edge effect (0.06%), and detection efficiency (0.2%). Xenon related uncertainties

are already described in the previous section. Detector energy scale is shown in later. Xe-LS edge effect comes from the events near the IB surface. These events deposit their energy both in the Xe-LS and KamLAND-LS. Its contribution to the systematic error is evaluated by Monte Carlo simulation. The detection efficiency is estimated from event selection. Total systematic uncertainty is evaluated to 5.2% from the quadratic sum of individual contribution.

Table 7.1: Systematic uncertainties evaluated for ^{136}Xe $2\nu\beta\beta$ decay half-life measurement. Total uncertainty is 5.2%.

Source	Uncertainty
Live Time	0.003%
Fiducial Volume	5.2%
Enrichment of ^{136}Xe	0.05%
Xe Concentration	0.34%
Detection Efficiency	0.2%
Detector Energy Scale	0.36%
Xe-LS Edge Effect	0.06%
Total	5.2%

7.5 Spectral fit

7.5.1 Spectral fit

The decay rate of ^{136}Xe double-beta decay is estimated from likelihood fit to the binned energy distribution between 0.5 and 4.8 MeV. Although the event selection and backgrounds are already described in Chapter 5 and 6, respectively, we again remarks that the selected events are in the 1.2-m-radius fiducial volume, and an exposure of ^{136}Xe is 38.6 kg·yr. The $2\nu\beta\beta$, $0\nu\beta\beta$ decays, and backgrounds are fitted simultaneously. It searches for the minimum of χ^2 with 17 free parameters, 8 constrained parameters and 3 energy scale (constrained) parameters. It is summarized in Table 7.2. A χ^2 is defined as follows;

$$\chi^2 = \chi^2_{energy} + \chi^2_{time} + \chi^2_{penalty}, \tag{7.4}$$

where, χ^2_{energy} is obtained from the number of events in each energy bin (86 bins), χ^2_{time} is calculated with each run's events in $0\nu\beta\beta$ window ($2.2 < E < 3.0$ MeV), and $\chi^2_{penalty}$ is evaluated from 8 constrained backgrounds and 3 energy scale parameters. A χ^2_{energy} is defined with n_i (the number of observed events in i-th energy bin) and ν_i (the number of expected events in i-th energy bin) as follows;

$$\chi^2_{energy} = \begin{cases} 2 \times \sum_i [\nu_i - n_i + n_i \log(\mathrm{n_i}/\nu_\mathrm{i})] & (n_i \neq 0) \\ 2 \times \sum_i [\nu_i - n_i] & (n_i = 0). \end{cases} \tag{7.5}$$

The χ^2_{time} is evaluated from events in $2.2 < E < 3.0$ MeV energy region. Relevant isotopes for this calculation are ^{136}Xe $0\nu\beta\beta$ decay, ^{110}Ag^m, ^{208}Bi, ^{88}Y, ^{60}Co and ^{238}U

Table 7.2: Fit parameters.

		Unconstrained parameters	Constrained parameters
Signal		$2\nu\beta\beta$ decay	
		$0\nu\beta\beta$ decay	
Background	(Externals)	^{40}K	^{222}Rn-^{210}Pb
			^{228}Th-^{208}Pb
			^{137}Cs, ^{134}Cs
	(Xe-LS)	^{238}U-^{222}Rn (^{234}Pa)	^{222}Rn-^{210}Pb
		^{232}Th-^{228}Th (^{228}Ac)	^{228}Th-^{208}Pb
		^{85}Kr, ^{210}Bi, ^{40}K, ^{207}Bi	
		^{60}Co, ^{88}Y, ^{110}Ag^m, ^{208}Bi	
		^{129}Te^m, ^{95}Nb, ^{90}Y, ^{89}Sr	
	(Spallation)		^{10}C, ^{11}C
Energy scale			α, k_B, r

decay series (^{222}Rn-^{210}Pb) from the IB. With m_j (the number of observed events in run j) and μ_j (the number of normalized expected events in run j considering half life of each isotope), χ^2_{time} is defined as,

$$\chi^2_{time} = \begin{cases} 2 \times \sum_j [\mu_j - m_j + m_j \log(\mathrm{m_j}/\mu_\mathrm{j})] & (m_j \neq 0) \\ 2 \times \sum_j [\mu_j - m_i] & (m_j = 0). \end{cases} \tag{7.6}$$

The $\chi^2_{penalty}$ is calculated from observed event rate ($\mathrm{r_{obs}}$), expected event rate ($\mathrm{r_{exp}}$) and error of expected event rate ($\mathrm{r_{exp\_err}}$) as

$$\chi^2_{penalty} = [(\mathrm{r_{obs}} - \mathrm{r_{exp}})/\mathrm{r_{exp\_err}}]^2. \tag{7.7}$$

Backgrounds from decay chains of ^{222}Rn-^{210}Pb and ^{228}Th-^{208}Pb in the Xe-LS, spallation products ^{10}C and ^{11}C, contribution from the IB such as decay chains of ^{222}Rn-^{210}Pb and ^{228}Th-^{208}Pb, ^{134}Cs and ^{137}Cs are allowed to vary in the fit, but constrained by each estimated rate. Uncertainties of 3 energy scale parameters are constrained from ^{208}Tl calibration and radon-induced ^{214}Bi data. Other events, such as $2\nu\beta\beta$ signals, contribution from the Xe-LS such as ^{210}Bi ^{85}Kr, possible contamination from fallout such as ^{129}Te^m, ^{95}Nb and 4 nuclei searched from ENSDF (^{110}Ag^m, ^{208}Bi, ^{88}Y and ^{60}Co) are unconstrained in the fit.

7.5.2 Decay rate of ^{136}Xe $2\nu\beta\beta$ and limit on ^{136}Xe $0\nu\beta\beta$

The result of the fit is presented in the Figure 7.4 (top) with best-fit components. Its residuals calculated by the number of observed events (N_{obs}) and the number of expected events[1] (N_{exp}) is also shown in Fig. 7.4 (bottom). Almost all points are within $\pm 2\sigma$ except for around 3 MeV, less statistical region. Residuals of penalty

[1] In the energy spectrum, it is denoted as "Total".

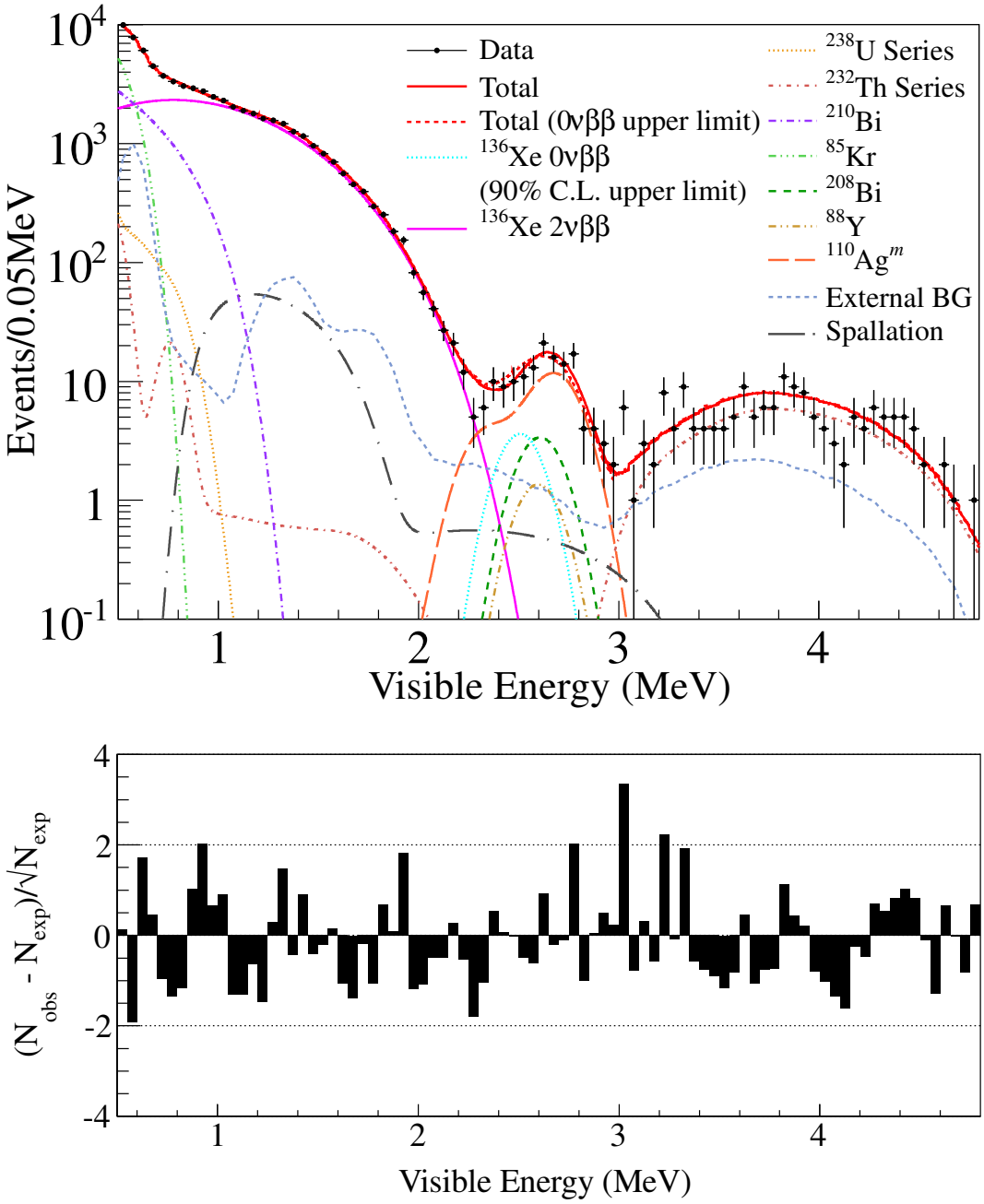

Figure 7.4: (top) Energy spectrum of ^{136}Xe $2\nu\beta\beta$ decay (solid magenta line) and best fit backgrounds in $0.5 < E < 4.8$ MeV. The 90% C.L. upper limit of $0\nu\beta\beta$ decay is also shown with cyan dotted line in $2.2 < E < 2.8$ MeV.
(bottom) Those residuals calculated by the number of observed event ($N_{\rm obs}$) and the number of expected events ($N_{\rm exp}$). Horizontal axis (visible energy) is correspond to the energy spectrum shown in above. Almost all points are within $\pm 2\sigma$ except for around 3 MeV, less statistical region.

(constrained) paramters of 8 backgrounds calculated from observed events, expected events and error of expected events are shown in Fig. 7.5. All of them are within $\pm 2\sigma$.

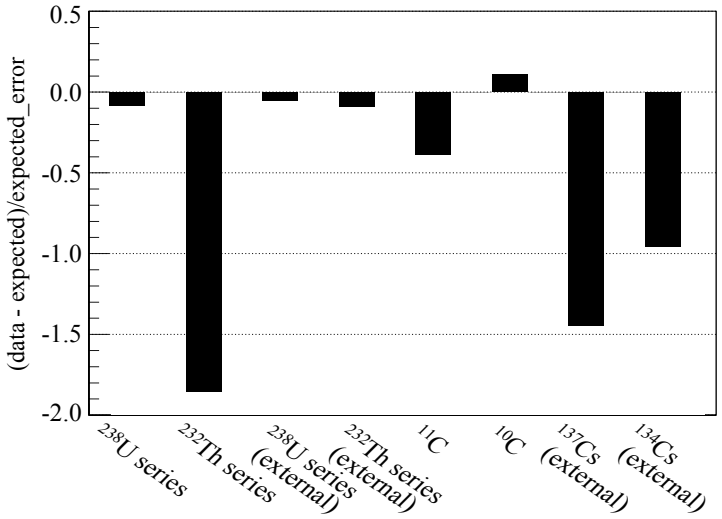

Figure 7.5: Residuals of penalty parameters of 8 backgrounds. In the external and Xe-LS backgrounds, ^{222}Rn-^{210}Pb denotes as ^{238}U series and ^{228}Th-^{208}Pb denotes ^{232}Th series. All of them are within $\pm 2\sigma$.

Decay rate of ^{136}Xe $2\nu\beta\beta$

The expected energy spectrum of the ^{136}Xe $2\nu\beta\beta$ decay is calculated from Ref. [96] and it is indicated with magenta solid line. It has good S/N ratio and we can see very clear $2\nu\beta\beta$ spectrum. Totally 80% of ^{136}Xe $2\nu\beta\beta$ spectrum is in the fitting range and the best-fit number of the decay is $(5.16 \pm 0.04) \times 10^4$, which corresponds to an event rate of 81.3 ± 0.6 (ton·day)$^{-1}$. It has a χ^2/d.o.f. = 100.4/87, obtained from comparison of the binned data and the best fit expectations. Stability of the number of events in $1.2 < E < 2.0$ MeV is shown in Fig. 7.6.

Energy uncertainty

The energy uncertainty ($\Delta_{\rm energy}$) is included in the spectral fitting. The uncertainty of the fit ($\Delta_{\rm fit}$) is expressed with quadratic sum of energy uncertainty and statistical uncertainty ($\Delta_{\rm stat}$) as, $\Delta^2_{\rm fit} = \Delta^2_{\rm stat} + \Delta^2_{\rm energy}$. Then the systematic uncertainty coming from the energy estimation is evaluated from fixed energy related parameters (scaling parameter, Birk's constant and ratio of scintillation photons to Cherenkov photons). When these three parameters fixed, obtained rate of ^{136}Xe $2\nu\beta\beta$ decay is 81.116 ± 0.519 (ton·day)$^{-1}$ and its error corresponds to 0.64%. On the contrary, observed rate (shown in above paragraph) is 81.294 ± 0.597 (ton·day)$^{-1}$ and 0.73%. Then the uncertainty of energy is calculated to be 0.295 (ton·day)$^{-1}$ or 0.36%.

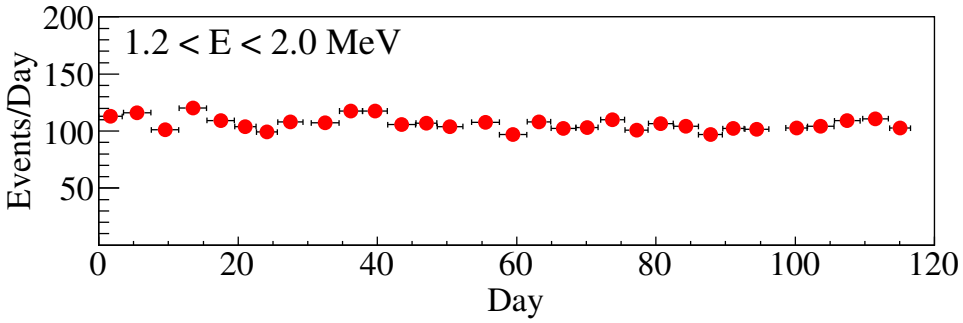

Figure 7.6: Time variation of events in the fiducial volume and in the energy range 1.2< E <2.0 MeV

Limit on ^{136}Xe $0\nu\beta\beta$ decay rate

As shown in Fig. 7.7, in the $0\nu\beta\beta$ region, the 2.6 MeV peak is fitted with 4 nuclei (^{110}Ag^m, ^{208}Bi, ^{88}Y and ^{60}Co) selected from ENSDF search. Combined background decay rate is 0.20±0.03 (ton·day)$^{-1}$, and ^{110}Ag^m indicated with orange dotted line is the most dominated in this region. The breakdowns of each isotope are 0.159, 0.029, 0.012, and 6.4 $\times 10^{-4}$ (ton·day)$^{-1}$ for ^{110}Ag^m, ^{208}Bi, ^{88}Y and ^{60}Co, respectively. In the simultaneous fitting, $0\nu\beta\beta$ decay rate becomes zero. The 90% C.L. upper limit of $0\nu\beta\beta$ decay is estimated from $\Delta\chi^2$ compared with the best fit spectrum. Then, limit is estimated to < 19 events in this data-set, and corresponding event rate is 0.03 (ton·day)$^{-1}$. Stability of the number of event in 2.2 < E < 3.0 MeV is already shown in Fig. 6.13.

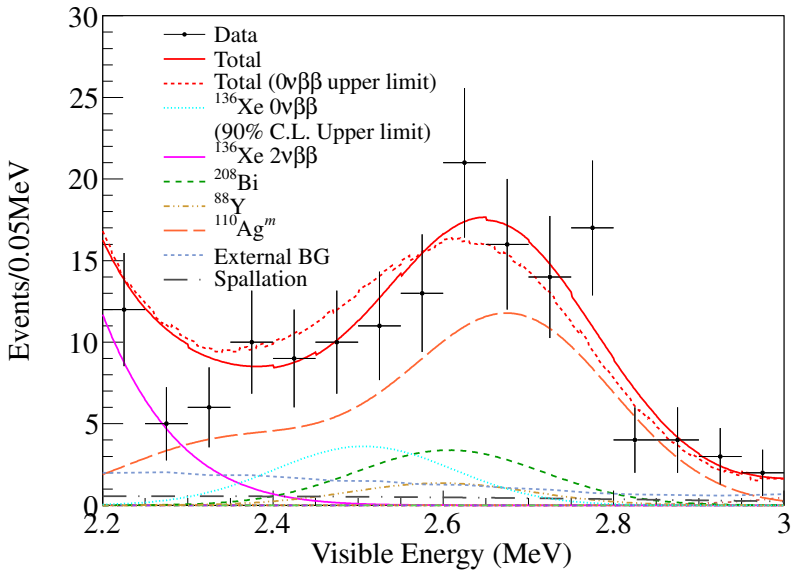

Figure 7.7: Close up of Figure 7.4 for 2.2 < E < 3.0 MeV. The 90% C.L. upper limit of $0\nu\beta\beta$ decay is indicated together. Red dotted line is total spectrum with those $0\nu\beta\beta$ events.

Chapter 8

Discussion and conclusion

The KamLAND-Zen results of ^{136}Xe $2\nu\beta\beta$ and $0\nu\beta\beta$ decays in an exposure of 112.3 days with 125 kg of ^{136}Xe (38.6 kg·yr) are presented.

8.1 Half-life and nuclear matrix element of ^{136}Xe $2\nu\beta\beta$ decay

Half-life of $2\nu\beta\beta$ decay

The observed rate of ^{136}Xe $2\nu\beta\beta$ decay is 81.3 ± 0.6 (ton·day)$^{-1}$, where the mass-unit ton refers to the amount of liquid scintillator. From this result, the half-life is measured to be

$$T^{2\nu}_{1/2} = 2.30 \pm 0.02(\text{stat}) \pm 0.12(\text{syst}) \times 10^{21} \text{ yr},$$

where the statistical and systematic uncertainty is 0.74% and 5.2%, respectively. It is the longest half-life among the direct $2\nu\beta\beta$ decay measurements of the various double-beta decay isotopes. This result is consistent and slightly improves the uncertainty with the previous (first published) result of KamLAND-Zen with 26.6 kg·yr exposure [97],

$$T^{2\nu}_{1/2} = 2.38 \pm 0.02(\text{stat}) \pm 0.14(\text{syst}) \times 10^{21} \text{ yr}.$$

Only a lower limit of half-lives of ^{136}Xe $2\nu\beta\beta$ decay was measured before 2011. The most stringent limit was reported by the DAMA experiment in 2002 as $T^{2\nu}_{1/2} > 1.0 \times 10^{22}$ yr at 90% C.L. [49]. In 2011, the EXO-200 experiment reported the first measured half-life to be $T^{2\nu}_{1/2} = 2.11 \pm 0.04(\text{stat}) \pm 0.21(\text{syst}) \times 10^{21}$ yr [98], and this value was recently updated to be $T^{2\nu}_{1/2} = 2.23 \pm 0.017(\text{stat}) \pm 0.22(\text{syst}) \times 10^{21}$ yr [52]. There is almost a factor of five discrepancy between the DAMA and the EXO-200 results.

KamLAND-Zen provides an improved measurement of the ^{136}Xe $2\nu\beta\beta$ decay half-life. The most precise result is consistent with the results of EXO-200, and supports the conclusion that the directly measured half-life is significantly below the lower limit reported by the earlier experiments. Figure 8.1 summarizes the measured half-lives of ^{136}Xe $2\nu\beta\beta$ decay. A precision measurement of $2\nu\beta\beta$ decay

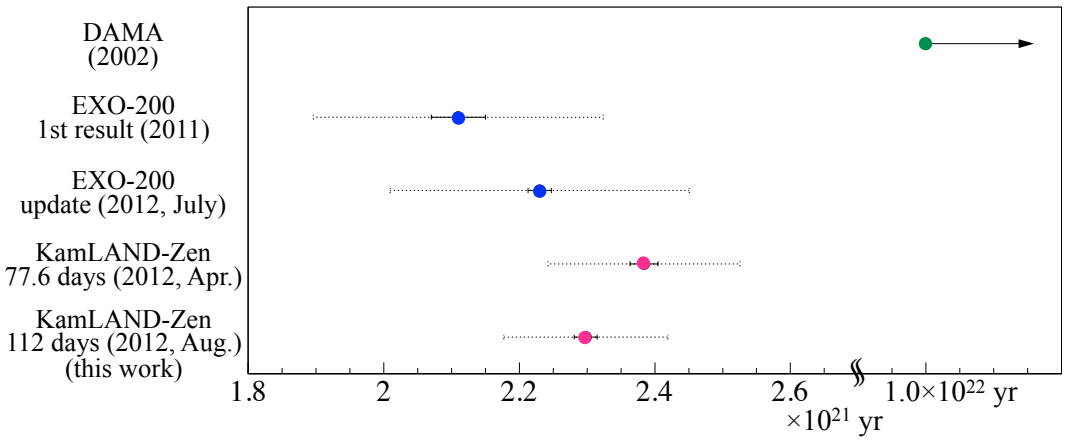

Figure 8.1: Measured half-lives of ^{136}Xe $2\nu\beta\beta$ decay. In KamLAND-Zen and EXO-200, solid bars indicate statistical uncertainties and dotted errors show the quadratic sum of statistical and systematic errors. Result of the DAMA experiment shows the lower limit of the half-life.

half-life allows a more accurate determination of the nuclear matrix element of $2\nu\beta\beta$ decay.

Nuclear matrix element

Nuclear matrix element of $2\nu\beta\beta$ decay ($M^{2\nu}$) is determined experimentally from the obtained $2\nu\beta\beta$ half-life with the following relation (reprint of Eq. 2.13);

$$(T^{2\nu}_{1/2})^{-1} = G_{2\nu}|M^{2\nu}|^2. \tag{8.1}$$

For ^{136}Xe, the phase space factor ($G_{2\nu}$) is evaluated to be $G_{2\nu} = 4.9 \times 10^{-18}$ yr^{-1} with $g_A = 1.254$ [54]. The nuclear matrix element ($M^{2\nu}$) is then

$$\begin{aligned} M^{2\nu} &= (9.42 \pm 0.25) \times 10^{-3} \cdot m_e^{-1} \\ &= (18.4 \pm 0.5) \times 10^{-3}\ \text{MeV}^{-1}, \end{aligned}$$

where m_e is the mass of electron (0.511 MeV).

The evaluated value will be used for the investigation of g_{pp} parameters of the QRPA model to improve the calculation of the nuclear matrix element of $0\nu\beta\beta$ decay ($M^{0\nu}$), which causes the largest uncertainty in determining the effective neutrino mass.

8.2 Limits on the half-life of ^{136}Xe $0\nu\beta\beta$ decay and the effective neutrino mass

No ^{136}Xe $0\nu\beta\beta$ decay signal was observed. The lower limit for the half-life (90% C.L.) is estimated from the decay rate of 3.0×10^{-2} (ton·day)$^{-1}$ to be

$$T^{0\nu}_{1/2} > 6.2 \times\ 10^{24}\ \text{yr}.$$

An upper limit on the effective neutrino mass, $\langle m_{\beta\beta}\rangle$, is obtained from the following relation (reprint of Eq. 2.15);

$$(T^{0\nu}_{1/2})^{-1} = G_{0\nu} \left|M^{0\nu}\right|^2 \langle m_{\beta\beta}\rangle^2, \tag{8.2}$$

assuming that the $0\nu\beta\beta$ transition mechanism is simply the exchange of light Majorana neutrinos. Recent shell model [40] and QRPA model (CCM SRC) [41] nuclear matrix elements are summarized in Table 8.1, together with the upper limit on the

Table 8.1: Relevant nuclear matrix elements (NME) and predicted half-lives ($T^{0\nu}_{1/2}$) used for the evaluation of effective neutrino mass. Half-lives corresponding to evaluated nuclear matrix elements assuming a certain neutrino effective mass (here, 1 eV and 50 meV) are calculated in each Reference. In Ref. [41], NME values are evaluated within QRPA and renormalized QRPA (RQRPA), with standard ($g_A = 1.254$) and quenched ($g_A = 1.0$) axial-vector couplings and with two functions of the short-range correlations. Ref. [41] remarks that these ranges quantify the uncertainty of the calculation of nuclear matrix elements.

	Shell Model [40]	QRPA (CCM SRC) [41]
NME value	1.77	1.57 - 3.24
$T^{0\nu}_{1/2}$	1.78×10^{24} yr ($\langle m_{\beta\beta}\rangle = 1$ eV)	$(1.68 - 7.17) \times 10^{26}$ yr ($\langle m_{\beta\beta}\rangle = 50$ meV)

effective neutrino mass ranges in

$$\langle m_{\beta\beta}\rangle \ < \ 0.26 - 0.54 \text{ eV (90\%C.L.)}.$$

This value is one of the best limits for $0\nu\beta\beta$ decay at the moment.

The claim of the observation of ^{76}Ge $0\nu\beta\beta$ decay gives a measured half-life $T^{0\nu}_{1/2} = 2.23^{+0.44}_{-0.31} \times 10^{25}$ yr, and the corresponding effective neutrino mass is 0.32 $\pm$ 0.03 eV [13]. If we apply the same matrix element described above (QRPA model) for this half-life, it ranges in $\langle m_{\beta\beta}\rangle$ = 0.15 - 0.39 eV at 3 sigma range. Current best limits coming from Heidelberg-Moscow (^{76}Ge) for $T^{0\nu}_{1/2} > 1.9 \times 10^{25}$ yr [36] is $\langle m_{\beta\beta}\rangle <$ 0.20 - 0.32 eV, and from EXO-200 (^{136}Xe) for $T^{0\nu}_{1/2} > 1.6 \times 10^{25}$ yr [52] is $\langle m_{\beta\beta}\rangle <$ 0.16 - 0.34 eV with the same matrix element. The claim for the observation of $0\nu\beta\beta$ decay is still controversial. However, we are only one step away to come to a conclusion.

For KamLAND-Zen, to conclude the discrepancies, background rejection of the $0\nu\beta\beta$ region and more statistics are required. Future prospects are discussed in the next section.

8.3 Future prospects

Near future

To improve the sensitivity of $0\nu\beta\beta$ decay search, removal of contaminants in the Xe-LS (especially for 2.6 MeV peak) is absolutely imperative. Thanks to the advantage of xenon, which is easily extracted from liquid scintillator, we can replace the whole volume of Xe-LS with a distilled one without pulling out the IB from the detector. Procedure is (1) extraction of xenon from the liquid scintillator by circulating Xe-LS with the Xe system, (2) replacement of the remainig liquid scintillator with dummy LS (Xe-free-LS), (3) distillation of xenon and production of a new clean liquid scintillator, and (4) replacement of dummy LS with newly purified Xe-LS. The IB keeps its shape and location in the detector, and data taking continues during these operations. It provides the condition for real-time background monitoring. A targeted value of reduction rate is 1/100 of the radioactive impurities. Combining the 80% of ^{10}C tagging with dead-time-free electronics, gives a target sensitivity of $\sim$80 meV.

In addition, future exposure including the enlargement of the fiducial volume will also improve sensitivity. In the future, the largest systematic uncertainty coming from the fiducial volume determination will be reduced by source calibrations inside of the IB.

Inverted hierarchy

For the search of neutrinoless double beta decay, to cover the inverted hierarchy is of a profound significance even if no signal is obtained. If accelerator or other experiments succeed in the determination of the mass hierarchy and it is the inverted hierarchy, non-observation of $0\nu\beta\beta$ decay will prove the Dirac nature of neutrinos.

KamLAND-Zen will start to explore the inverted hierarchy with $\sim$700 kg of xenon and a cleaner inner balloon without requiring large modifications of the detector. In this phase, the biggest background will be ^{214}Bi in the IB, and a clean balloon enables to enlarge the fiducial volume effectively. The target sensitivity is $\sim$40 meV, covering half of the inverted hierarchy. The required developments and installation method will not be much different from the current KamLAND-Zen.

To cover the inverted hierarchy completely ($\langle m_{\beta\beta}\rangle \sim 20$ meV), we need $\sim$1 ton of xenon and improved energy resolution since the tail of the $2\nu\beta\beta$ decay will become a serious background at this level. Large detector modifications will be necessary to cover the full inverted hierarchy. It will require an improved energy resolution by exchanging the liquid scintillator to a brighter scintillator and increasing the photo cathode area by, e.g., attaching Winston cones to the PMTs. The updated detector is called "KamLAND2-Zen", and the targeted sensitivity is $\sim$20 meV.

Appendix A

Majoron-emitting double-beta decay

A.1 Majoron-emitting double-beta decay

Many other mechanisms alternative to exchange of a light Majorana neutrino have been proposed. One of them is Majoron-emitting double-beta decay. Originally, a massless Nambu-Goldston (NG) boson associated with spontaneous symmetry breaking is denoted as Majoron. However, LEP showed that severe fine-tuning is required for traditional Majoron models [99]. Then, various models which avoid the fine-tuning have been proposed [100, 101]. So the term "Majoron (χ^0)" used here denotes massless or light bosons coupling with neutrinos. Some proposed Majorons are not NG bosons. Both lepton number violating and conserving Majoron-emitting double-beta decay are also considered. Majoron-emitting double-beta decay is accompanied by the one or two Majorons;

$$(A, Z) \rightarrow (A, Z+2) + 2e^- + \chi^0 \,, \tag{A.1}$$

$$(A, Z) \rightarrow (A, Z+2) + 2e^- + 2\chi^0 \,. \tag{A.2}$$

Feynman diagram of the one Majoron-emitting decay is shown in Fig. A.1. A energy

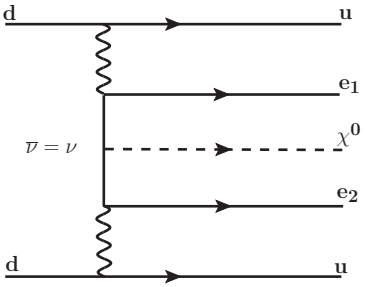

Figure A.1: Feynman diagram of Majoron-emitting double-beta decay. χ^0 stand for Majoron.

spectrum of Majoron-emitting double-beta decay becomes continuum like $2\nu\beta\beta$ decay. Its peak position is different depending on the model's spectral index, n, regardless of the features of Majorons such as their leptonic number and NG boson or not. The spectral index is defined from the phase space factor G that $G \sim (Q_{\beta\beta} - K)^n$, where $Q_{\beta\beta}$ is Q value of the double-beta decay, and K is the summed energy of electrons. A spectral index, $n = 1$, is denoted as "ordinary" Majoron emission, and $n = 5$ presents $2\nu\beta\beta$ decay.

The decay rate can translate into the effective coupling constant of the Majoron to neutrino, $\langle g_{ee} \rangle$, as follow;

$$T_{1/2}^{-1} = |\langle g_{ee} \rangle|^2 |M|^2 G \quad \text{for } 0\nu\beta\beta\chi^0 , \tag{A.3}$$

$$T_{1/2}^{-1} = |\langle g_{ee} \rangle|^4 |M|^2 G \quad \text{for } 0\nu\beta\beta\chi^0\chi^0 , \tag{A.4}$$

where M is nuclear matrix element. It is same with used for neutrinoless double-beta decay. Upper limit of $\langle g_{ee} \rangle$ is also evaluated from various double-beta decay experiments. It is summarized in Table A.1.

Table A.1: Lower limit of ordinary Majoron emitting $0\nu\beta\beta$ decay half-lives and corresponding upper limits of effective coupling constant $\langle g_{ee} \rangle$ (Q value > 2 MeV). All values are at 90% C.L.

Isotope	$T_{1/2}^{0\nu\chi^0}$, yr	$\langle g_{ee} \rangle$	Experiment	Ref.
^{76}Ge	6.4×10^{22}	8.1×10^{-5}	Heidelberg-Moscow (2001)	[36]
^{82}Se	1.5×10^{22}	$(0.66 - 1.9) \times 10^{-4}$	NEMO-3 (2006)	[102]
^{96}Zr	1.9×10^{21}	$(1.5 - 5.7) \times 10^{-4}$	NEMO-3 (2010)	[31]
^{100}Mo	2.7×10^{22}	$(3.5 - 8.5) \times 10^{-5}$	NEMO-3 (2011)	[28]
^{116}Cd	8×10^{21}	$(4.6 - 8.1) \times 10^{-5}$	Solotvina (2003)	[62]
^{130}Te	1.6×10^{22}	$(0.6 - 1.6) \times 10^{-4}$	NEMO-3 (2011)	[34]
^{136}Xe	2.7×10^{24}	$(0.8 - 1.6) \times 10^{-5}$	KamLAND-Zen (2012, this work)	[35]
	5.0×10^{23}	$(2 - 3) \times 10^{-5}$	DAMA (2002)	[49]
^{150}Nd	1.52×10^{21}	$(1.7 - 3.0) \times 10^{-4}$	NEMO-3 (2009)	[29]

A.2 Decay rate limit on Majoron emitting double-beta decay

The data-set to estimate the limit on Majoron emitting double-beta decay is same as $2\nu\beta\beta$ and $0\nu\beta\beta$ decays, as already shown in Fig. 7.4 in Chapter 7. With high statistics, four kinds of Majoron emitting double-beta decay (spectral index $n =$ 1, 2, 3, 7) are searched for. Calculated visible energy spectra in KamLAND-Zen are shown in Fig. A.2. The $2\nu\beta\beta$ decay ($n = 5$) and $0\nu\beta\beta$ peak without Majoron emission are also indicated. The energy resolution and energy scale non linearities in KamLAND-Zen are convolved in these spectra. Differences of spectra coming from

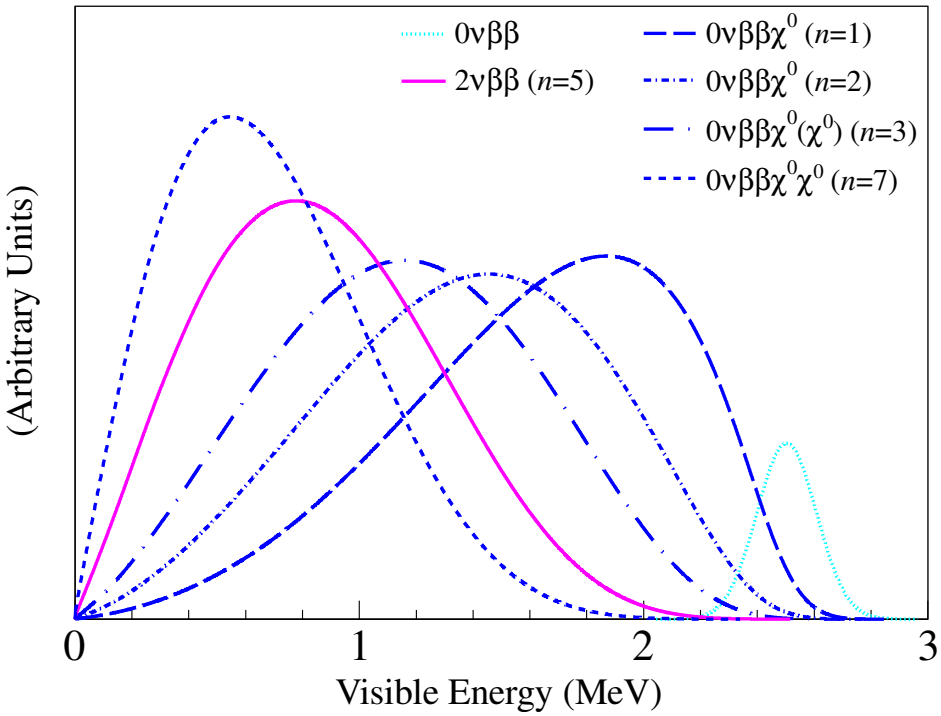

Figure A.2: Calculated energy spectra of ^{136}Xe, $2\nu\beta\beta$, $0\nu\beta\beta$ and Majoron emitting decay (linear scale).

the spectral index provide limits of Majoron emitting decay. To estimate the upper limit of each mode, the dominant contribution from $2\nu\beta\beta$ decay is fit simultaneously. The energy spectrum of selected events is shown in Fig. A.3. The decay rates are estimated from likelihood fit to the binned energy distribution between 0.5 and 4.8 MeV. Backgrounds in this fit are same as $2\nu\beta\beta$ and $0\nu\beta\beta$ decay estimation. Then total background is shown here and not shown individuals. The 90% C.L. upper limits for the different Majoron-emitting mode are drawn in blue lines. Estimation method is same as $0\nu\beta\beta$ decay. For a reference, that of $0\nu\beta\beta$ decay is also shown. Obtained decay rates are 0.07, 0.18, 0.41, and 1.8 (ton·day)$^{-1}$ for n = 1, 2, 3 and 7, respectively. Due to the peak position in each spectrum, $n = 1$ provides the most stringent limit since its peak is placed in the valley of the total spectrum, while n = 7 is the worst limit in this data set due to much backgrounds in low energy region.

A.3 Limits on the half-life of ^{136}Xe Majoron emitting $0\nu\beta\beta$ decay and the effective coupling constant

Lower limits on half-lives (90% C.L.) of ^{136}Xe Majoron emitting $0\nu\beta\beta$ decay with spectrum index n = 1, 2 , 3 and 7 are estimated to be

$$T_{1/2}^{0\nu\chi^0} > 2.6 \times 10^{24} \text{ yr } (n = 1),$$

$$T_{1/2}^{0\nu\chi^0} > 1.0 \times 10^{24} \text{ yr } (n = 2),$$

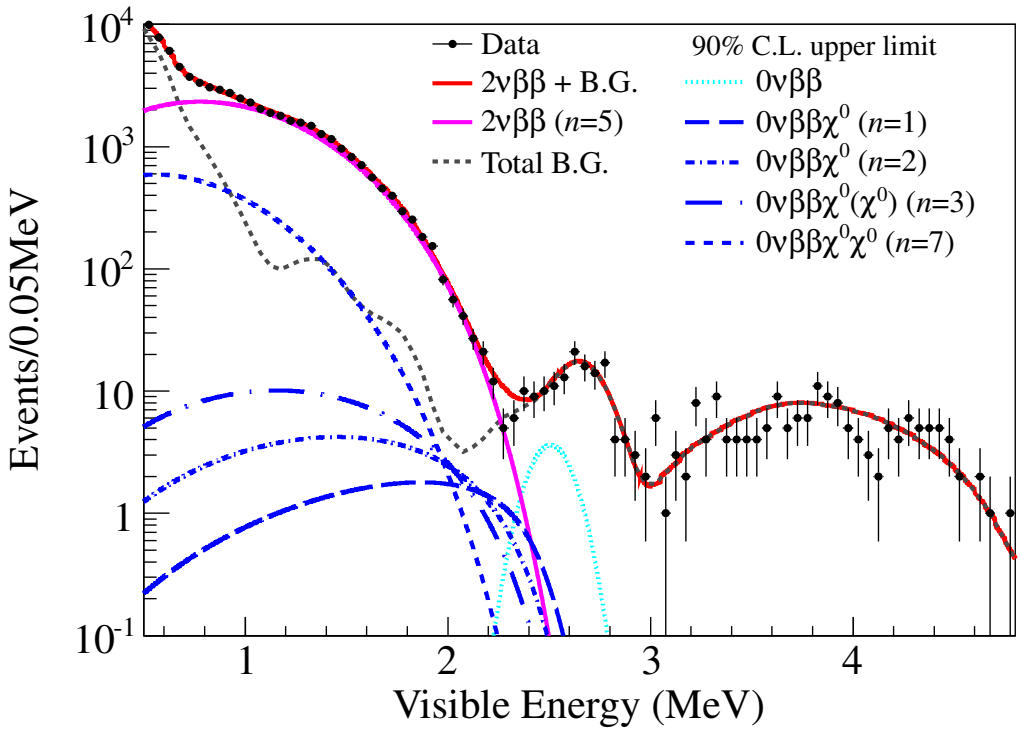

Figure A.3: Energy spectrum of ^{136}Xe $2\nu\beta\beta$ decay and best fit backgrounds in $0.5 < E < 4.8$ MeV. The 90% C.L. upper limit of $0\nu\beta\beta$ decay is also shown.

$$T_{1/2}^{0\nu\chi^0(\chi^0)} > 4.5 \times\ 10^{23}\ \text{yr}\ (n = 3),$$
$$T_{1/2}^{0\nu\chi^0\chi^0} > 1.1 \times\ 10^{22}\ \text{yr}\ (n = 7).$$

A lower limit on the ordinary (spectral index $n = 1$) Majoron-emitting decay is a factor of five more stringent than previous limits [49], and other decays of ^{136}Xe are estimated for the first time. The corresponding upper limit on the effective Majoron-neutrino coupling, $\langle g_{ee} \rangle$, is evaluated from Eq. A.3 and A.4. The relevant nuclear matrix elements M and the phase space factors G are summarized in Table A.2. From the half-life limit of the ordinary Majoron emitting $0\nu\beta\beta$ decay, the corre-

Table A.2: Relevant nuclear matrix elements and the phase space factors

	Nuclear Matrix Element		Phase space factor
n=1 (χ^0)	$M_F - M_{GT}$	1.57 - 3.24 [40, 41]	6.02×10^{-16} [54]
n=3 (χ^0)	M_{CR}	0.05 [103]	5.15×10^{-18} [103]
n=3 ($\chi^0\chi^0$)	$M_{F\omega^2} - M_{GT\omega^2}$	$10^{-3\pm1}$ [103]	1.06×10^{-17} [103]
n=7 ($\chi^0\chi^0$)	$M_{F\omega^2} - M_{GT\omega^2}$	$10^{-3\pm1}$ [103]	4.54×10^{-17} [103]

sponding upper limit on the effective Majoron-neutrino coupling $\langle g_{ee} \rangle$ is estimated to be

$$\langle g_{ee} \rangle < (0.8 - 1.6) \times 10^{-5} \text{ (90\% C.L.)},$$

where the range comes from nuclear matrix elements. This result is the most stringent limit on $\langle g_{ee} \rangle$ for all double-beta decay nuclei [28, 29, 31, 34, 36, 49, 62, 102]. It improves a limit more than a factor of 2 from the previous best measurement by NEMO-3 (^{100}Mo) as $\langle g_{ee} \rangle < (3.5 - 8.5) \times 10^{-5}$ [28]. The limits on the $\langle g_{ee} \rangle$ for various spectral index and models are presented in Table. A.3.

Table A.3: Different Majoron emission models [101, 103, 104, 105] and the corresponding limits on half-lives and $\langle g_{ee} \rangle$ (90% C.L.).

Model	Decay Mode	NG boson	L	n	Results from this work	
					$T_{1/2}$ (yr)	$\langle g_{ee} \rangle$
IB	$0\nu\beta\beta\chi^0$	no	0	1	2.6×10^{24}	$(0.8 - 1.6) \times 10^{-5}$
IC	$0\nu\beta\beta\chi^0$	yes	0	1	2.6×10^{24}	$(0.8 - 1.6) \times 10^{-5}$
ID	$0\nu\beta\beta\chi^0\chi^0$	no	0	3	4.5×10^{23}	0.68
IE	$0\nu\beta\beta\chi^0\chi^0$	yes	0	3	4.5×10^{23}	0.68
IIB	$0\nu\beta\beta\chi^0$	no	-2	1	2.6×10^{24}	$(0.8 - 1.6) \times 10^{-5}$
IIC	$0\nu\beta\beta\chi^0$	yes	-2	3	4.5×10^{23}	0.013
IID	$0\nu\beta\beta\chi^0\chi^0$	no	-1	3	4.5×10^{23}	0.68
IIE	$0\nu\beta\beta\chi^0\chi^0$	yes	-1	7	1.1×10^{22}	1.2
IIF	$0\nu\beta\beta\chi^0$	gauge boson	-2	3	4.5×10^{23}	0.013
"bulk"	$0\nu\beta\beta\chi^0$	bulk field	0	2	1.0×10^{24}	–

Note. The model notation in the first column follows references [101, 102]. The third, fourth, and fifth columns indicate whether the Majoron is a NG boson or not, its leptonic charge (L), and the model's spectral index (n), respectively.

The $\langle g_{ee} \rangle$ is also constrained from geochemical half-life measurement of ^{128}Te double-beta decay, and neutrino observation of SN1987A. The measurement of ^{128}Te provides the Majorana coupling constant as $\langle g_{ee} \rangle < 3 \times 10^{-5}$ [106]. From astrophysics, the $\langle g_{ee} \rangle$ constraint comes from neutrino time distribution of SN1987A and it indicates that Majoron emission does not play a dominant role in core collapse process. It exclude the range, $4 \times 10^{-7} < \langle g_{ee} \rangle < 2 \times 10^{-5}$ [107, 108, 109]. Thus, combination of our result and SN1987A's excludes a previously unconstrained region for the first time, and the limit down to $\langle g_{ee} \rangle < 4 \times 10^{-7}$ as shown in Fig A.4. From the relation of Eq. 2.15 and Eq. A.3, multiplying the square-root of the ratio of phase space factors to $\langle g_{ee} \rangle$ indicates that possible contribution of ordinary Majoron emitting decay mode to light Majorana neutrino exchange is strongly limited for $\langle m_{\beta\beta} \rangle > 20$ meV, which almost cover the inverted hierarchy.

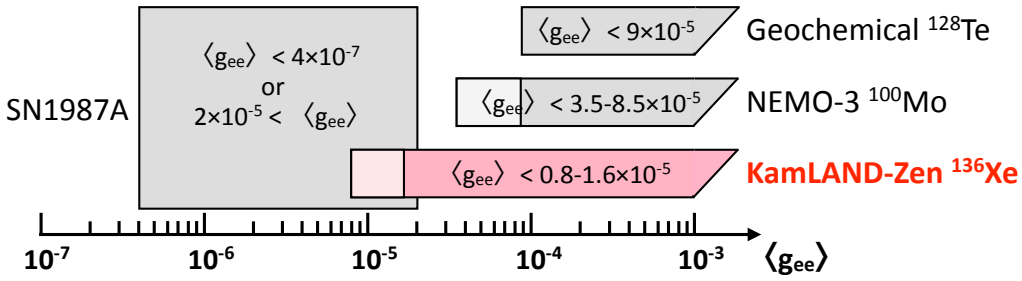

Figure A.4: Limits on $\langle g_{ee} \rangle$ from double beta decay experiments and SN1987A.

Appendix B

Decay chain of ^{238}U and ^{232}Th

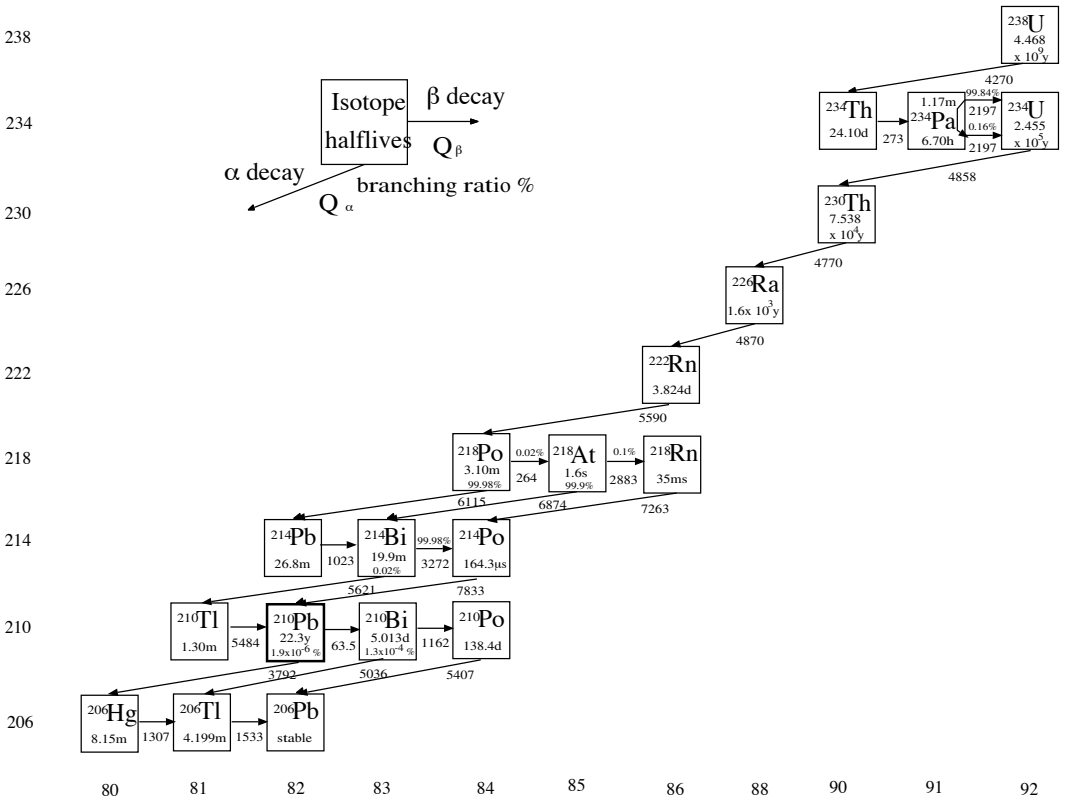

Figure B.1: Decay chain of ^{238}U

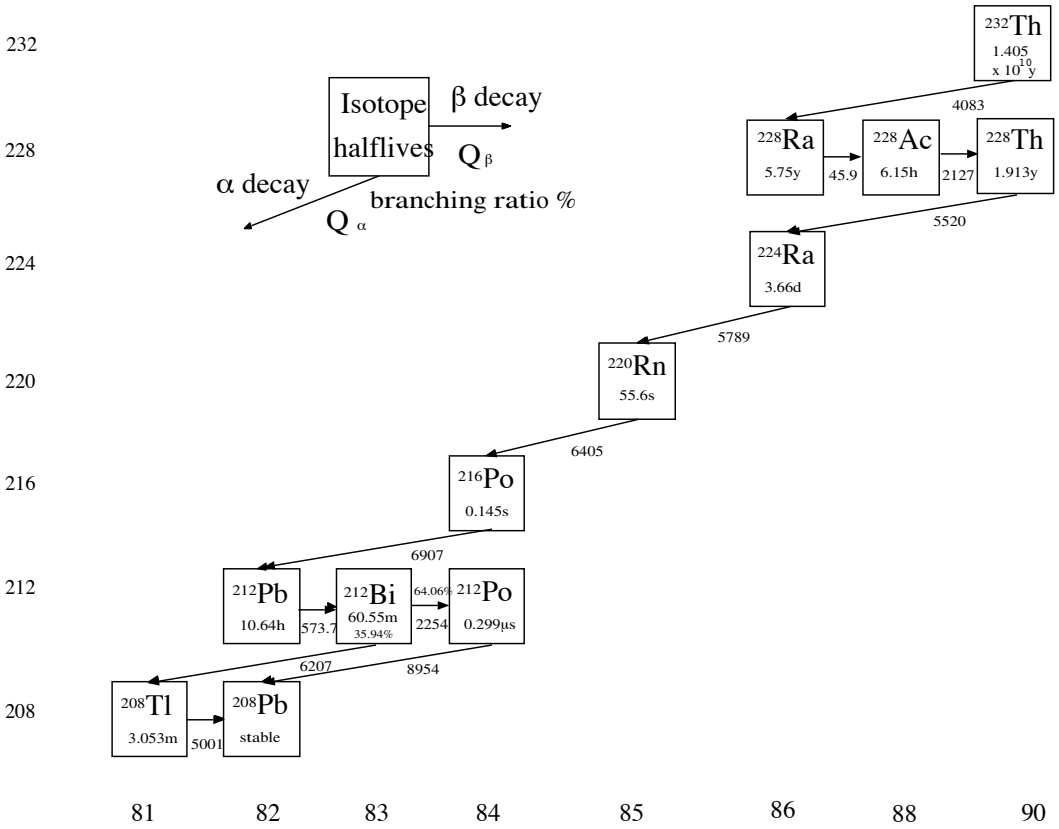

Figure B.2: Decay chain of ^{232}Th

Appendix C

Level diagrams

C.1 Calibration source

C.1.1 ^{208}Tl

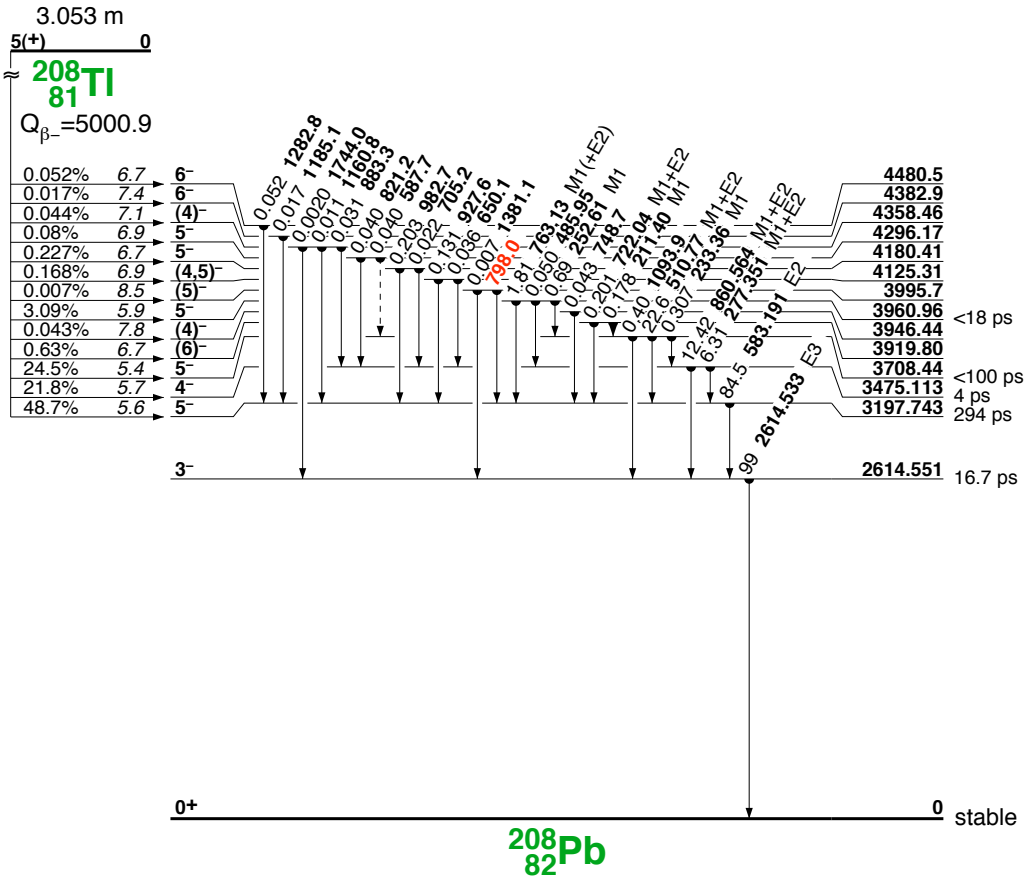

Figure C.1: A level diagram of ^{208}Tl [110].

C.1.2 ^{214}Bi

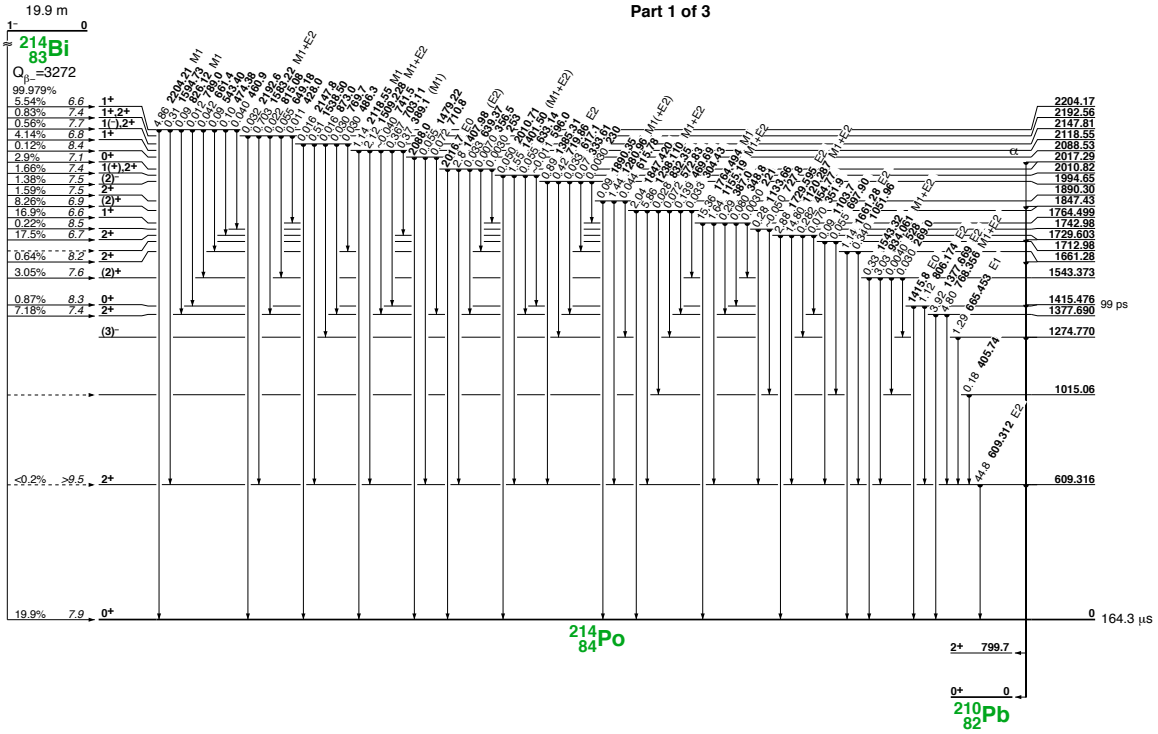
19.9 m
Part 1 of 3
214 83 Bi
Q(β-)=3272
99.979%
5.54% 6.6 1+
0.83% 7.4 1+,2+
0.56% 7.7 1(−),2+
4.14% 6.8 1+
0.12% 8.4
2.9% 7.1 0+
1.66% 7.4 1(+),2+
1.38% 7.5 (2)−
1.59% 7.5 2+
8.26% 6.9 (2)+
16.9% 6.6 1+
0.22% 8.5
17.5% 6.7 2+
0.64% 8.2 2+
3.05% 7.6 (2)+
0.87% 8.3 0+
7.18% 7.4 2+
(3)−
<0.2% >9.5 2+
19.9% 7.9 0+
2204.17
2192.56
2147.81
2118.55
2088.53
2017.29
2010.82
1994.65
1890.30
1847.43
1764.499
1742.98
1729.603
1712.98
1661.28
1543.373
1415.476
1377.690
1274.770
1015.06
609.316
0
99 ps
164.3 µs
214 84 Po
2+ 799.7
0+ 0
210 82 Pb

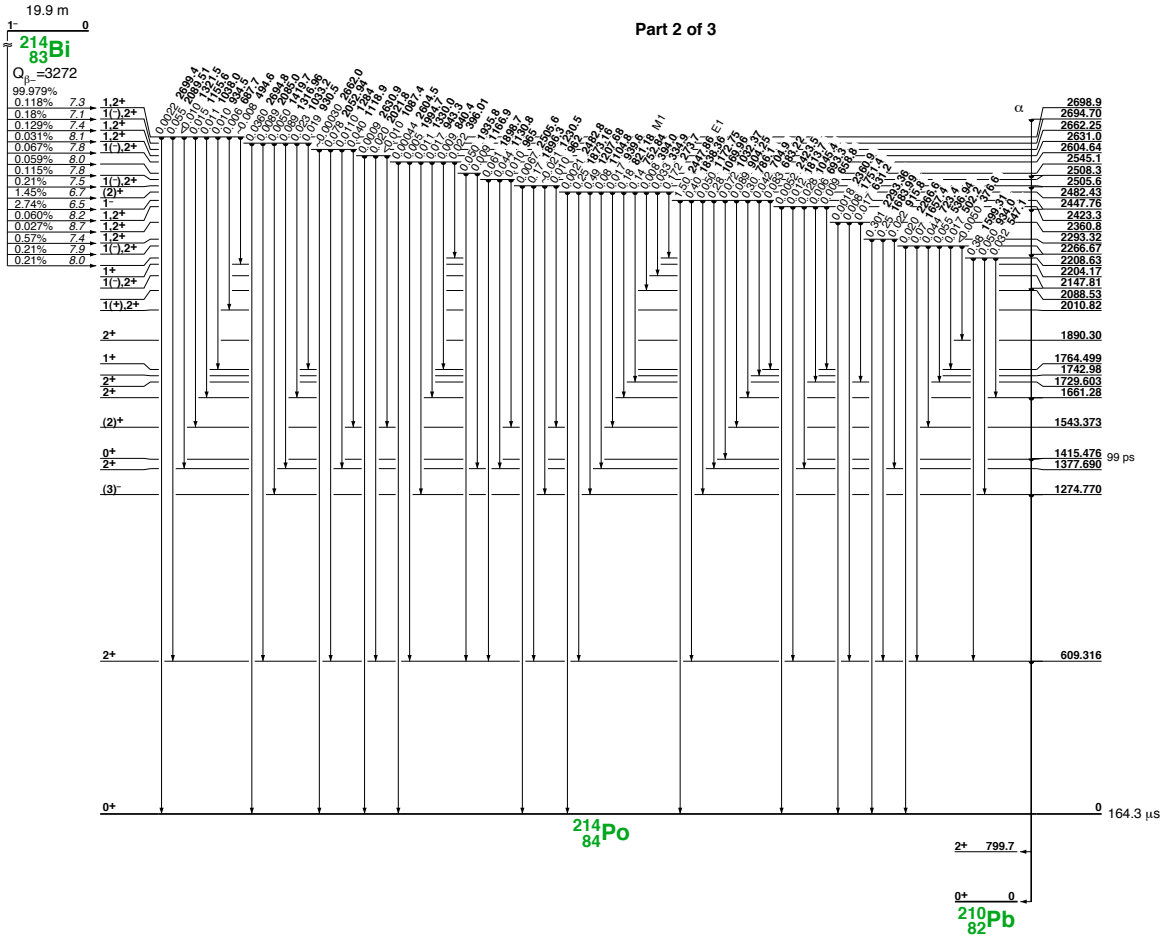
Part 2 of 3
19.9 m
1⁻ 0
214 83Bi
Q_β⁻=3272
99.979%
214 84Po
210 82Pb
2+ 799.7
0+ 0
α
99 ps
164.3 μs

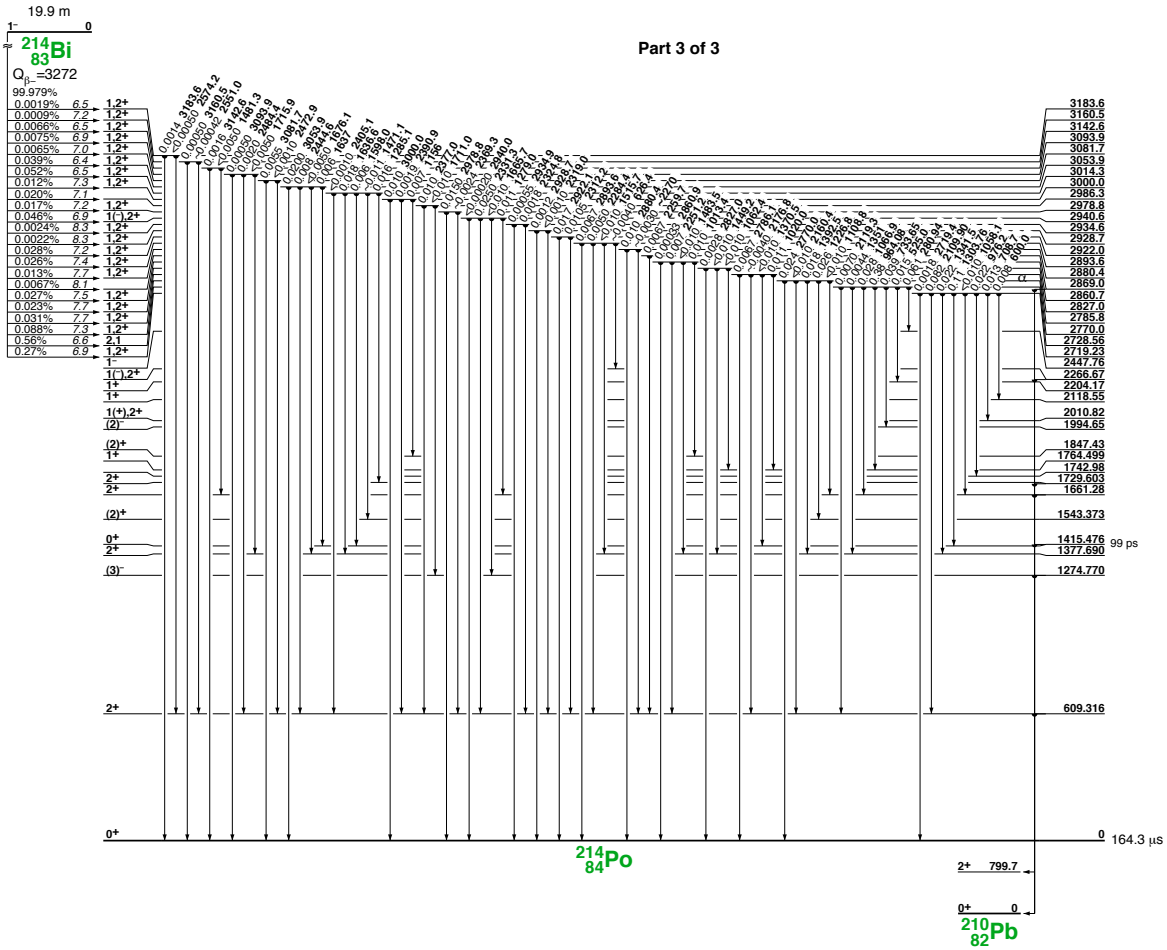

Figure C.2: Level diagrams of ^{214}Bi [110].

C.2 Four remained backgrounds in $0\nu\beta\beta$ region

- $^{110}\mathrm{Ag}^{m}$

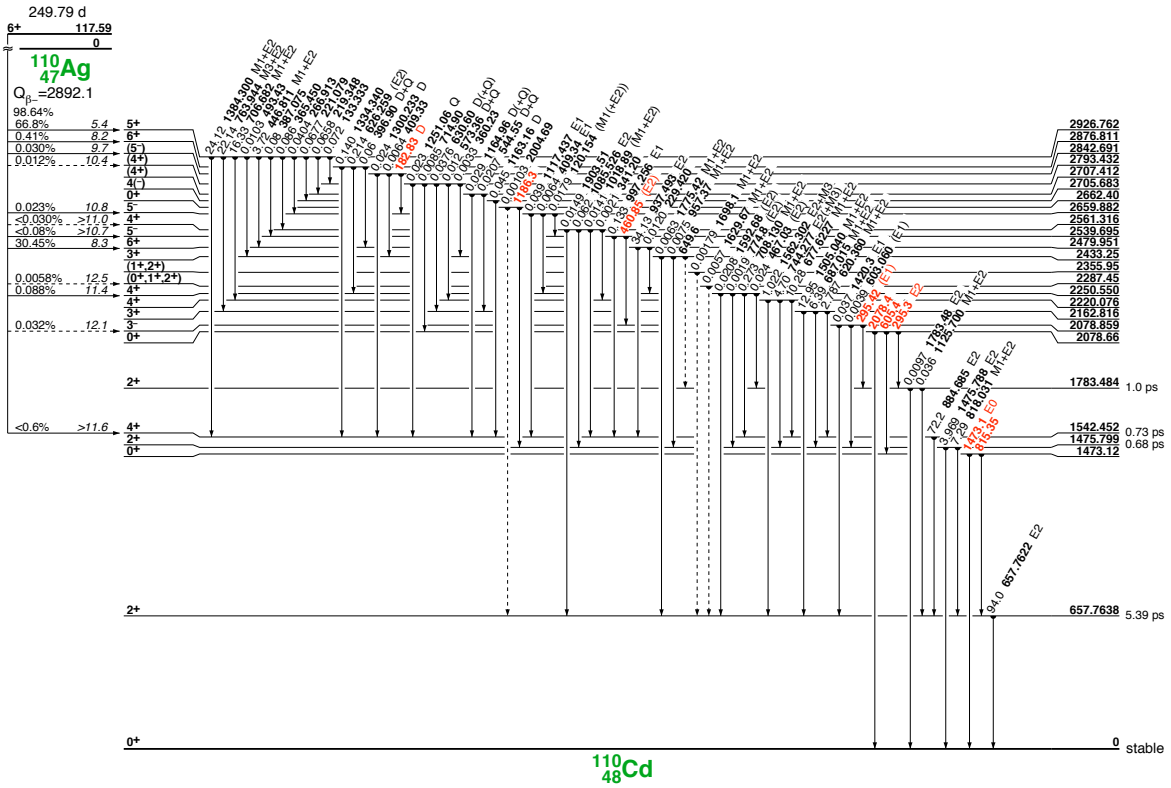

Figure C.3: A level diagram of $^{110}\mathrm{Ag}^{m}$ [110].

- ^{208}Bi

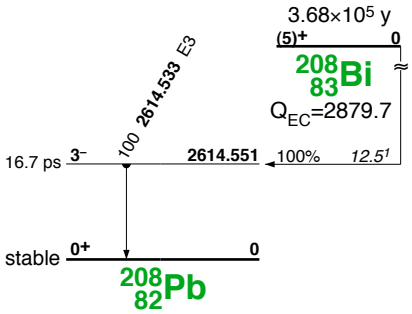

Figure C.4: A level diagram of ^{208}Bi [110].

- ^{88}Y

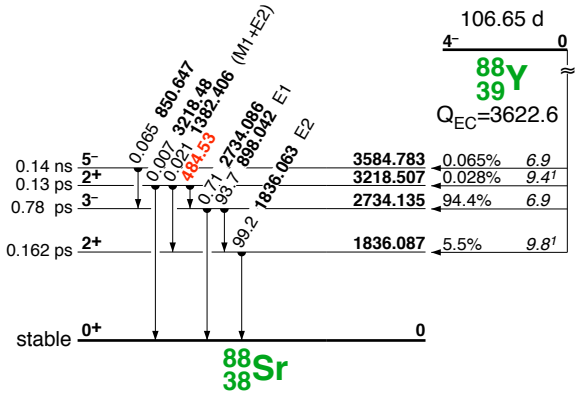

Figure C.5: A level diagram of ^{88}Y [110].

- ^{60}Co

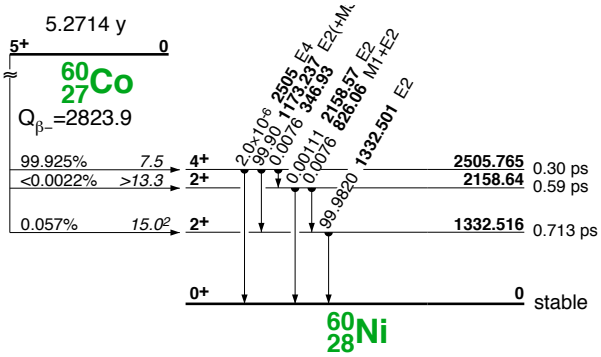

Figure C.6: A level diagram of ^{60}Co [110].

C.3 Cesium

- ^{134}Cs

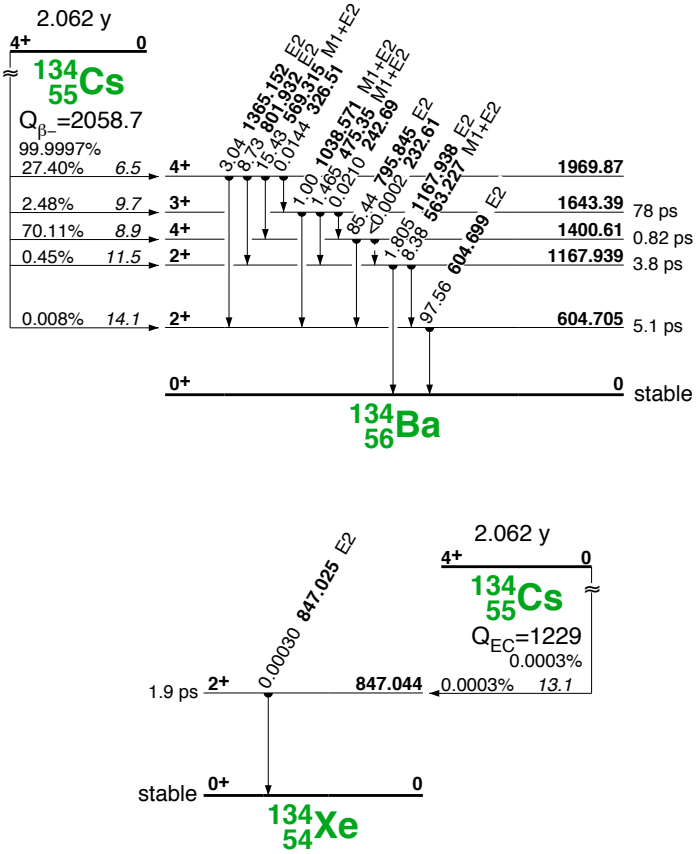

Figure C.7: Level diagrams of ^{134}Cs [110].

- ^{137}Cs

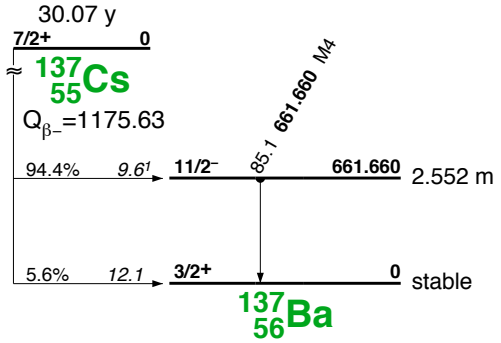

Figure C.8: A level diagram of ^{137}Cs [110].

Bibliography

[1] W. Pauli, Letter to L. Meitner and her colleagues (letter open to the participants of the conference in Tubingen) (1930).

[2] F. Reines and C. L. Cowan, Jr., Phys. Rev. **92**, 830 (1953).

[3] Y. Fukuda *et al.* (Super-Kamiokande Collaboration), Phys. Rev. Lett. **81**, 1562-1567 (1998).

[4] Q. R. Ahmad *et al.* (SNO Collaboration), Phys. Rev. Lett. **89**, 011301 (2002).

[5] K. Eguchi *et al.* (KamLAND Collaboration), Phys. Rev. Lett. **90**, 021802 (2003).

[6] K. Nakamura *et al.* (Particle Data Group), J. Phys. G **37** (2010).

[7] E. Majorana, Nuovo Cim. **14**, 171 (1937).

[8] M. Goeppert-Mayer, Phys. Rev. **48**, 512 (1935).

[9] W. H. Furry, Phys. Rev. **56**, 1184 (1939).

[10] J. Schechter and J. W. F. Valle, Phys. Rev. D **25**, 2951 (1982).

[11] H. V. Klapdor-Kleingrothaus, A. Dietz, H. L. Harney, I. V. Krivosheina, Mod. Phys. Lett. A **16**, 2409 (2001).

[12] H. V. Klapdor-Kleingrothaus, I. V. Krivosheina, A. Dietz, O. Chkvorets, Phys. Lett. B **586**, 198-212 (2004).

[13] H. V. Klapdor-Kleingrothaus, and I. V. Krivosheina, Mod. Phys. Lett. A **21**, 1547 (2006).

[14] The ALEPH Collaboration, The DELPHI Collaboration, The L3 Collaboration, The OPAL Collaboration, The SLD Collaboration, The LEP Electroweak Working Group, The SLD Electroweak and Heavy Flavour Groups, Phys. Reports **427**, 257 (2006).

[15] J. J. Gómez-Cadenas, J. Martín-Albo, M. Mezzetto, F. Monrabal, and M. Sorel, Riv. Nuovo Cim. **35**, 29 (2012); arXiv:1109.5515v2 [hep-ex].

[16] A. D. Sakharov, Pis'maZh. Eksp. Teor. Fiz. **5**, 32 (1967) [JETP Lett. **5**, 24 (1967)].

[17] A. G. Cohen, D. B. Kaplan, and A. E. Nelson, Nucl. Phys. B **349**, 727 (1991). A. E. Nelson, and D. B. Kaplan, Nucl. Phys. B **373**, 453 (1992).

[18] A. D. Linde, Phys. Lett. B **70**, 306 (1977).
A. H. Guth, E. J. Weinberg, Phys. Rev. Lett. **45**, 1131 (1980).
P. J. Steinhardt, Nucl. Phys. B **179**, 492 (1981).

[19] M. Fukugita, T. Yanagida, Phys. Lett. B **174**, 45 (1986).

[20] G. L. Fogli, E. Lisi, A. Marrone, D. Montanino, A. Palazzo, and A. M. Rotunno, arXiv:1205.5254v2 [hep-ex].

[21] E. Komatsu *et al.*, Astrophys. J. Suppl. **192**, 18 (2011).

[22] Ch. Kraus *et al.*, Eur. Phys. J. C **40**, 447-468 (2005).

[23] V. M. Lobashev *et al.*, Phys. Lett. B **460**, 227 (1999).

[24] KATRIN collaboration, Letter of Intent, arXiv:hep-ex/0109033v1

[25] K. Assamagan *et al.*, Phys. Rev. D **53**, 6065 (1996).

[26] R. Barate *et al.* (ALEPH Collaboration), Eur. Phys. J. C **2**, 395 (1998).

[27] F. T. Avignone III, S. R. Elliott, J. Engel, Rev. Mod. Phys. **80**, 481 (2008).

[28] A. S. Barabash, and V. B. Brudanin (NEMO Collaboration), Phys. At. Nucl. **74**, 312 (2011).

[29] J. Argyriades *et al.* (NEMO Collaboration), Phys. Rev. C **80**, 032501(R) (2009).

[30] A. S. Barabash, Ph. Hubert, A. Nachab, and V. I. Umatov, Phys. Rev. C **79**, 045501 (2009).

[31] J. Argyriades *et al.* (NEMO-3 Collaboration), Nucl. Phys. A **847**, 168 (2010).

[32] R. Arnold *et al.*, Phys. Rev. Lett. **95** 182302 (2005).

[33] M. F. Kidd, J. H. Esterline, W. Tornow, A .S. Barabash, V. I. Umatov, Nucl. Phys. A **821** 251 (2009).

[34] R. Arnold *et al.* (NEMO-3 Collaboration), Phys. Rev. Lett. **107**, 062504 (2011).

[35] A. Gando *et al.* (KamLAND-Zen Collaboration), Phys. Rev. C **86**, 021601(R) (2012).

[36] H. V. Klapdor-Kleingrothaus *et al.*, Eur. Phys. J. A **12**, 147 (2001).

[37] O. K. Manuel, J. Phys. G: Nucl. Part. Phys. **17**, s221 (1991);
T. Bernatowicz, J. Brannon, R. Brazzle, R. Cowsik, C. Hohenberg, and F. Podosek, Phys. Rev. C **47**, 806 (1993);
A. P. Meshik *et al.*, Nucl. Phys. A **809**, 275 (2008);
H. V. Thomas, R. A. D. Pattrick, S. A. Crowther, D. J. Blagburn, and J. D. Gilmour, Phys. Rev. C **78**, 054606 (2008).

[38] A. P. Meshik, C. M. Hohenberg, O. V. Pravdivtseva, and Y. S. Kapusta, Phys. Rev. C **64**, 035205 (2001).

[39] A. L. Turkevich, T. E. Economou, and G. A. Cowan, Phys. Rev. Lett. **67**, 3211 (1991).

[40] J. Menéndez, A. Poves, E. Caurier, and F. Nowacki, Nucl. Phys. A **818**, 139 (2009).

[41] F. Šimkovic, A. Faessler, H. Müther, V. Rodin, and M. Stauf, Phys. Rev. C **79**, 055501 (2009).

[42] M. G. Inghram, and J. H. Reynolds, Phys. Rev. **78**, 822 (1950).

[43] S. R. Elliott, A. A. Hahn, and M. K. Moe, Phys. Rev. Lett. **59**, 2020 (1987).

[44] A.M. Bakalyarov, A.Ya. Balysh, S.T. Belyaev, V.I. Lebedev, S.V. Zhukov, Phys. Part. Nucl. Lett. **2**, 77 (2005); arXiv:hep-ex/0309016.

[45] C. E. Aalseth *et al.*, Mod. Phys. Lett. A **17**, 1475 (2002).

[46] Yu. G. Zdesenko, F. A. Danevich, V. I. Tretyak, Phys. Lett. B **546**, 206 (2002).

[47] C. E. Aalseth *et al.* (The IGEX Collaboration), Phys. Rev. C **59**, 2108 (1999).

[48] C. E. Aalseth *et al.* (IGEX Collaboration), Phys. Rev. D **65**, 092007 (2002).

[49] R. Bernabei *et al.*, Phys. Lett. B **546**, 23 (2002).

[50] E. Andreotti *et al.*, Astropart. Phys. **34**, 822-831 (2011).

[51] E. Andreotti *et al.*, Phys. Rev. C **85**, 045503 (2012).

[52] M. Auger *et al.* (EXO Collaboration), Phys. Rev. Lett. **109**, 032505 (2012).

[53] S. Umehara *et al.*, Phys. Rev. C **78**, 058501 (2008).

[54] J. Suhonen and O. Civitarese, Phys. Rep. **300**, 123 (1998).

[55] E. Caurier, J. Menéndez, F. Nowacki, and A. Poves, Phys. Rev. Lett. **100**, 052503 (2008).

[56] J. G. Hirsch, O. Castaños, and P. O. Hess, Nucl. Phys. A **582**,124 (1995).

[57] K. Chaturvedi *et al.*, Phys. Rev. C **78**, 054302 (2008).

[58] M. Kortelainen and J. Suhonen, Phys. Rev. C **76**, 024315 (2007).

[59] M. Kortelainen and J. Suhonen, Phys. Rev. C **75**, 051303(R) (2007).

[60] F. Šimkovic *et al.*, Phys. Rev. C **77**, 045503 (2008).

[61] J. Barea and F. Iachello, Phys. Rev. C **79**, 044301 (2009).

[62] F. A. Danevich *et al.*, Phys. Rev. C **68**, 035501 (2003).

[63] A. Staudt, K. Muto, and H V. Klapdor-Kleingrothaus, Europhys. Lett. **13**, 31 (1990).

[64] O. Civitarese, and J. Suhonen, JoP Conf. ser. **173**, 012012 (2009) .

[65] T. R. Rodriguez and G. Martínez-Pinedo, Phys. Rev. Lett. **105**, 252503 (2010).

[66] M. J. Hwang *et al.* (KIMS Collaboration), Astroparticle Physics **31**, 412-416 (2009).

[67] M. Aunola and J. Suhonen Nucl. Phys. A **643**, 207 (1998).

[68] E. Caurier, F. Nowacki, A. Poves, and J. Retamosa, Nucl. Phys. A **654**, 973c (1999).

[69] W. C. Haxton, G. J. Stevenson, Jr., and D. Strottman, Phys. Rev. D **25**, 2360 (1981).

[70] P. Vogel and M. R. Zirnbauer, Phys. Rev. Lett. **57**, 3148 (1986).

[71] O. Civitarese, A. Faessler, and T. Tomoda, Phys. Lett. B **194**, 11 (1987);
T. Tomoda and A. Faessler, ibid. **199**, 475 (1987).

[72] E. Caurier, F. Nowacki, A. Poves, and J. Retamosa, Phys. Rev. Lett. **77**, 1954 (1996).

[73] M. Redshaw, E. Wingfield, J. McDaniel, and E. G. Myers, Phys. Rev. Lett. **98**, 053003 (2007).

[74] T. Araki *et al.* (KamLAND Collaboration), Phys. Rev. Lett. **94**, 081801 (2005).

[75] S. Abe *et al.* (The KamLAND Collaboration), Phys. Rev. Lett. **100**, 221803 (2008).

[76] A. Gando *et al.* (The KamLAND Collaboration), Phys. Rev. D **83**, 052002 (2011).

[77] T. Araki *et al.*, Nature **436**, 499-503 (2005).

[78] A. Gando *et al.* (The KamLAND Collaboration), Nature Geoscience **4**, 647-651 (2011).

[79] S. Abe *et al.* (KamLAND Collaboration), Phys. Rev. C **84**, 035804 (2011).

[80] A. Gando *et al.*, Astrophys. J. **745**, 193 (2012).

[81] O. Tajima, Master thesis, Tohoku University (2000).

[82] S. Enomoto, Doctor thesis, Tohoku University (2005).

[83] KiNOKO, Kinoko Is Network- distributed Object-oriented Kamland Online-system available at http://www.awa.tohoku.ac.jp/˜sanshiro/kinoko/

[84] B. E. Berger *et al.* (KamLAND Collaboration), JINST **4**, P04017 (2009).

[85] I. Shimizu, Doctor thesis, Tohoku University (2004).

[86] K. Nakajima, Doctor thesis, Tohoku University (2009).

[87] T. Hagner *et al.*, Astroparticle Physics **14**, 33-47 (2000).

[88] S. Abe *et al.* (KamLAND Collaboration), Phys. Rev. C **81**, 025807 (2010).

[89] G. J. Feldman and R. D. Cousins, Phys. Rev. D **57**, 3873 (1998).

[90] P. Napolitani *et al.*, Phys. Rev. C **76**, 064609 (2007).

[91] ENSDF, the Evaluated Nuclear Structure Data File available at http://ie.lbl.gov/databases/ensdfserve.html (2006).

[92] S. R. Elliott, V. E. Guiseppe, B. H. LaRoque, R. A. Johnson, and S. G. Mashnik, Phys. Rev. C **82**, 054610 (2010).

[93] A. S. Barabash *et al.*, JINST **6**, P08011 (2011).

[94] A. Shinohara, T. Saito, and H. Baba, Appl. Radiat. Isot. **37**, 1025 (1986).

[95] V. E. Noshkin, W. L. Robison, J. A. Brunk, T. A. Jokela, Journal of Radioanalytical and Nuclear Chemistry **248**, 741 (2001).

[96] W. C. Haxton and G. J. Stephenson, Jr., Prog. Part. Nucl. Phys. **12**, 409 (1984).

[97] A. Gando *et al.* (KamLAND-Zen Collaboration), Phys. Rev. C **85**, 045504 (2012).

[98] N. Ackerman *et al.* (EXO Collaboration), Phys. Rev. Lett. **107**, 212501 (2011).

[99] M. Günther *et al.*, Phys. Rev. D **54**, 3641 (1996).

[100] C. P. Burgess and J. M. Cline, Phys. Rev. D **49**, 5925 (1994).

[101] P. Bamert, C. P. Burgess, and R. N. Mohapatra, Nucl. Phys. B **449**, 25 (1995).

[102] R. Arnold *et al.* (NEMO Collaboration), Nucl. Phys. A **765**, 483 (2006).

[103] M. Hirsch, H. V. Klapdor-Kleingrothaus, S. G. Kovalenko, and H. Päs, Phys. Lett. B **372**, 8 (1996).

[104] C. D. Carone, Phys. Lett. B **308**, 85 (1993).

[105] R. N. Mohapatra, A. Pérez-Lorenzana, and C. A. de S. Pires, Phys. Lett. B **491**, 143 (2000).

[106] T. Bernatowicz *et al.*, Phys. Rev. Lett. **69**, 2341 (1992).

[107] M. Kachelriess, R. Tomàs, and J. W. F. Valle, Phys. Rev. D **62**, 023004 (2000).

[108] Y. Farzan, Phys. Rev. D **67**, 073015 (2003).

[109] R. Tomàs, H. Päs, and J. W. F. Valle, Phys. Rev. D **64**, 095005 (2001).

[110] R. B. Firestone, Table of Isotopes (Eighth Edition, Version 1.0, March 1996)